

The Lithium-Sulfur Battery: Design, Characterization, and Physically-based Modeling

Von der Fakultät für Energie-, Verfahrens- und Biotechnik
der Universität Stuttgart zur Erlangung der Würde eines
Doktor-Ingenieurs (Dr.-Ing.) genehmigte Abhandlung

Vorgelegt von
David Norman Fronczek
aus Würzburg

Hauptberichter: Prof. Dr. Wolfgang G. Bessler
Mitberichter: Prof. Dr. K. Andreas Friedrich
Prof. Dr. Stefano Passerini
Tag der mündlichen Prüfung: 1. Dezember 2015

Institut für Thermodynamik und Wärmetechnik
der Universität Stuttgart

2015

species amount dissolved
battery polysulfides specific
parameter USA transport
charge state active
discharge cycle value
cell size cycling
 table record image
experiment process
coating surface modeling
result volume total equilibrium

Li/S mechanism
mol thickness
electrode initial profile
 profile to compare
voltage implementation source
 area various
electrolyte similar source
 lithium sulfide tube
reaction present equation improve
 equation corresponding
Ce good CVD
 degree temperature
refinement solution theory
 theory report
carbon calibration
 energy liquid
 volume fraction
constant effect
 cathode SEM
 approach activation
capacity diffusion test
 dissolution shuttle
model determine entire
 formation fit conductivity
simulation shuttle
 furnace study
particle charging lithium
 Germany dissolution
work glovebox density
 step positive protocol
sulfur protocal
 positive
concentration

Contents

Abstract	9
1 Introduction	11
1.1 The need for better batteries	11
1.2 The lithium-sulfur system	13
1.3 Approach and scope of this work	15
2 Experimental work on lithium sulfide cathodes – materials and methods	17
2.1 The goal – coated lithium sulfide	17
2.2 Active material preparation	19
2.2.1 Ball milling	19
2.2.2 Chemical vapor deposition	20
2.3 Other materials and cell assembly	23
2.3.1 Anode materials and preparation	23
2.3.2 Separator	24
2.3.3 Electrolyte materials and preparation	24
2.3.4 Cathode additives	25
2.3.5 Electrode preparation	26
2.3.6 Cell assembly	27
2.4 Analysis and characterization methods	29
2.4.1 Microscopy	29
2.4.2 Chemical/physical methods	30
2.4.3 Electrochemical methods	30
2.5 Dead ends	32
3 Experimental work on lithium sulfide cathodes – results and discussion	34
3.1 Analysis of materials and electrodes	34
3.1.1 Scanning electron microscopy of materials	34
3.1.2 Scanning electron microscopy of electrodes	39
3.1.3 Transmission electron microscopy	44
3.1.4 Chemical/physical tests	45
3.1.5 Electrolyte optimization	48

3.2	Analysis of full cells	50
3.2.1	Introduction	51
3.2.2	Metrological considerations	53
3.2.3	Slow cyclic voltammetry	54
3.2.4	Impedance spectroscopy	56
3.2.5	Charge/discharge profiles	59
3.2.6	Cycling	61
3.3	Conclusions	65
3.3.1	Achievements	65
3.3.2	Possible improvements and outlook	66
4	Modeling the lithium-sulfur battery – theory and methods	68
4.1	Background	68
4.2	Modeling approach	71
4.2.1	Model design and basic assumptions	71
4.2.2	Transport	72
4.2.3	Electrochemistry	74
4.2.4	Electrical properties	77
4.2.5	Microstructure	78
4.2.6	Reaction mechanisms	79
4.2.7	Degradation	83
4.3	Simulation methodology	85
4.3.1	Implementation and computational framework	85
4.3.2	Parametrization and validation techniques	87
4.3.3	Quality control and error analysis	88
5	Modeling the lithium-sulfur battery – calibration and simulation results	91
5.1	Global two-step model	91
5.2	Multi-step model – literature parametrization	97
5.2.1	Introduction	97
5.2.2	Discharge at different rates	97
5.2.3	Cycling	99
5.2.4	Impedance	102
5.2.5	Conclusions	102
5.3	Multi-step model – reparametrization	104
5.3.1	Parameters determined from independent sources	104
5.3.2	Parameters calculated from experimental data	106
5.3.3	Parameters determined by equilibration	106
5.3.4	Parameters fitted to experimental data	107

5.4	Multi-step model – validation attempts	116
5.4.1	Rate capability	117
5.4.2	Cyclic voltammetry	118
5.5	Multi-step model – further simulations	120
5.5.1	Galvanostatic charge/discharge profiles	120
5.5.2	Transport	121
5.5.3	Impedance	125
5.5.4	Microstructure	128
5.6	Multi-step model – polysulfide shuttle extension	129
5.7	Conclusions	132
5.7.1	Achievements	132
5.7.2	Shortcomings	133
5.7.3	Possible improvements and outlook	134
6	Conclusions and outlook	137
6.1	Summary of achievements	137
6.2	Limitations of this work and ideas for future research	140
6.3	Outlook beyond academia	141
A	Appendix	143
A.1	List of symbols	143
A.2	Calculation of specific capacities, energy densities and state of charge .	146
A.3	List of chemicals	148
A.4	List of equipment	149
A.5	Parameter sets for the models	150
Bibliography		153
Cited publications		153
Own publications		180
Academic résumé of David N. Fronczek		184
Acknowledgments		186

List of abbreviations

AN	negative electrode (anode during discharge)
AFM	atomic force microscopy
BET	Brunauer, Emmett & Teller method (for determining surface areas)
CA	positive electrode (cathode during discharge)
CCCV	constant current – constant voltage (charging protocol)
CFD	computational fluid dynamics
CTR	charge-transfer reaction
CV	control volume – or – cyclic voltammetry
CVD	chemical vapor deposition
DAE	differential-algebraic equation
DFT	density-functional theory
EIS	electrochemical impedance spectroscopy
EL	battery separator (filled with liquid electrolyte)
elde	electrode
elyte	electrolyte
FVM	finite volume (discretization) method
MEA	membrane-electrode assembly (i.e. cathode, separator, and anode)
OCV	open-circuit voltage
PDE	partial differential equation
P&ID	piping and instrumentation diagram
ppm	parts per million
PS	polysulfide(s)
RTIL	Room-temperature ionic liquid
SCCM	standard cubic centimeter per minute (flow rate)
SBR	styrene butadiene rubber
SEI	solid electrolyte interphase
SEM	scanning electron microscopy
SoC	state of charge
SoH	state of health
TEM	transmission electron microscopy

Abstract

The lithium-sulfur (Li/S) battery is a promising candidate for next-generation electrochemical energy storage. Its unique combination of electrochemical performance, cost effectiveness, and environmental sustainability are unprecedented among battery materials. As of today, however, Li/S batteries are only used for few niche applications; a broader adoption of this technology is impeded by the yet unsatisfactory energy efficiency, self discharge, and limited lifetime. This work contributes to the advancement of Li/S technology in two respects: First, a novel kind of positive electrode, based on coated lithium sulfide (Li_2S), was prepared, tested and optimized. Second, the understanding of the complex chemical and physical processes in the cell was improved by creating and utilizing a computational model of the Li/S battery.

For the experimental part of this work, a chemical vapor deposition process was developed to apply a carbon coating to Li_2S particles. The focus of this work was on the optimization of the process chain from commercially available chemicals to the final coin cell in general and on the characterization of the materials and electrodes during various processing steps in particular.

For the modeling part, an existing multiscale electrochemical modeling framework was extended to enable full-cell simulations of Li/S batteries. The model includes a detailed description of electrochemistry, transport, and the evolution of solid phases in the cell, but also accounts for the electrical double layer and, in a generic fashion, the microstructure of the electrodes. Finally, a phenomenological description of the shuttle effect and associated cell degradation was implemented and analyzed. The parametrization and partial validation of the model makes use of original data collected for this purpose, but also data from literature.

Simulation results comprise charge/discharge profiles, cyclic voltammetry, impedance spectra, and the evolution of the chemical composition of both the electrolyte and the electrodes over time. The analysis of these results reveals limiting factors and suggests improved operating conditions.

The apt combination of theoretical and empirical methods enabled an improvement of the performance and cycle life of the novel cathode material, but also contributed to a more profound understanding of the Li/S battery.

Zusammenfassung

Lithium-Schwefel (Li/S)-Batterien sind eine vielversprechende Technologie für elektrochemische Energiespeicher der nächsten Generation. Sie vereinen auf bisher unerreichte Weise hervorragende Leistungsdaten, Kosteneffizienz und Umweltverträglichkeit. Bisher kommen Li/S-Batterien jedoch nur für wenige Spezialanwendungen zum Einsatz. Der Eignung für ein größeres Marktsegment stehen die derzeit noch unbefriedigende Energieeffizienz, Selbstentladung und Lebensdauer entgegen. Die vorliegende Arbeit trägt zur Weiterentwicklung der Li/S-Technologie in zweifacher Weise bei: Zum einen wurde ein neuartiger Elektrodentyp, basierend auf beschichtetem Lithiumsulfid (Li_2S), hergestellt, getestet und optimiert; zum anderen wurde durch die Modellierung und Simulation einer Li/S-Zelle das Verständnis der komplexen chemischen und physikalischen Vorgänge in der Batterie verbessert.

Für den experimentellen Teil der Arbeit wurde ein Verfahren zur chemischen Gasphasenabscheidung von Kohlenstoff auf Li_2S -Partikeln entwickelt. Das Hauptaugenmerk der Arbeit lag jedoch auf der Optimierung der gesamten Prozesskette ausgehend von kommerziell erhältlichen Chemikalien bis zur fertigen (Knopf-)Zelle, insbesondere aber auf der dazu notwendigen Charakterisierung der Materialien und Elektroden.

Für den theoretischen Teil wurde ein skalenübergreifendes elektrochemisches Modell so erweitert und kalibriert, dass damit Simulationen der Li/S-Batterie möglich sind. Das Modell enthält eine detaillierte Beschreibung der elektrochemischen Reaktionsmechanismen, der Transportvorgänge im flüssigen Elektrolyten und der Ausfall- und Auflösungsreaktion in den porösen Elektroden. Daneben werden die elektrochemische Doppelschicht sowie eine effektive Beschreibung der Mikrostruktur berücksichtigt. Schließlich wurde eine phänomenologische Beschreibung des Shuttle-Effekts sowie der Degradation der Zelle implementiert und ausgewertet. Die Parametrierung und teilweise Validierung des Modells erfolgte anhand der eigenen experimentellen Daten sowie anhand ausgewählter publizierter Daten und Ergebnisse aus der Literatur. Mit dem solchermaßen kalibrierten Modell wurden Lade- und Entladekurven, Cyclicvoltammetrie, Impedanzspektren sowie die zeitliche Entwicklung der chemischen Zusammensetzung des Elektrolyten und der Elektroden simuliert. Von den Ergebnissen lassen sich unter anderem Rückschlüsse auf limitierende Prozesse oder günstige Betriebsbedingungen ziehen.

Durch die Kombination von theoretischen und empirischen Verfahren konnten die Leistung und Lebensdauer des neuen Kathodenmaterials erhöht sowie gleichzeitig ein Beitrag zum besseren Verständnis der Li/S Batterie geleistet werden.

1 Introduction

Today, batteries are ubiquitous and many appliances and products we use in our daily life would not be possible at all without portable and affordable electrochemical energy storage. Still, further advances in capacity, lifetime, and cost of batteries will open up new possibilities and markets. Some of the future uses have long been anticipated, but could not yet be put into practice because of these limitations, while others may have been unthought of before.

1.1 The need for better batteries

Since the emergence of modern batteries in the mid 19th century, their performance has been improving continuously [1]. For decades, however, batteries were not widely used except for small gadgets (clocks, torches, remote controls, ...) and as starting, lighting, and ignition (SLI) automotive batteries. The situation changed with the advent of portable electronics in the 1980s and the pace at which battery technology evolves has increased ever since [2, chap. 2]. Durability and safety of batteries were mostly improved by engineering and design optimizations, whereas capacity and power density saw the biggest improvements whenever new battery chemistries were introduced to the market. Looking at Fig. 1.1, one can see that actually most of the improvement in terms of energy density up to date was due to new chemistries. Especially when Li-ion batteries were introduced in the 1980s [3, 4], they enabled many new applications including truly portable communication, sensors, and entertainment. While the cheaper Pb-acid batteries still dominate the SLI and backup power market, today's high-capacity state-of-the-art rechargeable batteries are almost exclusively Li-ion systems with graphite anodes and intercalation cathodes made from various host materials such as cobalt oxide or olivines [5]. Even though one has to be careful when comparing performance metrics for different cells without full knowledge about data acquisition and validation [6], the upper limits in terms of energy density are commonly agreed to be well below 500 Wh/kg for Li-ion batteries, a value that is considered to be too low for many practical applications including long-range electromobility [7, 8]. Additionally, the cost of today's technologies is too high for many large-scale applications, such as grid storage [9]. Finally, there is a growing concern about the supply, processing and recycling of battery materials both in terms of technical availability and cost [10–13].

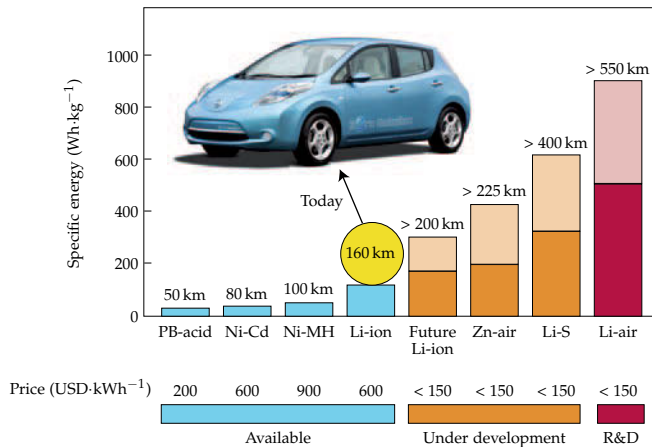


Figure 1.1: Energy density of various battery chemistries compared. The lighter regions of the bars show the range of anticipated practical energy densities. Reproduced from [14].

New chemistries are not invented out of the blue, though. From a theoretical point of view, the properties of many potential future battery systems are well known, including those of Li/S. The challenge is to exploit this potential without compromising security, reliability, or durability known from established materials [15, 16]. In Germany, two national goals were formulated that cannot be achieved without significant investments in battery development, production, and deployment: the “energy revolution” and the advent of electromobility. Regarding the former, 80 % of Germany’s total electrical energy (and 60 % of the total gross domestic energy consumption) shall be supplied by renewables no later than 2050 [17, pp. 4f]; regarding the latter, one million electric cars shall be deployed by 2020 [18, 19]. Several national research programs support these goals [19–23] and some noteworthy results have already been obtained [23, 24]. In the U.S., national goals include 25 % of electricity consumed to be generated by cost-competitive solar and wind power by 2025 as well as one million all-electric or plug-in hybrid electric vehicles on the road by the same time [25]. Founded in 2012, the JCESR [26] is funding and conducting research to meet these targets. Also, there are dozens of ARPA-E¹ projects dedicated to the development of advanced batteries. Similar programs exist in many industrialized and developing countries worldwide. Finally, there are several high-stake industrial ventures such as the USABC [27] or KLIB [28] which support research and development of next-generation batteries as part of their mission.

¹Advanced Research Projects Agency-Energy, U.S. Department of Energy, 1000 Independence Ave. SW, Washington, DC 20585, USA

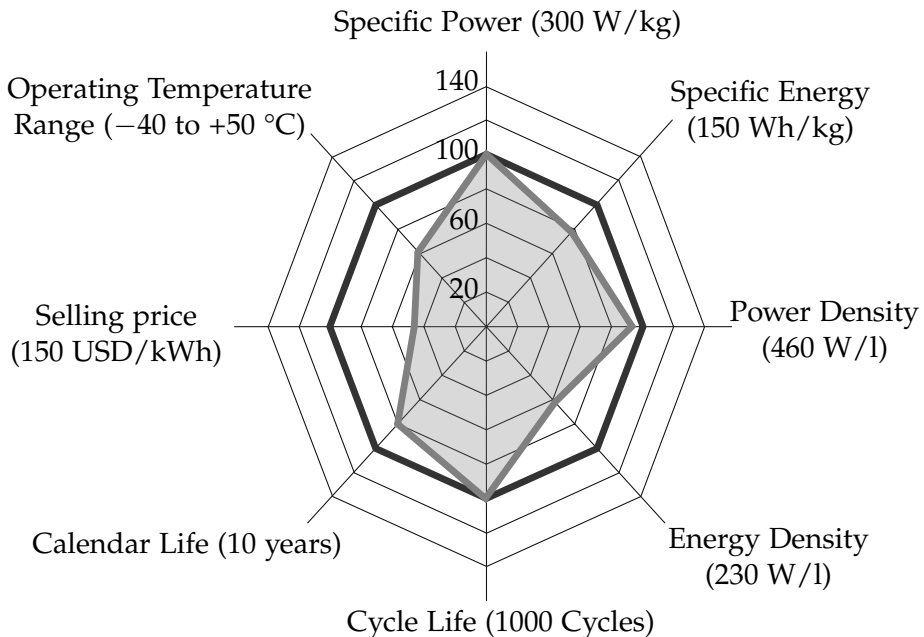


Figure 1.2: A “spider plot” showing the various requirements for batteries in all-electric vehicles (numbers = 100 % = USABC targets). The shaded area represents commercial Li-ion technology in 2006. Reproduced from [35].

While advances in Li-ion technology are to be expected [29, 30], their maximum specific capacity and energy density are constrained by fundamental limits, see appendix A.2. Also, the requirements for batteries are complex (Fig. 1.2) and Li-ion based cells may not fit every application’s profile. This is where lithium-sulfur (Li/S) batteries come into play: They have the potential to overcome most of the aforementioned limitations by providing considerably increased energy density at a lower cost [31, 32]. Although a thorough analysis of all raw materials and processing costs of this type of cell at an industrial scale has not yet been done in detail, there is a very promising case study by students of the Haas School of Business², cf. Ref. [33]. Additionally, sulfur, as well as all other components of sulfur cathodes, are relatively abundant, environmentally benign and conflict-free [10–13, 34].

1.2 The lithium-sulfur system

The Li/S cell is a conversion cell, where sulfur is reduced from S₈ to Li₂S according to the following global reaction:



²Haas School of Business, University of California, 2220 Piedmont Ave, Berkeley, CA 94720, USA

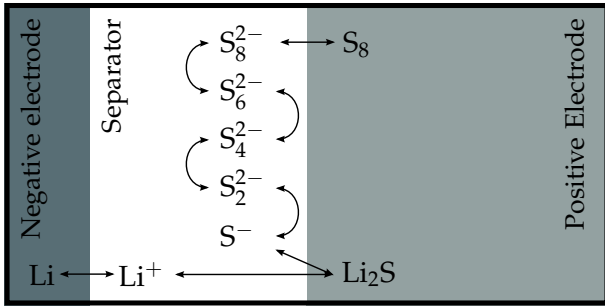


Figure 1.3: General layout of a liquid-electrolyte lithium-sulfur cell and proposed reaction mechanism.

Assuming pure, solid reactants and products at room temperature, the specific energy of the Li/S cell is $\sim 2600 \text{ Wh/kg}$ [36], its energy density $\sim 2800 \text{ Wh/l}$ [29, 37], and its specific capacity 1675 Ah/kg , cf. appendix A.2. These values are considerably higher than those of today's batteries. Taking into consideration that only a fraction of the theoretical capacity can be practically exploited, it is expected that Li/S cells can still achieve 2–3 times the performance of the best cells in use today [30, 33, 37].

Li/S cells have been known for decades; the first patent involving Li/S technology was filed in 1958 [38]. Initially, however, the Li/S system was investigated as a high-temperature battery only [39, 40], i.e. operating at a temperature above 115°C , the melting point of sulfur. In this setup, the positive electrode of the cell is liquid so that material transport and microstructure are of no concern. This concept is widely used in sodium-sulfur (Na/S) batteries [41], but the development of high-temperature Li/S batteries never reached commercialization.

In the late 1970s, first attempts were made to build Li/S cells using liquid electrolytes at room temperature [42, 43]. With this kind of cell, both sulfur and lithium sulfide are present as solids, but the reduction/oxidation reactions take place among polysulfide species dissolved in the liquid electrolyte. While the precise reaction mechanism is still discussed controversially [44], it definitely includes several dissolved species of the form Li_2S_x and/or S_x^{2-} . The general layout of such a Li/S battery along with the reaction mechanism assumed for this study is shown in Fig. 1.3.

Despite their very attractive properties, Li/S batteries have not yet been introduced to the battery market, except for some special niches. There are only few companies offering Li/S cells [45–47], but many more are engaged with research and development as well as material supply. Besides issues with the commonly used lithium metal negative electrode [15, 48, 49], there are two main problems causing degradation and other side effects preventing widespread adoption of Li/S batteries so far: First, there is the large mechanic stress induced by the expansion and shrinkage of the electrode due to volume changes of the active material during cycling [50], which eventually

leads to structural degradation of the cathode and possibly loss of electronic contact between the active material and the current collector. Second, there is the polysulfide shuttle, which has long been known to cause chemical degradation as well as poor charging efficiency, at least under certain circumstances [51]. On the other hand, the shuttle provides an inherent means of overcharge protection – a feature sometimes artificially added to Li-ion batteries [52]. There are many more side reactions and degradation mechanisms; most of them have not yet been studied in detail [53].

Close to 500 articles on Li/S batteries and related technologies were published in the past year alone, more than in the entire scientific history before³. Some of these publications are of purely academical interest, since they require very exotic or expensive materials, processing, or analysis steps, e.g. [55–57]. Most of them, however, contribute directly to the improvement of specific material components, electrode and cell designs or analysis techniques, thereby bringing Li/S batteries closer to actual applications. These findings gradually enable building better batteries, but more fundamental research is needed to truly understand this complex and challenging, but also very promising electrochemical system.

1.3 Approach and scope of this work

This work contributes to a better understanding of Li/S batteries by analyzing their properties and performance both experimentally and theoretically. For the experimental part, a new method for synthesizing carbon-coated lithium sulfide (Li_2S) nanoparticles for use in porous electrodes was tested and optimized. Also, various electrolyte compositions and additives were investigated in terms of cycling performance and compatibility with the novel electrode. The materials were studied by means of microscopy, physical and chemical analysis methods. In addition, full cells with lithium metal counter electrodes were assembled and tested electrochemically.

The modeling part comprises the design, implementation, parametrization, and application of a model of the Li/S cell, based on the state of the literature. Extensions to the existing electrochemical modeling framework DENIS [58, 59] were implemented, enabling computer simulations of the Li/S battery in various kinds of experiments including charge/discharge cycling, electrochemical impedance spectroscopy, and cyclic voltammetry. The model was calibrated, partly validated against experimental results, and used to investigate the charge/discharge mechanism, rate performance, electrolyte composition and – phenomenologically – the degradation of the cell. Besides using data available from literature, original experiments were conducted to specifically record data for the purpose of validating the model. Contrariwise, preliminary modeling results provided feedback to improve material and electrode design.

³data according to Thomson Reuters Web of Science, April 2014; see also Ref. [54]

This thesis is structured in six chapters. Following this introduction, the materials and experimental methods are described in chapter 2. In addition to listing and describing the experiments, the rationale behind each material or methodology choice is explained. Also, the design, setup, and optimization of the carbon coating furnace and the corresponding protocol is treated in this chapter. The results obtained are presented and discussed in chapter 3. Besides the successful demonstration of the use of carbon-coated lithium sulfide in a Li/S cell, valuable information on the material and cell level was collected and improvements to the performance and lifetime of Li/S cells are reported. Chapter 4 contains information on the modeling and model calibration methodology as well as a description of the Li/S model itself. Some theoretical background including detailed explanations of the governing equations used for transport, thermodynamics, and electrochemistry is also part of this chapter. The proposed reaction mechanism is discussed along with possible routes of degradation. In chapter 5, the results of the simulations are presented, interpreted and discussed. Finally, the last chapter summarizes and interprets the achievements of this work and the impact on Li/S research. In the closing remarks, suggestions for future research are discussed alongside with progress in the field of electrochemical energy storage and its applications in general. Lengthy calculations, listings, and full bibliographic records can be found in the appendix.

2 Experimental work on lithium sulfide cathodes – materials and methods

The experimental part of this work was carried out from 04/2012 to 05/2013 at Lawrence Berkeley National Laboratory¹ under the supervision of Prof. Elton J. Cairns and in collaboration with his research group as well as the inorganic chemistry team at The Molecular Foundry² and other members of the BATT program [60].

2.1 The goal – coated lithium sulfide

Lithium-sulfur cells have been studied for more than four decades. While the optimization of electrolytes, additives and counter-electrodes is critical for the long-term success of Li/S batteries, most research currently focuses on the design of the cathode's microstructure. Many different approaches for optimizing it have been tried with some success, as discussed in several review articles [14, 30, 37, 61, 62].

Most conventional electrode designs suffer from poor cyclability, which has its ultimate cause in the mechanic stress induced by the swelling and shrinking of the active material during (de-)lithiation as well as side reactions of the dissolved polysulfides. Thus, a straightforward approach to mitigate degradation is to prevent polysulfide dissolution altogether. This can be achieved by a) choosing a gel or solid electrolyte with virtually no polysulfide solubility [63–66], or b) chemically modifying the electrode's active surface so that sulfur is more strongly bound [67, 68], or c) introducing mechanical barriers on top of the electrode [69, 70] or inside the electrode [71, 72]. For the latter approach, carbon coatings have been suggested [71, 73], but conductive polymer coatings [72] have also been tried, as well as combinations thereof [74]. Of the above references, however, only [73] had been published at the time this work was started. The goal of this work is to prepare stable electrodes for Li/S cells synthesized from carbon-coated lithium sulfide. The coating around the active material, illustrated in Fig. 2.1, is intended to prevent direct contact between sulfur and the electrolyte,

¹Environmental Energy Technologies Division, Lawrence Berkeley National Laboratory, 1 Cyclotron Road, Berkeley, CA 94720, USA

²The Molecular Foundry, Lawrence Berkeley National Laboratory, 1 Cyclotron Road, Berkeley, CA 94720, USA

ensure electronic conductivity, provide a stable, large surface area for Li^+ exchange between the electrolyte and the active material, and maintain mechanic stability all at the same time. In order to meet these requirements, the average size of the individually coated particles must not exceed a few micrometers. For larger particles, both the mechanical stability and the speed of diffusion inside the particles pose significant problems.

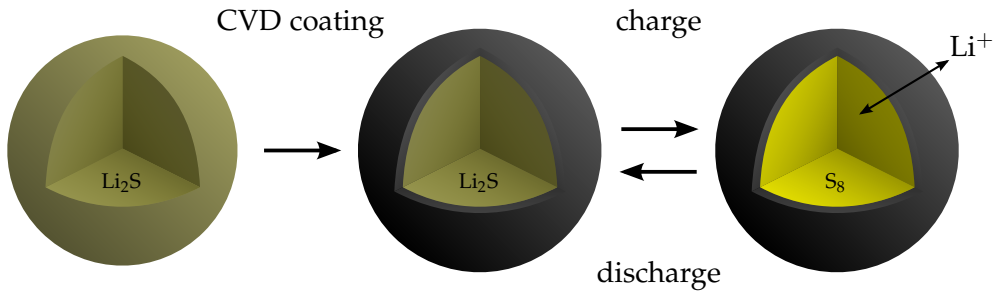


Figure 2.1: Schematic of the core-shell material concept.

Despite recent progress in terms of cycling stability [75, 76], all cathodes synthesized from elemental sulfur suffer from a common problem: During discharge, the sulfur is converted to lithium sulfide, the density of which is considerably lower than that of sulfur. Whether the material is converted in place or dissolved and re-precipitated, the volume of the fully discharged active material (Li_2S) is 172 % that of the fully charged active material (S_8). If the initial structure of the electrode is formed while (mostly) S_8 is present, either the whole electrode will grow and shrink during cycling [50] or at least some of the active material will deposit in places where there was no sulfur initially. Regardless of how elaborate the structure of the cathode may be prepared initially, this poses a high risk of destroying or downgrading the electrode's microstructure during cycling.

The alternative approach, followed in this work, is to synthesize the electrode in the discharged state, i.e. from Li_2S . While this does not prevent any degradation by itself, it ensures that there is enough room for all the active material in the porous structure of the pristine electrode. Besides, this approach is compatible with most other techniques for improving the performance and durability of Li/S cells such as nanostructured electrode design [77–80], electrolyte additives [81–83], or protective layers on either electrode [55, 84, 85]. The downside of using Li_2S is that this material is extremely sensitive to moisture and oxygen, so that the processing needs to be done in an inert and dry atmosphere. This disadvantage is mitigated, to some degree, by the carbon-coating strategy outlined above: Once the coating has been applied, the material should be considerably less reactive and could thus be processed without special precautions.

Electrodes are prepared from the materials and tested in coin cells. Except for the ready-made separator membranes, the cells were prepared from scratch. The individual steps of the preparation process are outlined in Fig. 2.2 and described in detail in the following sections.

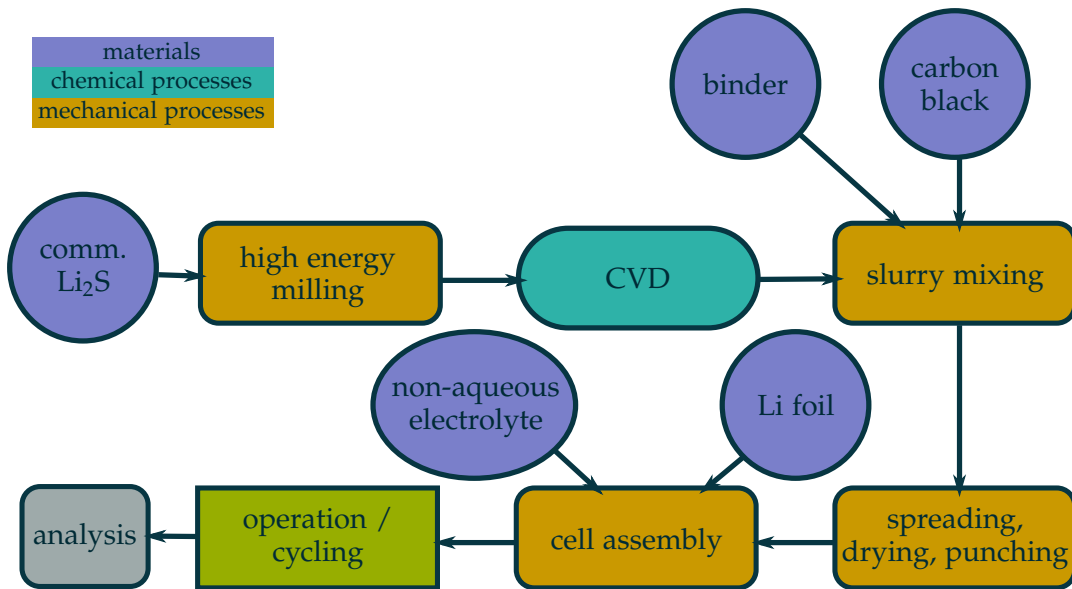


Figure 2.2: Flowchart illustrating the basic steps of the cell preparation process.

2.2 Active material preparation

Undoubtedly, the most delicate step of this project is the preparation of the cathode active material. To meet the requirements outlined in section 2.1, a novel coating procedure was established and optimized. It consists of a ball-milling step, followed by subsequent alternating steps of chemical vapor deposition and mechanical mixing. Since Li₂S is highly susceptible to trace moisture and – to some degree – to oxygen, all preparation steps must be carried out in an inert Argon atmosphere.

2.2.1 Ball milling

As a first step, pure, commercially available lithium sulfide (Sigma Aldrich, St. Louis, MO, USA) is ball-milled to reduce the particle size to $\lesssim 2 \mu\text{m}$. While even smaller particle sizes are considered beneficial for both sulfur utilization and rate performance, ball-milling provides an easy, affordable and reproducible way of reducing the particle size to a reasonable value. The instrument used for ball-milling is a 8000M Mixer/Mill

(Thomas Scientific, Swedesboro, NJ, USA) rotating at 1060 RPM. For each run, its air-tight stainless steel milling chamber is loaded with 1–2 mg of Li₂S and a set of yttria stabilized zirconia (YSZ) grinding balls (type 4039GM, Inframet Advanced Materials, Manchester, CT, USA). The milling balls come in three sizes (3.0, 5.0, and 10.0 mm), which are added to the Li₂S powder in the ratio of 4:6:4:1 by weight (large : medium : small : Li₂S). In order to keep the sulfur content of the active material as high as possible, no carbon black or other material is added to the milling container, even though it is known to improve the milling performance slightly [77]. To avoid exposure to moisture or air, the material is loaded into and collected from the milling chamber inside the glovebox. The milling procedure itself consists of six milling rounds, 20 min. each, with a 20 min. break between subsequent runs to avoid overheating. The ground up material is collected inside the glovebox and stored in a sealed glass vial until used.

2.2.2 Chemical vapor deposition

In order to apply the carbon coating to the Li₂S particles, a CVD furnace installation had to be designed and set up which allows for the treatment of the material without exposure to ambient air.

Furnace design and installation. The tube furnace used for the coating (Lindberg Blue M Mini-Mite; Thermo Fisher Scientific, Waltham, MA, USA) consists of a quartz tube with a diameter of 1.0 " which can be inserted into the heating chamber so that both ends protrude from the furnace. The quartz tube's ends are sealed by an O-ring seal each with a flange for connecting Swagelok tubing. A P&ID drawing of the final CVD setup is presented in Fig. 2.3.

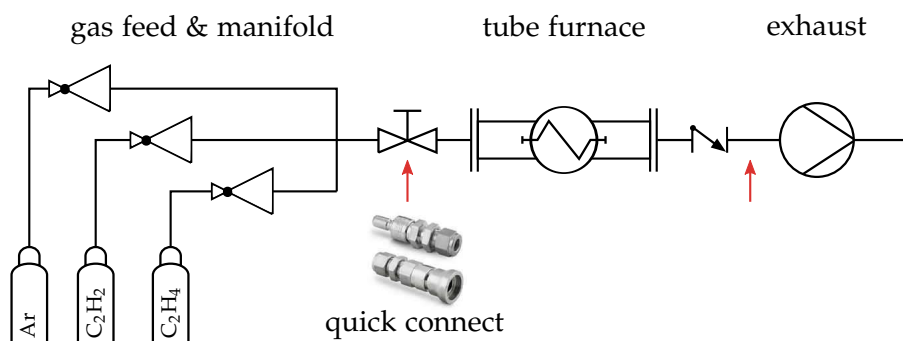


Figure 2.3: Design of the tube furnace installation used for CVD coating. The furnace's quartz tube containing the sample can be disconnected from the setup at the positions indicated by the arrows and removed without exposing the material inside to ambient air.

Argon, ethylene, and acetylene are supplied to the gas manifold. The flow rates can be adjusted individually using electronically operated mass flow controllers (58xx series; Brooks Instruments, Hatfield, PA, USA). The gas feed ends in a Swagelok quick connect, a special valve that is automatically sealed on both ends upon disconnection (see inset in Fig. 2.3). The residual volume for this type of quick connect is just 0.1 ml. The exhaust side of the tube has a low pressure one-way check valve attached, preventing backflow of exhaust gas or ambient air into the tube even when it is not pressurized or installed in the CVD setup. The entire quartz tube can thus be hermetically sealed and removed from the furnace by disconnecting it at the quick connect and behind the check valve.

Coating considerations. In order to obtain optimal coating results, it is important to quantify the amount of carbon deposited during each run. Lacking other practical and reliable means, this is done by weighing the sample before and after deposition. Assuming no material loss, spherical particles, and uniform coating, the thickness of the carbon shell can be calculated from the carbon weight and the particle's geometry using the following relation (see also Fig. 2.4):

$$\frac{m_{\text{carbon}}}{m_{\text{total}}} = \frac{m_{\text{shell}}}{m_{\text{core}} + m_{\text{shell}}} = \frac{\rho_C \cdot 4/3\pi (r_{\text{shell}}^3 - r_{\text{core}}^3)}{\rho_{\text{Li}_2\text{S}} \cdot 4/3\pi r_{\text{core}}^3 + \rho_C \cdot 4/3\pi (r_{\text{shell}}^3 - r_{\text{core}}^3)}. \quad (2.1)$$

For particles with a diameter of 1 μm , adding 2 % carbon by weight would already result in a coating of ~ 300 nm thickness. In order to obtain reasonably thin coatings, the amount of carbon deposited should stay below 1.0 % for all but the smallest particles. Since the above assumptions are typically not fulfilled, this calculation can only serve as a first approximation and further measurements are required to determine the thickness and uniformity of the coating more precisely.

Coating procedure. Before starting the actual coating, the following preparatory steps need to be completed: The gas manifold is assembled and flushed with Argon for several minutes. Next, the quartz tube is removed at the quick connects so that the inlet side of the manifold is now closed, but under pressure. The caps are removed from the quartz tube, which is then cleaned, dried and transferred into the glovebox using its large antechamber. Inside the glovebox, the previously ball-milled Li_2S is put into a ceramic boat and weighed (Fig. 2.5); typically 500–2000 mg go in a large boat so that its floor is only thinly covered. The boat is placed in the quartz tube and aligned centered before the caps are attached and tightened. Next, the loaded quartz tube is transferred out of the glovebox and installed in the gas manifold (outlet side first). The pressurized Argon in the gas manifold immediately starts to flush the tube. A mechanical stand is used to stabilize the tube during the following CVD run to

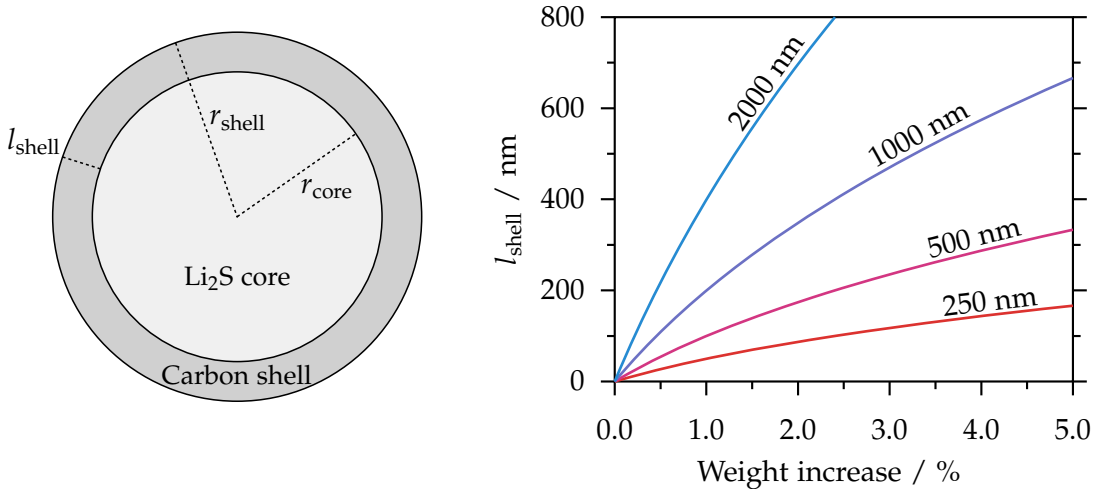


Figure 2.4: Left: illustration of the carbon/Li₂S core-shell structure. Right: Weight increase (\approx carbon deposition) vs. coating thickness l_{shell} for different particle radii ($r_{\text{core}} = 250\text{--}2000\text{ nm}$).

avoid any forces on the O-ring seals. Once the tube is installed in the gas manifold, the furnace is closed and quickly heated to CVD temperature. When that temperature is reached, the Argon flow is reduced and a defined amount of hydrocarbon gas is added to the flow. After the specified coating time has elapsed, the flow is reset to pure Argon and the sample in the tube is cooled down. In order to speed up the process, once the hydrocarbon gas is turned off, the furnace may be opened at temperatures below 500 °C to increase convection. At 100 °C, the tube may be removed from the furnace and transferred back to the glovebox. There, the CVD boat (cf. Fig. 2.5) is removed from the tube and the partially coated Li₂S is stirred up mechanically by grinding it using a mortar and pestle for about 30 s. After the first round of coating, the material usually forms a very brittle pellet, which breaks apart easily when applying the slightest force. For subsequent runs, the material is already a powder before grinding, but the coating may not be uniform in the direction of the gas flow as well as across the powder from top to bottom. The sample is weighed directly before and after the coating step in order to estimate the amount of carbon deposited on the sample. For small samples, the amount of material lost during the grinding step is about equal to



Figure 2.5: Small CVD boat containing a sample of carbon-coated Li₂S nanoparticles.

Table 2.1: Standard protocol for coating Li₂S nanoparticles.

step	duration	procedure
1	30 min.	CVD with 70 SCCM Ar, 10 SCCM C ₂ H ₂ @ 440 °C
2	2 min.	grinding with mortar & pestle
3	60 min.	CVD with 70 SCCM Ar, 10 SCCM C ₂ H ₂ @ 440 °C
4	2 min.	grinding with mortar & pestle
5	120 min.	CVD with 70 SCCM Ar, 10 SCCM C ₂ H ₂ @ 440 °C
6	2 min.	grinding with mortar & pestle

the amount of carbon deposited, therefore the weighing has to be repeated for each CVD run, i.e. after collecting the sample from the mortar.

Various coating protocols were tested in order to come up with an optimal procedure before the most effective coating method was established as a standard; see Tab. 2.1 for the full protocol. Heating, cooling and evacuation times are not included in the list, but account for half of the total processing time: approximately 10 min. heating, 30 min. cooling, 15 min. evacuation (transfer in the glovebox), and 10 min. general handling time per step.

2.3 Other materials and cell assembly

Besides the carbon-coated Li₂S, several other materials are needed to build a functional cell. All raw materials used are listed in Tab. A.3; the rationale behind each choice is outlined in the following paragraphs.

2.3.1 Anode materials and preparation

For the anode, plain lithium foil with a thickness of 180 µm is used (Lectro Max 100; FMC, Philadelphia, PA, USA). While there are known issues with lithium metal anodes [15], it can be safely assumed that for the cell configuration presented here, none of these are critical. Room-temperature ionic liquids [86, 87] as well as the additive lithium nitrate [81, 88, 89] can considerably improve the cyclability of lithium metal electrodes, so that more than 1000 cycles could be demonstrated with an electrolyte similar to the one used in this study [76]. The lithium foil is stored inside the glovebox at < 1 ppm oxygen and virtually no water vapor. Directly before use, it is cut into 5/8" discs, roughened using a plastic brush, and firmly pressed onto a stainless steel plate by hand.

2.3.2 Separator

The separator is composed of a single porous polypropylene membrane (type 2400; Celgard, Charlotte, NC, USA). A large number of suitable separators is commercially available for lithium batteries [90]. While there are some interesting developments in the separator regime lately [91, 92], the material chosen for this work is known to work well from previous studies [77, 93, 94]. Also, assuming it can be wetted properly, the choice of separator does not affect the performance of the cell much — at least for low to medium discharge/charge rates, as can be told from the resistances reported in [95]. Therefore, the optimization of the separator membrane is beyond the scope of this work.

2.3.3 Electrolyte materials and preparation

The separator as well as the porous electrode are filled with a liquid electrolyte. Unfortunately, carbonate based electrolytes, which are commonly used for Li-ion cells [96, 97] are not suitable for Li/S batteries because of their reactivity with dissolved polysulfides [98]. Instead, popular choices have been glymes, ethers and dioxolane-based electrolytes [99–103]. Only recently, the first review on electrolytes for Li/S batteries was published by Scheers et al. [103]; a generic scheme for the classification of various electrolytes can also be found in Ref. [104]. For this work, electrolytes based on room-temperature ionic liquids (RTILs) are used, which are known to work well with Li/S batteries [104–107]. By selecting and chemically modifying the anion or cation, RTILs can be designed to have properties matching the requirements of a specific application. Various combinations have been used for energy applications [12, 108]. In general, RTILs are known for their good ionic conductivity as well as their excellent thermal and electrochemical stability. Additionally, they offer technical and environmental benefits including a very low vapor pressure, nonflammability, low toxicity and synthesis methods which are both scalable and environmentally friendly [108, 109]. Recent reports indicate that RTILs can even contribute to a better reversibility of lithium metal electrodes by dynamically forming a favorable, protective SEI layer at the lithium | electrolyte interface [87]. If required, these electrolytes can also be turned into gels easily, as reported by [110].

For this work, several different compositions of liquid electrolytes were tested, all of them based on 1-butyl-1-methylpyrrolidinium bis(trifluoromethanesulfonyl)imide (Pyr₁₄TFSI) with 1.0 mol/kg LiTFSI dissolved. Tab. 2.2 lists the compositions tested and Tab. 2.3 shows the chemical structure of the components used. Liquids are stored in sealed vials together with activated type 4 Å molecular sieves (TRICAT, Hunt Valley, MD, USA) in order to reduce the amount of trace water. Salts are dried under

vacuum at 140 °C overnight before use. Electrolytes are prepared in an Argon-filled, water-free (dew point: –70 °C) glovebox (UNILab/LabMaster 130; MBraun, Garching, Germany). All ingredients are added to a brown 20 ml glass vial at once and stirred with a magnetic stir bar in the glovebox bar until the salt is entirely dissolved (at least 24 h for the saturated solutions). The water content of the liquids as well as of the final electrolyte is tested by a Karl Fischer Coulometer (DL39; Mettler Toledo, Greifensee, Switzerland).

Table 2.2: List of electrolytes tested

#	composition (liquid)	salt	additive
1	PEGDME, Pyr ₁₄ TFSI 1:1	1 mol/kg LiTFSI	0.3 mol/kg LiNO ₃
2	TEGDME, Pyr ₁₄ TFSI 1:1	1 mol/kg LiTFSI	0.3 mol/kg LiNO ₃
3	TEGDME, Pyr ₁₄ TFSI 2:1	1 mol/kg LiTFSI	0.3 mol/kg LiNO ₃
4	TEGDME, Pyr ₁₄ TFSI 2:1	saturated with LiTFSI	0.3 mol/kg LiNO ₃
5	DOL, DME, Pyr ₁₄ TFSI 1:1:2 by vol.	1 mol/kg LiTFSI	0.5 mol/kg LiNO ₃
6	DOL, DME, Pyr ₁₄ TFSI 1:1:2 by vol.	saturated with LiTFSI	0.5 mol/kg LiNO ₃
7	PC, EC, DEC 5:1:1	1 mol/kg LiPF ₆	–

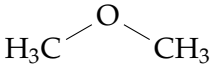
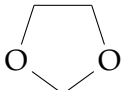
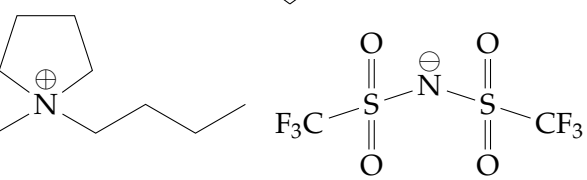
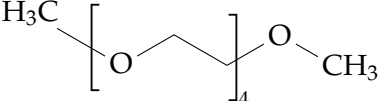
Unless otherwise noted, all following experiments use electrolyte #5 (see Tab. 2.2), a mixture of DOL, DME, and Pyr₁₄TFSI, 1:1:2 by volume with 1.0 mol/kg LiTFSI and 0.5 mol/kg LiNO₃ dissolved.

2.3.4 Cathode additives

Unlike the negative electrode, the positive electrode cannot be composed of solid bulk material because of the poor electronic conductivity of both sulfur and lithium sulfide. Even though the active material is already coated with carbon, additives are needed to build a more durable and reliable electrode.

First, additional carbons provide increased and more stable conductivity: Carbon black (Super C65, Timcal, Bodio, Switzerland) is interspersed between the active material particles to increase the contact area. Multi-walled carbon nanotubes (MWCNT; Cheap Tubes, Brattleboro, VT, USA) are added to enhance long-range electronic conductivity [111] and to obtain a more uniform, well-distributed cathode morphology [112]. Even though the electronic conductivity of carbon-coated particles themselves is sufficiently high, the total electronic resistance would be unacceptably high for thicker electrodes without added carbon because the current would have to pass through countless point contacts between adjacent carbon-coated particles. Prior to their first use, the carbon additives are dried under vacuum at 130 °C for at least 16 h to remove residual water.

Table 2.3: Chemical structure of materials used in the liquid electrolyte. Full names, properties, and sources of the chemicals are listed in the appendix (Tab. A.3).

component	structure
DME	
DOL	
Pyr ₁₄ TFSI	
TEGDME	

Second, a binder ensures mechanical stability and structural integrity of the porous matrix. Conventionally, polyethylene oxide (PEO), polyethylene terephthalate (PET), or polyvinylidene fluoride (PVDF) have been used as binders in sulfur cathodes [113–116]. However, these binders are not very elastic and thus struggle to accommodate the large volume changes associated with charging and discharging the sulfur electrode [117, 118]. Several alternatives were suggested and evaluated, among them alginates [118], gelatin [119], sodium carboxymethyl cellulose (CMC) [120, 121], styrene-butadiene rubber (SBR) [77], and combinations thereof [122, 123]. Besides the improved elasticity, these advanced binders are known for their better dispersive properties. They are also considerably cheaper than PVDF and finally, they facilitate recycling of the electrode materials after use since they can be easily removed from a waste electrode by pyrolysis. For this work, plain SBR (Sigma Aldrich, St. Louis, MO, USA) was chosen as a binder, because of its reported compatibility with the electrolyte used, easy processing, and previous studies indicating good performance for a similar system [77].

2.3.5 Electrode preparation

While electrodes for coin cells can be prepared individually with very small amounts of electrode slurry, for this work a batch of electrodes was prepared at once, yielding higher loadings and better reproducibility among the electrodes of that batch. The only downside of this approach is that individual electrodes cannot be weighed before and after application of the slurry; implications of this issue will be discussed below.

The typical batch size used in this work is $90 \times 180 \text{ mm}^2$, resulting in 20–30 coin cell sized electrodes.

The slurry and electrode preparation can have a big impact on the electrode's performance [124], therefore this procedure needs to be analyzed and optimized carefully. The electrodes are prepared from a slurry mixed according to the composition in Tab. 2.4. A stock slurry is prepared in advance as follows: 120 mg of carbon black are predispersed in 3000 mg of toluene by vigorously stirring with a magnetic stir bar (120V Stirrer; Corning Inc., Corning, NY, USA) overnight at room temperature. Next, 30 mg of MWCNT are added while stirring continuously. After another 90 min., 1500 mg of a toluene solution containing 10 wt.% SBR are added. The stock slurry is kept on the stir plate until used up. The actual slurry is made by dispersing 72 mg of active material in 550 mg of toluene, then adding 270 mg of the previously prepared stock slurry. Two different techniques for optimizing the dispersion of the final slurry were evaluated: a short treatment with an ultrasonic tip homogenizer (Digital Sonifier 450; Branson, Danbury, CT, USA) or sonicating in an ultrasonic bath (2510, Branson) for 20–30 min. with the vial being held upright and partly immersed into the bath. Either way, once the slurry is properly dispersed, it is transferred onto a primed, i.e. carbon-coated, aluminum foil in the glovebox and cast into a film of 200 μm thickness using a hand-operated doctor blade. The film is dried in the glovebox for a few minutes until it looks blunt and dry. The coated foil is then enveloped between two sheets of weighing paper and subsequently cut into individual $1/2''$ disc electrodes using a mechanic punch. Initially, an additional drying step (4 h at 60°C on a heat plate) was applied. It turned out, however, that this step does not affect the performance of the electrodes and hence it was skipped for all the experiments presented in this work. There is even a report which indicates that small amounts of residual toluene may be beneficial for both rate capability and Coulombic efficiency [125] – no such effects were observed, though. During the casting and drying process, the circulation purifier of the glovebox is deactivated in order to spare the copper catalyst. Afterwards, the box is purged for 5 min. and circulation is reactivated. The cut-out electrodes are stored in a 20 ml glass vial which is sealed and kept in the glovebox until used.

2.3.6 Cell assembly

Except for some special experiments, coin cells were used throughout this work. The components assembled into a cell are shown in Fig. 2.6. The stainless steel cell casing parts (National Research Council Canada, Montreal, QC, Canada) are dried overnight at 140°C under vacuum before use to avoid contamination of the electrolyte by residual water. Cells are assembled in a glovebox filled with Argon 5.0 (Praxair, Danbury, CT, USA), compressed using a custom-build Argon-driven pneumatic press and rest

in the glovebox for at least 12 h at room temperature before being tested. Since the amount of electrolyte can have a great effect on the performance of the cell [126, 127], its dosing is done extra carefully: Each cell contains 50–60 µl of liquid electrolyte; in order to ensure optimal wetting of all surfaces, the electrolyte is added to the cell in two portions: the first one is applied on top of the cathode before adding the separator, the second one on top of the separator before adding the anode. The separator is larger than both the anode and cathode and the amount of electrolyte is slightly more than is needed to fully soak the separator. Thus, there is a surplus of liquid electrolyte which causes an adhesive force between the separator and the stainless steel casing around the electrodes and also serves as a reservoir – in case some electrolyte is decomposed or otherwise lost during cell operation.



Figure 2.6: Components of a CR2032 cell (left to right): Stainless steel bottom casing, positive electrode (Li_2S composite on Al foil), separator (Celgard 2400 membrane), negative electrode (Li foil), stainless steel spacer, bell washer, rubber seal, stainless steel top casing. Ruler: inches.

Table 2.4: Standard composition of the positive electrode slurry.

compound	amount wt.% of solids	total amount mg
active material	80	72
carbon black	10	9
binder	10	9
toluene	(~900)	804

2.4 Analysis and characterization methods

2.4.1 Microscopy

To check materials and electrodes, Scanning Electron Microscopy (SEM) was used primarily. Li/S type samples are somewhat difficult to image because both S₈ and Li₂S are insulators. Nevertheless, for most samples, the microscope used (JSM-7000F; JEOL, Akishima, Tokyo, Japan) allows for magnifications of 10 000–50 000× while still producing reasonably clear and crisp images. Also, energy dispersive X-ray spectroscopy (EDX) can be performed simultaneously. Sample preparation is straightforward: electrodes or powders are fixed on top of an aluminum cylinder by means of conductive carbon tape. To prepare cross-section images of an electrode, it is ripped apart in the glovebox, bent into an L-shape, and affixed to the SEM sample holder so that one of the edges is pointing upwards. For powders, it is important to shake off any material that is not sticking firmly in order to avoid pollution of the microscope and other samples. The aluminum cylinder is installed into a sample holder while still in the glovebox, which is subsequently installed in the microscope via an evacuable antechamber. The entire sample holder is kept in a sealed container until the antechamber is ready. Then, it is quickly installed in the corresponding adapter; the chamber is closed and pumped down immediately. If exposure to air must be absolutely avoided, a glovebag may be installed around the opening of the antechamber and flushed with Nitrogen or Argon prior to installing the sample.

Using SEM, the particle size, agglomeration state, and uniformness is investigated, but the presence of cracks, defects or other types of degradation can also be detected. To estimate the composition and purity of the samples, they are also analyzed by EDX while in the microscope. EDX detects the characteristic X-ray emissions [128] of the atoms in the sample which are excited by the incident electron beam. From the spectrum and the known absorption cross-sections of each element, the composition of the sample can be calculated [129, chap. 7.2]. For very light elements such as H or Li, however, both the absorption cross-section and the energy of the emitted X-rays are too small to produce accurate results, given the spectral resolution of the instrument.

Additionally, Transmission Electron Microscopy (TEM) images can be recorded to analyze the structure of the carbon-coated Li₂S particles. TEM images were recorded at the facilities of the National Center for Electron Microscopy³.

³National Center for Electron Microscopy, Lawrence Berkeley National Laboratory, 1 Cyclotron Road, Berkeley, CA 94720, USA

2.4.2 Chemical/physical methods

Coating test. A special test was developed in order to test the integrity of the carbon coating and its properties as a barrier for (lithium) polysulfides. The idea behind this test is that polysulfides are intensely colored [104, 105] so that their presence in a clear liquid can be easily detected. Also, because of disproportionation reactions, they are formed readily when dissolved S₈ and Li₂S are mixed. Therefore, in a suitable solvent which is able to dissolve sufficient amounts of both S₈ and Li₂S, the presence of Li₂S can be detected quickly and easily. A selection of solvents including toluene, tetrahydrofuran, carbon disulfide, tetraethylene glycol dimethyl ether, 1,3-dioxolane, and N-methyl-2-pyrrolidone (NMP) was screened for suitable components (data not shown). Also, different mixing protocols were evaluated.

The most suitable combination turned out to be a mixture of NMP and toluene: First, 10 mg/ml of S₈ are dissolved in pure toluene to create a “test solution”. Next, about 1 mg of the material to be tested is dispersed or immersed in 200 µl NMP and incubated for 1 min. so that any Li₂S exposed to the solution will be dissolved (at least partly). Finally, 50 µl of the test solution are added with a pipette. If dissolved Li₂S is present, polysulfides will be formed immediately, coloring the solution. For this combination of solvents, the intensely blue S₃^{•-} radical is most prominently visible. If there is no Li₂S, the solution will stay clear; otherwise it will turn blue. Even though the intensity of the color does vary depending on the amount of Li₂S present, this test is by no means quantitative.

There may be more simple methods for detecting Li₂S, e.g. by adding water to the sample (vigorous reaction) or trying to detect the smell of H₂S, which is formed when Li₂S is exposed to air. The advantage of this special test is that it is highly sensitive, reliable, safe, and quick all at once.

Beaker cell. A transparent beaker cell was built from a 3 ml glass vial, see Fig. 2.7. This cell contains significantly more electrolyte than a regular coin cell, and is generally not very suitable for quantitative electrochemical measurements [127]. However, the formation and movement of polysulfides can be directly visually analyzed with this kind of cell [130].

2.4.3 Electrochemical methods

For analyzing full cells, a range of electrochemical methods is exploited using several different potentiostats.

Impedance spectroscopy. Initially, all cells are tested for their open-circuit voltage (OCV) and their electrochemical impedance spectrum (EIS) [131]. Besides providing

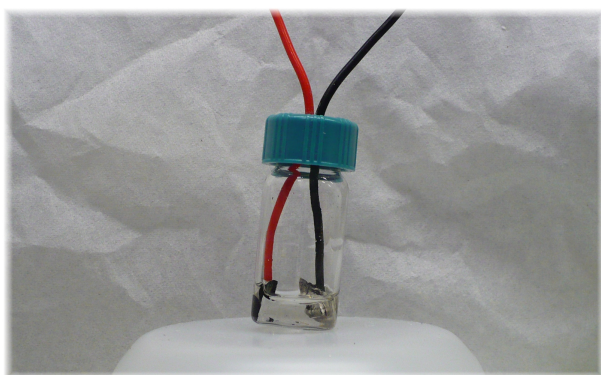


Figure 2.7: A transparent beaker cell for optically investigating polysulfide formation and transport.

important information on the cell, this data can be used to identify faulty cells and to estimate the uniformity of a batch of electrodes. Impedance spectra are recorded using a 10 mV sinusoidal excitation around OCV in the frequency range of 1.0 MHz to 50 mHz with a VSP potentiostat (BioLogic, Claix, France). For some cells, impedance was also recorded during stabilization or intermittently during cycling. For the latter, the discharge was stopped 15–60 s before the EIS recording so that the cell voltage can relax (almost) to OCV. The experimental results are plotted in Nyquist representation [132, chap. 16.1].

For all tests except EIS, cells are stored in controlled temperature chambers (TEC1; TestEquity, Moorpark, CA, USA) at 30 °C in order to minimize the effect of circadian, seasonal, or weather-dependent temperature changes.

Cyclic voltammetry. In order to study electrolyte stability and to evaluate different charging procedures, slow-sweep cyclic voltammetry (CV) was employed, using a VMP3 potentiostat (BioLogic, Claix, France). “Slow” in this context means that the voltage is changed quasistatically, i.e. the rate at which the voltage changes is slow compared to the time it takes for the current to stabilize at the new voltage. Practically, it means that the SoC of the cell is following the voltage so that one CV cycle corresponds to one full charge/discharge cycle. In the cyclic voltammetry (CV) plots, the current (i.e. charge passed per time) is plotted vs. the externally applied voltage. Because of the slow and steady voltage ramp, the current is approximately proportional to the total charge which would be passed if the cell was held at that voltage indefinitely. A typical CV experiment, utilizing a voltage ramp in the range of 10–25 µV/s, runs for several days.

Cycling. All cycling experiments start with an initial slower activation cycle followed by the regular cycling, which consists of an initial rest time, a constant-current (CC) discharge to 1.5 V, a variable rest time, a CC charge to 2.8 V, and finally a constant voltage (CV) charge which ends once the current drops below a certain threshold, typically 5 % of the CC charging current.

2.5 Dead ends

More materials, techniques and procedures were tested and applied, but not found to be particularly helpful or constructive. For completeness, this information is also included here, but the corresponding results are not presented or discussed. These “dead ends” include:

- Thermogravimetric analysis (TGA): The measurements did not work out very well because of the high reactivity of Li₂S which decomposes rapidly in ambient air. TGA samples need to be sealed in aluminum containers in the glovebox, which are then opened by the TGA machine right before the heating starts. Still, the drift is quite high and there is considerable weight loss even before the temperature starts to rise.
- Impedance of symmetrical cells (both Li/Li and S/S): The former turned out to be highly dependent on the Li pretreatment, an effect which is deemed to be irrelevant for real cells after completing the first cycle. For the latter it was very difficult to obtain reproducible results, especially for SoC ≠ 0 %. The most promising method is to remove a positive electrode from a cell cycled to the desired SoC, cut it into half, and build a new cell using the two halves as electrodes. However, it is tricky to cut and align the two parts perfectly symmetrically. Also, most of the original electrolyte is lost (even if the separator is reused) and has to be replaced, which causes a significant loss of polysulfides and thus a change in SoC.
- Baking electrodes after fabrication: In addition to drying, electrodes were baked for 2–4 h at 70–100 °C. While the electrodes look rather similar in SEM images (except for some cracks), their electrochemical performance and lifetime was always significantly worse than that of non-baked electrodes.
- Atomic Force Microscopy (AFM) was used as an analysis method complementary to SEM. An environmentally protected holder including the AFM tip can be loaded with the sample in the glovebox, and directly installed in the instrument (MFP-3D, Asylum Research, Santa Barbara, CA, USA). While the resolution is

typically slightly better than that of the SEM, the morphological information which can be extracted out of the images is roughly similar. However, AFM imaging takes considerably more time and also, conducting and insulating areas cannot be told apart easily. Therefore, AFM was no longer used after the initial testing, which confirmed that the SEM images look very similar to the actual structure as detected by AFM.

- Three electrode cell measurements: A Swagelok-type three-electrode cell was used to obtain impedance spectra and discharge curves relative to a Li reference potential. Besides technical complications, this approach was not pursued further because this cell is quite different from the coin cell in many respects. Therefore, an interpretation of the results requires many additional assumptions which are difficult to verify.
- Spraying electrodes: Spraying can be superior to doctor blading in many respects, especially for smaller batch sizes. Initial tests of spraying carbon suspensions outside of the glovebox with a hand-operated nozzle worked out quite well. To match and surpass the performance of doctor blading, however, an automated spraying setup would have had to be installed inside the glovebox, which was not feasible for time, cost, and glovebox space reasons.

3 Experimental work on lithium sulfide cathodes – results and discussion

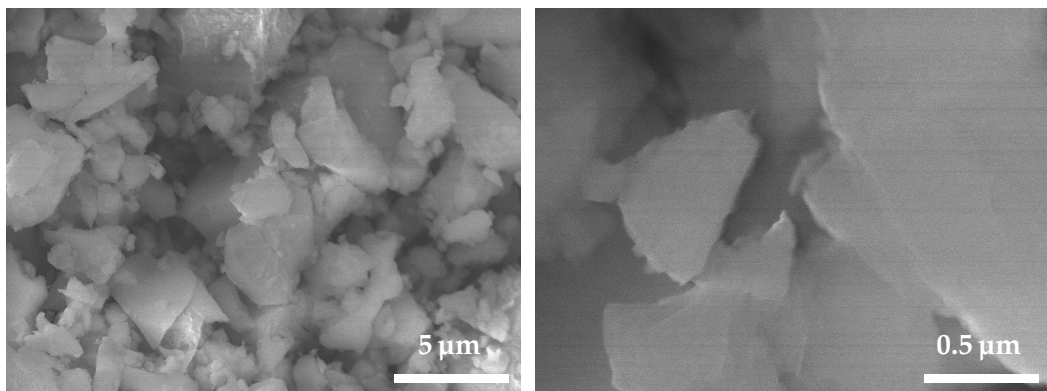
In this chapter, the results of the experiments and analyses outlined in chapter 2 are presented. First, the characterization of materials by means of microscopy, spectroscopy, and chemical methods is reported and discussed in section 3.1 with a focus on the processing of the Li₂S particles. Next, the impact of the core-shell structure on the cells' performance is analyzed. Electrochemical tests of full cells are presented and discussed in section 3.2, including cycling, impedance spectroscopy, and cyclic voltammetry. A critical assessment of the results is conducted in section 3.3 and finally, conclusions are drawn.

3.1 Analysis of materials and electrodes

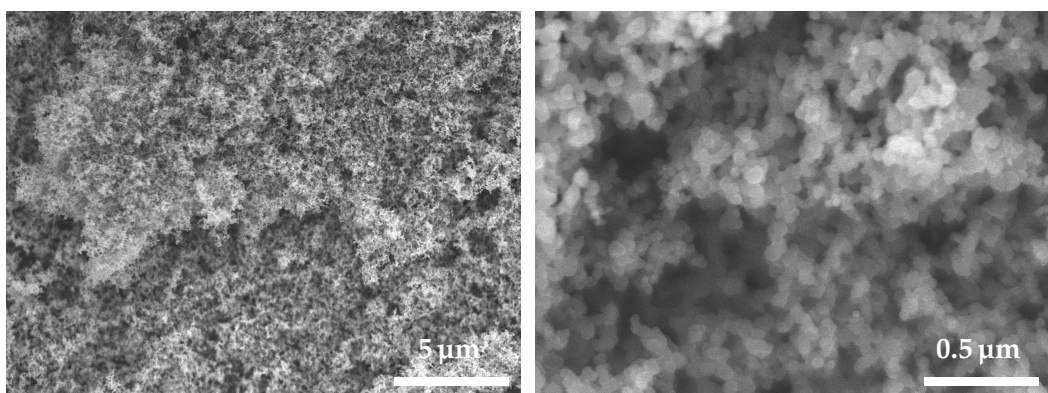
Various techniques have been employed to study the materials in the Li/S cell in order to understand and optimize the carbon coating as well as the electrode preparation steps. In the following, these results will be presented and discussed.

3.1.1 Scanning electron microscopy of materials

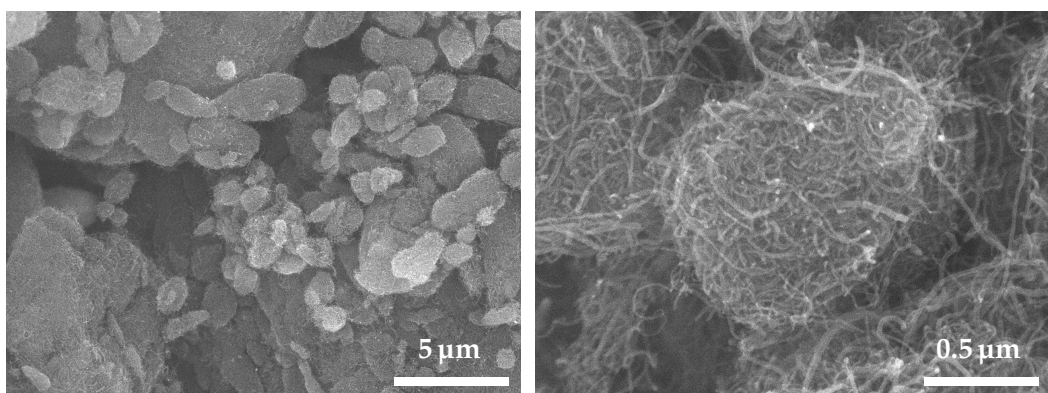
Microscopy is one of the main analysis methods used in this work. SEM images and EDX spectra of the raw materials in the positive electrode are shown in Figs. 3.1 and 3.2, respectively. One ingredient of the electrode, the binder SBR, is missing because it is rapidly decomposed by the microscope's electron beam, making imaging and spectroscopy impractical. Besides giving an estimate of the materials' purity, particle size, and agglomeration state, these images are recorded for comparison with the material after treatment. Thereby, the effect of each step of the preparation may be investigated, which is of particular interest for the processing of the Li₂S powder. For the pristine, commercial Li₂S, the particle size is determined to be $4.0 \pm 2.0 \mu\text{m}$, with some outliers as big as $50 \mu\text{m}$. This finding confirms that the commercial material is not suitable for use in Li/S batteries unless the particle size is significantly reduced.



(a) Commercial Li₂S powder



(b) Carbon black



(c) Multi-walled carbon nanotubes

Figure 3.1: SEM images of the raw materials of the positive (sulfur) electrode. Left column: 5000 \times magnification, right: 50000 \times magnification.

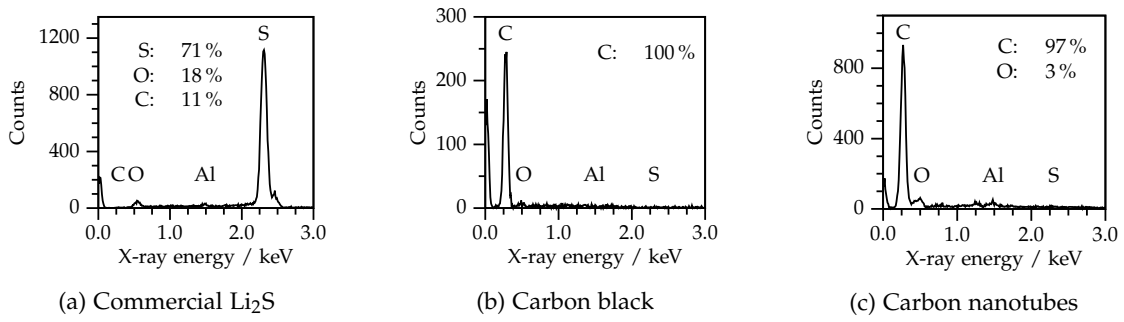


Figure 3.2: EDX spectra of the raw materials of the positive (sulfur) electrode. All spectra are recorded at 15 keV incident electron beam energy. Labels indicate the position of the $K\alpha_1$ line of each detected element and atom percentages for prominent elements.

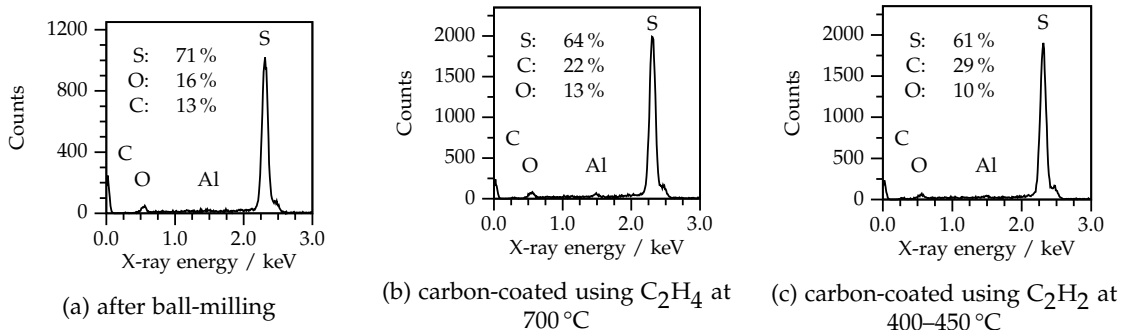


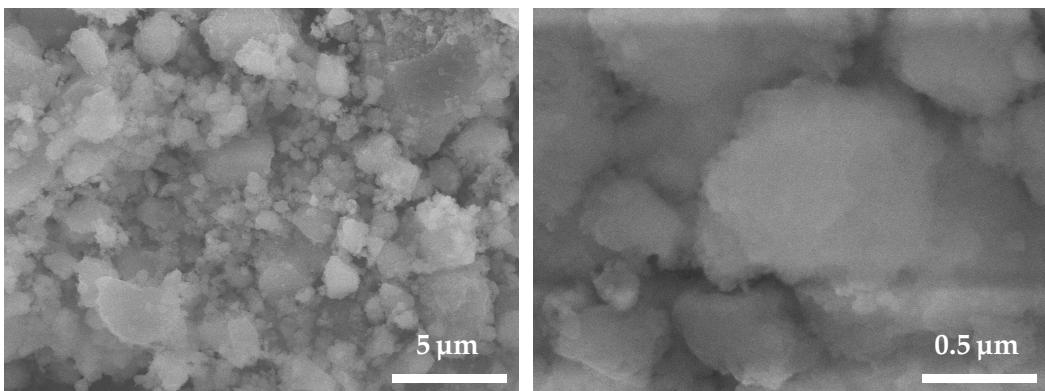
Figure 3.3: EDX spectra of the active material at various steps during the preparation process. All spectra are recorded at 15 keV incident electron beam energy. Labels indicate the position of the $K\alpha_1$ line of each detected element and atom percentages for prominent elements.

From the recorded EDX spectra, presented in Fig. 3.2, the composition of the samples can be calculated. Note that H and Li are not detected by EDX, cf. section 2.4.1. Judging from the spectra, the carbon components are indeed very pure. Small amounts of oxygen may have been introduced during the installation of the samples in the microscope, e.g. in the form of adsorbed trace water. For the Li_2S , however, the situation is different. A pure Li_2S sample should ideally show up as 100 % sulfur. The additional carbon content might be caused by stray carbon black particles, which are easily spilled across the sample holder during the evacuation step. Also, the carbon tape used to affix the powder to the aluminum sample holder may be detected by EDX. There is no similar explanation for the high amount of oxygen in the specimen, though. The EDX signature of oxygen is relatively small so that the composition is only accurate to plus/minus several percent. Nevertheless, it has to be assumed that the Li_2S particles have been partly converted to LiOH and LiO_2 at least at their surfaces. Unfortunately,

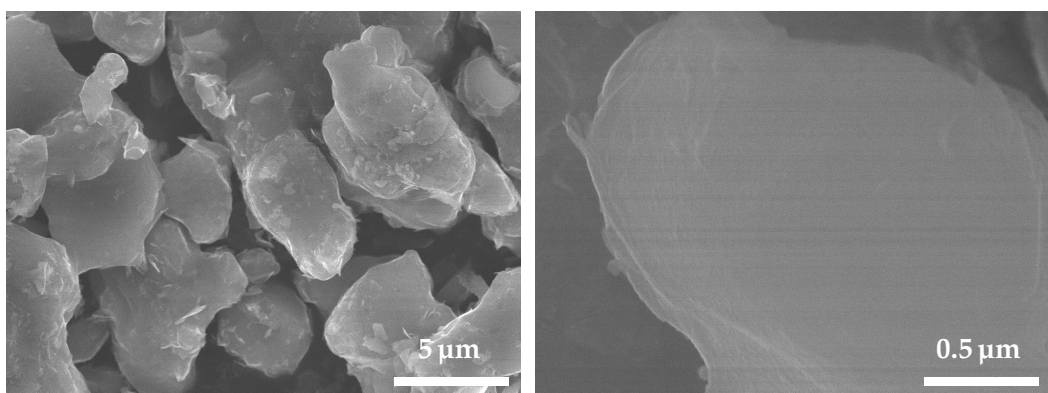
the same result was obtained for all Li₂S samples tested (from three different batches, data not shown) and there is no practical way of purifying them or even determining the precise composition of the impurities. Therefore, the material was used for the experiments nevertheless, keeping in mind that the composition of the final electrode may differ from what is intended, cf. section 3.2.2.

The material is also imaged during the refinement process. Fig. 3.4a shows Li₂S particles after high-energy ball milling. It becomes clear that the particle size is successfully reduced during that step. More precisely, it averages to $1.2 \pm 0.8 \mu\text{m}$. Even after ball-milling, the particle size distribution is not very uniform and outliers as large as $4 \mu\text{m}$ can be found regularly and up to $20 \mu\text{m}$ rarely.

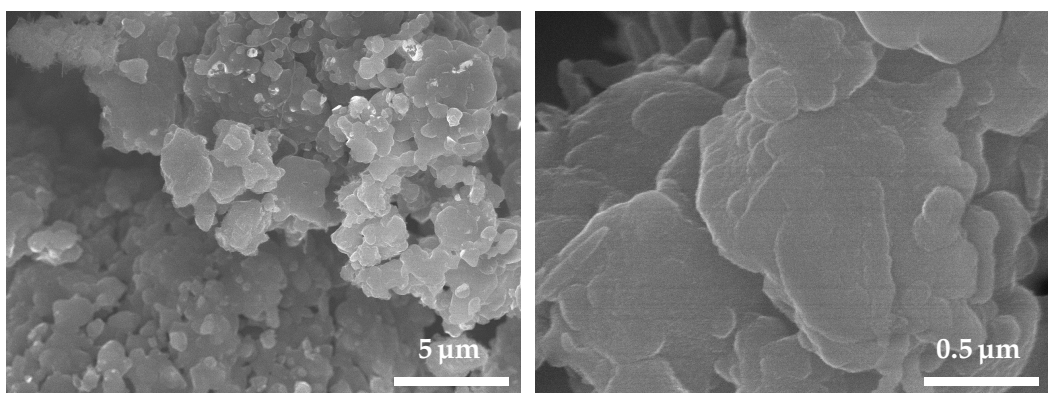
Finally, the coated material is analyzed. An immediate effect of the conductive coating is that the quality of the SEM images is visibly improved because the sample is no longer charged during imaging, cf. [129, chap. 15]. The coating smoothly conforms to the particle shapes, which are still not very regular (compared e.g. to synthesized nanoparticles [133]). Unfortunately, two types of agglomeration can also be observed: First, coated particles stick to each other, creating a cross-linked network. This kind of agglomeration seems to be ubiquitous after coating, but does most likely not pose a problem with regard to the electrochemical performance. On the contrary, it might even improve the long-range electronic conductivity of the electrode and is thus not considered harmful. Second, however, particles which stick to each other before or early during the carbon deposition are coated collectively and are thus trapped under a common “carbon veil”. This may well have a negative impact on the material’s performance because less area is exposed to the electrolyte, causing longer diffusion distances and thereby higher overpotentials in the particles. As a consequence, sulfur utilization is expected to be lower. During the optimization of the coating protocol, it was observed that this kind of agglomeration can be broken up partly during the intermittent grinding steps. Also, it can be decreased by reducing the continuous coating time. Still, even for coating times of only 30 min. per run, agglomeration was detected (data not shown). To improve the situation, a rotary furnace may be needed, as discussed in section 3.3.2.



(a) Li₂S powder after high-energy ball-milling



(b) Li₂S powder after ball-milling and carbon coating with ethylene at 700 °C



(c) Li₂S powder after ball-milling and carbon coating with acetylene at 400–450 °C

Figure 3.4: SEM micrographs of ball-milled and carbon-coated Li₂S. Left column: 5000 \times magnification, right: 50000 \times magnification. Note how coating at elevated temperature causes agglomeration (b), whereas coating at lower temperatures (c) nearly preserves the particle size distribution of the ball-milled, uncoated material (a). For comparison, the pristine material is shown in Fig. 3.1a.

When looking at Fig. 3.4, it also becomes obvious that treating the material at elevated temperatures significantly increases agglomeration. The samples shown in Figs. 3.4b and 3.4c are prepared from the same batch of ball-milled Li₂S, coated with roughly the same amount of carbon. Because of different carbon precursors (Fig. 3.4b: ethylene, Fig. 3.4c: acetylene), the CVD process was run at different temperatures. At 700 °C, the secondary particle size is increased almost tenfold compared to 400–450 °C. When using methane, which decomposes at around 900 °C, the agglomeration is even worse (data not shown).

EDX confirms that neither the oxygen nor the carbon content is increased during the ball-milling step, compare Figs. 3.2 and 3.3. As expected, an increased carbon content is detected after the CVD coating. In principle this increase could be used to calculate the amount of carbon deposited and thereby the thickness of the coating according to Fig. 2.4. However, measurements of various coating runs report 3–16 % increase in carbon content, yielding a carbon coating with an average thickness of 200–900 nm, depending on the particle size distribution. This result is way beyond the intended amount of coating and does not agree with the visual impression of the SEM images. The reason for this discrepancy is the limited penetration depth of the incident electron beam [129, chap. 6.3]. Electrons are preferentially scattered in the top layers of the particles, which of course inflates the share of the carbon detected, since most of the bulk Li₂S does not contribute to the EDX signal.

3.1.2 Scanning electron microscopy of electrodes

Besides the handling of the active material, the optimization of the electrode preparation was the processing step which needed the most tweaking and tuning. In the following section, SEM micrographs of sulfur/carbon electrodes are presented, illustrating problems encountered and solutions found.

The newly developed active material requires optimized handling, processing, and examination. In particular, the mixing and doctor blading of the electrode slurry needed adjustments in order to achieve good results. Because of the susceptibility of the material and the small batch size, no automatic coating machine is used, but all electrodes are doctor bladed by hand. In this context, SEM images are used for quality control and process optimization. First, electrodes prepared from differently mixed slurries are compared in Fig. 3.5. An electrode prepared according to the recipe published in Ref. [77] is depicted in Fig. 3.5a. This electrode is prepared from a very thin, low-viscosity slurry. Even though it looks nicely solid and uniform, the loading of 0.1–0.5 mg/cm² is considerably lower than the target range of 1.5–2.5 mg/cm². While alternating steps of coating and drying could build up a thicker electrode, this procedure is associated with various problems ranging from poor mechanical stability

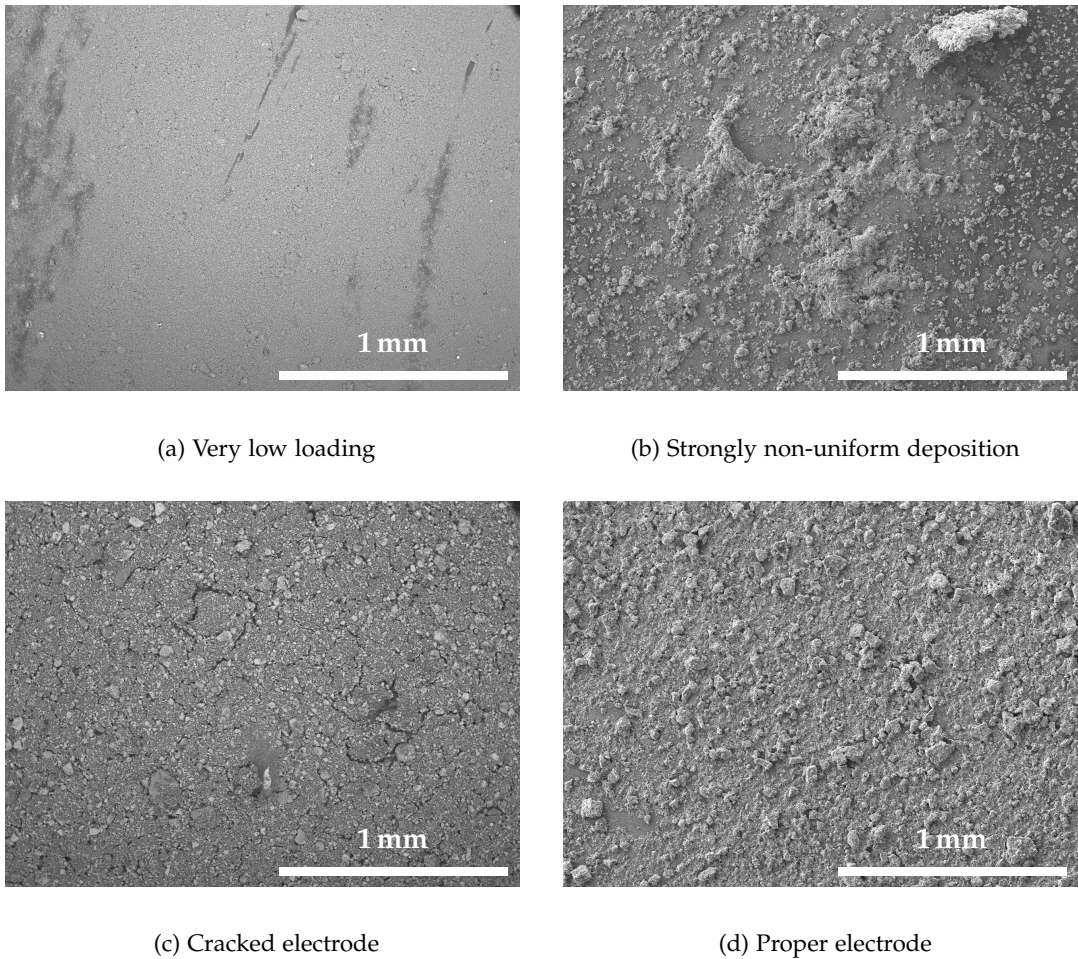


Figure 3.5: SEM micrographs of differently prepared electrodes, illustrating various issues with the preparation process. Magnification: 50×. Details see text.

to loss of electronic contact. Therefore, the slurry composition had to be changed in order to deposit more electrode material in one coating run. Subsequently, the active material content was increased from 68 % to 80 %. Simultaneously, the consistency of the slurry was increased to a solid:solvent ratio of 1:7, compared to an initial 1:20. Efforts to further increase the ratio, e.g. to 1:4, were abandoned, since the high viscosity causes severe problems with the doctor blading step (data not shown). When subjected to the same processing as before, however, the improved slurry yielded poor electrodes, shown in Fig. 3.5b. A strongly non-uniform deposition was observed, caused by poor dispersion of the active material powder and the carbon black. Dispersion is considerably improved if the mixing step is longer and more powerful. If the mixing is too powerful, however, it may not be suitable for this material despite the superior dispersion. Fig. 3.6 shows an electrode whose slurry was mixed in a 20 ml

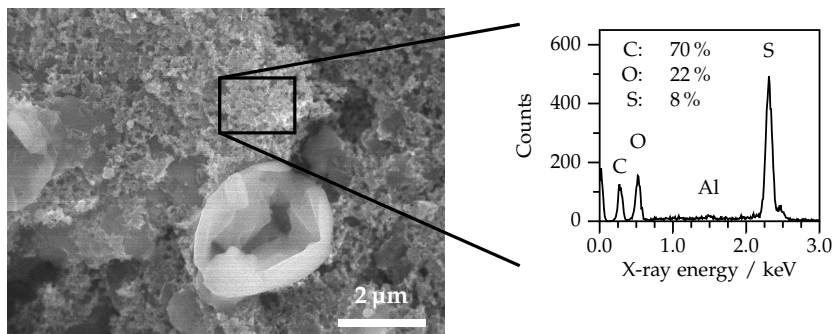


Figure 3.6: SEM micrograph of an electrode prepared from an electrode slurry mixed with the ultrasonic tip. Magnification: 5 000 \times . The large sulfur particle is obviously broken. Inset: EDX spectrum of a selected region next to the broken particle, which contains significant amounts of sulfur.

glass vial with the ultrasonic tip for 1 min. at a power of only 40 W. The large particle in Fig. 3.6 is obviously broken and its sulfur content spilled all over the electrode even before it got in contact with the electrolyte. As an immediate conclusion of this finding, the ultrasonic tip was no longer used. Instead, the much more gentle magnetic stirrer and ultrasonic bath were favored, at the cost of prolonged mixing times. After a discussion with the supplier of the carbon black material (Timcal, Bodio, Switzerland), the procedure described in section 2.3.5 was established. Indeed, the dispersion and hence the spreading are significantly improved over the previous approach as shown in Fig. 3.5c. This electrode, however, suffers from another issue associated with the higher loading: if a thick electrode is dried too rapidly (e.g. at elevated temperature) tension builds up in the material which can cause cracks. These cracks in turn are related to irreversible structural degradation [134]. To overcome this issue, the electrodes are cut into coin cell sized pieces immediately once they are dry enough, i.e. no longer sticky, and collected in a sealed vial. This measure slows down drying by lack of convection and the accumulation of the toluene solvent in the vial's atmosphere, thus effectively preventing the formation of cracks, see Fig. 3.5d. In addition, the initial drying can be slowed down by placing the electrode inside a closed petri dish directly after the doctor blading. Despite the increased drying time, however, this did not seem to further improve the quality of the electrodes (data not shown).

Another electrode prepared according to the recipe optimized for uniformity, coverage, and sulfur loading is presented in Fig. 3.7 at a higher magnification in top-down and cross-section view. While its thickness does vary, it is obvious from the cross-section that the composition of the electrode is uniform. No sedimentation or additional agglomeration is observed. At the bottom of the cross-section image, the aluminum current collector with a thin layer of carbon priming is discernible.

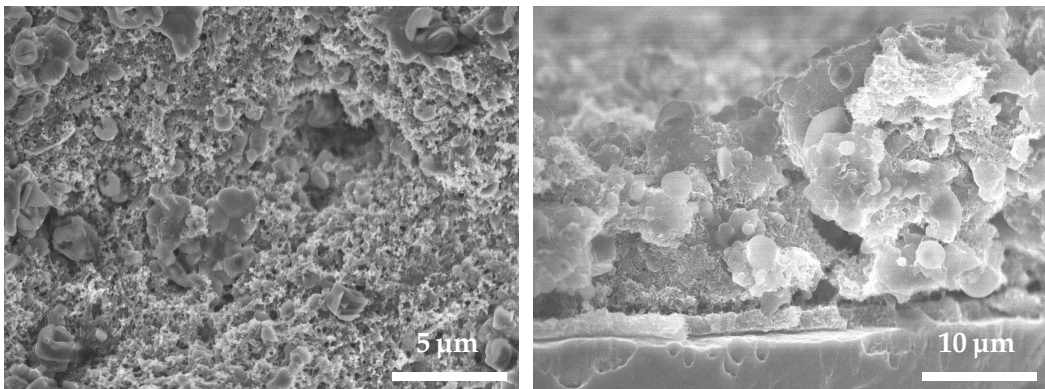


Figure 3.7: SEM image of an optimized electrode. Left: top down, 5000 \times ; right: cross-section, 2500 \times .

SEM was not only used for quality control and optimization, but also to investigate changes to the electrode structure during cycling. Micrographs of the sulfur electrode recorded at different SoC are presented in Fig. 3.8. More precisely, these are images of several similar electrodes removed from identical cells at different times during the formation and first discharge. The changes to the morphology are apparent: After the initial charge (activation) a film has formed on the entire electrode (Fig. 3.8b). During the first discharge, the film is temporarily removed to a great extent (Fig. 3.8c), but re-deposited before the end of the discharge (Fig. 3.8d). The results are comparable to those of Refs. [134, 135], both of which used a cell design without any polysulfide confinement. This is a strong indication that – despite the carbon coating – some of the sulfur can actually move around freely in the cell. In fact, this behavior can be explained nicely by the model as presented on pages 93ff.

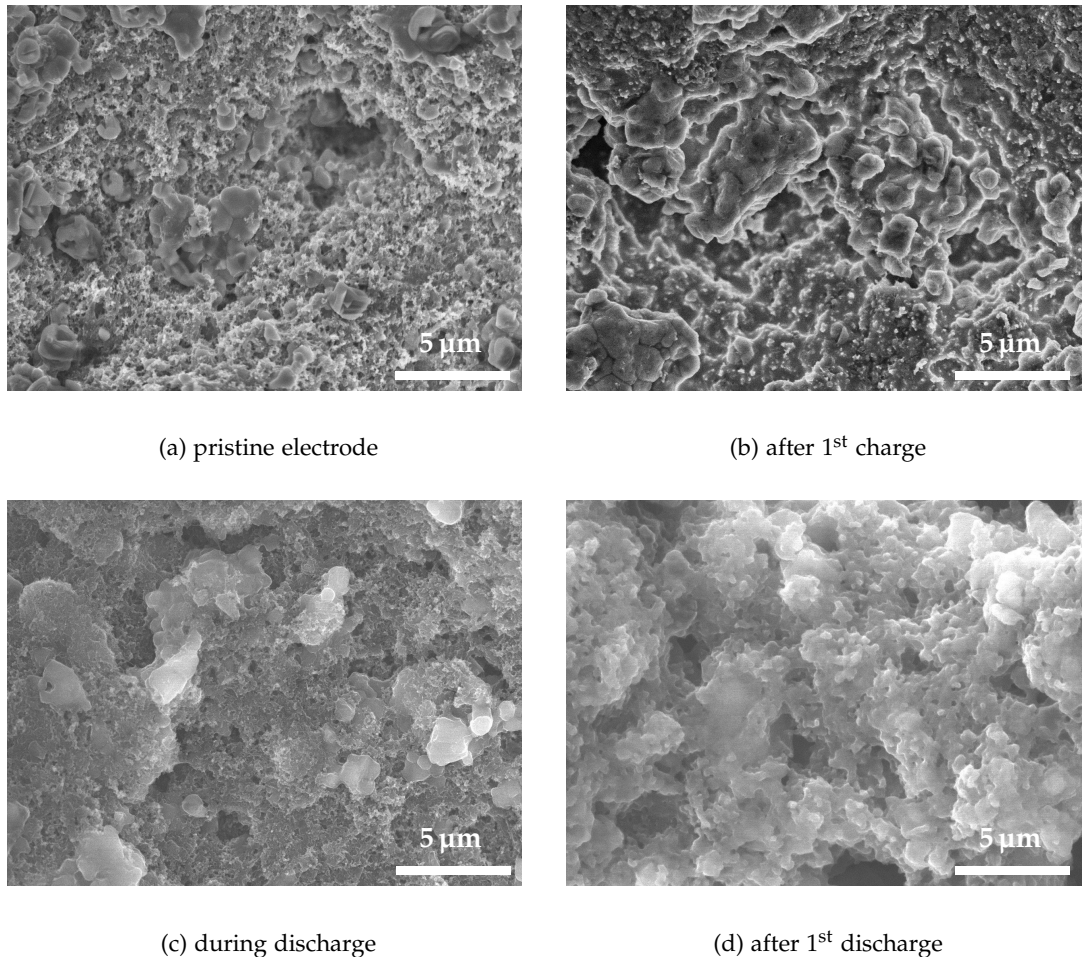


Figure 3.8: SEM micrographs of Li₂S electrodes during cycling. All electrodes are from the same batch, built into similar cells. The cells are stopped and the electrodes removed at different SoC during the first cycle. Magnification: 5 000×.

3.1.3 Transmission electron microscopy

To confirm that a core-shell structure is actually formed when coating the Li₂S particles, transmission electron microscopy (TEM) is used. The resulting micrographs were provided by Xiangyun Song¹ and can be found in Fig. 3.9. The images suggest that the Li₂S core particles are mostly crystalline (pattern on the right hand side of Fig. 3.9) and coated by a thin and rather uniform carbon layer. Based on the TEM images, its thickness is 16–29 nm. The material used for these images has an average particle size of $1.1 \pm 0.3 \mu\text{m}$ (determined by measuring the diameter of numerous particles in a low magnification SEM micrograph) and contains $1.9 \pm 0.9 \text{ wt.\%}$ of carbon coating (determined by weighing during the CVD process). Choosing $m_{\text{carbon}} : m_{\text{total}} = 1.9 \%$ and $r_{\text{core}} = 1.1 \mu\text{m}$ in Eq. (2.1), the coating's thickness is calculated to be $370 \pm 140 \text{ nm}$. This tremendous discrepancy can be explained by two effects: either the average particle size is considerably smaller than determined or carbon is trapped in the agglomerates. To match the results, however, the particles need to be as small as 100 nm or $> 80 \%$ of the carbon needs to be unavailable for coating, both of which seems unlikely. Another possible but equally unlikely explanation is that the carbon is preferentially deposited on the CVD boat instead of the Li₂S particles, forming carbon black. Since TEM micrographs are the most direct way to examine the coating, the figure extracted from these images is considered to be more accurate than the calculations based on weight and geometry.

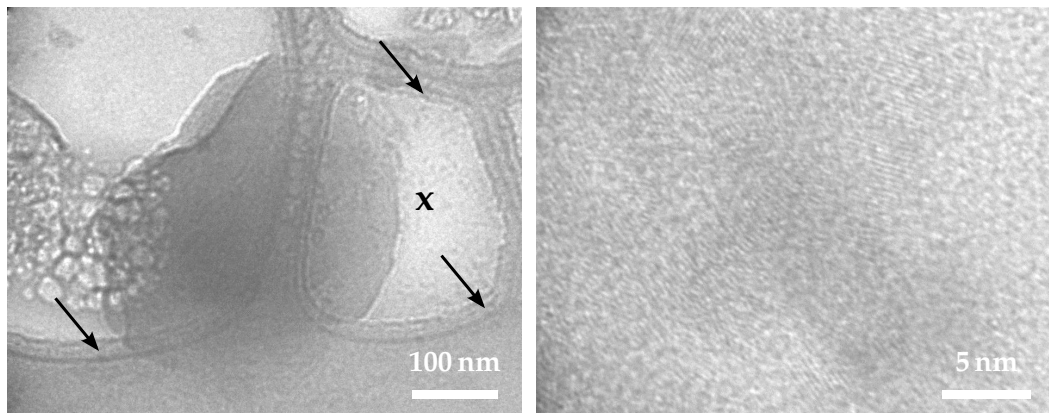


Figure 3.9: TEM images of carbon-coated Li₂S particles. Left: core-shell structures, 250 000 \times ; right: close-up of the Li₂S core, 1 000 000 \times (at the position marked by “x”). The arrows indicate the carbon coating.

¹Senior technician, Environmental Energy Technologies Division, Lawrence Berkeley National Laboratory, 1 Cyclotron Road, Berkeley, CA 94720, USA

3.1.4 Chemical/physical tests

Raman spectroscopy. Using TEM, one can only take a close look at a few random samples of the material. In order to further analyze the effect of the coating, Raman spectroscopy is used which can simultaneously or subsequently scan comparatively large amounts of material, averaging over hundreds of particles. Raman spectra were kindly provided by Simon F. Lux². Fig. 3.10 shows spectra of three samples of carbon-coated Li₂S powder. The samples were coated for 1 h, 2 × 1 h, and 3 × 1 h, respectively, and ground up in the glovebox in between subsequent coating runs as described in section 2.2.2.

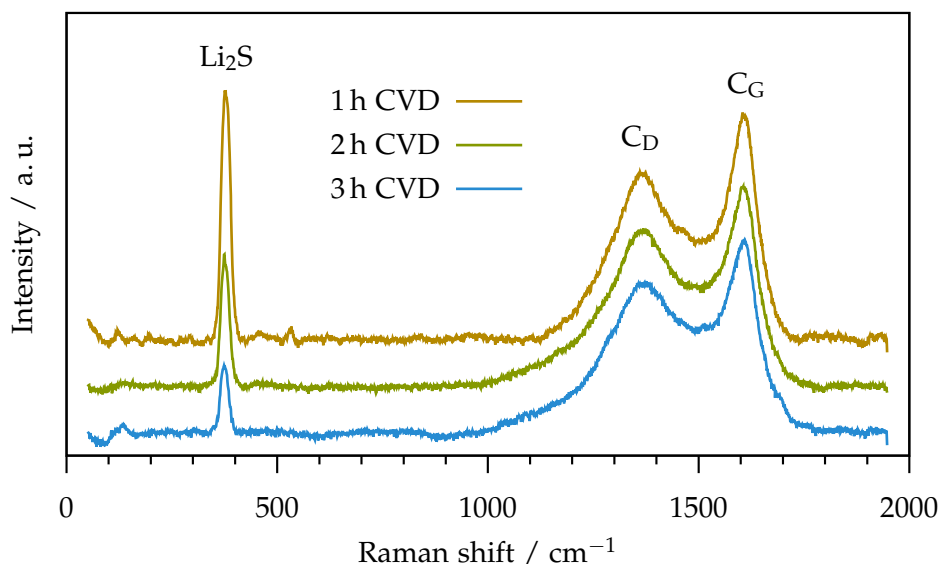


Figure 3.10: Raman spectra of carbon-coated Li₂S recorded after different coating times. The main Li₂S signal is labeled as well as the carbon's D and G bands.

The powders look uniformly dark gray after 1 h and black after 2 or 3 h coating time. As expected, the Raman signal of Li₂S is damped for longer coating times. Note that the Raman activity of Li₂S is considerably higher than that of carbon. In all three cases, the carbon shell constitutes the majority of the volume analyzed, which is confirmed by the virtually unchanged carbon signal. Spectra recorded at different positions look very similar (data not shown). Even after 3 h of coating, however, there is still some Li₂S signal left. While Raman spectroscopy is often called a surface-sensitive technique, the incident laser beam (with a wavelength of 488 nm) has a finite penetration depth of a few hundred nanometers [136, 137]. Since the carbon coatings can be even

²Electrochemist post-doc fellow, Environmental Energy Technologies Division, Lawrence Berkeley National Laboratory, 1 Cyclotron Road, Berkeley, CA 94720, USA

thinner, the underlying bulk material does still contribute to the Raman signal, even if it is not exposed. Unfortunately, it cannot be told whether the remaining signal after 3 h of coating is due to the faint contribution of the bulk Li₂S or whether some particles are not perfectly coated. Additionally, because of the way Raman spectroscopy works, the results do not rule out the possibility that the coating is uniformly applied, but meso- or microporous. In that case, it could still be penetrated by the electrolyte and dissolved polysulfides.

Chemical coating test. Since both TEM and Raman spectroscopy cannot convincingly answer the question whether the carbon coating can be penetrated by dissolved polysulfides or not, the test described in section 2.4.2 is applied to the material. This test examines the properties of the carbon coating as a barrier for polysulfide movement in a realistic setting. Images of a test are presented in Fig. 3.11, whereas Tab. 3.1 lists the sample compositions and the corresponding test results.

Table 3.1: Chemical test of the carbon coating as a polysulfide barrier. Composition and test result of each sample shown in Fig. 3.11 are listed. For the electrodes, the size of the patches is chosen such that they contain about 0.5 mg of active material.

label	composition	result
0	NMP and test solution only	negative
-	5.0 mg carbon black	negative
+	electrode prepared from non-coated Li ₂ S (according to [77])	positive
++	0.5 mg Li ₂ S	positive
1	electrode prepared from coated Li ₂ S	positive
2	0.5 mg coated Li ₂ S powder	positive
3	electrode prepared from coated Li ₂ S (extra thick coating)	positive

In order to build confidence in the test, four controls are included in the series: First, pure testing solution is added to NMP in order to confirm that the sulfur contained in the testing solution does not cause any coloration by itself. Second, plain carbon black is tested as a negative control. Third, an electrode containing Li₂S without any coating is tested as a positive control and finally, pure Li₂S is dissolved in NMP in order to confirm that Li₂S actually causes the coloration. All of the controls result in the expected outcomes. There is a difference in the intensity of the blue color for samples “+” and “++”, which is most likely caused by different amounts of dissolved Li₂S; nevertheless the interpretation of the results is unambiguous.

Three samples are tested in this experiment: one electrode prepared according to

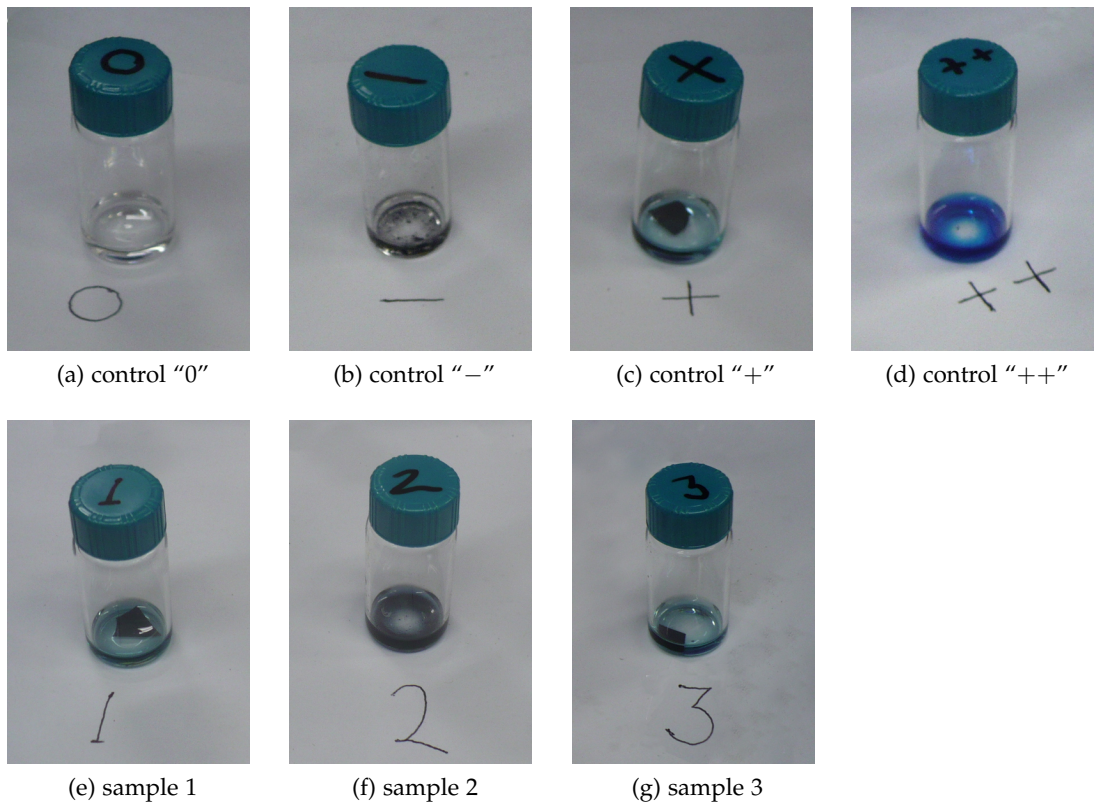


Figure 3.11: Chemical test of the carbon coating as a polysulfide barrier. Blue color indicates that polysulfides are present in the solution. The composition of each sample is reported in Tab. 3.1. Details see text.

the standard recipe (1), the corresponding active material powder (2), and another electrode (3) prepared from Li₂S powder with an extra-thick coating (total CVD time 5 h at 400 °C; 6.5 wt.% carbon). Unfortunately, dissolved polysulfides were detected for all three samples (as for all other Li₂S-containing samples, data not shown). Therefore, despite the uniform black look of the coating as well as the encouraging Raman and TEM results, it has to be stated that the coating does not prevent polysulfide formation and dissolution in the liquid electrolyte – at least not completely.

In the full cell, the situation might actually even be worse, since the coating may also be damaged during the Li extraction at elevated voltages during activation, cf. section 3.2.3. Also, there is considerably less solvent in the cell than in this test, therefore the concentrations of the polysulfides may be quite high, even if only a small fraction of the active material is leaked into the electrolyte.

Beaker cell runs. The failure to prevent polysulfide dissolution is also evident when looking at the beaker cell during operation. The photos in Fig. 3.12 picture the cell at

various stages during the first charge. A constant current is applied (corresponding to a nominal C/4 rate) by the potentiostat until the cell voltage reaches 4.0 V. Intensely colored polysulfides are visible in the electrolyte already at moderate SoC and potential, as reported for conventional electrodes without sulfur retention in Ref. [130]. Of course, the geometry of this cell is rather particular and the amount of electrolyte used is very high; nevertheless, there is no reason to believe that the leakage would be any less severe in a coin cell.

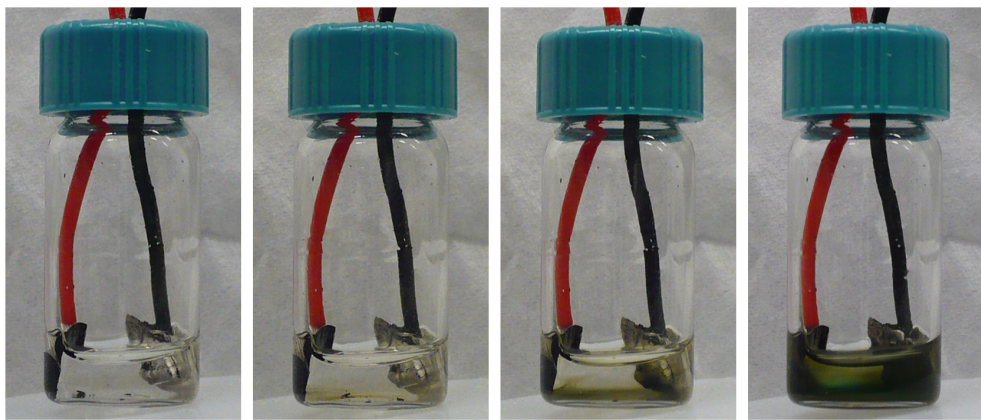


Figure 3.12: Images of the beaker cell taken at various times during the first charge.
From left to right: 0 h, 1 h, 2 h, end-of-charge (~ 4 h).

While these findings are somewhat discouraging, they do not necessarily mean that the approach followed in this work is generally unsuitable. The coating still serves other purposes such as providing electronic conductivity, a large reactive surface area, and (micro-)mechanical stability, cf. section 2.1. It does mean, however, that polysulfides will be present outside of the carbon shells and hence the electrolyte is important for the performance of the cell beyond providing a means of Li^+ transport. Therefore, the electrolyte's composition and its optimization will be discussed next.

3.1.5 Electrolyte optimization

Initially, it was planned to use the ionic liquid based electrolyte reported in Ref. [109] for this work because of its thermal stability, good ionic conductivity, and safety. Using this electrolyte, however, the best cycling performance could not be obtained. Investigating the issue, it turned out that the PEGDME component – which additionally contains a polymerization inhibitor and up to 4000 ppm trace water – can disintegrate and dissolve significant amounts of metallic lithium, see Fig. 3.13.

When drying the solvent using molecular sieves, or adding salts to the solution, this problem can be alleviated greatly. Nevertheless, this finding set off a search for

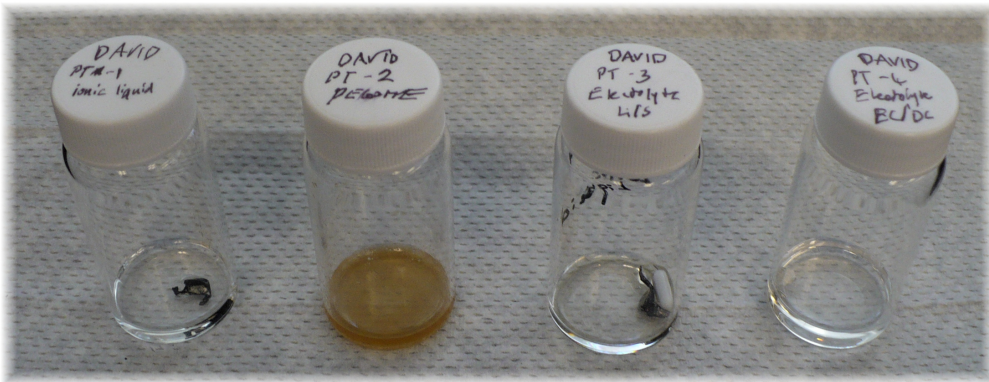


Figure 3.13: Lithium foil incubated in different solvents for 24 h at room temperature. From left to right: Pyr₁₄TFSI ionic liquid (Li intact, dark), PEGDME (Li completely dissolved), electrolyte according to Ref. [109] (Li intact, dark), EC:DEC 1:1 (Li intact, shiny).

alternative electrolytes. As discussed in the previous section, it simultaneously became clear that – despite the coating of the active material – there will still be dissolved polysulfides during operation. Therefore, most electrolytes used for conventional Li-ion batteries, such as mixtures of ethylene carbonate (EC) and diethyl carbonate (DEC), can be ruled out right away. Of course, the new electrolyte should maintain as many of the attractive properties reported in Ref. [109] as possible. Therefore, the ionic liquid portion, responsible for most of the benefits, is not changed. Instead, different combinations are evaluated as listed in Tab. 2.2 on page 25. Various properties of these electrolytes are compared against the base electrolyte (#1). Since the density and the mean molecular weight of the PEGDME used are very similar to that of pure TEGDME (i.e. PEGDME with $n = 4$), this solvent is a natural choice. In addition, the mixture of DOL/DME is evaluated because various references reported good performance of either the pure solvent or various blends: according to Ref. [103], DOL/DME is actually the most commonly used electrolyte for Li/S batteries. Finally, a mixture of PC, EC, and DEC, an electrolyte typically used for Li-ion cells, is tested for comparison.

The conductivity is calculated from high frequency impedance measurements. Electrochemical stability was analyzed by cycling the electrolyte in cells with two stainless steel electrodes in the voltage range of 0.0–5.0 V. The column “wetting” relates to the time it takes for the electrolyte to soak the separator, which ranges from ~ 1 s for DOL/DME to about 30 s for the PEGDME based electrolytes. The cycling performance was evaluated at various rates by Min-Kyu Song³ (data not shown). The data was obtained using a different kind of sulfur cathode, as reported in Ref. [76]. Nevertheless, the results are considered to be qualitatively applicable for this work as well.

³The Molecular Foundry, Lawrence Berkeley National Laboratory, 1 Cyclotron Road, Berkeley, CA 94720, USA

electrolyte	conductivity	electrochem. stability	wetting/ viscosity	cycling	rate capability
#1	0.044 S/m	? [†] –4.4 V	poor	poor	decent
#2	0.051 S/m	1.5–3.7 V	poor	good	decent
#3	0.096 S/m	1.5–3.6 V	poor	good	decent
#4	— [†]	1.6–3.4 V	poor	good	decent
#5	0.199 S/m	1.3–4.2 V	good	good	good
#6	0.047 S/m	1.4–4.0 V	good	good	good
#7	0.232 S/m	1.5–4.2 V	very good	very poor	— [‡]

Table 3.2: Summary of the properties of various electrolytes evaluated as a replacement of electrolyte #1. The composition of each electrolyte is listed in Tab. 2.2. Annotations: [†]data not available. [‡]cell capacity smaller than instrument noise.

Because of the combination of good wetting and rate capability, the mixture containing DOL/DME is chosen as the new standard electrolyte. Another benefit of the DOL/DME mixture is its low dielectric constant ($\epsilon_r = 7.2$), which correlates to a lower voltage hysteresis compared to otherwise similar electrolytes [138]. Since the higher salt concentration does not seem to provide any advantages, the variant with the lower concentration (#5) is chosen. Of course, DOL and especially DME has a higher vapor pressure and lower flashpoint than PEGDME, thereby partly compromising the inherent safety of the electrolyte. A systematic study investigating exactly this mixture was reported by Matic et al. [139], unfortunately only after this work was completed. Their findings indicate that the optimum mixture contains only 5–15 % DOL/DME. Already a small addition of organic solvent to the ionic liquid can result in considerably lower viscosity, better wetting, and higher ionic conductivity while still maintaining high safety, see also Ref. [140]. Nevertheless, the electrolyte identified in this study works very well with the novel cathode material, as can be seen in the following sections.

3.2 Analysis of full cells

While the investigations at the material and electrode level presented above are most important for understanding and improving the composition and structure of the cell’s components, it is the analysis of full cells that matters most from the application’s point of view. Therefore the performance at cell level is a key criterion for the evaluation of battery materials.

3.2.1 Introduction

Many different properties of a battery can be studied by means of various electrochemical full-cell measurements. The most common and most direct way to analyze a battery is the recording of charge/discharge traces, either voltage vs. time or voltage vs. capacity. A characteristic charge/discharge profile is shown and annotated in Fig. 3.14. Several distinct stages are visible in the plot: Starting from a fully charged cell, the voltage stabilizes at an upper plateau (I), while solid S₈ is available and accessible [141]. The concentration of polysulfides increases during that phase, both because of the dissolution of S₈ and because of the reduction and disproportionation of polysulfides, forming dissolved S_x²⁻ species with $8 > x \geq 4$, cf. Refs. [141, 142]. These processes are balanced until the supply of S₈ diminishes. Once it cannot keep pace with the reduction reactions anymore, the average length x of the dissolved polysulfides starts to decrease. The solubility and the molar Gibbs free energy are lower for shorter polysulfides [143], which directly translates to a lower free energy of reaction ΔG_q for the reduction steps forming shorter polysulfides. Since the equilibrium potential is proportional to ΔG_q (see e.g. [144, chap. 1.2]), this corresponds to a decreasing cell voltage during this stage (II). When x approaches 4, the formation of even shorter polysulfides ($x = 1-3$) is enhanced [142]. Their solubility is considerably lower [145], so that the saturation concentration of S²⁻ will be reached quickly and precipitation of Li₂S starts to occur. Whether or not S₂²⁻ may also precipitate as Li₂S₂ is a current subject of debate, beyond the scope of this explanation [146, 147]. Depending on the cell's design and composition, a significant level of supersaturation is required to induce nucleation of Li₂S, though. Once a sufficient amount of precipitate is formed, a dynamic equilibrium is established, buffering the concentrations of the short polysulfides [141, 148, 149] and hence the cell voltage (III). Most of the discharge capacity is actually obtained at this low-plateau phase during which the polysulfides are continuously converted to solid Li₂S (or maybe also other solids, see note above). The discharge ends if a) there is no pathway for electrons to meet with the dissolved ions anymore [150], e.g. if the entire carbon surface is covered by insulating material [151, 152], or b) the electrode is clogged by precipitate so that any remaining active material is not accessible to the electrolyte [153], or c) all active material is actually used up [99]. Depending on a cell's composition, the rate of discharge, and the SoH, either of these factors may trigger the end of discharge.

During charging, the situation is different: Dissolved S²⁻ is oxidized along with the other dissolved polysulfides, so that its concentration quickly drops below the saturation concentration and Li₂S is re-dissolved. The solubility of dissolved S_x²⁻ increases with increasing x [154]. As a result, the concentrations of all polysulfide species are replenished more or less simultaneously, as confirmed by simulations in section 5.2.3.

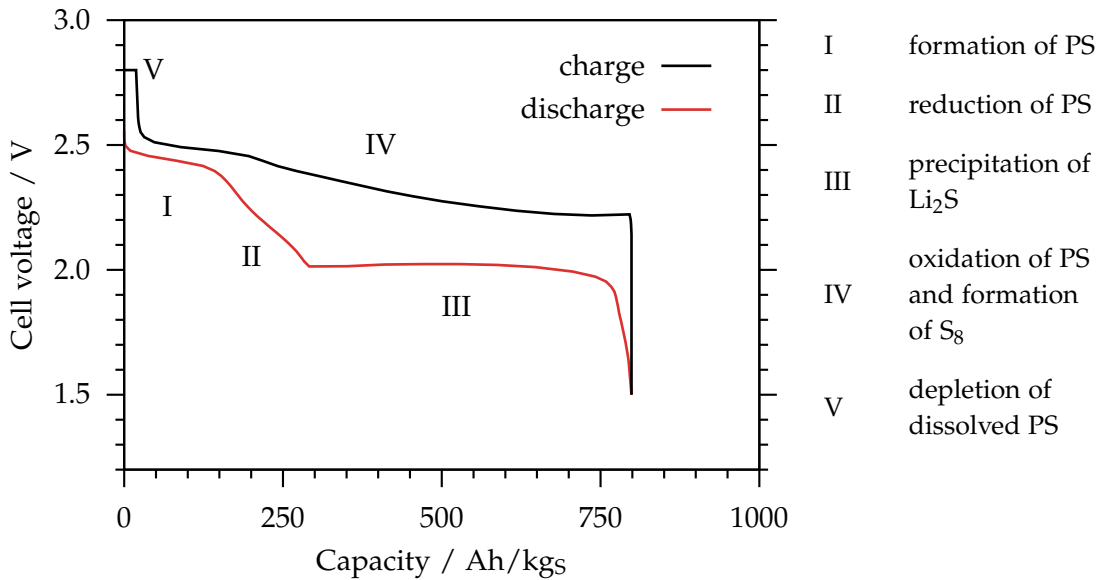


Figure 3.14: Representative discharge/charge profile of a liquid-electrolyte Li/S cell. Characteristic stages are labeled and described in the text.

When the concentration of dissolved S_8 becomes high enough, solid S_8 can be formed again [155, 156]. The average length of the dissolved polysulfides increases steadily and therefore, plateaus are hardly discernible (IV). Since the precipitating S_8 occupies a smaller volume than the corresponding amount of Li_2S , pore clogging is usually not an issue during charging. Instead, the end of charge is triggered by the depletion of the electrolyte of polysulfides, whether all material is used up [148] or the dissolution of Li_2S cannot keep up with the oxidation reactions [157]. Either way, this causes a steep rise of the cell voltage. In order to fully recharge the cell, a constant voltage phase is applied at the end of charge (V), during which the current density drops steadily, but not immediately, until it reaches the order of magnitude of the leak current. This technique is known as CCCV charging and also used for many other types of batteries, cf. [158]. This way, additional capacity is recovered without the need for hazardously high voltages or excessively long charging times. Whether or not Li/S cells are also suitable for boost charging [159] has not yet been investigated.

Of course, the specific shape of the profile does depend on the composition of the cell. For dissimilar systems, e.g. with solid electrolytes, the charge/discharge profiles look rather different. For liquid-electrolyte Li/S cells, however, the profile shown in Fig. 3.14 is very typical and was observed for all cells in this work.

3.2.2 Metrological considerations

For comparison with other published results, the most useful figure besides the cell voltage is the specific capacity of the cell, i.e. the charge transferred per unit mass. It is measured in $\text{Ah} \cdot \text{kg}^{-1}$, either specified with respect to the mass of sulfur ($1675 \text{ Ah} \cdot \text{kg}^{-1}$ being the maximum theoretical capacity), or with respect to the total electrode mass, see also section A.2 in the appendix. As already mentioned, there are various issues associated with the determination of the true capacity of each individual coin cell. Before results will be reported in the following sections, an attempt is made to quantify the error by summing up the sources of deviations and uncertainties:

- First, the amount of LiOH , LiO_2 , and impurities in the sample is estimated to be $10 \pm 8\%$ of the Li_2S weight as determined by EDX.
- A fraction of the Li_2S particles is very large even after ball milling. While there are only very few large particles, they contain a disproportionately high fraction of the Li_2S , estimated to be $4 \pm 2\%$. Some of these particles will be scraped off the electrode in the doctor blading step, but anyway, they do not contribute to the cell's capacity, since the bulk material of those large particles is not electrochemically accessible because of high diffusion overpotentials.
- During CVD coating, the amount of additional carbon is only known to $\pm 1\%$.
- Weighing and mixing precision during slurry preparation is $\pm 4\%$.
- Weighing of the final electrodes is precise to $\pm 2\%$.
- The electrodes are always weighed including the current collector, which accounts for the largest part of the electrodes' weight and is not perfectly uniform. The fluctuation is determined to be $\pm 0.13 \text{ mg}$ by a dedicated series of measurements (data not shown). This corresponds to an uncertainty in the capacity of $\pm 9\%$ for a 10 mg electrode containing 1.5 mg of active material.

In summary, the true capacity is expected to be $14 \pm 13\%$ higher than specified. This uncertainty is unpleasantly high, but also difficult to improve. Nothing is really known about the impurity of the initial Li_2S powder and without exchanging the material or equipment, the other sources of uncertainty cannot be eliminated. Except for the weighing precisions, however, the above errors affect all cells – or at least all cells of one batch – in a similar way, so that a comparison of different results within this work is still possible with reasonably good accuracy. The absolute values reported most probably underestimate the true capacity, however.

3.2.3 Slow cyclic voltammetry

As reported in Ref. [78], positive electrodes made from Li₂S need to be activated in order to access the full capacity of the material. This effect is also observed for the cells presented here. Without activation, the capacity obtained for the first cycle is considerably lower. It may slowly rise during the following cycles, but even the maximum capacity – typically reached within the first 50 cycles – is lower than that of similar cells after activation (data not shown). Therefore, a first activation (or “formation”) cycle is run with a different protocol to access the full capacity. Cyclic voltammetry was used to optimize this activation protocol.

In general higher voltages, higher temperature, slower charge rates, and longer rest times at elevated voltage can increase material utilization during the activation cycle. To begin with, a very simple approach is tested: The cell is charged up to 4.0 V, i.e. to the edge of the window of electrochemical stability of the electrolyte (cf. Tab. 3.2). Starting from the pristine (discharged) state, the cell was cycled three times at a fixed rate of 25 µV/s in the range of 1.5–4.0 V, see Fig. 3.15.

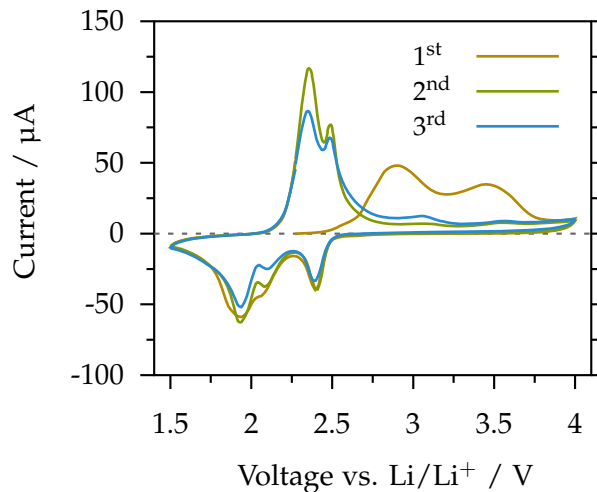


Figure 3.15: The first three cycles of a cell. Voltage sweep rate: 25 µV/s. Charging up to 4.0 V is needed to activate all of the Li₂S. Only during the first cycle, however, a significant amount of charge is passed above 2.8 V.

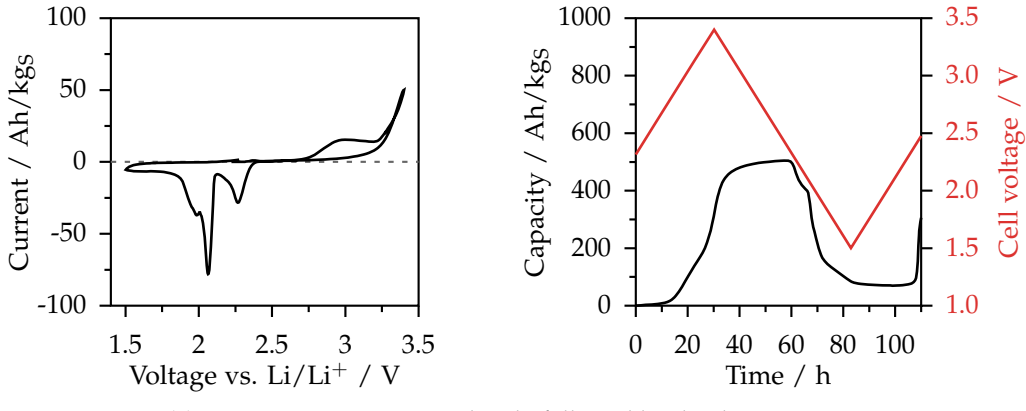
Since the voltage changes quasistatically and with a constant sweep rate, peaks in Fig. 3.15 correspond to voltage plateaus in a galvanostatic discharge profile, as in Fig. 3.14. During the discharging step, two cathodic peaks are apparent which are well separated, with a small peak or shoulder in between. After activation, i.e. for the second and third cycle, two anodic peaks are detected during the charging step, which are relatively close to each other and overlap significantly. Since in this representation, one peak corresponds to one electrochemical reaction (or one set of simultaneously

occurring electrochemical reactions), it becomes immediately clear that the chemistry of the cell is dominated by different reactions during the early and late discharge and charge, respectively. Regardless of the specific cell geometry or composition, this is a characteristic feature of the Li/S system.

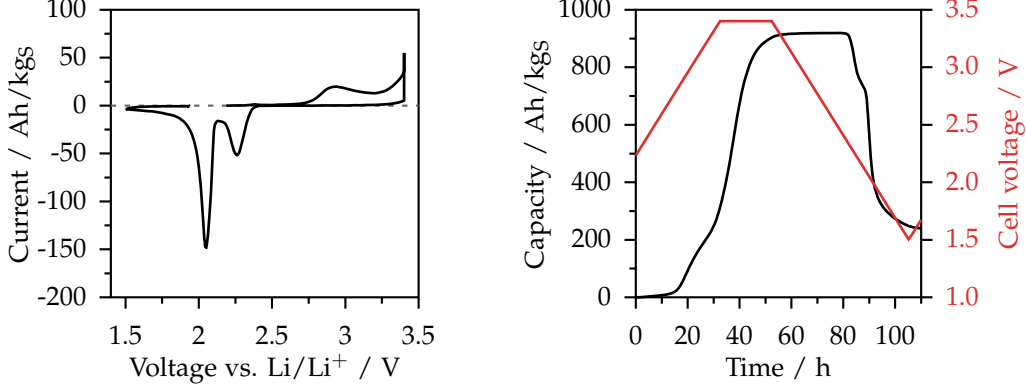
The results confirm the behavior reported in Ref. [78]: The first charge looks distinctively different from the following charges. Two conclusions can be drawn from the results presented in Fig. 3.15: First, during the initial charge most of the capacity is obtained at voltages above 2.8 V, i.e. above the charge cutoff voltage used throughout this work. Therefore, in order to access as much capacity of the cell as possible, it is necessary to exceed 2.8 V during activation. Second, for the following cycles, almost all of the capacity is recovered within the peaks at 2.3 and 2.5 V. While a little capacity is lost from the second to the third cycle, the shape of the CV profiles remains the same. There is virtually no benefit in using a higher voltage for a second time. Actually, it is not even clear whether the little remaining capacity above 2.8 V is reversible. Operating the cells at high voltages is potentially harmful, since it increases stress in the electrode material. Also, it might open up pathways for electrochemical degradation reactions, causing a leak current which must not be attributed to Li_2S oxidation. Thus, for subsequent tests, lower voltages are used instead, but for prolonged times. After the initial activation, the cells are charged up to 2.8 V only.

An improved activation protocol is presented in Fig. 3.16a: The voltage is increased to 3.4 V instead of 4.0 V, but at a lower rate of $10 \mu\text{V/s}$. While almost the same capacity is obtained, a significant current is still passed at 3.4 V. In order to collect all the charge associated with that current, but without further lowering the sweep rate, the following protocol was tested: After the upsweep, the voltage is held at 3.4 V for 20 h. This way, even more capacity can be accumulated, cf. Fig. 3.16b. The standard I_{tot} vs. E plot of this experiment looks unintuitive, though. To better analyze the situation, the plot is changed from the traditional I_{tot} vs. E to a Q_{tot} and E vs. t plot as presented in the right column of Fig. 3.16. Here, the cell voltage E (red line) is enforced by the potentiostat and can be interpreted as the “input”, whereas the total accumulated capacity Q_{tot} (black line) is the “response”. In this representation it becomes obvious that at the time the charge cutoff voltage is reached, the capacity is not yet at its maximum, see Fig. 3.16a. Even while the voltage is swept down, the capacity still increases until E drops below the cell’s OCV. In Fig. 3.16b, however, the capacity levels off during the constant voltage phase, meaning that all charge available at that potential is actually collected.

As a result, the activation protocol presented in Fig. 3.16b is established as a standard for the following experiments. As a slight variation, this protocol is usually preceded by a constant-current charging step.



(a) Upsweep to 3.4 V, immediately followed by the downsweep to 1.5 V.



(b) Upsweep to 3.4 V, followed by a 20 h rest at constant voltage and a downsweep to 1.5 V. Note that in the left representation, the extra capacity collected during the constant voltage phase is hidden in the vertical line at 3.4 V.

Figure 3.16: Two different activation protocols, analyzed by slow cyclic voltammetry. Left column: Standard representation, i.e. current plotted vs. voltage. Right: Voltage (red) and charge capacity (black) plotted vs. time.

3.2.4 Impedance spectroscopy

A typical impedance spectrum of a Li/S cell is shown in Fig. 3.17. There are several distinct features, which can be evaluated qualitatively directly from the graphical representation, see [132, chap. 18]: First, the high frequency intersect with the real axis directly correlates to charge transport in the liquid electrolyte. Second, the size of the semicircle correlates to the average charge-transfer resistance at the carbon surface. Additional overlapping or separate semicircles may be discernible, representing different surfaces, e.g. the lithium electrode. Third, the low-frequency tail is governed by material transport and changing SoC. A straightforward phenomenological approach to interpret EIS results is the creation of equivalent circuit analogs [132, chap. 9]. While this method is suitable for describing even complex electrode morphologies, the val-

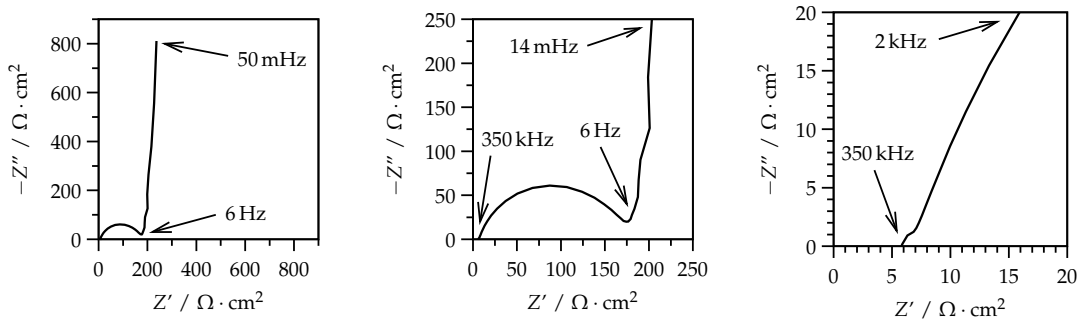


Figure 3.17: Example impedance spectrum of a pristine Li/S cell at three different magnifications, emphasizing different features of the spectrum.

ues assigned to the various circuit elements have only limited physical meaning. Often, they represent complex processes in an oversimplified fashion. Nevertheless, the recorded impedance spectra have a very high information content and are thus equally useful for the determination of parameters in more complex models as presented in chapter 4.

EIS can also be performed at intermittent intervals during operation. Since the composition of the cell changes during cycling, so do the impedance spectra. In principle, these results can be used to estimate the SoC of the cell. Impedance spectra recorded at four distinct stages during the discharge are plotted in Fig. 3.18.

Unfortunately, it turned out that the impedance spectra are not very reproducible, even when looking at cells of the same batch, see Fig. 3.19a. Also, the spectra of one cell, recorded continuously at short intervals do not vary smoothly, but rather messily, see Fig. 3.19b. This is either because the spectrum actually has a very sensitive and complicated dependence on the SoC or – more likely – because the EIS measurements themselves interfere with the cell’s behavior.

This instability was found to have its origin mainly in the lithium electrode, see Fig. 3.19c. Here, spectra of several symmetrical cells (composed of two similar lithium metal electrodes) are plotted. The variance is almost as large as the entire fluctuation observed for regular Li/S cells in Fig. 3.19a. Even worse, the electrodes’ impedance also changes to a great extent during storage and cycling, see Fig. 3.19d, where the EIS results obtained from one Li electrode at different times are plotted. The fluctuations were discovered to become smaller after several charge/discharge cycles (data not shown); nevertheless, the above findings disqualify EIS as a tool for quantitative SoC or SoH analysis for the present cells. Unstable impedance of the lithium metal electrode is a phenomenon reported for various electrolytes in the literature, e.g. in Ref. [160].

In order to separate the contributions of the anode and the cathode, either measurements with a three-electrode cell or with symmetrical cells would be needed.

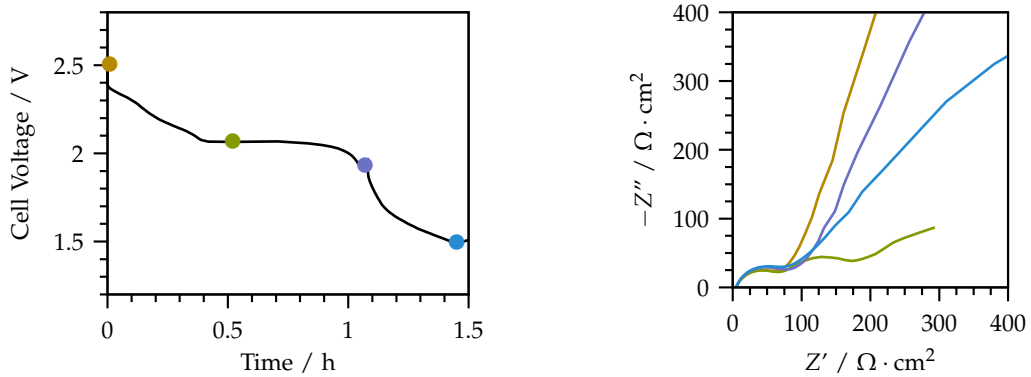
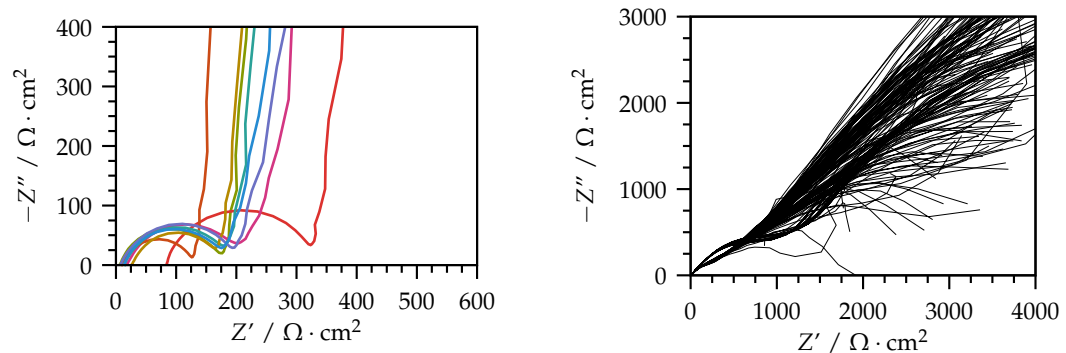
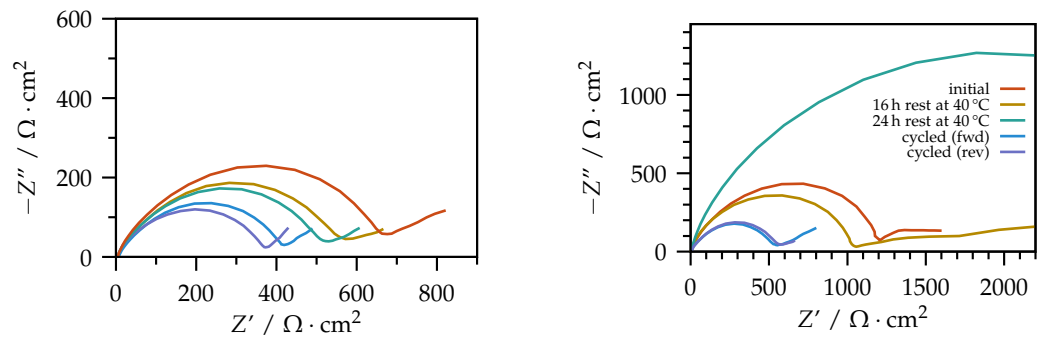


Figure 3.18: Impedance spectra recorded at regular intervals during discharging. Left: discharge profile. Right: corresponding impedance spectra. Colored spots indicate the times at which each spectrum was recorded.



(a) EIS of several similar, freshly assembled cells. (b) EIS of a single cell, recorded every minute during an entire charge/discharge cycle.



(c) EIS of several similar, symmetrical Li/Li cells. (d) EIS of one Li/Li cell at different times.

Figure 3.19: Impedance spectra of similar cells. The purpose of this figure is not to represent the data in detail but to illustrate issues with the reproducibility of the EIS measurements.

For the reasons outlined in section 2.5, however, such data is not available. Therefore, the value of the impedance spectra is limited and they cannot be used for model calibration below.

3.2.5 Charge/discharge profiles

The typical shape of a galvanostatic charge/discharge profile was already explained above. In the following, the evolution of such profiles over several cycles is analyzed. To this end, the first ten cycles of a Li/S cell are plotted as a continuous line in Fig. 3.20. The cell is activated at 3.4 V as discussed in section 3.2.3. Notably, almost half of its capacity is extracted during the constant voltage phase, emphasizing both the need for and the effectivity of the constant-voltage step. After activation, cycling is performed at a C/10 rate. Here, it is interesting to note that – despite a little degradation during each cycle – the plot collectively “drifts” to the left.

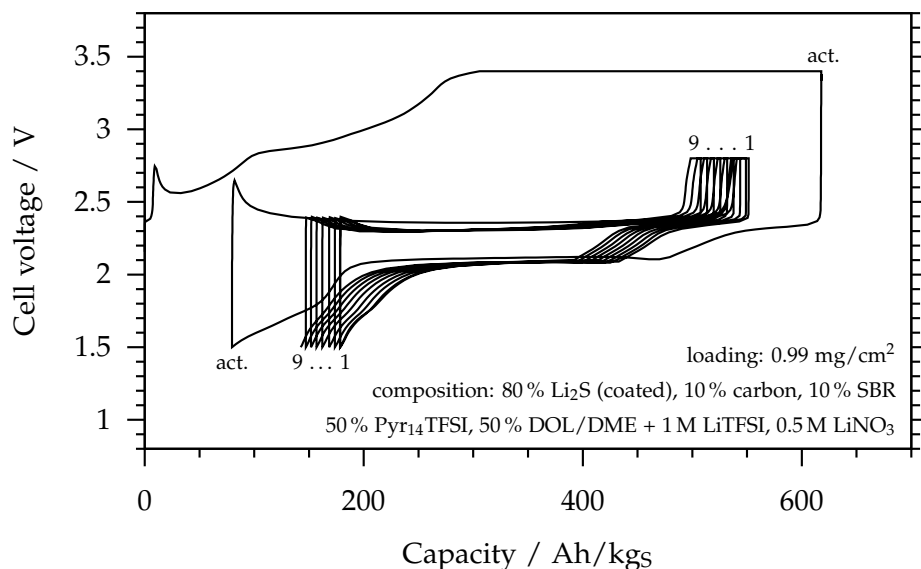


Figure 3.20: Activation and first ten cycles plotted continuously against the total capacity. Activation at C/50 (charge) and C/20 (discharge). Subsequent cycles at C/10 (charge and discharge). The experiment starts with a fully discharged cell, i.e. at capacity = 0. Labels indicate the cycle index.

While the reasons for this “drift” are not clear, two reasonable explanations can be proposed: First, additional Li₂S could be activated during each cycle. While not all of the theoretical capacity is made available in the activation step, this does not necessarily mean that all of the remaining Li₂S is completely inaccessible. Instead, the material may be released slowly during subsequent cycles, for example from the bulk of very large particles or agglomerates. This effect happens predominantly during the first 50

cycles and can actually lead to a temporary increase of the capacity, cf. e.g. Fig. 3.24. For reasons unknown, the SBR binder used in these cells is often associated with this behavior [161]. Second, a small fraction of the electrons transferred may not contribute to sulfur oxidation, but instead fuel side reactions such as the polysulfide shuttle. This cell configuration does not suffer from the shuttle effect much and consequently, no infinite charging [51, 113] was observed ever. Still, some of the charge capacity might enter this pathway or other side reactions.

The voltage trace can also be illustrated differently: Fig. 3.21 shows results of another cell, this time plotting voltage vs. the capacity transferred during each half cycle, resetting the abscissa to zero at the end of each charge or discharge. In this representation, each half cycle can be directly compared to the following (or preceding) one. This way, any discrepancy can be spotted and quantified easily. Degradation can be observed by comparing subsequent discharges. To enhance the effect, only every 10th cycle is plotted in Fig. 3.21.

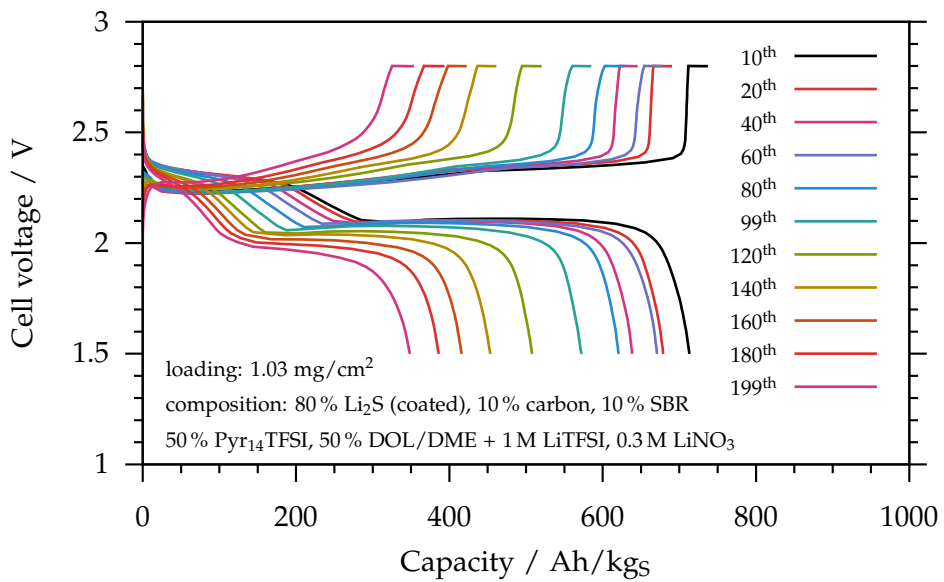


Figure 3.21: Continuous capacity fade over 200 cycles. Charge and discharge at a rate of C/10. The cell voltage is plotted against the capacity transferred during each half-cycle.

Besides the capacity fade, the most prominent effect of degradation is the increased voltage hysteresis, which almost doubles during the first 200 cycles for the cell presented in Fig. 3.21. The hysteresis, i.e. the difference in voltage at the same SoC during charge and discharge, is directly proportional to the anergy, i.e. the energy lost as heat during one cycle. The exergy, in contrast, is proportional to the integrated area under the discharge curve and finally, the total work performed is equal to the area under the

charge curve. An increased hysteresis therefore means a lower charge/discharge energy efficiency of the cell. In addition, it makes it increasingly harder to fully recharge the cell. Finally, the shape of the discharge/charge profiles alters over time, too. The most obvious changes are the upper plateau to lower plateau ratio during discharge and the voltage slope of the charging branch. A quantification of these (and other) features for comparison with data extracted from reference profiles would allow for a phenomenological SoH estimation without the need for a detailed analysis of degradation effects [162].

The first and most obvious conclusion from this data, however, is that degradation of the cell happens at a non-negligible rate, thereby limiting the cyclability of the cell. This effect is best analyzed by looking at plots of capacity vs. cycle number, presented in the following section.

3.2.6 Cycling

Since both cycle and calendar life of the Li/S cells presented in this work are rather limited, the quantification of the SoH is very important. To this, the measured capacity of a cell is plotted vs. cycle number in Fig. 3.22. The data was recorded from one of the first batches of the novel electrodes based on carbon-coated Li_2S , using the material presented in Fig. 3.4b. The results confirm that this material is generally suitable for Li/S cells, despite the agglomeration. However, they also indicate an unattractively high rate of degradation. This cell was built and tested before the electrolyte was optimized (cf. section 3.1.5). Whether or not the degradation is influenced by the agglomeration and/or the deficient electrolyte was not investigated.

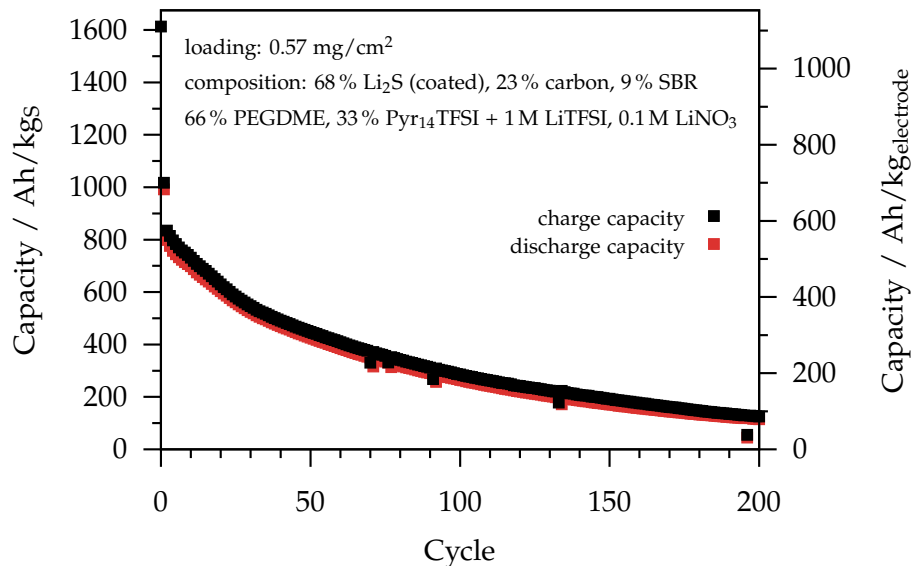


Figure 3.22: Performance of the initial material and cell composition. Charge and discharge at a C/5 rate.

Cells are also tested at different rates. For many applications it is a crucial property of the battery to be able to deliver power at various rates. Results of a cell cycled with different discharge currents are presented in Fig. 3.23. This cell uses the best active material (see Fig. 3.4c), but the electrode preparation is not fully optimized yet (no images available, but processing similar to the electrode presented in Fig. 3.5c). This particular batch of cells did not perform outstandingly and the experiment was not repeated with later batches, due to lack of channels. In addition, the previously mentioned effect of increasing capacity during the first couple of cycles is observed and overlaps with the rate survey – compare for example cycles 10 and 35 (both C/20). Nevertheless, this plot proves that the Li₂S based cells with a high content of active material can still be operated at moderately high rates, albeit with a significant performance penalty for rates above C/5. Adding more carbon and binder would most likely improve the rate capability further, but at the expense of the cell's specific energy.

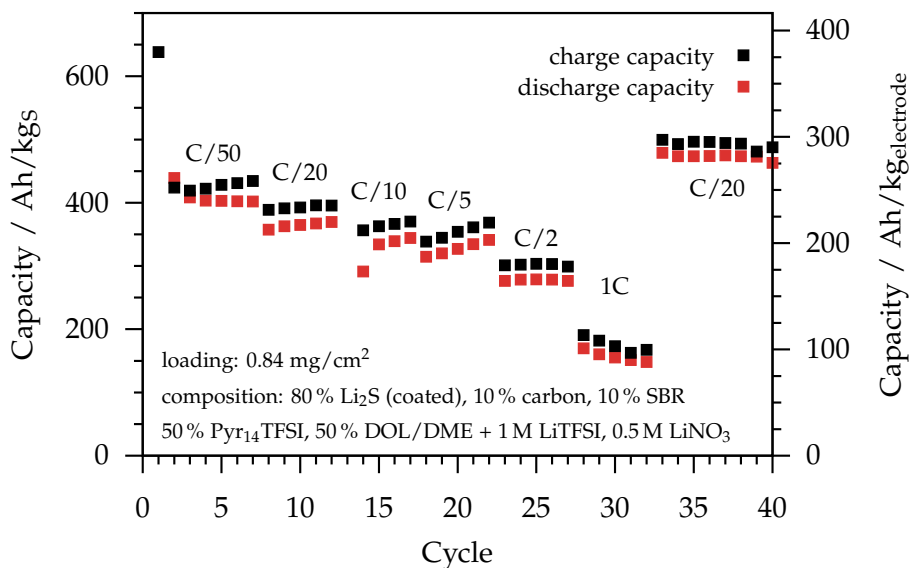


Figure 3.23: Rate capability test. The cell was charged with a constant rate of C/20. Outlier suppressed.

After the various improvements to the slurry composition, coating, mixing, and casting procedure as well as the electrolyte and activation protocol, described in the previous sections, the performance of the cells is improved substantially, see Fig. 3.24. This cell utilizes the active material presented in Fig. 3.4c and electrodes as presented in Fig. 3.5d. Here, a slow cycle is added every 25 cycles to test for the maximum charge which can still be extracted (but not at the regular C/10 cycling rate). Again, the capacity rises slightly during the first 60 cycles, before the usually observed continuous decay takes over. While the loading is still slightly lower than intended, it is

considerably higher than in previous studies. The initial capacity is not significantly improved, but the rate of degradation is reduced by more than 60 % and averages to a mere 3.9 ‰ per cycle on average, and 6.1 ‰ per cycle at the 200th cycle.

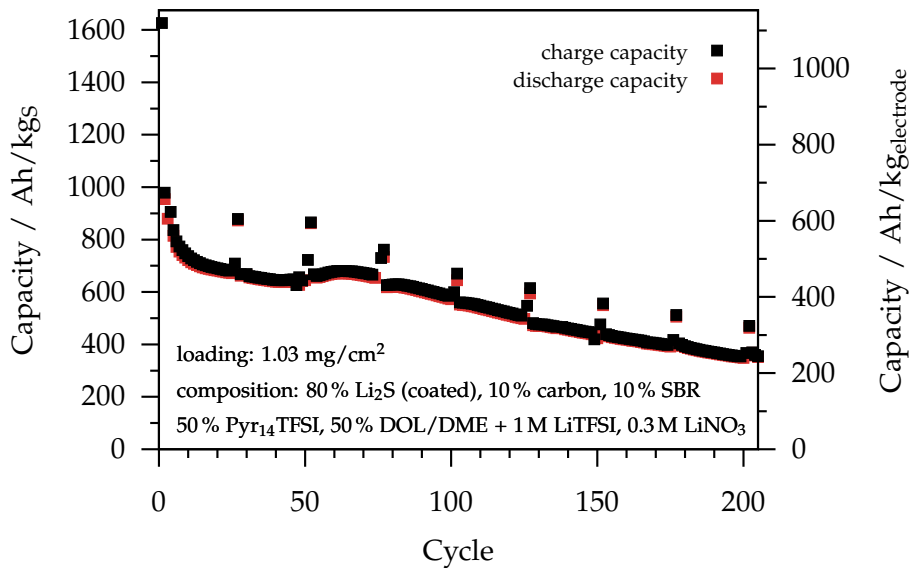


Figure 3.24: Performance of the optimized electrodes. Charge and discharge at a C/10 rate; every 25th cycle at C/50.

Still, there is lots of room for improvement. This is especially apparent when looking at the Coulombic efficiency for the above experiment, presented in Fig. 3.25. The slow cycles (25, 50, 75, ...) are suppressed in this plot, but their effect is still visible: The Coulombic efficiency is slightly increased for several cycles after most of the slow cycles – an effect probably related to the “refreshing” character of slower cycles, discussed in the next chapter on the basis of Fig. 5.3. Disregarding these fluctuations, the Coulombic efficiency stabilizes at around 98.5 %, a value that is considerably too low for stable long-term operation [163, 164]. In effect, this result indicates that ~1.5 % of the current enters parasitic reactions, eventually causing loss of material and degradation. Unfortunately, the analysis and mitigation of these effects could not be completed within this study and remains a goal for future efforts.

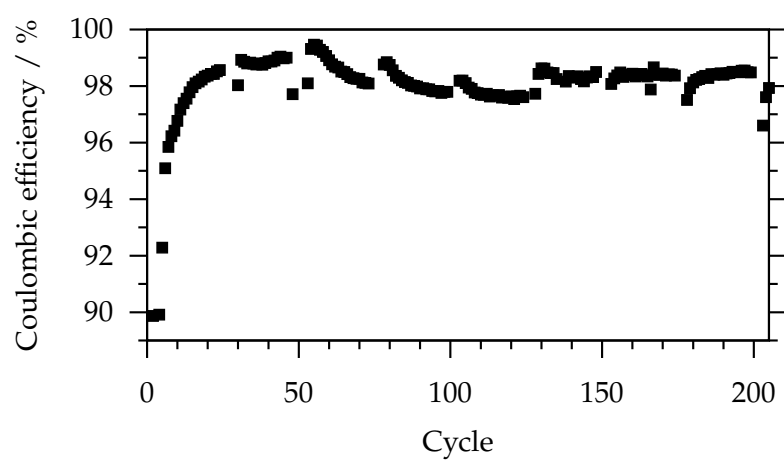


Figure 3.25: Coulombic efficiency of the cell presented in Fig. 3.24. Slow cycles suppressed.

3.3 Conclusions

3.3.1 Achievements

A setup and protocol for chemical vapor deposition of carbon films onto Li_2S particles was developed and optimized. To this end, the CVD process, but also the entire material and electrode preparation was analyzed and adjusted. The coating was applied to several batches of ball-milled Li_2S . The resulting material, as well as full cells built from the material, were characterized. Considering the results reported in section 3.1, the coating method developed in this work is falling short of its primary goal, i.e. the prevention of polysulfide dissolution. Despite this drawback, the material is well suited for advanced Li/S batteries. While the cycling performance is still far from perfect, it is considerably increased compared to published results of Li_2S -based electrodes, cf. Fig. 3.26. The interpretation of the plot is somewhat hindered by the fact that the data reported was recorded at different charge/discharge rates. Still, Fig. 3.26 clearly makes the point of showing the capability of the novel material to achieve state of the art cycling performance.

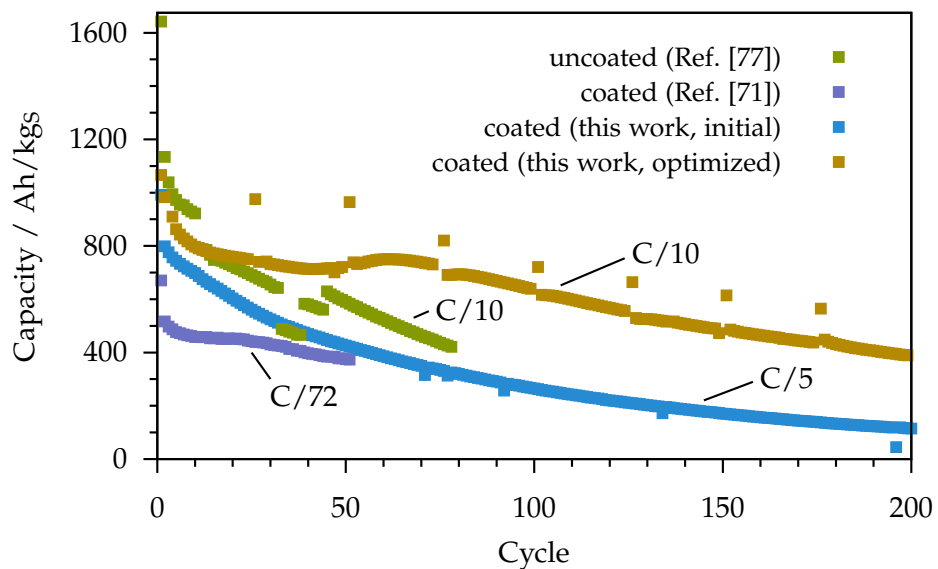


Figure 3.26: Comparison of the cycle life of various Li_2S based electrodes.

Since these experiments were reported at several conferences before similar results were published, it is the merit of this work to demonstrate for the first time that functional electrodes can be built from carbon-coated Li_2S particles. Significant improvements were achieved concerning the initial capacity and cycle life. Ultimately, this effort builds the groundwork for later achievements, e.g. Refs. [133] and [165], by establishing the CVD coating procedure, electrode preparation, and analysis methods.

3.3.2 Possible improvements and outlook

This section is not to be confused with the outlook in chapter 6.3. While in the latter a look at the big picture is presented, this section elaborates on more immediate improvements to the existing experimental methods and setup.

Processing. After the work for this thesis was completed in late 2013, the issue of non-uniform particle size associated with the ball-milling of Li_2S was solved in Elton Cairns' group by synthesizing particles of well-defined size and shape, see Ref. [133]. Additionally, coating uniformness could be greatly improved while simultaneously reducing the complexity of the coating process by using a rotary furnace. This way, the intermittent mixing steps could be omitted and the continuous stirring is expected to reduce particle agglomeration, too. This would enable an additional annealing step at elevated temperature after the coating is completed without causing excessive agglomeration. These advantages were already known at the time the experiments were conducted. However, no rotary furnace was available for testing. Therefore, a simple hand-operated rotary furnace tube was designed and tested in the regular tube furnace, cf. Fig. 3.27. While the properties of the coating were essentially unchanged, initial results suggest that agglomeration could be prevented to some degree even with this simple setup.

Actually, on grounds of these findings, a rotary furnace was set up at LBNL recently, which enables a more uniform coating of the Li_2S particles. As a result of these measures, the performance of the new active material is expected to improve further.



Figure 3.27: Photo of the self-made, hand-operated “rotary furnace” (left). The inner tube is fixed inside the outer quartz tube eccentrically (right). When rotating the outer tube, the inner tube is turned upside down, stirring up the Li_2S powder inside.

Concerning the electrodes, spraying instead of doctor blading could improve both uniformness and loading [166, 167]. Finally, calendering, a standard step in the preparation of electrodes, was omitted because no calendering press was available inside a glovebox, but also because a low porosity might cause problems when operating the cell at higher rates, see section 5.1. Besides reducing the porosity of the positive electrode and thereby the amount of electrolyte needed, calendering is known to enhance electronic conductivity and mechanical durability [168].

Materials. Concerning the choice of materials, a few possible improvements come to mind: First, the separator is not specifically optimized for Li/S cells. Both functionalized polypropylene and carbon nano-/microfiber separators are available which could probably improve the wetting along with other benefits [92, 169–172]. Second, concerning the electrolyte, Pyr₁₄TFSI could be exchanged for Pyr₁₄FSI which is not only less corrosive, but also considerably cheaper. Furthermore, mixtures of these and other anions are known to improve conductivity as well as low temperature performance [173–175]. The same is true for the cations, where Pyr₁₃, Pyr₁₄, and Pyr₁₅ could be mixed as well as pyrrolidinium derivatives, like Pyr₁₂O₁, cf. Fig. 3.28. Third, more electrolyte additives could be tested, e.g. those mentioned in Refs. [82, 83, 160, 176].

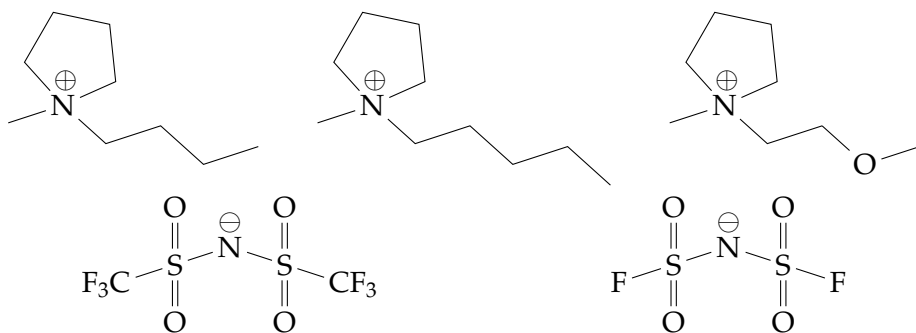


Figure 3.28: Possible improved composition of the ionic liquid portion of the electrolyte as suggested by Ref. [177]. Details see text.

While the experimental results reported above constitute a noteworthy piece of work in their own right, they also serve as input to the modeling study presented in the following chapters.

4 Modeling the lithium-sulfur battery – theory and methods

4.1 Background

Modeling has become an established, if not essential part of the toolset of electrochemical analysis methods. Not only can it save considerable cost and time in the research and development of batteries, but also it enables a more profound understanding than possible by mere experimentation. Therefore, modeling has penetrated all aspects of battery development and design, ranging from system layout to atomistic reaction kinetics [178], see also Fig. 4.1. Small-scale models typically perform ab initio calculations, which make use of quantum mechanics and fundamental physical constants to determine parameters of materials and reactions without experimental input [179]. Despite some simplifying assumptions, this approach is computationally very intensive and thus limited by the size of the system (typically to a few dozen atoms). It needs to be complimented by other techniques, e.g. Monte-Carlo simulations, in order to bridge the gap to electrochemical applications [180, 181]. Large scale, system level simulations on the other hand mostly use an equivalent circuit [91] or black box representation of the battery, which is described by an entirely empirical set of equations, see e.g. Ref. [182]. This approach is computationally inexpensive to the point where the algorithms can be implemented in real-time, embedded battery management systems [183–185]. With regard to the electrochemistry, however, the insight which can be gained by using such a model is very limited as is its extent of validity [186, 187]. An overview of the different types of models can be found in Ref. [188]. For this work, an intermediate level is chosen both in terms of scale and computational complexity: A physically-based continuum approach is taken to model the membrane-electrode assembly (MEA) of the cell in detail. The system is determined by a set of differential algebraic equations describing physical processes such as reaction kinetics, transport, or the evolution of phases on a length scale larger than individual structural details of the electrodes, which is why this type of model is often referred to as continuum model.

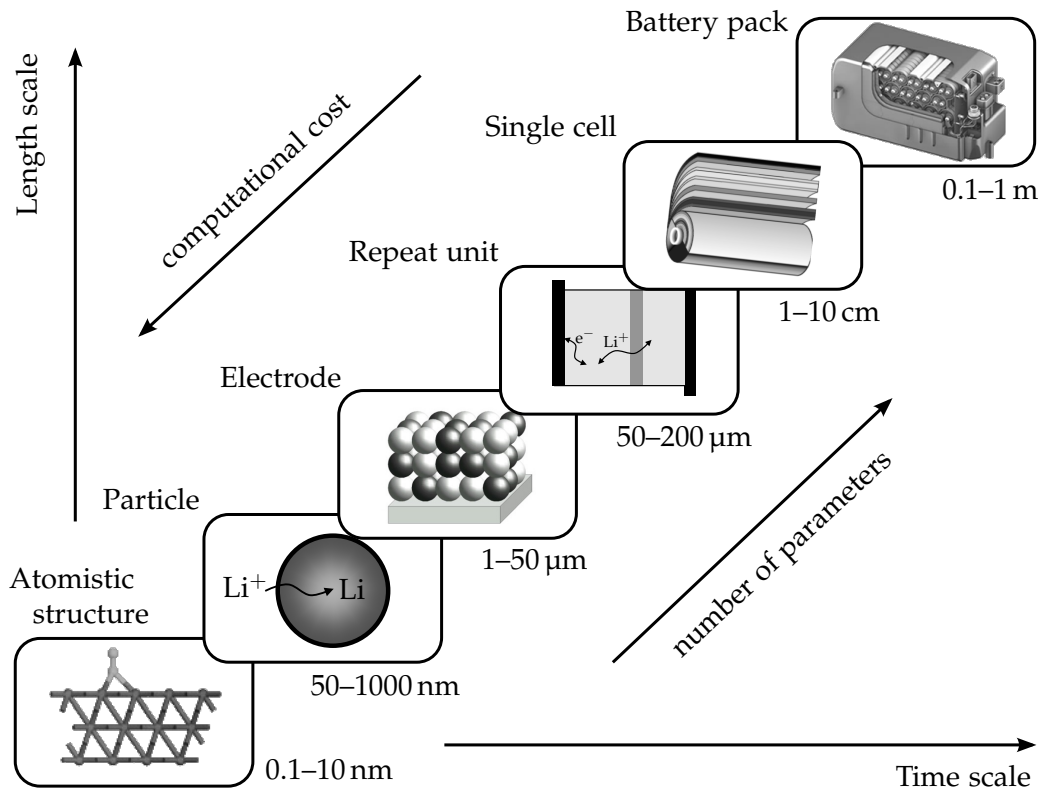


Figure 4.1: Hierarchy of modeling detail and system size. Adapted from [189]; battery pack image reproduced from [190].

The modeling activities were carried out in the group of Prof. Wolfgang G. Bessler at the German Aerospace Center¹ (DLR) as well as the group of Prof. Arnulf Latz at DLR and the Helmholtz Institute Ulm for Electrochemical Energy Storage (HIU)². Parts of this work have already been published in [P1–P4].

The process of building a physically-based model essentially consists of three steps:

1. choosing a set of phenomena to be described by the model
2. formulating the governing equations and connecting them in a meaningful way to come up with a consistent description of the problem
3. assigning values to all parameters introduced in step two

This work is building on top of an existing modeling framework (see below). Hence, for most aspects of the model step one and for several even step two have been completed in advance. Before the steps taken in this work are described in detail, however,

¹Institute of Engineering Thermodynamics, German Aerospace Center (DLR), Pfaffenwaldring 38–40, 70569 Stuttgart, Germany

²Helmholtz Institute Ulm for Electrochemical Energy Storage, Helmholtzstr. 11, 89081 Ulm, Germany

existing implementations of Li/S models shall be discussed. The selection presented here is strictly limited to Li/S continuum models. A rigorous derivation of nonequilibrium thermodynamics of porous electrodes can be found in Ref. [193]; a more comprehensive overview of battery modeling literature can be found in Refs. [188] or [194, chap. 2.5]. Despite this restriction, there are several noteworthy works whose achievements (and shortcomings) shall be analyzed in the following.

One of the early protagonists in the recent advancement of Li/S batteries is Sion Power Corporation [45], which started developing a model of the Li/S cell as early as 2003 [51]. In this model, the chemistry of the cell is described by only two electrochemical reactions, implemented as a Nernst equation each. Only during charging, the polysulfide shuttle is described by one additional phenomenological parameter, the so-called shuttle constant k_s , which is in effect a measure of the speed of the reactions responsible for the shuttle relative to the charge/discharge reactions. This rather simple zero-dimensional model does not include any description of transport, double-layer capacity, or phase changes and only a very simple temperature dependence.

In a joint project of the same company with the group of R. E. White at the University of South Carolina, a more detailed model was developed in 2007 [195, 196]. This model is, by design, similar to the work presented here. It differs, however, at the choice of processes to be included in the model as well as at the formulation of the governing equations. It does include a physically-based one-dimensional description of the transport in the liquid electrolyte as well as electrochemical reactions among the dissolved polysulfides and the evolution of phases. However, the model does not treat the negative electrode explicitly, but just as a boundary condition (a source of Li^+ ions). For this reason, the model cannot accommodate processes like the polysulfide shuttle or degradation mechanisms, which require additional chemical reactions at the lithium electrode. Also, the model does not include a description of the Helmholtz double layer nor a sophisticated representation of the electrodes' microstructure. It does not include any side or disproportionation reactions and the publications do not report anything on the impedance of the cell, the charging process, cycling, or degradation. Finally, the end of discharge cannot be explained conclusively. Nevertheless, Ref. [197] rightfully states that this is the first reasonably complete model of the Li/S cell.

Only recently (2014), another effort was started to model the Li/S cell by the group of P. Chen at the University of Waterloo [198, 199]. This model is conceptually very similar to the model presented in [196]. In fact, only a few parameters were chosen differently. Instead of advancing the model itself, the merit of this two-part publication is that it presents lots of simulation results, including a rather comprehensive sensitivity analysis of the model. Unfortunately, the report is still limited to the discharge only. A third part was announced, but never published.

Another notable contribution to the field comes from the group of Y. Cui at Stanford University [78]. Taking a close look at the charge process starting from pure, solid Li₂S, simulations using a physically-based two-dimensional model indicate that the rate-limiting step for charging is the initial oxidation of Li₂S. This process is modeled to occur only at the triple phase boundary of Li₂S, carbon and the liquid electrolyte. Unfortunately, this particle-scale model was never extend to describe a full cell and Ref. [78] includes only very few simulation results.

Finally, at the Technische Universität München the groups of H. A. Gasteiger and A. Jossen are working on what might soon be the most comprehensive and complete model of a Li/S cell so far. An original rotating disk electrode study [44] led to the conclusion that disproportionation reactions play an important and previously underestimated role for the charge/discharge mechanism. While the aforementioned publication proposes a detailed novel reaction mechanism, it does not present any modeling or simulation results. Early reports of the modeling work disclosed at the UECT2014 conference [200] indicate that the goal is a physically-based 2D or 3D model including the detailed chemistry proposed in [44] as well as transport in the liquid electrolyte and multi-phase management, implemented in a way conceptually similar to this work.

Following this brief literature overview, the design of our model and its benefits over existing models will be discussed in detail, including explanatory notes on its implementation as well as the sources and choice of parameters.

4.2 Modeling approach

4.2.1 Model design and basic assumptions

While by origin and design this work is not merely a re-implementation of the popular porous electrode model published by Newman and Tiedemann in 1975 [201], it may still be called a Newman-class model, since it shares the model layout as well as the description of the electrical properties of the cell and large parts of the description of transport in the liquid electrolyte. However, it also features some extensions not present in the 1975 model such as a detailed description of multiple phases in the electrodes or an implementation of the complex chemistry in Li/S cells, as opposed to a single Butler-Volmer type current source term.

Our model is composed of a one-dimensional representation of the cell, discretizing the volume of the MEA in the direction of Li⁺ transport (hereinafter called *y*-direction), see Fig. 4.2. Because of this, the structure of the porous electrodes is not resolved in morphological or even atomistic detail, but represented by many effective, volume-averaged variables and parameters. To keep the parameter space manageable,

simplifying assumptions are needed that reduce the amount of unknown parameters. Probably the most important of these assumptions is that the system be isothermal. While this does limit the scope of the model, it is not expected to affect the quality of the results. For small (coin) cells, the temperature can be controlled very effectively by putting them in an isothermal temperature chamber, so that the assumption $T = \text{const.}$ is justified. Especially for the rather low rates used, thermal gradients in the cell are negligible. Other important simplifying assumptions include the lack of convection in the liquid electrolyte and constant 100 % activity of dissolved species which will be discussed below.

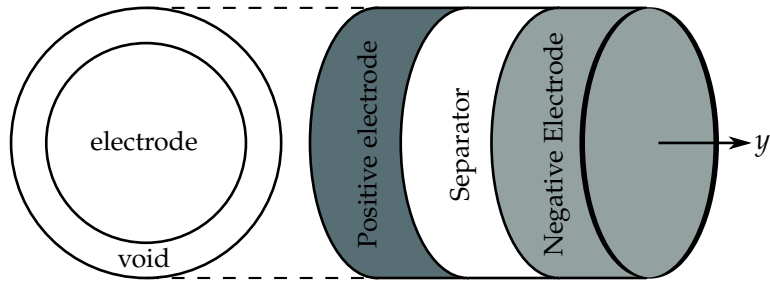


Figure 4.2: Sketch of the computational domain of the 1D model. Current collectors and cell casing are not part of the modeling domain. Discretization is performed in y -direction. Each CV represents the entire cross section of the cell, potentially including void space inside the casing.

Before describing the phenomena and governing equations in detail, nomenclature and naming conventions need to be introduced. Except for the more precise indices, notation in this work follows Ref. [59]; a full list of the symbols used can be found in Tab. A.1. In each control volume (CV), several interfaces (denoted by index m) may exist, at which chemical species (index n) present in the adjacent phases (index p) take part in reactions (index q). Note that the same interfaces, species, phases, and reactions are by design present in each CV within one layer of the cell (cathode, separator, anode) but may differ from layer to layer. That said, the amount of a phase, the concentration of a species or the active surface area of an interface may still be zero in some CVs. Unless otherwise noted, all quantities are considered functions of space (y) and time (t), e.g. $\varepsilon_n \equiv \varepsilon_n(y, t)$. The entire set of equations, boundary conditions, and parameters discussed below can also be found in Tabs. 4.1 and A.5–A.7.

4.2.2 Transport

There are numerous models of transport in the liquid electrolyte [144, 202–209]. Most models published to date cannot be easily adapted to the Li/S system, however, because they assume explicitly or by the formulation of the governing equations that

there be only two charged species in the liquid electrolyte, e.g. [144, chap. 12], a common situation for Li-ion intercalation cells. This restriction is imposed for simplicity, but also because of practical constraints: For a thermodynamically correct description of the transport in liquid-electrolyte batteries [203], one interaction parameter is needed for each pair of dissolved species. For a system with many intermediate species, the determination of these numerous parameters is difficult and often not feasible, cf. [144, chap. 14.3]. Another approach to model cells with multiple species in the liquid electrolyte was devised by C. Delacourt [209]. Following this work, the interaction among the less concentrated “minor” species can be neglected and only their interaction with the conducting salt needs to be taken into account. This model is primarily targeted at electrolyte additives (and not catholytes), therefore some assumptions of [209] do not apply to the situation of the Li/S cell. Instead, for our work the liquid electrolyte is described as a dilute solution of ions as in Ref. [144, chap. 11].

In addition, to further simplify the problem, convection in the liquid electrolyte is neglected, i.e. $v \equiv 0$. As a consequence, there is no need to calculate momentum, which completely vanishes from the governing equations so that the system is fully described by diffusion, migration, and the conservation of mass and charge.

The conservation of species, which of course also implies the conservation of mass can be formulated as

$$\frac{\partial c'_n}{\partial t} = -\frac{\partial J_{n,\text{tot}}}{\partial y} + \dot{s}_n , \quad (4.1)$$

where t is the time, y the spatial coordinate and c'_n and $J_{n,\text{tot}}$ the volume-averaged concentration and total flux of species n , respectively. The chemical concentration c_n within a phase p relates to c'_n as $c'_n = \varepsilon_p c_n$, where ε_p is the volume fraction of the phase in the CV. The additional term \dot{s}_n is a volume-specific term which represents all sources or sinks of particles such as chemical reactions. For heterogeneous reactions, the specific surface area A_m^V of the corresponding interface m needs to be taken into account so that \dot{s}_n can be expressed as

$$\dot{s}_n = \sum_m A_m^V \dot{s}_{n,m} , \quad (4.2)$$

with $\dot{s}_{n,m}$ being the net production rate of species n at the interface m , see section 4.2.3. The total flux in Eq. (4.1) is defined as the sum of diffusion and migration

$$\begin{aligned} J_{n,\text{tot}} &= J_{n,\text{diff}} + J_{n,\text{migr}} \\ &= -D_{n,\text{eff}} \frac{\partial c_n}{\partial y} - \frac{z_n F}{RT} \cdot c_n D_{n,\text{eff}} \frac{\partial \phi_{\text{elyt}}}{\partial y} . \end{aligned} \quad (4.3)$$

Here, z_n denotes the electric charge of species n , F is Faraday’s constant, R the universal gas constant, T the temperature and ϕ_{elyt} the potential in the liquid electrolyte.

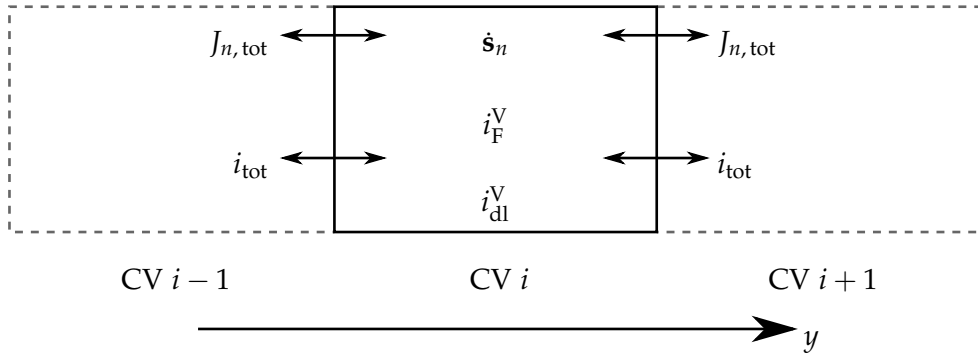


Figure 4.3: Layout of the i^{th} control volume (CV), illustrating the source terms and fluxes for chemical species, i.e. mass (\dot{s}_n and $J_{n,\text{tot}}$), and electrons, i.e. charge (i_F^V , i_{dl}^V , and i_{tot}).

Finally, $D_{n,\text{eff}}$ denotes the effective diffusion coefficient, which is defined as

$$D_{n,\text{eff}} = D_n \cdot \varepsilon_{\text{elyte}} / \tau_{\text{elyte}}^2 , \quad (4.4)$$

correcting Fick's diffusion coefficient D_n for the volume fraction $\varepsilon_{\text{elyte}}$ and the tortuosity τ_{elyte} of the liquid electrolyte phase, which is discussed e.g. in Ref. [210]. Of course, Eq. (4.1) needs to be solved for each species n . By postulating charge conservation and electroneutrality (at the scale of the CVs), the number of equations to be solved is reduced by one, since the condition

$$0 = \sum_{n,m} z_n F A_m^V \dot{s}_{n,m} - \sum_n z_n F \frac{\partial J_{n,\text{tot}}}{\partial y} \quad (4.5)$$

always holds and can be used to eliminate Eq. (4.1) for one (charged) species. In words, the flux of the n^{th} species is determined by the flux of the $(n - 1)$ other species so that the total flux (in units of charge) is equal to the amount of charge generated within the CV. Fig. 4.3 summarizes the source terms in and fluxes across the boundaries of a CV.

4.2.3 Electrochemistry

The derivation of the (electro-)chemical rate laws follows Ref. [58], which in turn is based on Ref. [211, sec. 9.3]. The following assumptions are required for a more compact formulation of the problem: pressure and temperature shall be constant and all electrochemical reactions occur only at interfaces (whereas chemical reactions may also occur within a bulk phase). For the species continuity equation, Eq. (4.1), a generalized source term \dot{s}_n (or \dot{s}_n) was already defined which in turn is calculated from

mass-action kinetics. For each reaction q , the term $\dot{s}_{n,q}$ is defined as

$$\dot{s}_{n,q} = \nu_{n,q} \left(k_{q,\text{fwd}} \prod_{n' \in q, \text{fwd}} a_{n'}^{\nu_{n',q}} - k_{q,\text{rev}} \prod_{n'' \in q, \text{rev}} a_{n''}^{\nu_{n'',q}} \right), \quad (4.6)$$

where k_{fwd} and k_{rev} are the forward and backward rate constants, ν_n the stoichiometric coefficients of species n in the corresponding reaction q , and a_n the activities. The products run over all reactants n' or n'' participating in the forward or reverse reaction, respectively. The total production rate of species n at interface m is simply the sum of the contributions of all reactions q at that interface:

$$\dot{s}_{n,m} = \sum_{q \in m} \dot{s}_{n,q}. \quad (4.7)$$

The equation for bulk reactions has exactly the same form, except that the units of activities and rate constants differ, so that \dot{s}_n is a volume-specific production/consumption rate instead of an area-specific one. The forward rate constant is given by a general modified Arrhenius expression (index q omitted in the following equations):

$$k_{\text{fwd}} = \tilde{k}_{0,\text{fwd}} T^\beta \exp\left(-\frac{E_{\text{act}}}{RT}\right) \exp\left(-\frac{(1-\alpha)zF}{RT} \Delta\phi\right). \quad (4.8)$$

Since there is no reason to assume otherwise, the symmetry factor α is chosen to be $1/2$ for all reactions. Also, because the model is assumed strictly isothermal, both the temperature factor T^β and the activation energy E_{act} may be eliminated so that Eq. (4.8) is reduced to

$$k_{\text{fwd}} = k_{0,\text{fwd}} \exp\left(-\frac{zF}{2RT} \Delta\phi\right), \quad (4.9)$$

with z being the number of electrons transferred, F Faraday's constant, R the universal gas constant, T the (now fixed) temperature, and $\Delta\phi$ the potential step at the corresponding interface: $\Delta\phi = \phi_{\text{elde}} - \phi_{\text{elyte}}$. The pre-exponential factor $k_{0,\text{fwd}}$ now incorporates the contributions of the two temperature-dependent terms in Eq. (4.8), which are reduced to a fixed factor in the case of constant temperature. For mere chemical reactions (i.e. $z = 0$), k_{fwd} is equal to $k_{0,\text{fwd}}$.

While reverse reactions rates may be specified analogously, i.e. in the form

$$k_{\text{rev}} = k_{0,\text{rev}} \exp\left(\frac{zF}{2RT} \Delta\phi\right), \quad (4.10)$$

this is not the case for most reactions in this model. Instead, reverse rates are calculated

in a thermodynamically consistent fashion using the relation

$$k_{\text{rev}} = k_{\text{fwd}} \exp \left(\frac{\Delta G}{RT} \right) , \quad (4.11)$$

which directly follows from the law of mass-action and ensures that the net production rates are zero in the equilibrium case. The molar Gibbs reaction enthalpy ΔG_q of reaction q is defined as

$$\Delta G_q = \sum_{n \in q} \nu_{n,q} \mu_n = \sum_{n \in q} \nu_{n,q} g_n . \quad (4.12)$$

Here, the sum n runs over all species participating in reaction q with stoichiometric coefficients ν_n , chemical potentials μ_n , and molar Gibbs free energies g_n . The values of g_n for each species are required as input parameters for the model. Note that in this work, g_n is defined to be 0 for the reference state, i.e. for pure elements. Since this model is assumed isothermal, this further simplifies the notation compared to the common choice of $h = 0$, but $s \neq 0$ at the reference state.

A remark on the units of k : In Eq. (4.6), the activities a_n of the dissolved species are often shorthanded replaced with the concentrations c_n , in which case Eqs. (4.6) and (4.11) require different units for k_{fwd} and k_{rev} . Instead, the true relation is

$$a_n = \gamma_n \frac{c_n}{c_{n,\text{ref}}} , \quad (4.13)$$

where γ_n denotes the dimensionless activity coefficient and $c_{n,\text{ref}}$ the concentration at the reference state at which the electrical potential is zero, cf. [212]. This potential must not be confused with the electrochemical potential ϕ_{elyte} as defined below. Without loss of generality, it may be chosen such that $c_{n,\text{ref}} = 1 \text{ mol} \cdot \text{l}^{-1}$. If additionally, all dissolved species are modeled to be available for reactions, i.e. $\gamma \equiv 1$, the values of a_n and c_n are identical except for the units. This is never strictly true for ions in aqueous or organic solutions, since they can form salts and are thus always only partly dissociated [204, sec. 3.3]. However, the ionic liquid used in this study is not a solvent in the strict sense, but a molten salt. The anion of the ionic liquid Pyr₁₄TFSI and the conducting salt LiTFSI are identical, limiting the usefulness of the concept of dissociation. While this does not imply that Li⁺ is never strongly bound or coordinated in the electrolyte, it means that there is no such thing as “non-dissociated LiTFSI” and, furthermore, no solvation shell surrounding Li⁺ cations. All ions are equally accessible for reactions, therefore the assumption $\gamma = 1$ is truly justified. The fact that the reactivity of Li⁺ can be different, e.g. for different temperatures, is better represented by adjusting the activation energies for reactions involving Li⁺ as well as the activation energy of Li⁺-diffusion [175], which are of no concern for this isothermal study.

4.2.4 Electrical properties

Next, the relationship of the cell's electrical properties to the chemistry explained above is presented. Since electrons are treated as yet another species (with zero mass), the Faradaic current density i_F^V in a CV follows directly from reaction kinetics. More precisely, it can be obtained by summing up the electrons produced or consumed at all interfaces:

$$i_F^V = \sum_m F A_m^V \dot{s}_{\text{electron}, m} . \quad (4.14)$$

"Free" electrons only exist in the electronically conductive materials, which are assumed to be in perfect contact with the current collector. The total, externally detected current density is defined as

$$i_{\text{tot}} = \int_{y=0}^{L_{\text{CA|AN}}} (i_F^V + i_{\text{dl}}^V) dy , \quad (4.15)$$

where $L_{\text{CA|AN}}$ is the thickness of the cathode or anode, i_F^V is the Faradaic, and i_{dl}^V the double-layer current source term in the CV, which in turn is calculated as

$$i_{\text{dl}}^V = A_m^V C_{\text{dl}, m} \frac{\partial (\Delta\phi)}{\partial t} , \quad (4.16)$$

with $C_{\text{dl}, m}$ being a constant, area-specific capacity of the interface and $\Delta\phi$ the potential step defined as in Eq. (4.9). Several different effects contribute to the double-layer capacity $C_{\text{dl}, m}$, see e.g. [213]. Nevertheless, it can be safely treated in this simplified fashion since the influence of its properties besides the amount of capacity are only relevant at time scales much shorter than those studied in this work. Note that in Eqs. (4.15) and (4.16) both electrodes must be considered for the double-layer current as well as for the integration of the local current densities. Per definition, the resulting value of i_{tot} is positive while discharging and negative while charging.

The total cell voltage E is simply defined as the potential difference between the cathode's and anode's conductive bulk material (which are carbon and lithium metal, respectively):

$$E = \phi_{\text{CA, elde}} - \phi_{\text{AN, elde}} . \quad (4.17)$$

At rest, this voltage is identical to the OCV, i.e. the equilibrium Nernst voltage of the electrochemical system [214]. Unlike the potential of the electrolyte ϕ_{elyte} , which is calculated for each CV, ϕ_{elde} is the same for all CVs within one electrode and thus just represented by a number each. Physically, this means that the Ohmic drop due to the electric resistivity within the electrode is negligible. Optionally, however, an

additional “global” resistance may be included so that

$$E = \phi_{\text{CA, elde}} - \phi_{\text{AN, elde}} - \rho^* i_{\text{tot}}, \quad (4.18)$$

with ρ^* representing the combined electric resistivity of the bulk lithium metal, carbon, and both current collectors. While ρ^* is typically constant, it may also be influenced by the microstructure of the cell, see below.

4.2.5 Microstructure

As previously mentioned, this one-dimensional model cannot explicitly describe the electrodes’ microstructure. Instead, each control volume is assigned properties which are representative of its morphology, namely the volume fractions ε_p of each phase p present in the control volume. From these, the tortuosities τ_p , effective diffusion coefficients $D_{n,\text{eff}}$, and specific surface areas A_m^V are derived. Volume fractions may change because of precipitation and dissolution of material, phase transitions, or (convective) phase transport. For this work, only the first option is taken into account so that the evolution of the volume fractions is completely described by the continuity equation

$$\frac{\partial (\varrho_p \varepsilon_p)}{\partial t} = R_p M_p, \quad (4.19)$$

which has to be evaluated for each phase p . Here, ϱ_p is the density and M_p the (average) molar mass of the phase, while R_p denotes its net production rate, which in turn is calculated from the (electro-)chemical source terms as defined in Eq. (4.6). Assuming that phases grow and shrink at their interfaces only, R_p can be obtained from the relation

$$R_p = \sum_{m,n \in p} \dot{s}_{n,m} A_m^V, \quad (4.20)$$

where the $\dot{s}_{n,m}$ is the net production rate of species n in phase p due to all reactions occurring at interface m . Since in the implementation used for this work the space occupied by each CV is fixed, the following relation needs to be fulfilled at all times:

$$\sum_p \varepsilon_p = 1. \quad (4.21)$$

While there are several more rigorous options for ensuring consistency (see e.g. [215, pp. 53ff]), a simple, yet straight-forward approach was chosen for this work: Using Eq. (4.21), Eq. (4.19) can be eliminated for one phase. This is done by setting the volume fraction of the gaseous phase to fill the entire space not occupied by the solid phases. The flow or pressure increase caused by the volume change is neglected,

since it does not affect either the transport in the electrolyte or the electrochemistry. A detailed, fully consistent treatment of Eq. (4.21) would require the introduction of convection in the model as proposed in Ref. [216] as well as a description of mechanical stress in the electrode's particles as proposed in Refs. [217–219].

The special case, where the gaseous phase becomes zero in a CV receives no special treatment, since it did never occur in any simulation reported here. However, if no gaseous phase is considered at all, e.g. for the global model, Eq. (4.21) is enforced by adjusting the volume fraction of the liquid electrolyte $\varepsilon_{\text{elyte}}$ to fill the remaining space in each CV. Since there is no convection in the liquid electrolyte (cf. section 4.2.2), no material may enter or leave the CV and hence the number of molecules in the electrolyte phase remains constant. If the solid phases grow, this causes a compression of the electrolyte, resulting in an increase of the concentrations of all species (including the solvent's). Considering the low compressibility of liquids, this assumption may not seem justified at a first glance. However, the pressure itself is not considered in this model and the resulting concentrations quickly equilibrate with the neighboring compartments by means of diffusion.

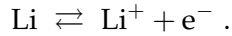
Once the volume fractions are determined, they can be used to calculate specific surface areas of each interface m according to

$$A_m^V = A_m^V(\varepsilon_p) \quad (4.22)$$

and, in the case of the liquid electrolyte, effective diffusion coefficients $D_{n,\text{eff}}$ of all dissolved species according to Eq. (4.4). This way, a feedback of the volume fractions in each CV on the chemical kinetics and transport is established. The functional relation of A_m^V and the volume fractions represents the electrode's geometry, e.g. $A_m^V = \text{const.}$ for a film, $A_m^V \propto \varepsilon^{3/2}$ for an electrode consisting of spherical particles which grow or shrink at the same rate, or $A_m^V \propto \varepsilon$ for particles which are consumed one after the other. As required, these expressions may be modified to include additional effects such as explicit nucleation or surface passivation.

4.2.6 Reaction mechanisms

Once the governing equations are defined, one still needs to plug in a reaction mechanism. The requirements for this mechanism are rather simple: It needs to provide at least one reaction generating or consuming electrons and one reaction generating or consuming dissolved ions in the liquid electrolyte at both the cathode and anode side. In this work, two different reaction mechanisms will be discussed. Both share the same reaction at the negative electrode,

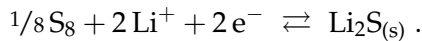


The anode is assumed to be able to supply an unlimited amount of lithium, which experimentally corresponds to adding a surplus of lithium to the cell. Its kinetics is chosen sufficiently fast, so that the anode overpotential is essentially negligible. While the addition of a more detailed anode model would be simple and straightforward, this assumption is made to simplify the interpretation of the results with regard to the sulfur electrode.

Global reaction mechanism. To begin with, the most simple reaction mechanism shall be discussed. It consists of one precipitation/dissolution reaction

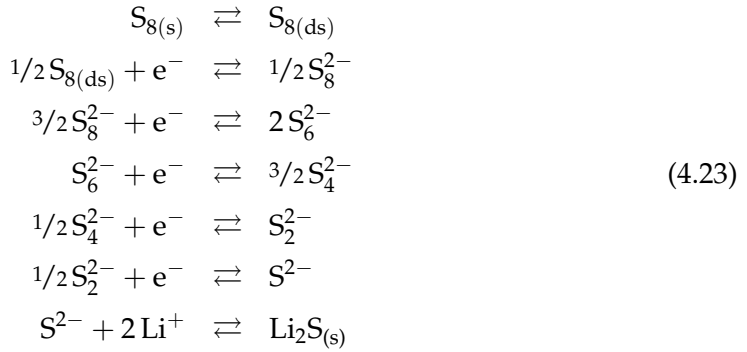


accompanied by only one electrochemical reaction at the positive electrode:



While technically, the electrochemical reaction takes place at a surface with a constant area (implemented as described above), the physical interpretation of the situation is similar to a triple phase boundary, a concept known from the field of heterogeneous catalysis. As pointed out by Yang et al. [78], the “active space” around the triple phase boundary of sulfur, carbon, and the liquid electrolyte (in which the above reaction could happen) is very small compared to the carbon and sulfur surfaces. Also, the solid Li_2S formed during discharge would rapidly block access to the active sites. Furthermore, this ansatz assumes that single sulfur atoms may react individually, which is virtually impossible because of the energetically unfavorable configuration left behind in the bulk. Not surprisingly, therefore, this reaction mechanism cannot reproduce the experimentally observed behavior of the Li/S cell very well. Nevertheless, it is interesting to observe its results with respect to Li^+ transport or material utilization for different geometries.

Multi-step reaction mechanism. To overcome the limitations of the global mechanism, two modifications are needed: First, lithium sulfide needs to be allowed to dissolve into and precipitate from the liquid electrolyte. Second, a more detailed implementation of the sulfur redox chemistry is needed. Ref. [192] discusses why there need to be at least three electrochemical reduction steps to reproduce the two-plateau discharge profile often detected experimentally. Various publications, however, suggest that there are at more or different intermediate steps, see e.g. Refs. [138, 142, 220, 221]. Our multi-step reaction mechanism consists of a linear chain of reactions involving several dissolved polysulfide intermediates:



Opposed to the mechanism presented in [196], the only solid products in the cell are sulfur and lithium sulfide, which is backed by X-ray diffraction and transmission X-ray microscopy studies [155, 156].

Surface areas are modeled to depend on the solid phases as

$$A_{S_8|elyte}^V = \left(\frac{\varepsilon_{S_8}}{\varepsilon_{0,S_8}} \right)^{\frac{3}{2}}, \text{ and} \tag{4.24}$$

$$A_{Li_2S|elyte}^V = \left(\frac{\varepsilon_{Li_2S}}{\varepsilon_{0,Li_2S}} \right)^{\frac{3}{2}}. \tag{4.25}$$

Here, $\varepsilon_{0,n}$ denotes the reference volume fraction of a phase, equal to either the initial or the maximum value of ε_n . These expressions represent as the surfaces of homogeneously expanding and shrinking particles. Since the initial volume fraction of Li_2S in the charged state is very low, this naturally generates a situation where particle growth of Li_2S is severely inhibited due to the very small $A_{Li_2S|elyte}^V$ until a certain amount of Li_2S is precipitated. This can be interpreted as an implicit, yet effective implementation of a nucleation phenomenon.

Multi-step reaction mechanism, revised. In order to reproduce experimental results more faithfully, a revised version of the multi-step model was prepared. Besides a rigorous reparametrization, described in section 5.3, two new phases are introduced:

First, each CV in the positive electrode is modeled to include 10% non-reactive, compressible Argon gas. In the coin cells used experimentally, the porous positive electrode disc has a smaller diameter than the separator and the casing, see Fig. 2.6. In the one-dimensional model, each CV represents the entire cross section of the coin cell, see Fig. 4.2. The gaseous phase in the revised model accounts for the gas filled volume between the outer diameter of the electrode and the casing of the coin cell. It is required to correctly represent the relative volumes of the positive electrode and separator in the model. The gaseous phase is not in intimate contact with the active material, but only surrounding the entire electrode. There is virtually no triple phase boundary and an explicit treatment of partial wetting [222] is not required.

Second, solid “passive Li₂S” may be present in the positive electrode, which is only accounted for in the model by its volume and weight. The rationale behind introducing this additional, nonreactive form of Li₂S is to account for the following experimental finding: While the total amount of Li₂S is the same for all cells made from the same recipe, not all of the Li₂S does actually contribute to the cell’s initial capacity. Instead, this figure depends on various factors, including particle size, porosity, and composition of the electrode as well as the protocol used for cell formation. The mechanisms causing this missing capacity are diverse and not well understood in detail. The most simple and straightforward way to deal with this situation is to introduce a constant amount of “passive Li₂S”, which can be fitted in order to match experimental results, but does not otherwise affect the behavior of the model. Originally, it was planned to adjust the values of the parameters only. However, one change was required to the model, regarding the deposition of Li₂S on the electrochemically active carbon|electrolyte interface. While the simple interface model described above is capable of reproducing the general behavior of a Li/S cell, it turned out to be insufficient for calibrating the model to match the experimentally obtained results. The reason for this discrepancy is the mechanism triggering the end of discharge. Besides pore clogging and depletion of active material, discussed in section 3.2.1, there is a third mechanism, related to the passivation of the active surface. This mechanism dominates for all cells analyzed experimentally, but it does not easily translate into a reduced surface area in the model. Instead, the carbon surface area itself is assumed constant, but the surface resistivity is modeled to increase when Li₂S is deposited on the surface as proposed by Albertus et al. for Li-air cells [223]. This is achieved by modifying the surface resistivity, which is included in ρ^* , see Eq. (4.18). The ansatz used is

$$\rho^* = \rho_0^* + l \cdot 1 \Omega m \cdot \exp [\xi_1 \cdot (l - \xi_2)] , \quad (4.26)$$

where ρ_0^* is the constant sum of all other contributions to the cell’s impedance (e.g. current collectors), ξ_1 is a dimensionless constant representing the microstructure of

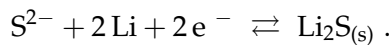
the film, ξ_2 is the distance electrons can travel through the film, e.g. by tunneling, and l is the thickness of the Li₂S film on the carbon substrate, calculated according to

$$l = \left[\left(\frac{\varepsilon_{\text{carbon}} - \varepsilon_{\text{Li}_2\text{S}}}{\varepsilon_{\text{carbon}}} \right)^{1/3} - 1 \right] \cdot r_{\text{carbon}} . \quad (4.27)$$

The radius of the carbon black particles, r_{carbon} as well as the constants ξ_1 and ξ_2 are additional input parameters. As long as l is smaller than ξ_2 , there is virtually no overpotential. Once enough Li₂S is precipitated to cover the entire surface, the resistivity increases quickly, triggering the end of discharge.

4.2.7 Degradation

A first extensive review of degradation mechanisms in Li-ion batteries was presented in Ref. [224] already in 1998. Many refinements were added over time, see e.g. Ref. [225]. However, with a few notable exceptions [226–231], not a lot of modeling work has been done concerning these issues. For Li/S cells, the situation is even more desperate. We presented the first – and so far only – modeling study of Li/S cell degradation in Ref. [P3]. To enable degradation in the model, two additional effects are added: First, the reduction of polysulfides may also happen at the lithium electrode. This is implemented by enabling the same set of charge transfer reactions (CTRs) that is assumed at the positive electrode. Since the reaction rate constants and activation energies strongly depend on the species' interaction with the surface, they must be chosen differently, though. For simplicity, the forward reaction rate constants k_{fwd} of all CTRs are scaled by the same factor ξ_{CTR} . Second, solid Li₂S is allowed to precipitate (and accumulate) at the negative electrode according to



Again, since the precipitation happens at the lithium surface, the reaction rate constant may be different than that used for the same reaction in the positive electrode. It is scaled by a factor of ξ_{precip} .

Additionally, the active surface area of the lithium electrode is modeled to depend on the amount of precipitated Li₂S according to the heuristic expression

$$A_{\text{Li} \mid \text{elyte}}^V = A_0 \cdot \left(\frac{\varepsilon_{0,\text{elyte}} - \varepsilon_{\text{Li}_2\text{S}}}{\varepsilon_{0,\text{elyte}}} \right)^{\xi_0} ,$$

where the expression in brackets is the fraction of the porosity remaining after Li₂S deposition and the factor $\xi_0 = 3.5$ phenomenologically quantifies the impact on the lithium's active surface area [192].

Table 4.1: Summary of the governing equations and boundary conditions. For a definition of symbols, refer to the above text or Tab. (A.1) in the appendix.

Transport in the liquid electrolyte

Species conservation	$\frac{\partial c'_n}{\partial t} = -\frac{\partial J_{n,\text{tot}}}{\partial y} + \dot{s}_n$	(4.1)
----------------------	--	-------

Species fluxes	$J_{n,\text{tot}} = -D_{n,\text{eff}} \frac{\partial c_n}{\partial y} - \frac{z_n F}{RT} \cdot c_n D_{n,\text{eff}} \frac{\partial \phi_{\text{elyt}}}{\partial y}$	(4.3)
----------------	---	-------

Electroneutrality and charge conservation	$0 = \sum_{n,m} z_n F A_m^V \dot{s}_{n,m} - \sum_n z_n F \frac{\partial J_{n,\text{tot}}}{\partial y}$	(4.5)
---	--	-------

Electrochemistry

Rate equations	$\dot{s}_{n,q} = v_{n,q} \left(k_{\text{fwd}} \prod_{n' \in q} a_{n'}^{v_{n',q}} - k_{\text{rev}} \prod_{n'' \in q} a_{n''}^{v_{n'',q}} \right)$	(4.6)
----------------	---	-------

Arrhenius rate law	$k_{\text{fwd}} = k_{0,\text{fwd}} \exp \left(-\frac{zF}{2RT} \Delta\phi \right)$	(4.9)
--------------------	--	-------

Calculation of the reverse rate	$k_{\text{rev}} = k_{\text{fwd}} \exp \left(\frac{\Delta G}{RT} \right)$	(4.11)
---------------------------------	---	--------

Cell voltage and current

Faradaic current source term	$i_F^V = \sum_m F A_m^V \dot{s}_{\text{electron},m}$	(4.14)
------------------------------	--	--------

Double-layer current source term	$i_{\text{dl}}^V = A_m^V C_{\text{dl},m} \frac{\partial (\Delta\phi)}{\partial t}$	(4.16)
----------------------------------	--	--------

Total current density	$i_{\text{tot}} = \int_{y=0}^{L_{\text{CA AN}}} (i_F^V + i_{\text{dl}}^V) dy$	(4.15)
-----------------------	---	--------

Cell voltage	$E = \phi_{\text{CA, elde}} - \phi_{\text{AN, elde}} - \rho^* i_{\text{tot}}$	(4.18)
--------------	---	--------

Multi-phase management

Continuity equation for bulk phases	$\frac{\partial (\varrho_p \varepsilon_p)}{\partial t} = M_p \cdot \sum_{m,n \in p} \dot{s}_{n,m} A_m^V$	(4.19), (4.20)
-------------------------------------	--	----------------

Feedback on diffusion coefficients	$D_{n,\text{eff}} = D_n \cdot \varepsilon_{\text{elyte}} / \tau_{\text{elyte}}^2$	(4.4)
------------------------------------	---	-------

Feedback on specific surface areas	$A_m^V = A_m^V (\varepsilon_p)$, mechanism-dependent	(4.22)
------------------------------------	---	--------

4.3 Simulation methodology

4.3.1 Implementation and computational framework

When looking at anything but the most trivial cases, there is no analytical solution of the set of governing equations and boundary conditions described above. Therefore, the model needs to be implemented in a computer program capable of solving the equations numerically. The software framework chosen for this work and its notable features are discussed next.

All simulations in this work were carried out using the software framework **DENIS**, which is shorthand for Detailed Electrochemical and Numerical Impedance Simulation. At the core of this framework, there is a C/C++ code initially designed by W. G. Bessler at the University of Heidelberg³ and now developed and maintained at the German Aerospace Center⁴, the University of Applied Sciences Offenburg⁵, and the Helmholtz Institute Ulm⁶. DENIS is best described by Refs. [58] and [59]. A component diagram of the modeling framework is presented in Fig. 4.4. Internally, it makes use of a set of third party libraries including **CANTERA** [232], a toolset for evaluating (electro-) chemical reactions, **MUPARSER** [233], a library for parsing and evaluating mathematical expressions, and **LIMEX** [234], a numerical solver based on the extrapolated implicit Euler scheme [235], capable of solving linear implicit index-1 DAEs of the form

$$B(\mathbf{y}(t), t) \cdot \mathbf{y}'(t) = f(\mathbf{y}(t), t) , \quad (4.28)$$

where \mathbf{y} is the solution vector containing all state variables of the system and B is a singular matrix (see also [211, chap. 15.3.2]). The “right-hand side” of the equation, $f(\mathbf{y}, t)$, is a vector containing all the physical and chemical information, i.e. governing equations, parameters and operating conditions. The solver will extrapolate \mathbf{y}' to estimate the size of the next time step and compute the system iteratively until the required absolute and relative tolerances are satisfied.

In order to solve the system numerically, the governing equations need to be discretized, which is accomplished using the finite-volume method (FVM). This method is starting from the integral form of a conservation equation

$$\frac{d}{dt} \int_V \Phi(\mathbf{y}, t) dV = - \int_{\partial V} f(\Phi(\mathbf{y}, t)) \cdot \vec{n}_{CV} dV , \quad (4.29)$$

³Interdisciplinary Center for Scientific Computing (IWR), Universität Heidelberg, Im Neuenheimer Feld 368, 69120 Heidelberg, Germany

⁴Institute of Engineering Thermodynamics, German Aerospace Center (DLR), Pfaffenwaldring 38–40, 70569 Stuttgart, Germany

⁵Institute of Energy System Technology (INES), Offenburg University of Applied Sciences, Badstr. 24, Offenburg, Germany

⁶Helmholtz Institute Ulm for Electrochemical Energy Storage, Helmholtzstr. 11, 89081 Ulm, Germany

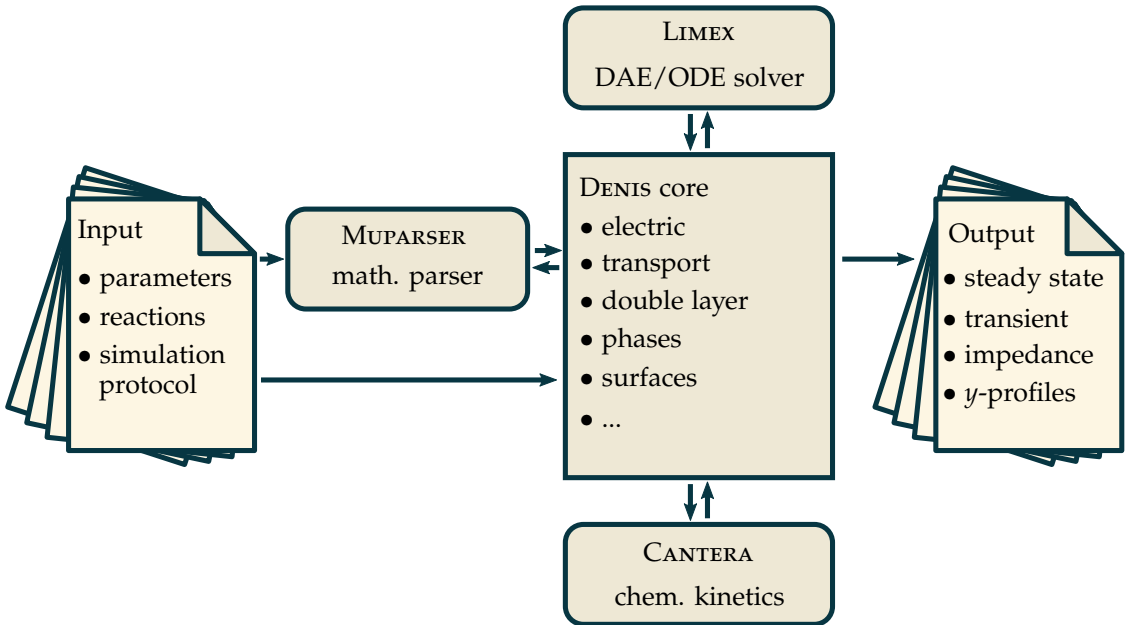


Figure 4.4: Schematic representation of the simulation framework.

where V_{CV} denotes a control volume (CV) with the corresponding surface ∂V_{CV} and the normal vector \vec{n}_{CV} , $f(\mathbf{y}, t)$ denotes the function to be discretized, and $\Phi(\mathbf{y}, t)$ the corresponding conserved quantity. From the form of Eq. (4.29), “it follows that a change in Φ can only occur in combination with a flux over the boundaries of the CV. Thus, the solution of the PDEs follows from approximation of the net fluxes over the boundaries of all volumes. [The] main advantage of the FVM is that it is conservative, meaning that the flux entering a control volume is always equal to the flux leaving the adjacent CV. It is the most common discretization method in computational fluid dynamics [236, chap. 4]⁷. The number of control volumes for the numerical discretization is chosen such that a further increase does not affect the calculated results significantly, as described in section 4.3.3.

For impedance simulations, a step excitation technique is used as described in Ref. [237]: A quick voltage jump is simulated, followed by a long relaxation period. The voltage jump contains contributions of all relevant frequencies. After finishing the simulation, the voltage and corresponding current traces need to be Fourier transformed in order to obtain the complex impedance Z in the frequency domain. The frequency range that can be analyzed is determined by the duration of the voltage jump (highest frequency) and the total simulation time (lowest frequency). In this work, a voltage jump of 1.0 mV relative to OCV is applied within 10^{-8} s, followed by a relaxation time of 10^4 – 10^6 s. Note that the impedance simulation is based on the full

⁷cited verbatim according to Ref. [215], p. 42

physicochemical model, including detailed chemistry and transport, without the use of equivalent circuits [191].

4.3.2 Parametrization and validation techniques

This section deals with the third step of the modeling process as defined on page 69: the determination of the parameters introduced by the previously discussed governing equations. From a theoretical point of view, there are three kinds of parameters: a) those which are ultimately based on natural constants and for which only one true value exists, e.g. the diffusion coefficient of Li^+ in a certain solvent or the enthalpy of formation of Li_2S , b) those which define morphological or technical properties, e.g. the porosity or the discharge current, and may take any (reasonable) value, and c) parameters that are not part of the physical description itself, such as the size of a control volume or the solver tolerances. In principle, parameters in group a) can be looked up or determined by independent measurements, those in group b) need to match the conditions of a given experiment and those in group c) just need to be set “right”, i.e. in a way that the simulation results do not heavily depend on the value chosen, cf. section 4.3.3.

From a practical point of view, however, it makes sense to group the parameters differently, to be specific: according to their source. The model needs lots of input to determine all parameters and thus one has to make use of every possible independent source. Three categories can be formed which do not necessarily correlate with those mentioned above:

- i) parameters known from literature with sufficient accuracy. This includes dedicated scientific measurements as collected in the CRC handbook [238], but also other modeling efforts, e.g. of 3D-resolved microstructures [239] or ab initio calculations [143].
- ii) parameters determined from dedicated experiments. This includes trivial parameters such as the dimensions and composition of the electrodes, but also more complex ones like the conductivity of the liquid electrolyte including all dissolved ions. Often, the parameters detected experimentally are not exactly the ones that are required as input by the model. In such cases, the relationship of the parameters needs to be analyzed to establish a rule for conversion.
- iii) fitted parameters. For statistical reasons, this category should be kept as small as reasonably possible [240, chap. 8]. Since the model’s behavior is strongly predetermined by the governing equations, its parametrization is not to be confused with a polynomial fit. Still, fitting too many free parameters significantly reduces the explanatory power of the model. Also, finding the optimal set of parameters becomes more and more difficult as the number of parameters increases [240, chap. 8.2]. In

this work, most parameters were fitted manually by adjusting parameters within a reasonable range. Some, however, were also determined – or at least fine tuned – by applying a least-squares fitting algorithm to the problem. To this, DENIS may be called with updated input files from the programming language Python, making use of the `denistools` package provided by K. Göckelmann⁸. Using SciPy’s [241] fitting and error analysis capabilities, parameters can be optimized according to

$$\chi^2 \equiv \sum_i \left\{ \frac{1}{\sigma_i^2} [y_i - y(x_i)]^2 \right\}, \quad (4.30)$$

where χ^2 is the goodness-of-fit parameter, x_i and y_i are the abscissa and ordinate of the experimentally obtained data points, respectively, σ_i is the uncertainty in y_i , and $y(x_i)$ is the simulation result corresponding to data point i [240, chap. 8.1]. Where necessary, the simulation output is linearly interpolated to exactly match x_i , which itself is assumed to be known precisely. This assumption is valid, since the effect of an uncertainty in x_i can always be expressed by an increased uncertainty in y_i [240, chap. A1]. Finally, because the solver’s precision is the same for all data points, σ_i^2 is expected to be constant and thus cancels out.

4.3.3 Quality control and error analysis

Science calls for quantitative statements and these are of questionable value when not accompanied by a confidence interval. The only true difference between a guess and a measurement is that for the latter, deviations are known and may be analyzed mathematically [240, chap. 3]. The absoluteness of this statement is somewhat put into perspective, however, since the aim of the modeling activities presented here is to generate knowledge about and insight into the system studied, which is not to be confused with the task of e.g. a battery management system, which needs to keep track of and predict the internal state of a given battery as precisely as possible. Still, this work would be incomplete without error analysis.

The simulations are carried out by deterministic machines, so that random errors should not exist [242]. Hence a general classification of errors as proposed by Bevington and Robinson [240, chap. 1.1] does not apply. Instead, all errors are systematic by definition. According to Ferziger and Perić [236, chap. 11.1], three kinds of errors are common in numerical simulations of this type, namely discretization, convergence, and modeling errors.

Discretization errors occur because time and space are continuous (at least on a relevant scale), but need to be discretized in order to apply the numerical solution

⁸Lead scientific programmer at the Institute of Engineering Thermodynamics, German Aerospace Center (DLR), Pfaffenwaldring 38–40, 70569 Stuttgart, Germany

methods described above. For example, one CV may represent a region which is not very homogeneous, but nevertheless described by one set of state variables. By decreasing the size of the CVs, the error can be decreased systematically [243]. The strategy followed in this work is to choose the CV size according to the expected gradients, see also [243]. Nevertheless, as long as the CV size is larger than the length scale of the “smallest” physical effect, the error will not vanish.

Convergence errors occur in all iterative algorithms. Except for trivial cases, the solver will never produce an exact solution of the system of equations. Instead, the solution is improved until the difference between two consecutive iterations is smaller than a certain tolerance. Typically one defines an absolute and relative upper boundary, which are a direct measure of the solution’s uncertainty. To improve the quality of the solution, the tolerance can be decreased, which in turn increases computation time. In order to limit the computational cost of finding a solution which satisfies the tolerance requirements, either all variables in the solution vector y should be scaled to the range [0:1] or the tolerance should be set independently for each variable in the solution vector.

Finally, modeling errors are errors which are present in the design or implementation of the model. While this includes plain mistakes, most errors of this type are introduced on purpose in order to reduce the complexity of the model, e.g. the assumption of dilute solutions or 100% activity of dissolved species as discussed above. Another important source of errors is the neglect of certain effects. What is tricky about modeling errors is that there is no way to systematically check for or even decrease them. Instead, assumptions and the errors associated with them can only be justified by additional studies or calculations.

Even though all errors present in modeling studies are systematical errors, it makes sense to discriminate between precision and accuracy of the results [240, chap. 1.1]. While convergence and discretization errors only affect the precision and can be reduced by increasing the computational effort, there is no systematic strategy to avoid modeling errors, which typically affect the accuracy of the results. The strategy followed in this work is to increase the precision of a given simulation until the results do not change significantly anymore. That way, a benchmark for the uncertainty is available. It is, however, by no means a measure for the true accuracy, i.e. the deviation of the simulation results from “reality” (however one may define this). It would be a daunting task (probably worth its own thesis) to define and analyze the effect of all modeling errors in this or any other reasonably complex model.

Finally therefore, it has to be stated that, even though the model was carefully designed, calibrated, and partly validated, there is no hard evidence that it actually describes something “true”. Confidence in the model must be built in the context of

specific questions, which the model has been proven to answer faithfully. Even then, one cannot expect this type of model to predict the outcome of any single experiment precisely, but rather to show up trends and prospects. In other words — to cite the late David G. Goodwin, one of the pioneers of numerical modeling of chemical processes: „We perform quantitative modeling in order to draw qualitative conclusions”⁹.

⁹D. G. Goodwin. Cited according to W. G. Bessler, personal communication.

5 Modeling the lithium-sulfur battery – calibration and simulation results

In this chapter, a detailed computational study of the liquid-electrolyte Li/S battery is presented. The structure of this chapter follows that of section 4.2.6, where the different reaction mechanisms have been introduced and discussed: First, the global two-step model is used to study the influence of the cell geometry, the electrolyte properties, and the cycling protocol on the performance of the battery. Chronologically, these results predate the experimental work and also influenced the cell and electrode design, reported in chapters 2 and 3. Next, the results of the multi-step model with literature parametrization are presented in section 5.2, including a technical discussion of the model’s features. The results of this work, including discharge profiles, chemical species concentrations, and impedance spectra are analyzed and discussed, as previously published in Ref. [P2]. The reparametrization of the model is detailed in section 5.3, including a full description of all calibration steps, using both data recorded experimentally and values available from literature. Note that this calibration is only valid for one type of Li/S cell. The same model can also be calibrated to describe different cells, as presented e.g. in Ref. [P4]. An attempt to validate the calibrated model is made in section 5.4 before more simulation results are delivered and analyzed in section 5.5. Simulations with the polysulfide shuttle enabled are reported in section 5.6. A discussion of the early results of this model extension concludes the simulation part of this work. Finally, a critical review of the model’s features, achievements, and limitations is presented in section 5.7, including a discussion of possible model improvements and extensions.

5.1 Global two-step model

The global two-step model, described in section 4.2.6 above, is simplistic by design and does not claim to represent the electrochemistry of any actual cell. Instead, its parameter set is mostly chosen intuitively. Given this limitation, this model is not capable of nor intended to reproduce experimentally obtained data. The discharge/charge profile shown in Fig. 5.1, for example, does not share a lot of similarity with the profile of a real Li/S cell as e.g. presented in Fig. 3.14. Because of the simplified

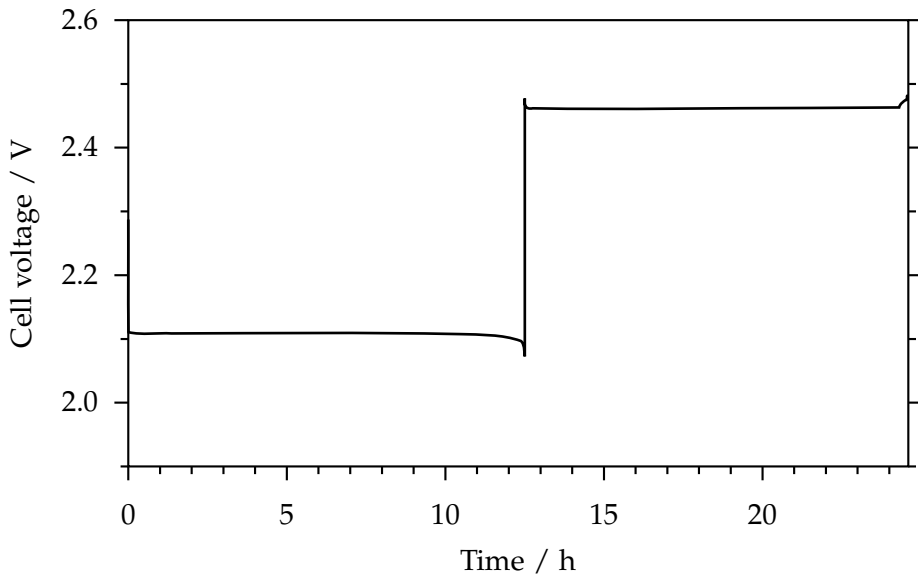


Figure 5.1: Discharge/charge profile resulting from the global model.

reaction mechanism, it lacks the typical two voltage plateaus during discharge and the slope during charge. Nevertheless, the OCV of the cell is reasonable as are the geometry and current densities. For this model, the typically used cycling protocol is: Discharge at a nominal rate of C/10 until $E \leq 2.05$ V, followed by a charge at a nominal rate of C/10 until $E \geq 2.4$ V. The charge and discharge cutoff voltages are chosen empirically to maximize capacity without simulating the almost vertical slopes at the end of discharge and charge. The results of such a cycling simulation are presented in Fig. 5.1.

Since geometry and transport parameters are physically meaningful regardless of the simplified chemistry, this model is perfectly apt for the study of a subset of features of the Li/S cell. This is true in particular for the transport in the liquid electrolyte. The main variables influencing transport are the concentration of ions and the applied current, which are chosen to represent the situation in the Li/S cell faithfully. In order to achieve this, dissolved polysulfides are included in the model, even though they do not participate in any reaction. Their concentrations as well as all other parameters of the model are summarized in Tab. A.5 on page 150.

The remainder of this section focuses on transport phenomena and cell composition. To begin with, the distribution of sulfur across the cell is plotted against time in Fig. 5.2. In this simple model, the amount of solid sulfur is directly proportional to the cell's SoC, which is, in turn, proportional to the discharge time – at least during

a galvanostatic discharge. When looking at the total amount of sulfur present in the cell (black line), this relation is perfectly fulfilled. The colored lines, however, which represent the amount of sulfur at various positions in the cell, do not follow the same pattern. The closer a control volume (CV) is to the negative electrode, the faster the conversion of sulfur in that CV. Close to the separator, the electrode is devoid of solid sulfur long before the end of discharge.

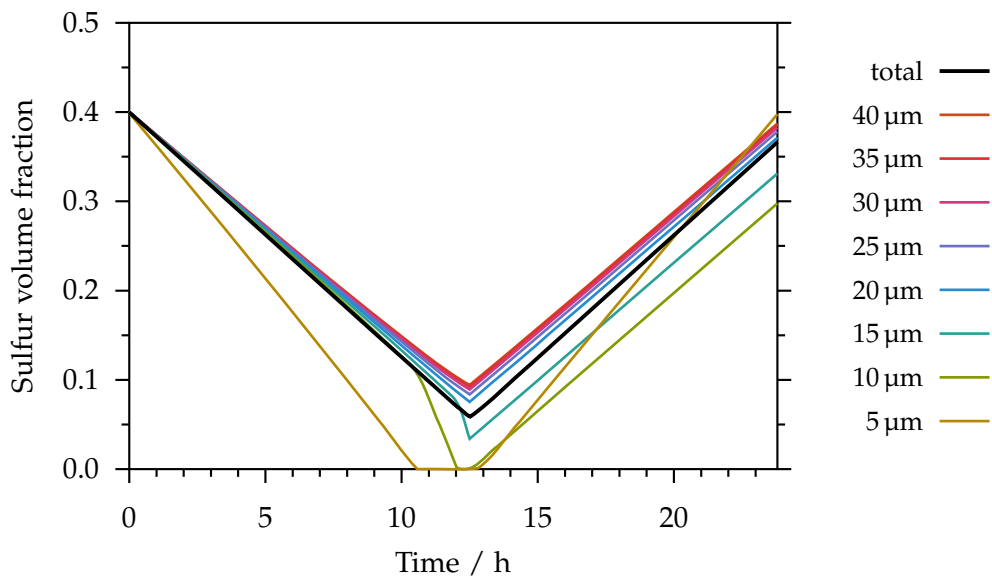


Figure 5.2: Changes in the distribution of solid sulfur during one cycle. Colors denote the position in the electrode: 0 μm = separator; 40 μm = current collector.

When charging, the situation is reversed: the region closer to the separator is recharged more quickly. This process is not perfectly balanced, however, so that the distributions of S_8 and Li_2S across the cell are slightly different after each cycle. The effect adds up over time, leading to an increasingly non-uniform composition of the cell. Due to the diffusion overpotential, the local electrochemical potential depends on the position in the positive electrode. Because of this and the sulfur redistribution, a slightly higher voltage is needed each cycle to access all the sulfur deposited in the previous cycle. When using a standard cycling protocol that enforces a constant charge/discharge cutoff voltage, the sulfur utilization is decreased during each cycle. This can be best observed when looking at the average volume fractions of active material plotted over time, see Fig. 5.3. The utilization of active material decreases rapidly, causing faster, but more shallow cycling.

Since there is no physical or chemical mechanism in this model which could cause irreversible degradation, the effect discussed above is naturally reversible. While less and less material is cycled over time, none of the S_8 or Li_2S is actually lost. Running a

slow “refresh” cycle, like the 11th cycle in Figs. 5.4 and 5.5, the material utilization can be increased to a level almost equal to a fresh cell. This refresh cycle also restores the uniformity of the sulfur distribution (data not shown).

Another issue directly associated with the composition of the cell still persists, though: When fully charged, there is only very little pore space left in the electrode (blue area in Fig. 5.3). As discussed in chapter 4, the microstructure is not simulated explicitly in this work. Instead, each phase is assumed to occupy one continuous volume. This assumption is not justified anymore for very low porosities. At some point, no continuous path may exist in the electrolyte phase, long before its volume fraction is exactly zero. Because of the above assumption, this is not an issue for the simulations, but the very low porosity is likely to cause problems in a real cell.

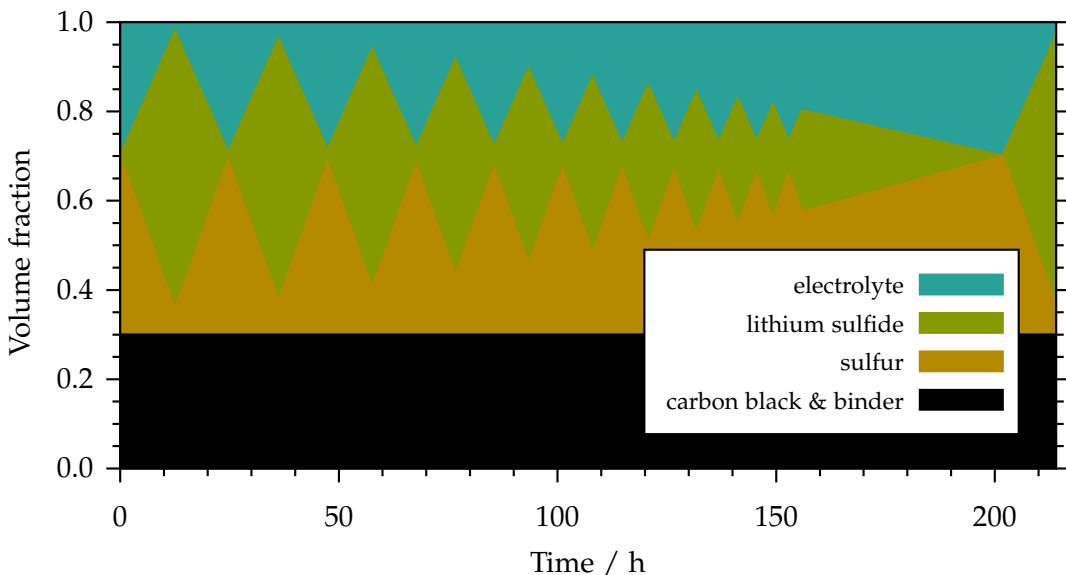


Figure 5.3: Volume fractions vs. time. The cell is cycled at a nominal rate of C/10, but the 11th cycle was run at a lower rate of C/100. The reversible degradation caused by regular cycling can be undone by the slow “refresh” cycle.

Discharge capacities for the simulation discussed above are plotted in Fig. 5.4, confirming that the reversible capacity fade can be all but undone. Nevertheless, it is desirable to reduce this effect as much as possible, which leads to the question of how to increase the highest tolerable rate, i.e. the rate at which no significant reversible degradation occurs due to material redistribution. It turns out that there are two options: The first and most obvious possibility to improve the situation is to choose a more suitable electrolyte. In Fig. 5.5, the cell simulated above is compared to another cell with a different electrolyte. In this electrolyte, the transport of dissolved sulfur (and polysulfides) is repressed. This is achieved by dividing diffusion coefficients by

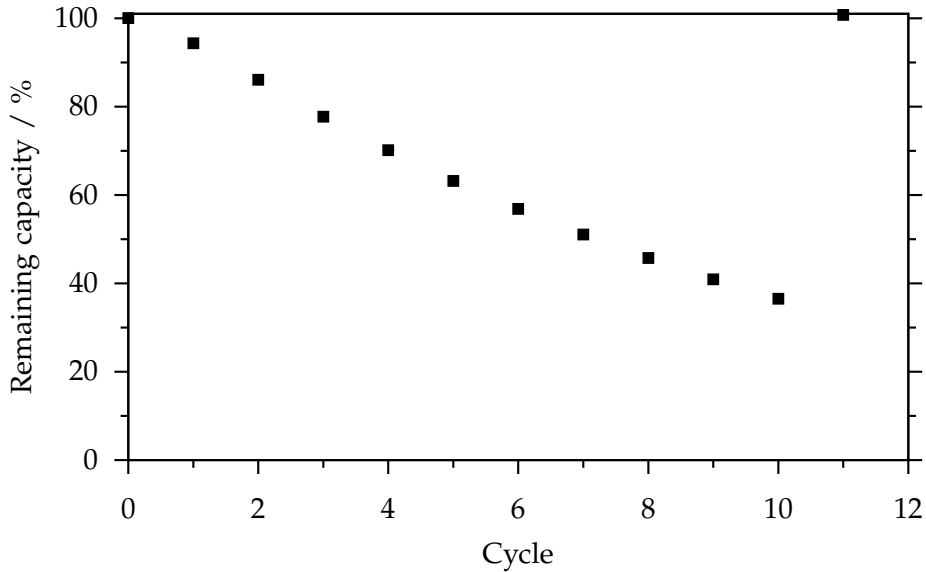


Figure 5.4: Discharge capacity of several cycles, simulated with the global model. The 11th charge was run at a lower rate of C/100.

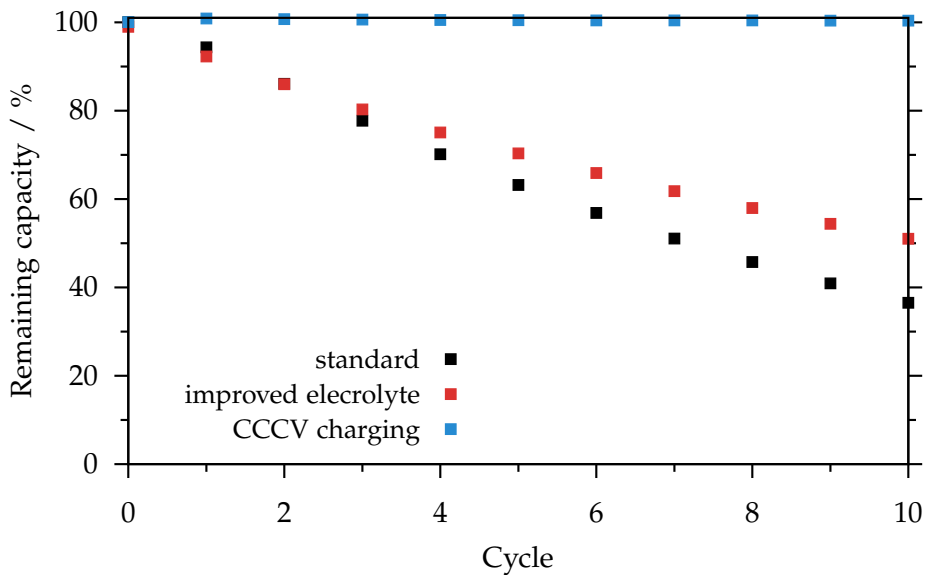


Figure 5.5: Mitigating capacity fade. Black: standard parameters and cycling protocol; red: standard cycling protocol, but lower diffusion coefficients for dissolved sulfur species (improved electrolyte); blue: standard parameters, but cycling protocol with CCCV charging. Details see text.

ten compared to Tab. A.5. The results clearly indicate that reversible degradation can be alleviated by the improved electrolyte to some degree.

Unfortunately, the choice of known electrolytes with a decent performance is rather limited [83]. Also, one is usually not free to choose an arbitrary electrolyte, since additional requirements need to be met, which are not represented in the model, namely chemical compatibility with all materials, safety, and cost.

The second option to reduce the capacity fade does not require any changes to the cell itself, but rather to the cycling protocol. Instead of simply stopping the charge at the predefined cutoff voltage, a constant voltage step is added: The voltage is fixed at the charge cutoff voltage until the current drops below 1 % of the nominal charge current. This measure, known as CCCV charging, is not only very effective in preventing reversible capacity fade, but also easy to implement and without negative side effects, except for the slightly increased charging time.

Conclusions. Using the global two-step model, transport in and cycling of the Li/S cell can be studied. The spatial homogeneity was shown to decrease during cycling, cf. Figs. 5.2 and 5.3. Also, the effect of the electrolyte's conductivity as well as CCCV vs. simple CC charging was investigated, cf. Fig. 5.5. The main conclusions are that a significant amount of porosity is needed to avoid pore clogging, and that CCCV charging is absolutely required, even at medium charge/discharge rates. This insight helped to avoid potential issues when designing the electrodes and cells for the experiments as outlined in chapter 2. In addition, the findings presented in Fig. 5.3 influenced the design of the cycling protocol in the experimental section, where a slow "refresh" cycle was added every 25 cycles, cf. pp. 62f.

While the global model can illustrate some aspects of the Li/S battery without too much complexity, it cannot reproduce the behavior of the cell precisely. The major limitation of the model is that it does not describe the electrochemical processes in sufficient detail, resulting in inaccurate results for the cell voltage in general and the discharge and charge profiles in particular. To overcome this issue, a more detailed description of the electrochemical reactions is needed as presented in the following section.

5.2 Multi-step model – literature parametrization

5.2.1 Introduction

The multi-step reaction mechanism presented next is described in section 4.2.6. While the implementation of the governing equations is identical to the global model, the reaction pathways as well as the surface areas and their dependency on the electrode composition are modified to match experimental conditions more closely. The development of the multi-step model happened in two separate stages: The basic design, implementation, literature parametrization, and testing was completed in mid-2012 based on data available from literature, as described in the following section. The reparametrization and partial validation presented in section 5.3 was performed in 2014 after having recorded and analyzed sufficient original experimental data. Finally, an addition of the shuttle mechanism to the model was implemented in 2013 in collaboration with Andreas F. Hofmann at DLR, see Ref. [P3], and later applied to the multi-step model.

In the first implementation, described in this section, no validation per se is performed, but the parameters are chosen according to Ref. [196] or assumed; see chap. 4.1 for a comparison of this work with Ref. [196] and other relevant publications. The entire set of parameters used for these simulations can be found in Tab. A.6 on page 151. Where reverse reaction rate constants are specified, the rates are calculated according to Eq. (4.10) instead of Eq. (4.11). This part of the work has already been published and the following paragraphs are cited verbatim from Ref. [P2]:

5.2.2 Discharge at different rates

Simulated discharge behavior of the cell is shown in Fig. 5.6 for different C rates, i.e. different discharge currents. Fig. 5.6a presents voltage-capacity curves. They show the typical three-stage behavior also known from experiments [115, 244], consisting of (I) a high-voltage plateau, followed by (II) a fast voltage drop (at low currents associated with a voltage dip), and finally (III) a long low-voltage plateau. The origin of this curve shape will be discussed below. The rate capability of the simulated cell is not very good (considerable voltage drop at increasing current), which is typical of Li/S batteries with high sulfur content. For all C-rates, S₈ is almost completely converted to Li₂S (close to 100 % sulfur utilization). The predicted energy density is 1300 Wh · l⁻¹ and 850 Wh · kg⁻¹ (per cathode volume/weight). Experimentally, lower values are typically observed due to side reactions or passivation of the cathode (e.g. by film formation); these effects are neglected in this model.

One of the most interesting aspects of the Li/S cell is the dissolution and re-formation of phases during cycling. Fig. 5.6b shows the volume fractions of solid S₈ and Li₂S

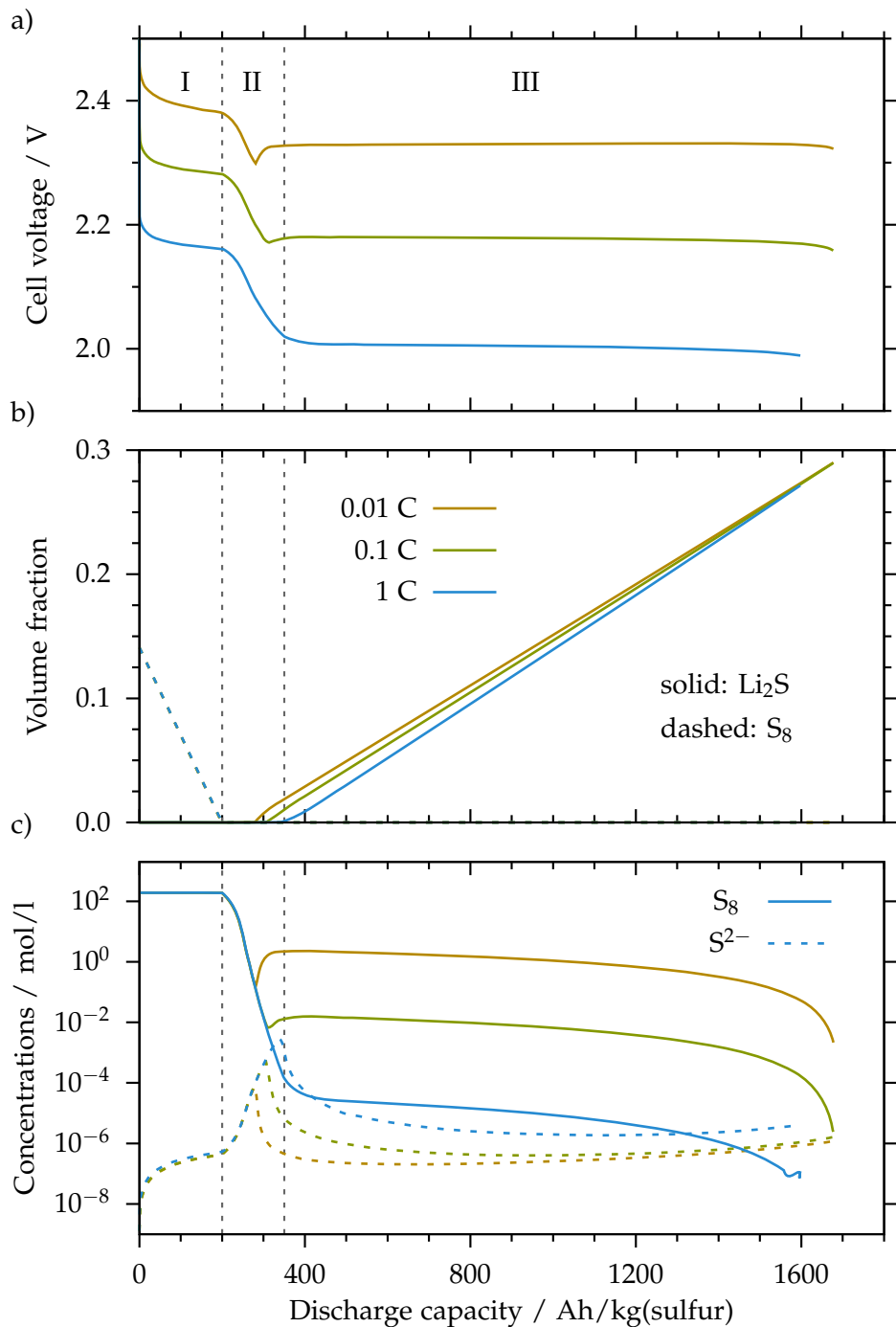


Figure 5.6: Simulated discharge at various current rates: a) cell voltage, b) solid volume fractions of S_8 and Li_2S , c) spatially averaged concentrations of selected species.

during discharge. During stage I, solid S_8 is completely dissolved. During stage II, all intermediates are present in dissolved form only. Finally, during stage III, Li_2S is formed and continuously precipitated. This behavior is observed for all C-rates investigated, i.e. there is no coexistence of solid S_8 and Li_2S phases during the initial discharge. Another characteristic feature of the Li/S cell is the difference in the total solid volume between the charged and discharged state: The volume of the product (Li_2S) is, in fact, 176 % that of the reactant (S_8) due to the large difference in density of the two phases, cf. Tab. A.6.

Fig. 5.6c shows spatially averaged concentrations of dissolved $S_{8(ds)}$ and S^{2-} species as representative intermediates. Using these profiles, the particular shape of the discharge behavior can be further interpreted. During the plateau stages I and III, the solid S_8 and Li_2S phases are in equilibrium with the corresponding dissolution product $S_{8(ds)}$ and S^{2-} respectively, buffering its concentration to a relatively constant value and thereby causing a cell voltage plateau. This is the typical behavior of phase conversion electrodes. During the intermediate stage II, however, there are no solid phases present and the complete electrochemistry occurs among the electrolyte-dissolved polysulfide intermediates. Within stage II, the concentration of $S_{8(ds)}$ strongly decreases, while the concentration of S^{2-} shows a peak. The cell voltage qualitatively follows the $S_{8(ds)}$ concentration profile, including the respective dip in voltage and concentration at low C-rates, which demonstrates the dominating role of the $S_{8(ds)}$ species for macroscopic discharge behavior. An interesting effect can be observed for the slower discharge rates: For the polysulfide concentrations to stabilize, it is required that the activity of the solid product be constant. As long as there is virtually no solid Li_2S in the cell, this is not the case: The more precipitate is formed, the higher its activity. Because the Li_2S precipitation reaction is not an electrochemical reaction, as a first approximation the rate of Li_2S formation is independent of the current applied. The voltage profile will only show the dip if no solid Li_2S is present at the beginning of the discharge and if the discharge rate is slow compared to the rate of Li_2S precipitation.

5.2.3 Cycling

Simulated cycling behavior is shown in Fig. 5.7. In panels a) and b) the transient cell voltage and current are plotted for the duration of the numerical experiment, consisting of CC discharge, CCCV recharge, and relaxation to OCV. Note that the model shows quite high charging overpotentials, which become particularly obvious at the end of the CCCV phase, when the relaxation of the cell to OCV is accompanied by a strong drop in voltage.

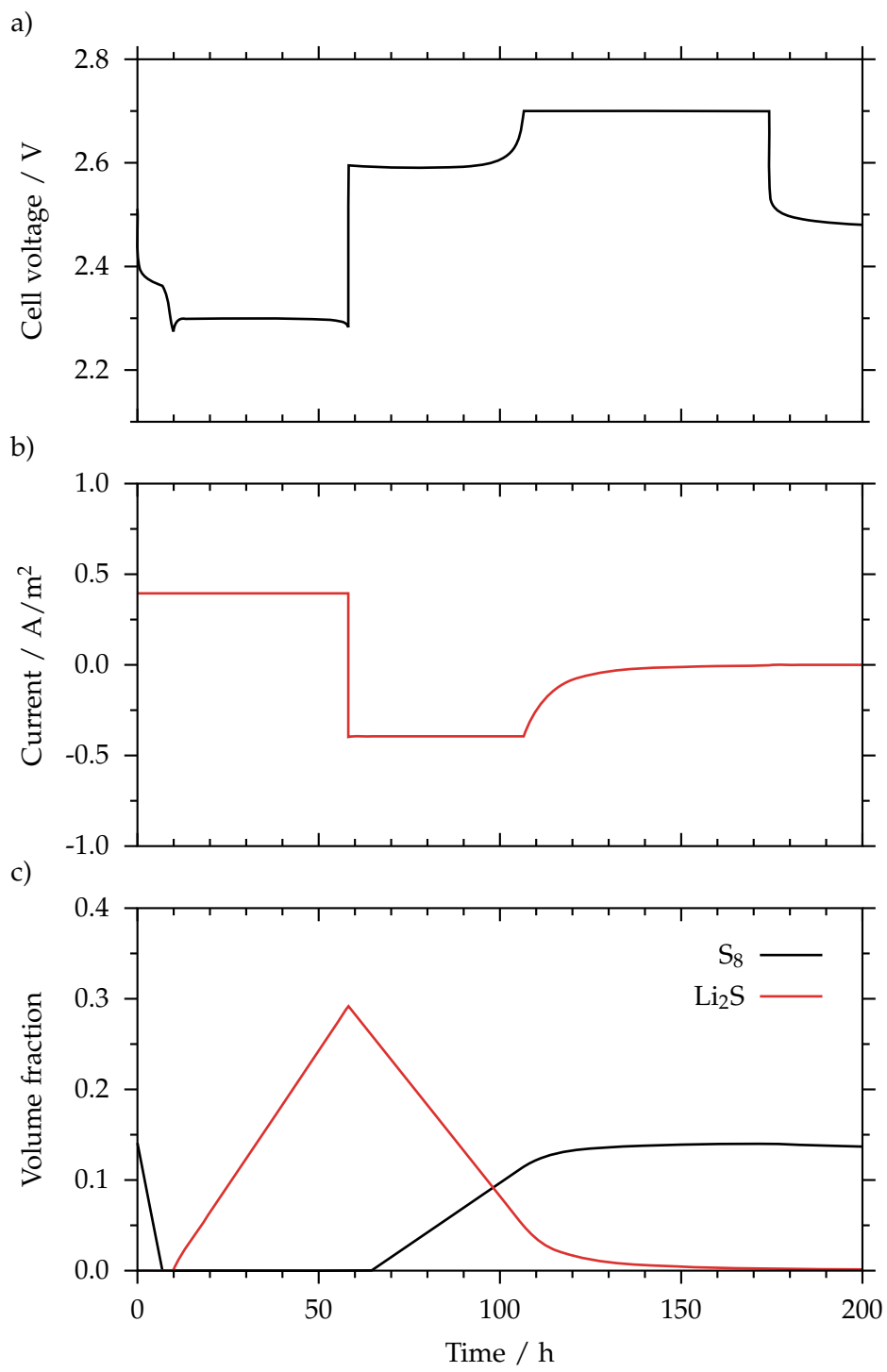


Figure 5.7: Simulated cycling with CC discharge and CCCV charge at a C/50 rate. a) cell voltage, b) current, c) volume fractions.

Fig. 5.7c shows the volume fractions of the bulk reactant and product phases in the composite cathode. The model predicts an asymmetric behavior during cycling: While Li_2S is not formed during discharge before all solid S_8 is dissolved, the two solid phases do coexist during charge. The reason for this asymmetry is the assumed kinetics of the system in general and the speed of the two dissolution reactions in particular. In case of a partial charge or discharge, this effect can introduce hysteresis to the system.

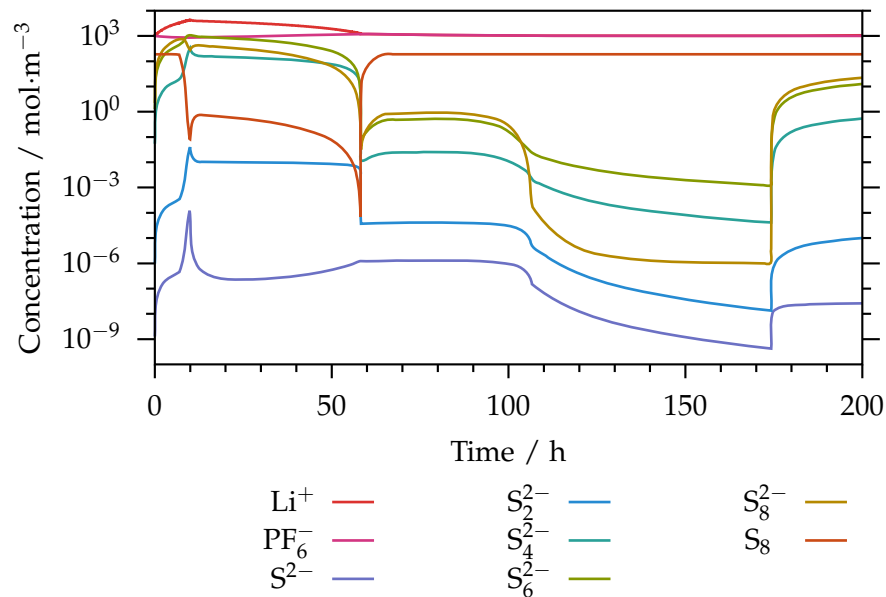


Figure 5.8: Simulated cycling with CC discharge and CCCV charge at a C/50 rate. Evolution of the spatially averaged concentrations of dissolved species.

Fig. 5.8 shows time traces of the spatially averaged concentrations of all electrolyte-dissolved species. Li^+ is the only cation present in the cell; due to charge neutrality, the total Li^+ concentration corresponds to the total concentration of anions in the solution. At the beginning and end of discharge, the non-reactive PF_6^- is the main counterion, while at intermediate state of charge (SoC), polysulfide anions contribute significantly to the total anion concentration. Both end of charge and end of discharge are characterized by strongly dropping concentrations of dissolved polysulfides (note the logarithmic scale of Fig. 5.8), until the reactants for the charge-transfer reactions cannot be supplied anymore. This leads to the final drop of cell voltage at end of discharge, and the final increase in cell voltage at end of charge.

Another interesting result is that polysulfide concentrations are considerably lower during charge compared to discharge. Therefore the conductivity of the electrolyte is lower and diffusion overpotentials are higher during charging. Over the complete

cycle, both the total amount and the composition of the ions vary to a great extent. Hence, the electrochemical response of the cell is expected to behave differently at different SoC. This will be further discussed in the following section.

5.2.4 Impedance

The results of impedance simulations for different SoC are shown in Fig. 5.9. The upper two panels show a Bode representation, i.e. the real and imaginary part of the cell's impedance Z versus logarithmic frequency. The lower panel shows the same information in Nyquist representation, i.e. imaginary part versus real part. The cell shows a complicated impedance behavior, which strongly depends on the SoC. At high SoC, a feature at ~ 0.5 Hz is dominating, with an additional smaller feature at ~ 10 Hz. At increasing SoC, these features merge at an intermediate frequency. Additionally, impedance strongly increases toward low frequencies < 10 mHz, which is typical of batteries.

5.2.5 Conclusions

From the above results, reproduced from Ref. [P2], the following conclusions can be drawn: First of all, the results of the multi-step model are much more realistic and detailed in terms of voltage, current, and dissolved species concentrations compared to the two-step model. Also, the more detailed description enables the simulation of representative impedance spectra – with regard to Li/S batteries, this is a unique feature as of today. Despite the slightly different reaction mechanism, the results are otherwise similar to previous simulations by Kumaresan et al. [196]: For the operating conditions simulated, the “behavior of the Li/S cell is governed by the presence of solid reactant and product phases. The volume fractions of S_8 and Li_2S in the cathode change considerably during cycling, providing an explanation of the distinct stages during discharge. The model also predicts an asymmetric behavior of phase formation/dissolution when comparing discharge and charge, as well as high charge overpotentials”¹.

¹cited verbatim from Ref. [P2], p. 187f

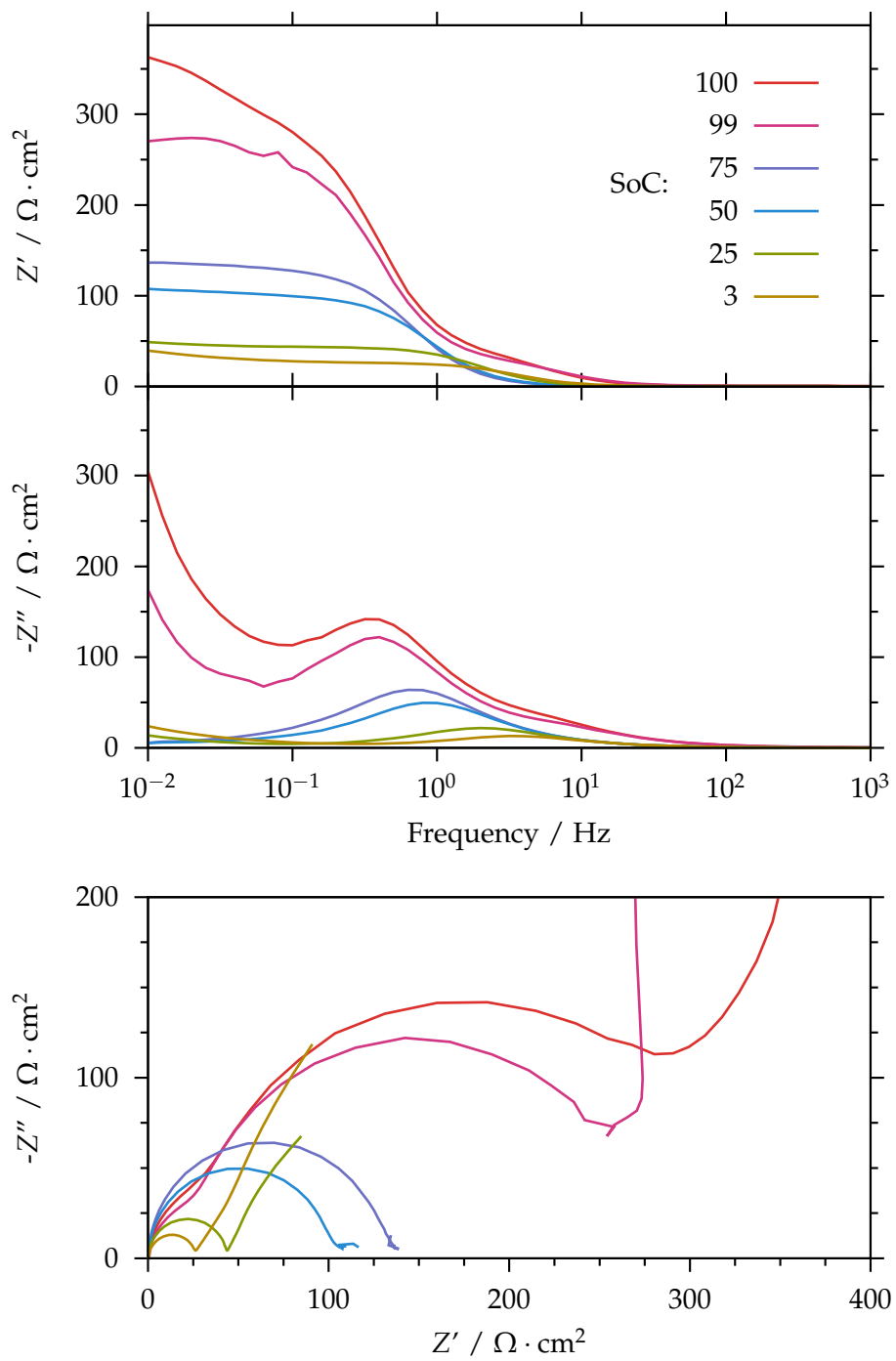


Figure 5.9: Simulated electrochemical impedance spectra for different SoC. Upper panels: Bode representation. Lower panel: Nyquist representation.

5.3 Multi-step model – reparametrization

In order to obtain more precise results from the model, proper parametrization and validation are required. While its behavior is strongly predetermined by the form of the governing equations, the predictions of the model still rely heavily on its many inputs. While a reasonable set of parameters was presented above (see also Tab. A.6), this set does not represent any actual battery, restricting its usefulness to general design considerations. In the following section, the calibration of the model is described, including a discussion of the origin and value of each parameter.

5.3.1 Parameters determined from independent sources

For any model, it is desirable to determine as many parameters as possible a priori, i.e. from preliminary studies, dedicated experiments, or from first principles. Unfortunately, despite the rapidly growing number of publications on Li/S batteries and materials, the data base is still very sparse and incomplete. Nevertheless, the values of some parameters could be acquired from literature:

- Molecular weights: The molecular weight of each compound is calculated from its known composition using the standard atom masses from Ref. [245], Tab. 4.
- Densities: The densities of the (pure) phases are available from Ref. [238]. For the liquid electrolyte, the density is adjusted to take the mass of the dissolved species into account. For the separator, the density of pure, amorphous polypropylene is used as reported in Ref. [246].
- Enthalpies of formation of pure species: For the pure species S₈ and Li, g_0 equals zero by definition. For Li₂S, the values for h_0 and s_0 are taken from Ref. [247] and converted to $g_{0,\text{Li}_2\text{S}} = -429.7 \text{ kJ} \cdot \text{mol}^{-1}$ at 30 °C.
- Enthalpies of formation of polysulfides g_n : Gas phase data taken from Ref. [143] and converted to effective values taking into account the effect of the liquid electrolyte by fitting the Gibbs free energy shift, see below. It is known that various polysulfide species can exist in different forms with slightly different enthalpies [248]. To keep things simple, each species is represented by just one form with one value for g_n .
- Specific double-layer capacity of carbon: Depending on the type of carbon used, different values are reported in the literature, ranging from $0.05 \text{ F} \cdot \text{m}^{-2}$ to $0.5 \text{ F} \cdot \text{m}^{-2}$ [249–254]. For this work, a specific capacity of $0.2 \text{ F} \cdot \text{m}^{-2}$ is chosen, which falls within the standard ranges reported for carbon in various electrolytes by Refs. [249] and [250].

Table 5.1: Geometry and initial composition of the cell as used for the validation experiments.

parameter	value	comment
electrode diameter	1/2"	punch size
macroscopic surface	$1.27 \cdot 10^{-4} \text{ m}^2$	electrode disc size
ambient pressure	101 325 Pa	standard ambient conditions
ambient temperature	303.15 K	controlled by temperature chamber
global	cathode thickness	25 μm
	Li_2S (% of solids)	78 %
	carbon (% of solids)	12 %
	binder (% of solids)	10 %
	S_8 (% of solids)	0 %
	τ_{elyte}	1.12
	specific surface area	$1.1 \cdot 10^7 \text{ m}^2 \cdot \text{m}^{-3}$
	thickness	25 μm
	ε_{sep}	0.59
	$\varepsilon_{\text{elyte}}$	0.41
cathode	τ_{elyte}	1.77
	thickness	180 μm
	effective thickness	1 μm
	ε_{Li}	0.63
	$\varepsilon_{\text{elyte}}$	0.37
	τ_{elyte}	1.05
	specific surface area	$3.58 \cdot 10^6 \text{ m}^2 \cdot \text{m}^{-3}$
	comment	assuming an average roughness of the top layer of $10 \text{ m}^2 \cdot \text{g}^{-1}$, cf. Refs. [48, 260]
	comment	calculated according to Ref. [255]: $\tau^2 = \varepsilon^{-0.5}$ according to Ref. [P4]
	comment	manufacturer's specification [256]
separator	ε_{sep}	manufacturer's specification [256]
	$\varepsilon_{\text{elyte}}$	manufacturer's specification [256]
	τ_{elyte}	calculated from τ^2 of Ref. [257]
	thickness	180 μm
	effective thickness	1 μm
	ε_{Li}	represents the top layer of the bulk lithium [259]
	$\varepsilon_{\text{elyte}}$	estimated from [259]
	τ_{elyte}	estimated from [259]
	specific surface area	assumed from [259]
	comment	cf. Refs. [48, 260]
anode	thickness	180 μm
	effective thickness	1 μm
	ε_{Li}	represents the top layer of the bulk lithium [259]
	$\varepsilon_{\text{elyte}}$	estimated from [259]
	τ_{elyte}	estimated from [259]
	specific surface area	assumed from [259]
	comment	cf. Refs. [48, 260]
	comment	calculated according to Ref. [255]: $\tau^2 = \varepsilon^{-0.5}$ according to Ref. [P4]
	comment	manufacturer's specification [256]
	comment	calculated from [257]

5.3.2 Parameters calculated from experimental data

Many parameters can be obtained from the experimental setup and results, either because they can – at least in principle – be chosen freely within reasonable constraints or because they can be easily measured, extracted, or calculated from the experimental results. All the macroscopic geometric parameters, the choice of materials, and the electrode composition fall into this category. A full list can be found in Tab. 5.1. In addition, the following parameters are readily extracted from experimental data:

- Volume fractions of all solids in the electrodes are calculated from the volume of the electrode, the known composition of solids (see Tab. 5.1), and their densities. In the (hypothetical) fully charged state they are for the positive electrode: 12.1 % for S₈, 0.0 % for Li₂S, 3.2 % for total carbon, 2.8 % for the binder, 70.9 % for the liquid electrolyte. The remaining 10.0 % are filled with non-reactive, compressible Argon gas in the model, as discussed in section 4.2.6 on page 81.
- The concentration of the LiTFSI conducting salt is $1.0 \text{ mol} \cdot \text{l}^{-1}$; that of the LiNO₃ additive is $0.5 \text{ mol} \cdot \text{l}^{-1}$ according to the standard recipe, cf. section 2.3.3.
- The total surface area of the active material can be derived assuming that all ball-milled Li₂S particles are spherical with an average diameter of 1.1 µm (cf. section 3.1). Their total surface area is calculated to be $1.20 \cdot 10^6 \text{ m}^2 \cdot \text{m}^{-3}$. Further assuming that the number of particles does not change when the material is converted to S₈, the surface area of all sulfur particles is $1.40 \cdot 10^6 \text{ m}^2 \cdot \text{m}^{-3}$.
- The electrochemically active surface area, i.e. the carbon|electrolyte interface, was measured to be $1.1 \cdot 10^7 \text{ m}^2 \cdot \text{m}^{-3}$ in Ref. [P4] by Krypton BET. Since the electrodes used for this work are very similar in carbon content and structure, the same value is used here.
- The radius of the carbon black particles in Eq. (4.27) is estimated to be 40 nm based on SEM images (see e.g. Fig. 3.1b).

5.3.3 Parameters determined by equilibration

More parameters can be determined without fitting by making smart use of the model: Only the composition of solids is known from experiments, not the composition of the electrolyte. The equilibrium concentrations of dissolved species, however, are readily obtained by simulating a cell at rest for a long time. Starting with volume fractions derived from the composition of the solid material (see Tab. 5.1) and an electrolyte with virtually no dissolved polysulfides, a simulation is run with $i_{\text{tot}} = 0$ for $t = 10^9 \text{ s}$ (several years). After this time, the cell is perfectly equilibrated and the final values

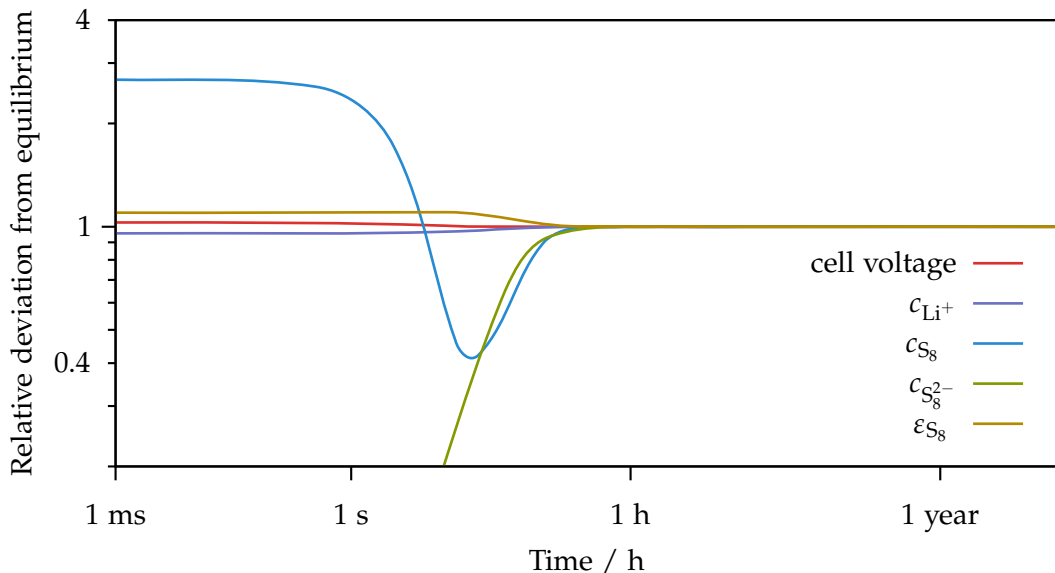


Figure 5.10: Initial equilibration. Time trace of a simulation with $i_{\text{tot}} = 0$ (in the fully charged state). For selected quantities, the relative deviation from the final values is reported. The latter are considered to be the true equilibrium values and are used as a starting point for subsequent simulations.

of this simulation are used as the starting values for all subsequent simulations of the same cell. The actual equilibration run is presented in Fig. 5.10.

5.3.4 Parameters fitted to experimental data

After making use of all known independent sources, many parameters are still unknown. In total, there are 26 parameters left, including the Gibbs free energy of formation of solvated species in the electrolyte Δg_0 , ten diffusion constants, and ten forward reaction rate constants as well as ξ_1 and ξ_2 in the expression for the surface resistivity, Eq. (4.26), and finally, the fraction of activated Li_2S . These parameters need to be fitted to experimental data, which will be discussed in the following.

Originally, it was planned to fit several parameters at once using a multidimensional optimization algorithm, cf. section 4.30. Because of the large number of parameters to be fitted on the one hand as well as the very different types of reference data on the other hand (single data points, sets of data points, x - y -curves, parameters of a family of curves), this turned out to be a futile approach. Instead, the parameters were grouped and each group was adjusted manually within a reasonable range. In the following, the fitting results are complemented by parameter variation plots and corresponding discussions. In all plots, circles represent experimental data, lines simulation results.

The amount of activated Li₂S. As discussed in section 4.2.6 on page 82, the amount of activated Li₂S is slightly different from cell to cell, even within the same batch. Even worse, it cannot be determined by simply looking at the initial charge capacity since it is impossible to tell regular charging apart from irreversible reactions. These happen predominantly during the activation cycle because of the elevated voltage, cf. section 3.2.3. Not surprisingly, this figure strongly determines the behavior of the cell in all experiments, therefore it needs to be fitted first. This is achieved as follows:

1. Choose a fast sulfur dissolution rate and electrochemistry (i.e. rate constants). Also, enough electrolyte is needed to dissolve the entire sulfur – though this is less of an issue for the highly porous cell configuration discussed here.
2. Starting from the fully charged cell, simulate a discharge with a relatively slow rate and plot voltage vs. capacity (see Fig. 5.11). The transition region between the upper and lower plateau is now very narrow.
3. Adjust the ratio of activated and non-activated (passive) Li₂S, keeping the total amount of sulfur in the cell constant. The best value is the one where the onset of the lower plateau matches experimental data (regardless of the end of discharge).

The best choice is a ratio of activated Li₂S to passive Li₂S of 2:3. From an engineering point of view, an increase in activated Li₂S is highly desirable. For the model calibration, this value is perfectly acceptable, though.

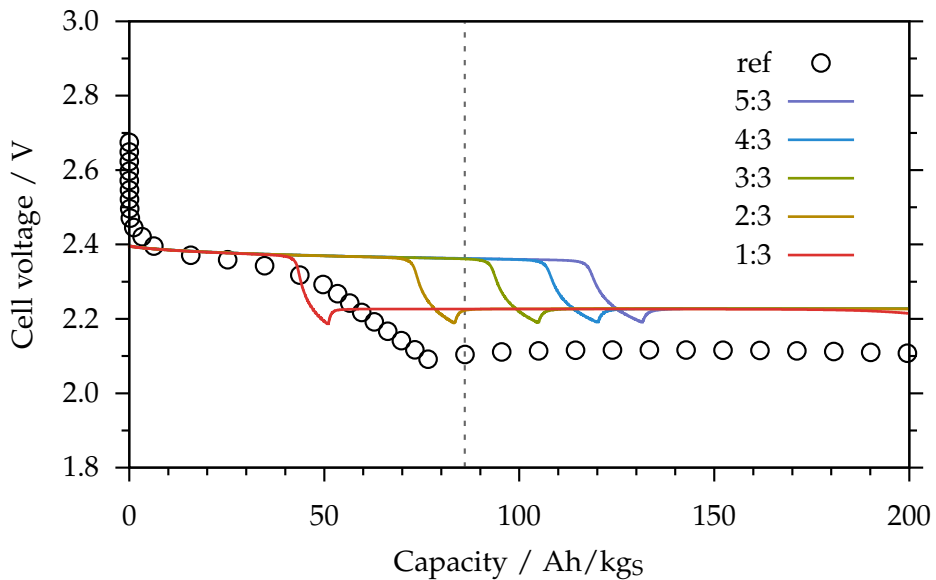


Figure 5.11: Parameter variation: Amount of activated Li₂S. The legend indicates the ratio of activated to passive Li₂S. A dashed line marking the onset of the lower plateau serves as a visual aid to the fitting target. Since the total capacity of the cell is irrelevant for this fit, the capacity range is restricted in the plot to better show the relevant region.

The active surface area expressions. Next, the expressions describing the active surface area need to be quantified. Their general form is derived and discussed in section 4.2.6. Only the parameters ξ_1 and ξ_2 in Eq. (4.26) remain to be fitted. This is done as follows:

1. Choose a moderately fast sulfur dissolution rate and electrochemistry (i.e. rate constants).
2. Starting from the fully charged cell, simulate a discharge with a relatively slow rate and plot voltage vs. capacity.
3. Adjust ξ_1 until the slope of the final voltage drop matches the reference data (without paying attention to the position, i.e. capacity, at which the voltage drop occurs).
4. Adjust ξ_2 until the onset of the voltage drop matches the reference data.

A parameter variation is presented in Fig. 5.12. Lines of one color share the same ξ_2 , whereas all dotted (dashed, solid) lines share the same ξ_1 . The best fit is obtained for $\xi_1 = 1.8$ and $\xi_2 = 5.0 \text{ nm}$. The value of ξ_2 is too large to be identified as the tunneling distance for electrons through the deposited, insulating Li_2S film. However, the passivating layer is not expected to grow perfectly uniformly: Instead, ξ_2 may be

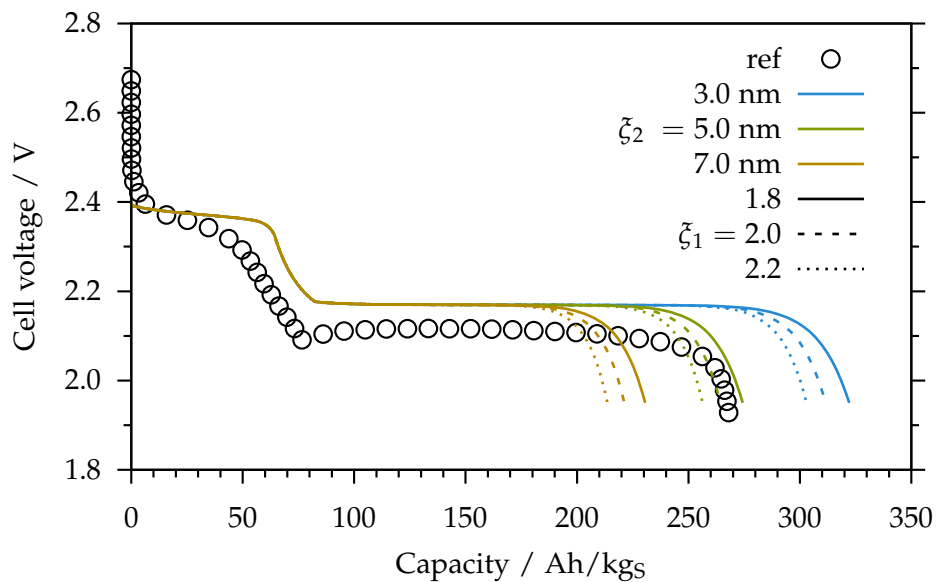


Figure 5.12: Parameter variation: Passivation of the carbon|electrolyte interface by precipitated Li_2S . The additional surface resistivity is described in Eq. (4.26) by the thickness of the Li_2S film and two additional parameters ξ_1 and ξ_2 , which are both varied in the above plot.

interpreted as the average thickness of the insulating layer at the time when electrons can no longer tunnel through its thinnest segment. This paragraph only deals with the calibration of ξ_1 and ξ_2 ; the formation of the passivating film is analyzed in more detail below, cf. Fig. 5.27 on page 128.

Enthalpy of formation of dissolved species. In order to correct the enthalpies of formation of the dissolved polysulfides for the effect of the liquid electrolyte, the gas-phase thermochemistry values taken from Ref. [143] are shifted by a fixed offset Δg_0 . The offset is determined as follows:

1. Choose fast rate constants.
2. Starting from a fully charged cell, simulate a discharge with a very slow rate and plot voltage vs. capacity (see Fig. 5.13).
3. Adjust the offset until the lower plateau voltage for charge and discharge is roughly centered between the charge and discharge branches of the reference data. The actual voltage will change when calibrating the reaction rates, but the center is virtually not affected.

Unfortunately, very slow discharges are difficult to obtain experimentally – or rather difficult to interpret since the discharge due to the externally applied current mixes

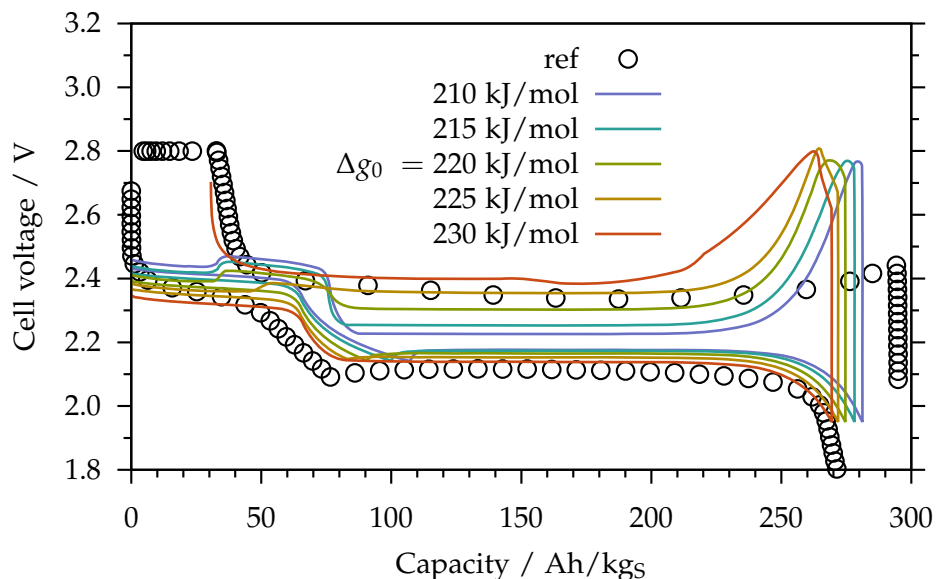


Figure 5.13: Parameter variation: Enthalpy of formation of the dissolved polysulfides. Δg_0 denotes the fixed offset to gasphase thermochemistry data. Reference data: discharge at C/50, charge at C/20. The different simulations may alternatively be interpreted as different electrolytes.

with internal self-discharge. Therefore, the slowest regular cycling data (with a discharge rate of C/50 and a charge rate of C/20) was used for the calibration of the offset in Fig. 5.13.

The best fit is obtained for $\Delta g_0 = 220 \text{ kJ} \cdot \text{mol}^{-1}$. Because of the different charge and discharge rates in the reference data, the calibration is difficult and even the best result looks slightly off-center.

Diffusion constants. Diffusion constants for different species are expected to be different in reality. Unfortunately, in the literature there is no direct measurement or even a clue to the values of D_n for all dissolved species n . The values chosen by Refs. [196, 198, 199] may serve as guidance values. However, they lack experimental references themselves and are assumed for different electrolytes. To handle this situation, all ten diffusion constants are assumed identical so that only one value needs to be fitted. In this study, the diffusion constants are varied in the range of 10^{-10} – $10^{-12} \text{ m}^2 \cdot \text{s}^{-1}$, which has been reported for ionic liquid based electrolytes [175, 261] and compared with cycling and impedance data in Figs. 5.14 and 5.15, respectively.

While the impact of the speed of diffusion is obvious in general, it is difficult to quantitatively distinguish between the data sets with smaller diffusion constants in Fig. 5.14. Therefore, impedance spectra are analyzed additionally. More precisely, the high-frequency intercept of the spectra with the x -axis is evaluated. This feature is related to the electrolyte's ionic conductivity, which in turn depends on the diffusion constants according to Eqs. (4.3) and (4.4).

EIS results are presented in Fig. 5.15. Note that the shape of the Nyquist plots does not match very well since the reaction rates are not yet calibrated. The effect of the diffusion constants on the Z' intercept is clearly visible. While there is a lot of variation in the reference data (cf. section 3.2.4), the plot still shows a clear trend and the diffusion constants can be calibrated to at least the right order of magnitude much more easily than on the basis of discharge profiles. The best agreement is obtained for $D_{\text{eff}} = 1.0 \cdot 10^{-11} \text{ m}^2 \cdot \text{s}^{-1}$.

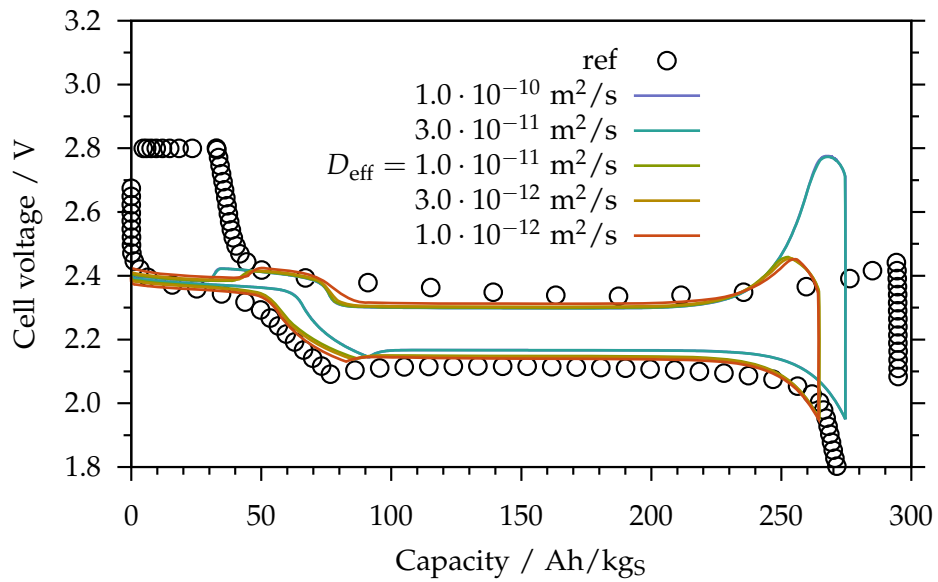


Figure 5.14: Parameter variation: Impact of the speed of diffusion in the liquid electrolyte on charge/discharge profiles.

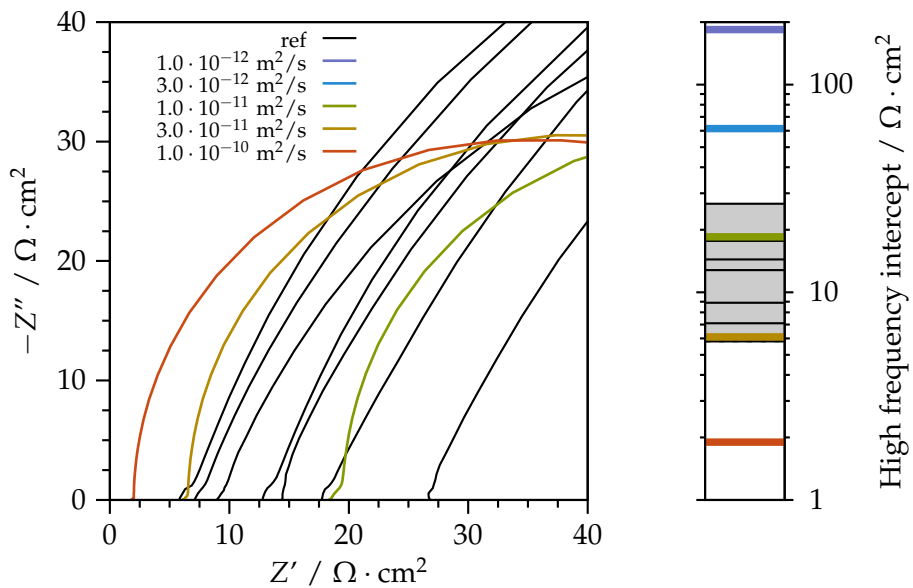


Figure 5.15: Impact of diffusion in the liquid electrolyte on the EIS high frequency intercept. Since there is considerable variation in the reference data, the spectra of several similar cells are plotted. Left: Nyquist plot (two simulations are not visible since they intercept at much higher Z'). Right: Comparison of the x -axis intercept for different diffusion constants. The experimentally confirmed range is shaded in gray.

Reaction rates. Finally, there are ten rate constants in the model, which are altogether unknown. An initial scan was performed testing dozens of combinations of rate constants for just one criterion: The solver needs to be able to calculate the initial equilibrium. This technique yielded an initial guess for the rate constants in the range 10^{13} – 10^{19} mol · m⁻² · s⁻¹ (data not shown). One exception is the rate of dissolution of sulfur, which is a non-electrochemical reaction that occurs at a much slower rate. Because of the model's high sensitivity on this value, it was chosen to be fitted independently as follows:

1. Choose the other rate constants fast.
2. Starting from a fully charged cell, simulate a discharge with a slow rate and plot voltage vs. capacity (see Fig. 5.16).
3. Adjust the rate of dissolution until the slope matches that of the reference data.

Even though it is somewhat off in absolute position, the best agreement for the slope is obtained for $k_{\text{fwd}} = 3.0 \cdot 10^{-4}$ mol · m⁻² · s⁻¹. All other rate constants were adjusted by studying the concentrations of polysulfides during cycling and increasing the rate constants for those reactions whose reactants accumulated excessively (data not shown). Those still random, but “normalized” rates, were then scaled by a common factor, which is fitted as follows:

1. Simulate a charge and discharge at a medium rate.
2. Adjust the factor until the voltage hysteresis, i.e. the difference between charge and discharge voltage matches experimental data.

Even for the rather slow experiment presented in Fig. 5.17 (charge: C/20, discharge: C/50), the reaction overpotential is considerably large. For the slowest rate constant, the solver did not even come up with a valid solution for the entire experiment. Since the cell is charged at a faster rate, the impact of slow electrochemical rate constants affects the charge branch more strongly than the discharge branch. In summary, the best fit is obtained for a scaling factor of ten.

At this point the model is fully calibrated, but not necessarily validated. In order to come up with the final values reported in Tab. 5.2, the manual fitting process was iterated three times, since the combined effect of all other fit parameters may significantly affect the best value of each single parameter. For the purpose of illustrating the process, the parameter variations shown here are selected from the second run. The first run still contains lots of aborted simulations and some which are really far off. During the third run, in contrast, the parameters are changed by tiny amounts only, making it hard to discern the effect they have on the simulation.

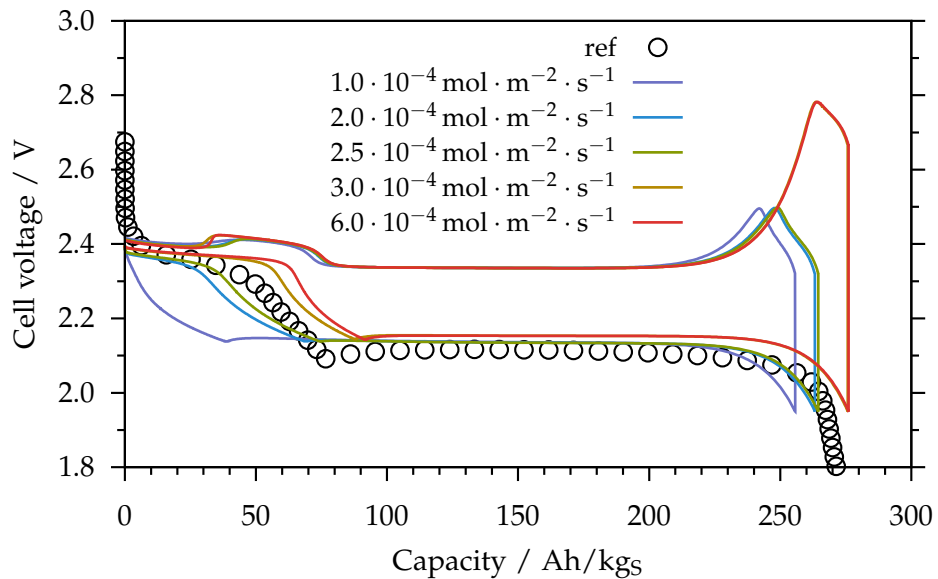


Figure 5.16: Parameter variation: Effect of the rate of dissolution for sulfur.

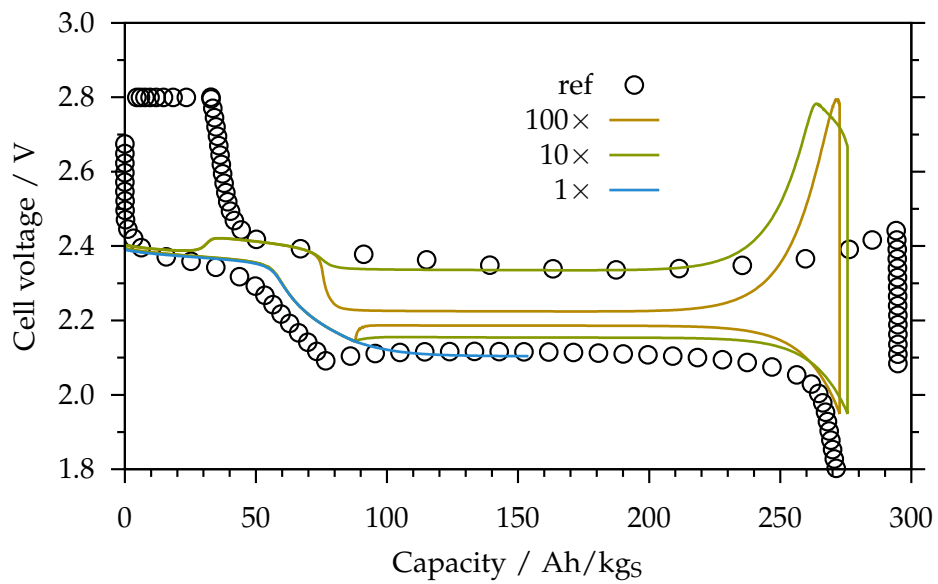


Figure 5.17: Parameter variation: Speeding up or slowing down electrochemical reactions. The legend indicates the common scaling factor which is applied to all electrochemical rate constants uniformly.

It is arguably unlikely that the global optimum of the 26-dimensional parameter space can be found this way. Also, it is obvious from the results that the match is indeed still far from perfect. Nevertheless, this multi-step, hierarchical fitting process allows for a systematical and deterministic calibration of the model with the limited set of reference data available.

Table 5.2: Parameters adjusted to match experimental results in the calibrated multi-step model. See Tab. A.7 on page 152 for a comprehensive list of all parameters used for the simulations.

Cathode volume fractions ε_n		
S ₈	0.04140	
Li ₂ S	0.00120	
Li ₂ S (passive)	0.10549	
carbon	0.03248	
binder (SBR)	0.02800	
electrolyte	0.69143	
void (Ar)	0.10000	
Surface areas A_0		
carbon electrolyte	$1.1 \cdot 10^7 \text{ m}^2 \cdot \text{m}^{-3}$	
S ₈ electrolyte	$1.4 \cdot 10^6 \text{ m}^2 \cdot \text{m}^{-3}$	
Li ₂ S electrolyte	$1.2 \cdot 10^6 \text{ m}^2 \cdot \text{m}^{-3}$	
Area-specific capacity C_{dl}		
carbon electrolyte	$0.2 \text{ F} \cdot \text{m}^{-2}$	
lithium electrolyte	$0.2 \text{ F} \cdot \text{m}^{-2}$	
Surface resistivity expression Eq. (4.26)		
r_{carbon}	40 nm	
ξ_1	5.0 nm	
ξ_2	$1.9 \cdot 10^9$	
Gibbs free energy g_0 of dissolved species and initial concentrations ²		
Li ⁺	$0.0 \text{ kJ} \cdot \text{mol}^{-1}$	$1.50 \text{ mol} \cdot \text{l}^{-1}$
TFSI ⁻	non-reactive	$1.00 \text{ mol} \cdot \text{l}^{-1}$
NO ₃ ⁻	non-reactive	$0.50 \text{ mol} \cdot \text{l}^{-1}$
S ²⁻	$-309.7 \text{ kJ} \cdot \text{mol}^{-1}$	$6.19 \cdot 10^{-25} \text{ mol} \cdot \text{l}^{-1}$
S ₂ ²⁻	$-354.1 \text{ kJ} \cdot \text{mol}^{-1}$	$3.65 \cdot 10^{-19} \text{ mol} \cdot \text{l}^{-1}$

²Note: The concentration of Li⁺ is not exactly $1.50 \text{ mol} \cdot \text{l}^{-1}$, but equal to the total concentration of negatively charged ions to the 10th digit.

S_4^{2-}	$-416.8 \text{ kJ} \cdot \text{mol}^{-1}$	$2.12 \cdot 10^{-7} \text{ mol} \cdot \text{l}^{-1}$
S_6^{2-}	$-432.2 \text{ kJ} \cdot \text{mol}^{-1}$	$7.16 \cdot 10^{-4} \text{ mol} \cdot \text{l}^{-1}$
S_8^{2-}	$-441.9 \text{ kJ} \cdot \text{mol}^{-1}$	$2.92 \cdot 10^{-1} \text{ mol} \cdot \text{l}^{-1}$
$S_{8(\text{ds})}$	$19.0 \text{ kJ} \cdot \text{mol}^{-1}$	$9.38 \text{ mol} \cdot \text{l}^{-1}$

Reactions, forward rate constants

$S_{8(\text{s})} \rightleftharpoons S_{8(\text{ds})}$	$3.0 \cdot 10^{-4} \text{ mol} \cdot \text{m}^{-2} \cdot \text{s}^{-1}$
$\frac{1}{2}S_{8(\text{ds})} + e^- \rightleftharpoons \frac{1}{2}S_8^{2-}$	$4.0 \cdot 10^{14} \text{ mol} \cdot \text{m}^{-2} \cdot \text{s}^{-1}$
$\frac{3}{2}S_8^{2-} + e^- \rightleftharpoons 2S_6^{2-}$	$4.0 \cdot 10^{14} \text{ mol} \cdot \text{m}^{-2} \cdot \text{s}^{-1}$
$S_6^{2-} + e^- \rightleftharpoons \frac{3}{2}S_4^{2-}$	$4.0 \cdot 10^{14} \text{ mol} \cdot \text{m}^{-2} \cdot \text{s}^{-1}$
$\frac{1}{2}S_4^{2-} + e^- \rightleftharpoons S_2^{2-}$	$4.0 \cdot 10^{11} \text{ mol} \cdot \text{m}^{-2} \cdot \text{s}^{-1}$
$\frac{1}{2}S_2^{2-} + e^- \rightleftharpoons S^{2-}$	$4.0 \cdot 10^{14} \text{ mol} \cdot \text{m}^{-2} \cdot \text{s}^{-1}$
$2 \text{ Li}^+ + S^{2-} \rightleftharpoons \text{Li}_2S_{(\text{s})}$	$3.2 \cdot 10^{12} \text{ mol} \cdot \text{m}^{-2} \cdot \text{s}^{-1}$

Molar Gibbs free energy g_0 of Li_2S : $-429.7 \text{ kJ} \cdot \text{mol}^{-1}$

Density of the liquid electrolyte ρ_{elyte} including dissolved species: $1535 \text{ kg} \cdot \text{m}^{-3}$

Diffusion constant D_n (for all dissolved species): $1.0 \cdot 10^{-11} \text{ m}^2 \cdot \text{s}^{-1}$

5.4 Multi-step model – validation attempts

Having determined all parameters of the model, an attempt is made to perform an initial validation. This measure is not to be confused with a regression model validation used e.g. for equivalent circuit models. A rigorous stochastic validation is not possible in this case for two reasons: First, practically, the data base available for validation is not sufficient to achieve a reasonable significance: Only experimental data not previously used for the parametrization may be employed for the validation. Also, neither the very best (or worst) performing cells, nor the first few cycles of any cell are used for the validation, since they are believed to be less representative. Second, fundamentally, the need to evaluate both the correctness of the assumed reaction mechanism and the set of parameters at the same time, poses fundamental limits to a mathematically sound validation.

Instead, simulation results are visually compared to corresponding experimental data and checked for plausibility, taking into account the considerations on model accuracy outlined in section 4.3.3.

5.4.1 Rate capability

In Fig. 5.18, simulation results are compared to the experimental data presented in Fig. 3.23, where one cell is discharged at subsequently increasing rates. For technical reasons, the cycling protocol for the simulation uses more restrictive charge and discharge cutoff voltages (1.95–2.7 V) than the experiment (1.5–2.8 V). Especially at the end of discharge, when the remaining active surface area of the cathode approaches zero, the calculation time would otherwise increase disproportionately even though very little charge is actually transferred. Experimentally, the larger voltage window is required to access more strongly bound sulfur that would otherwise stick to e.g. functional groups on the carbon surface or other impurities [67]. Also, note that in the experimental data, some degradation does occur from cycle to cycle, which is not the case for the simulated data. Additionally, an almost quasistatic discharge is simulated at a very low rate of approx. C/1000, representing the thermodynamics of the system.

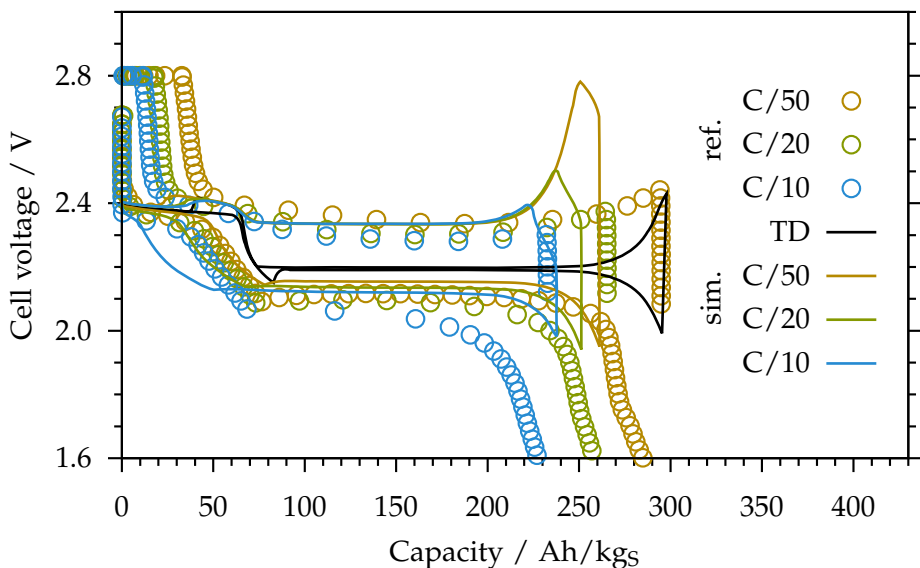


Figure 5.18: Simulated discharge profiles at various rates compared to experimental results. While there is no quantitative match, the simulations clearly reproduce the correct trend. TD: Thermodynamic, i.e. quasistatically slow discharge.

There is no full agreement between the experimental and simulated data: the increasing overpotential toward the end of discharge is reflected well, as is the decreasing discharge voltage. The charge plateau is matched correctly, even though the experimental data exhibits a little variation. Also, the shift of the onset of the lower voltage plateau and the disappearance of the voltage overshoot right before the plateau are faithfully reproduced. For three major features, however, the agreement is rather poor:

While the shape of the transition region between the upper and lower voltage plateaus during discharge does change with increasing rate, the effect is significantly overestimated by the model. A possible explanation is that the model does not include any disproportionation reactions, which could greatly speed up effective reaction rates. Due to the parallel reaction pathways, “bottlenecks” in the linear chain of electrochemical reduction reactions can be circumvented, lowering the reaction overpotential and thereby mitigating the impact of higher discharge rates.

The second discrepancy concerns the voltage profile at the end of charge, which is not even qualitatively reproduced by the simulations. Where the voltage starts to rise steeply in the experiments, hitting the charge cutoff voltage, it levels off or even decreases slightly in the simulations. While there is no plausible explanation for this behavior from a chemical point of view, this effect is technically related to the increasing active surface area available for the precipitation of S_8 , cf. Eq. (4.24). The voltage does reach the charge cutoff voltage eventually (data not shown). However, this only happens if the cell is considerably overcharged, until the electrolyte becomes depleted of polysulfides, as is the case with the multi-step model before reparametrization, compare Figs. 5.7a and 5.8.

The third debatable feature is the loss of discharge capacity with increasing rate. The effect is present in the simulations, albeit greatly underestimated. This leads to the question whether the end of discharge is actually exclusively triggered by surface passivation, as suggested by the simulations. One possible explanation for this discrepancy would be that the mean pore size is actually smaller than suggested by the electrode’s global porosity. If there are many very small pores, clogging might play a significant role despite the large total pore volume. A pore size distribution analysis could help to clarify this issue; such data is not available for the reference cells, though.

5.4.2 Cyclic voltammetry

Furthermore, a cyclic voltammetry run is simulated and analyzed. The experiment presented in Fig. 3.16a is used as reference. The results are plotted in Fig. 5.19. Note that this plot follows the usual convention of assigning a positive current to the anodic sweep (charge) and a negative current to the cathodic sweep (discharge). As for the rate capability plot, there is no quantitative match. Still, the simulation reproduces the main features of the experiment qualitatively very well: The discharge sweep is separated into two peaks, the upper one smaller, the lower one larger, corresponding to the upper and lower voltage plateau during a regular galvanostatic discharge. The charge sweep is composed of only one peak.

Still, there are three obvious differences: First, the total area under the curve (equal to the total charge transferred) does not match. This is easily explained, since the

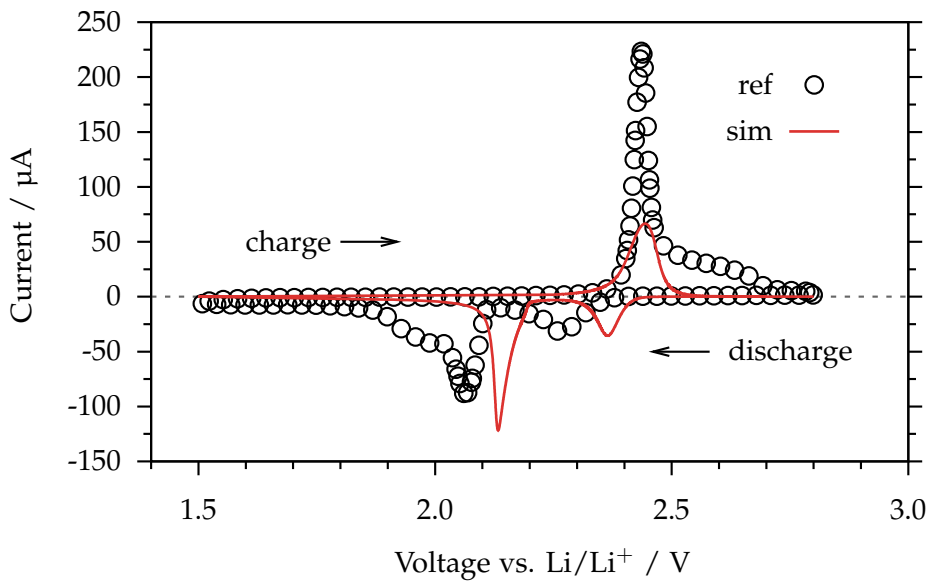


Figure 5.19: Cyclic voltammetry data compared to experimental results. Sweep rate: $25 \mu\text{V} \cdot \text{s}^{-1}$.

experimental data was recorded from a cell of a different batch than the data used for calibration. The performance of that batch was slightly better, therefore the total capacity of the reference cell is expected to be larger. Second, the position of the cathodic peaks is shifted compared to the reference, which most likely can be explained by a flaw in the calibration already discussed above: It is impossible to obtain experimental data of a quasistatically slow galvanostatic discharge. Lacking more precise information about the composition of the overpotential, the thermodynamics were calibrated using the midpoint between the charge and discharge voltage of a finitely fast discharge in Fig. 5.13. The thermodynamically correct voltage, however, is possibly off-center and indeed, judging based on Fig. 5.19, this seems to be the case for this system. Third, the shape of the peaks does not match precisely. In the experimental data set, both the charge peak and the lower discharge peak extend into a “tail”, blurred over several hundred mV. As already mentioned in the discussion of Fig. 5.18, these tails are most likely caused by sulfur that is more strongly (chemically) bound to the electrode matrix and thus only accessed at higher overpotential during both charge and discharge – a phenomenon which is not included in the model.

5.5 Multi-step model – further simulations

In the following sections, full-cell simulations with the reparametrized model are presented, illustrating various aspects of the simulated type of Li/S battery in detail.

5.5.1 Galvanostatic charge/discharge profiles

In the previous section, the parameter space was reduced to a single set of values in order to match a single set of experimental data, mostly recorded from a single cell. Some of the parameters – called type a) parameters in section 4.3.2 – represent natural constants and are valid for all simulations. Others – called type b) parameters – are only valid for a certain cell configuration or even only for a single cell. Changing those values is the computational equivalent to building a different cell. In the following simulation, the parametrization of the sulfur electrode is changed to represent different activation efficiencies, which can be achieved experimentally e.g. by smaller Li_2S particles or improved activation protocols, cf. section 3.2.3. The results are plotted in Fig. 5.20 for four different activation efficiencies, represented by different ratios of active to passive Li_2S . It is assumed that the morphology is not affected, i.e. the active surface area scales linearly with the amount of accessible Li_2S .

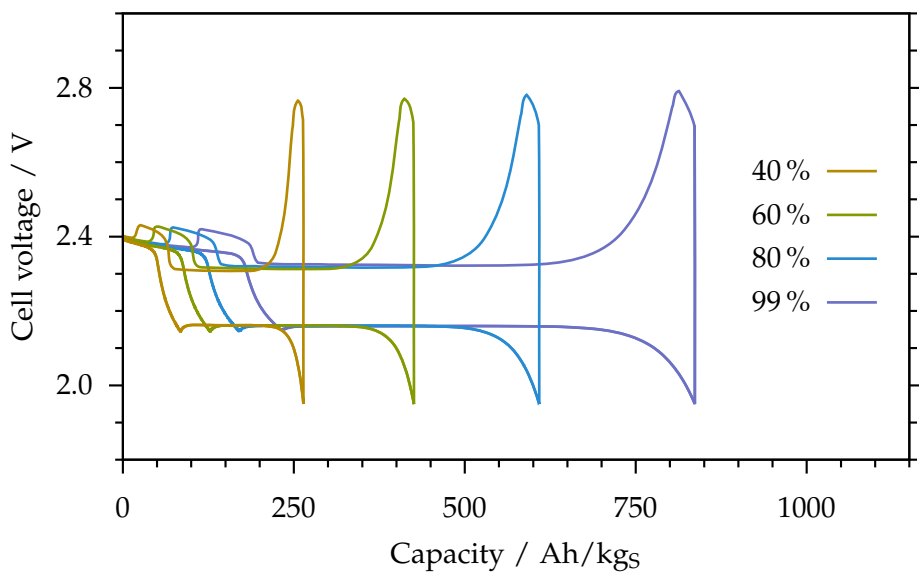


Figure 5.20: Voltage profiles of differently activated Li/S cells cycled at the same rate. The activation efficiency, i.e. the fraction of activated, electrochemically accessible Li_2S , is indicated by the plot key.

As expected, the discharge capacity increases with increasing activation efficiency. Other than that, the shape of the voltage profile is almost not affected. An interesting

result is that even at 99 % activation, the cell still only delivers about half of the theoretical capacity of 1675 Ah/kgs. In order to access the remaining capacity, changes to the electrode design are needed, preventing the passivation of the carbon | electrolyte interface by film formation, which eventually causes the premature end of discharge. One such measure could be to increase the carbon content in the electrode. Not surprisingly, carbon contents of 40–50 % of the positive electrode’s dry weight are often reported in experimental literature [62]. Another approach would be to prevent the formation of the film altogether, e.g. by preventing the dissolution of polysulfides in the liquid electrolyte as discussed in section 2.1.

5.5.2 Transport

Transport in the liquid electrolyte is difficult to analyze experimentally. Using the model, however, it can be studied easily by looking at the concentration of dissolved species or the distribution of solids across the cell during discharge. To begin with, the evolution of solids in the positive electrode is shown in Fig. 5.21.

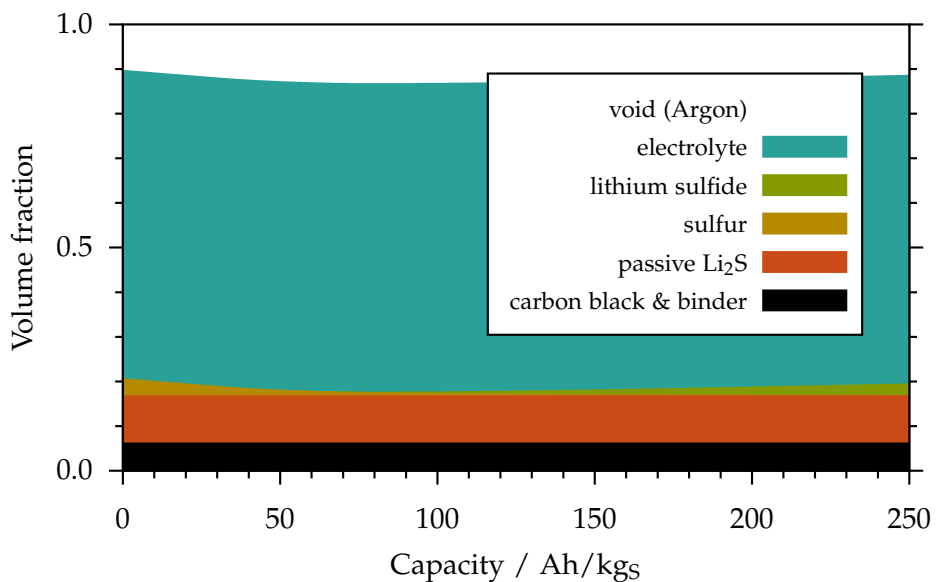


Figure 5.21: Evolution of the average volume fractions of all phases in the positive electrode during a C/50 discharge. For the cell design presented here, only a small fraction of the electrode’s volume is actually affected.

Compared to Fig. 5.3, which presents similar results for a much less porous cell, the changes to the volume fractions appear much smaller. Only a few percent of the total volume change during the entire cycle. Another interesting feature of this cell is that a considerable fraction of the sulfur is not present in the solid form during the entire cycle. The ratio of active to passive sulfur for this cell is 2:3 (see above). Even in the

fully charged or discharged state, only about half of the sulfur is precipitated. While this cell design is not suitable for commercialization, it is perfectly apt for the scientific study of the Li/S system. As discussed below, this cell design does not suffer from pore clogging, exhibits only very small diffusion overpotentials, and provides good access to the liquid electrolyte for the entire activated Li_2S . The large amount of passive weight does not restrain the study of the system either physically or computationally. Except for the different absolute and relative amounts of the phases, the results are very similar to those presented in Fig. 5.6b and the corresponding discussion on pages 98–99 is still fully valid for the calibrated model.

The dissolution and precipitation of solids presented in Fig. 5.21 is tightly coupled to the distribution of dissolved species in the liquid electrolyte, which shall be analyzed next. To this, the average concentrations of dissolved species and their evolution during a discharge/charge cycle are presented in Fig. 5.22. It is apparent from Fig. 5.22 that the concentrations of the various species are different by orders of magnitude.

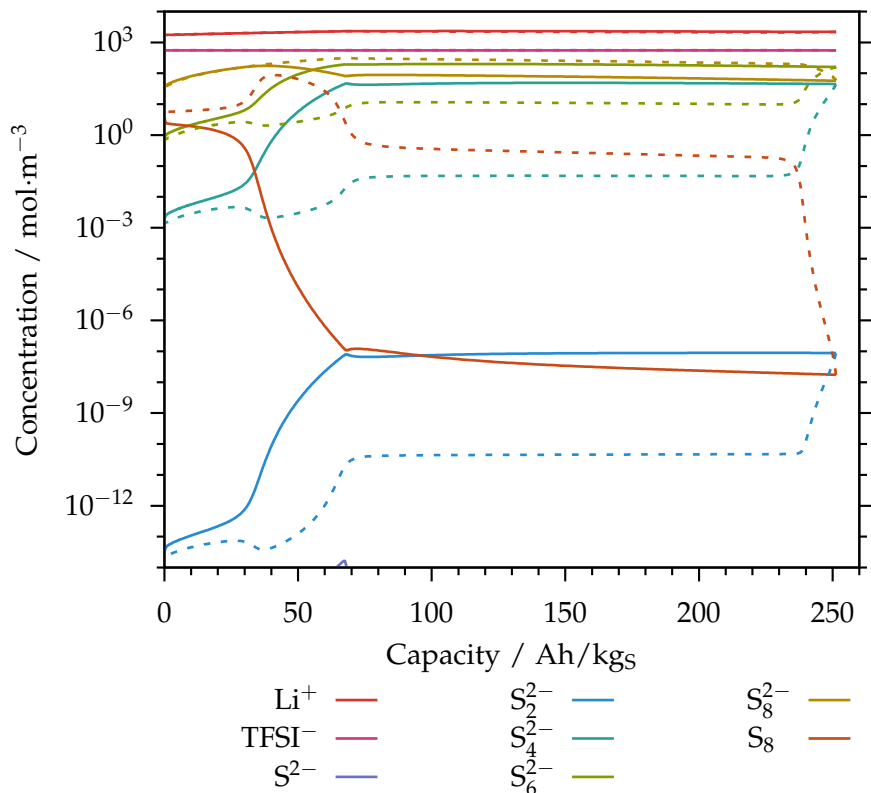


Figure 5.22: Evolution of the concentrations of dissolved species during charge (dashed lines) and discharge (solid lines) at a C/20 rate. The concentration of S^{2-} is so low that it is entirely outside the plot range.

Li^+ is most concentrated because it serves as the counter ion for all other charged species. Its concentration peaks at several $\text{mol} \cdot \text{m}^{-3}$, which is easily dissolved by the ionic liquid based electrolyte. All polysulfides S_x^{2-} with $x < 8$ get more concentrated during discharge and less concentrated during charge. The opposite is true for $\text{S}_{8(\text{ds})}$ and S_8^{2-} which get depleted during discharge and replenished during charge. Especially the concentration of $\text{S}_{8(\text{ds})}$ (orange line in Fig. 5.22) changes dramatically from its saturation concentration at around $4 \text{ mol} \cdot \text{m}^{-3}$ to a mere $10^{-8} \text{ mol} \cdot \text{m}^{-3}$. The concentration of S_2^{2-} and especially S^{2-} stays very low during the entire cycle. This is a major improvement over the initial literature parametrization, since the results are consistent with experimental findings, namely the fact that these two species are virtually insoluble in common electrolytes [133, 141].

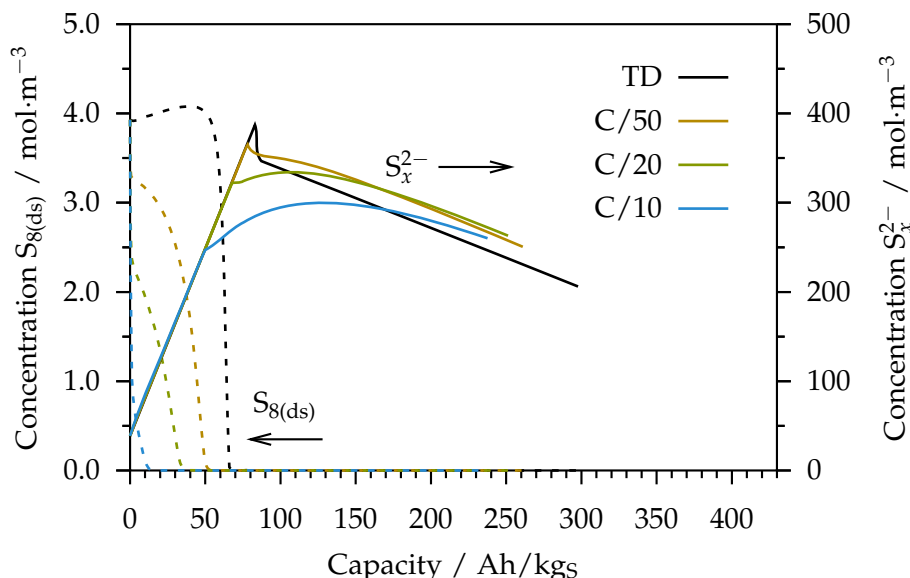


Figure 5.23: Concentrations of $\text{S}_{8(\text{ds})}$ (dashed lines) and all S_x^{2-} polysulfide ions (solid lines) during discharge for four different rates. TD: Thermodynamic, i.e. quasistatically slow discharge.

While Fig. 5.22 contains lots of information, its interpretation is not straightforward. Therefore, only the concentration of $\text{S}_{8(\text{ds})}$ and the sum of all polysulfide ions (solid lines) are plotted in Fig. 5.23, this time for different discharge rates. This plot illustrates the situation in the liquid electrolyte of a Li/S cell much more clearly than Fig. 5.22. The concentration of $\text{S}_{8(\text{ds})}$ represents the source of new sulfur species. For the quasistatic discharge, at a rate of approx. C/1000, it is buffered by the presence of solid S_8 and only decreases (but sharply so) once all accessible sulfur is dissolved. The higher the discharge rate, the lower the concentration of $\text{S}_{8(\text{ds})}$. As long as there are significant amounts of dissolved $\text{S}_{8(\text{ds})}$, the production of new dissolved species by dissolution can

at least keep up with the consumption by electrochemical reduction. Hence, there is a constant flow of sulfur in its highest oxidation state into the electrolyte, stabilizing a steady-state equilibrium, which in turn results in a constant cell voltage. If the reduction is much faster than the dissolution, the steady-state value for the concentration of $S_{8(ds)}$ is close to zero. More sulfur may still enter the system, but it will be reduced almost immediately. In that situation, the voltage decreases continuously as does the average oxidation state of the dissolved S_x^{2-} polysulfide species. As indicated by the solid lines in Fig. 5.23, their concentration increases more than fourfold during the first half of the discharge. This increase is fueled by both the dissolution of solid sulfur and the subsequent reduction of S_x^{2-} species producing shorter, but also more numerous molecules. Once no more sulfur dissolves into the electrolyte (or only at comparatively low rates, see above), the total concentration of polysulfides levels off. The continuous precipitation of Li_2S from the electrolyte is balanced by the progressive reduction of longer S_x^{2-} species down to S_4^{2-} . The shorter polysulfides are very short lived; they are fully reduced to S^{2-} and rapidly precipitate as solid Li_2S . Later during the discharge, when less longer species are available, most reduction products precipitate immediately, reducing the total amount of dissolved polysulfides. Depending on the discharge cutoff voltage, the total concentration may either become as low as that of a fully charged cell or remain close to the plateau level. Only for the quasistatically slow discharge the plateau does not exist, since the ratio of each pair of S_x^{2-} species is always equilibrated, i.e. constant. Therefore, each electron extracted from the system directly lowers all concentrations simultaneously, in the end precipitating $1/16$ molecule of S_8 per electron. As outlined by the above discussion, Fig. 5.23 contains the most relevant information about the liquid electrolyte system, which is also confirmed by various experimental characterization techniques, see e.g. Ref. [P4].

Next, the distribution along the y -axis (MEA cross section) of the cell is analyzed. Here, the concentration of Li^+ is plotted. Since Li^+ is the only cation in the model, its flux is directly proportional to the ionic current in the cell. The y -profiles represent different stages during the discharge, as indicated by the markers in Fig. 5.24.

It is obvious from Fig. 5.25 that there is little to no change in the concentration of Li^+ across the cell. The average concentration increases significantly during the first half of the discharge and decreases steadily thereafter, as discussed above, on the basis of Fig. 5.23. Even when the change is fastest, i.e. in the transition region between the upper and lower voltage plateau and at the end of discharge, the concentration gradient is hardly discernible. It amounts to only a few percent across the entire cell, less than 1% across the cathode. Because of charge neutrality, the gradient of negatively charged species is equally small. What is more, this is also true for the individual gradients of the soluble S_x^{2-} species, i.e. $x > 2$ (data not shown). While

the concentrations and volume fractions may change greatly during cycling, there is virtually no spatial variation across the electrode, which means that all active material can be accessed easily.

5.5.3 Impedance

Electrochemical impedance spectra simulated at different SoC are presented in Fig. 5.26. Starting from a fully charged cell, a regular galvanostatic discharge is simulated and stopped at different SoC. The cell is put to rest (i.e. $i_{\text{tot}} = 0$) for 15 min. before the spectra are simulated using the step excitation technique described in section 4.3.1 and analyzed in the frequency range of 1 mHz–1 MHz.

The spectra simulated at different SoC look qualitatively rather different. Given that the composition of the sulfur electrode is very different, as are the prevalent electrochemical reactions, this does not come as a surprise. At the very beginning, but especially at the end of discharge, a long “tail” is apparent, related to the high overpotentials seen in the charge/discharge profiles. Other than that, one large semi-cycle dominates the appearance of the Nyquist plots. A smaller cycle is discernible in the high-frequency region of some spectra which is associated with the lithium | electrolyte interface at the negative electrode.

Because of the volatility of the experimental measurements, the spectra could not be truly validated. The trend, however, is similar to that observed experimentally for the cells presented in section 3.2.4: The charge transfer resistance is smallest at medium SoC, i.e. at the end of the upper and beginning of the lower voltage plateau. As already discussed on the basis of Fig. 5.9, this can be attributed to the high concentrations of dissolved Li^+ and S_x^{2-} ions in the electrolyte. The cell could not fully relax to OCV within 15 min. in the transition region and at the end of discharge. The appearance of the corresponding spectra does depend on the relaxation time to some degree (data not shown), but the general behavior as described above is ubiquitous.

Regardless of the precise values, these results indicate that the spectra are highly sensitive to the internal state of the battery. Thus, EIS could prove to be a powerful tool for SoC and SoH analysis in Li/S batteries.

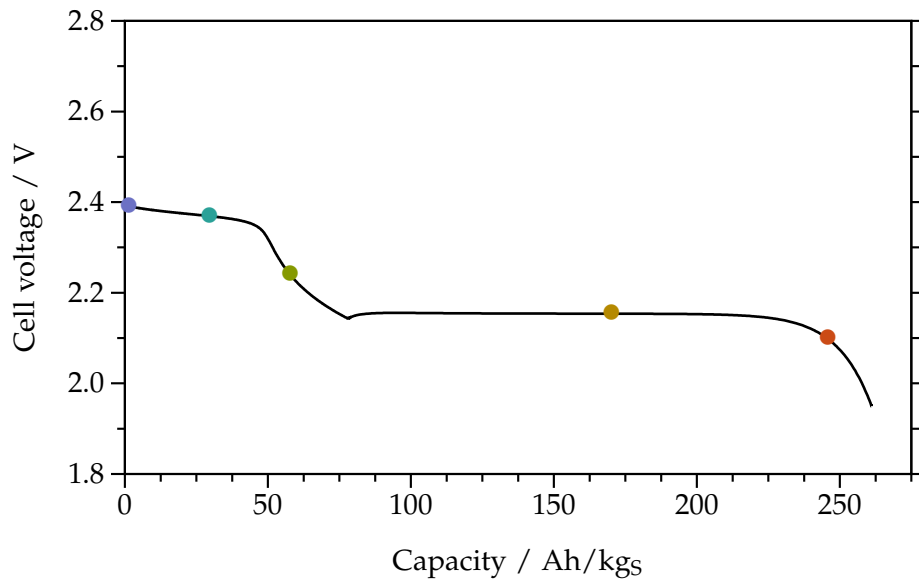


Figure 5.24: Overview of the discharge analyzed in Figs. 5.25 and 5.26. The nominal discharge rate is C/20.

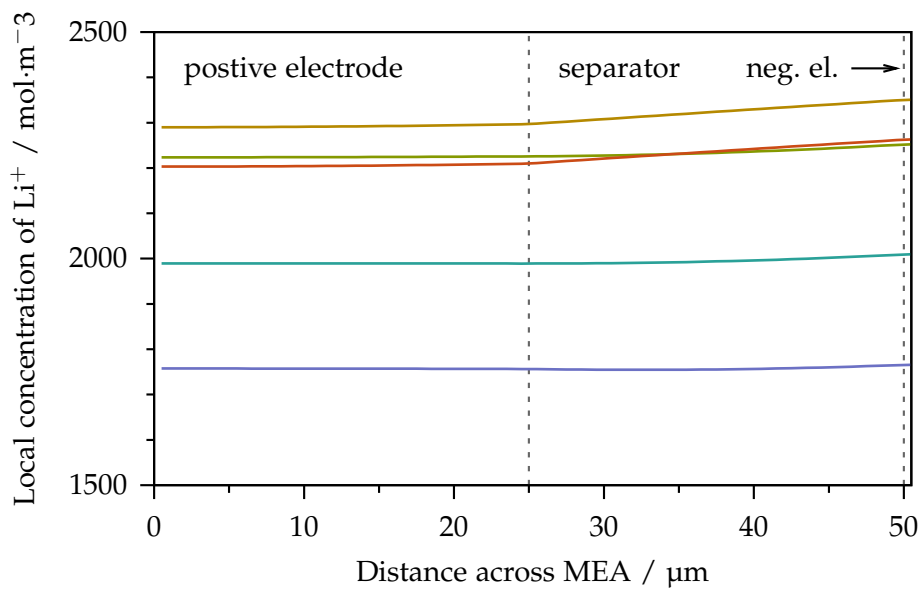


Figure 5.25: Concentration of Li^+ across the cell at different times during a discharge. Colors indicate the time each profile was simulated, see Fig. 5.24.

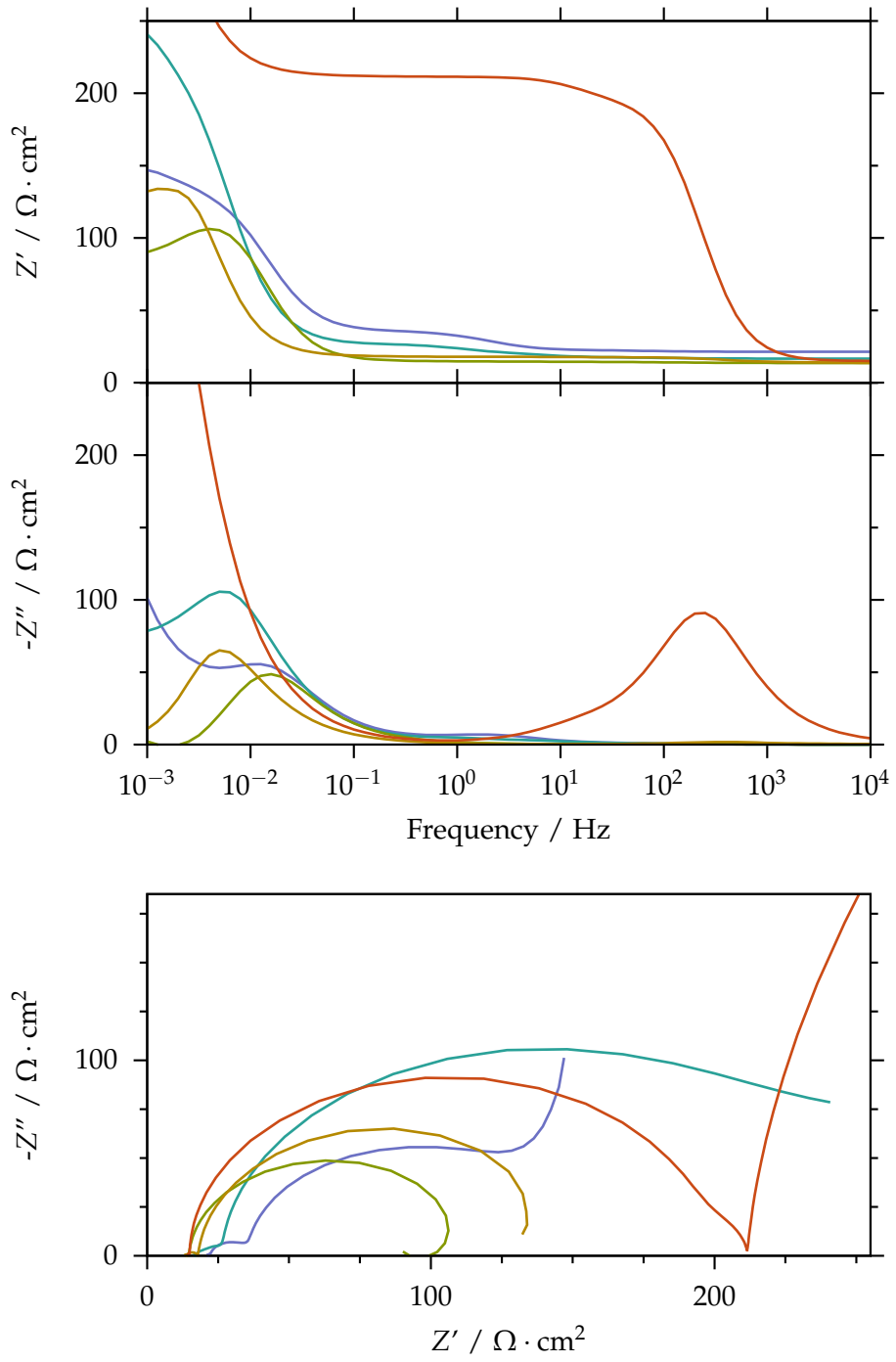


Figure 5.26: Electrochemical impedance spectroscopy during cycling. Upper panels: Bode representation. Lower panel: Nyquist representation. Simulated frequency range: 1 mHz–1 MHz. Colors of the spectra indicate the time the spectrum was simulated, see Fig. 5.24 on the previous page. The tail of the orange spectrum, simulated at the very end of discharge, ends outside the plotted area at approx. $(400 + 600i) \Omega \cdot \text{cm}^2$.

5.5.4 Microstructure

Since the model does not include an explicit description of the microstructure, the following section is rather short. The composition of the cell was already analyzed in section 5.5.2 above. Besides the trivial expressions in Eqs. (4.24) and (4.25), representing the S_8 | electrolyte and Li_2S | electrolyte interfaces, there is only one feature in the model dealing with the microstructure: the formation of a passivating Li_2S film on the positive electrode's carbon matrix. This film is studied in Fig. 5.27.

Once Li_2S starts to precipitate, the film grows almost linearly with time, reaching close to 10 nm at the end of discharge. This nicely matches the experimental findings presented in Fig. 3.8d on page 43. The film thickness cannot be measured directly in the SEM images, but it can be estimated: The smallest structures visible in the electrode without the film (Fig. 3.8c) are about 20 nm across. After deposition of the film, the smallest structures are about 100 nm in size. This means that the precipitated Li_2S can fill gaps of several tens of nanometers, but not hundreds. Therefore, a thickness 10 nm, as suggested by the simulations, is within the right order of magnitude.

In contrast to the film thickness, its resistivity does not grow initially, but remains very small as long as the film is thinner than the threshold set by ξ_2 in Eq. (4.26). Beyond that value, the resistivity increases sharply, causing a correspondingly high overpotential toward the end of discharge.

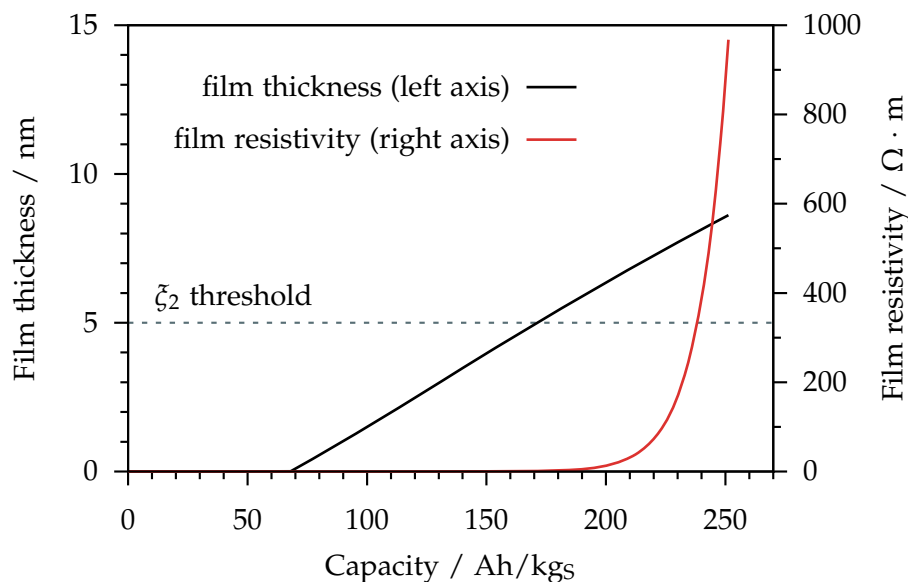


Figure 5.27: Thickness of the Li_2S film on the carbon matrix in the positive electrode and corresponding resistivity during a C/20 discharge.

5.6 Multi-step model – polysulfide shuttle extension

In this section, the cycling performance and degradation of the cell are analyzed, taking into account the polysulfide shuttle as described in section 4.2.7. Implementation and effects of the polysulfide shuttle model are discussed in detail in Ref. [P3], where this mechanism was applied to a simplified model of the Li/S battery.

The calibration performed in Ref. [P3], however, is not valid for the multi-step model, since the reaction mechanism for the polysulfide reduction/oxidation is different, as are the geometry and composition of the cell. For the cell described by Ref. [P3], the model predicts that the solid part of the negative electrode is composed of approximately 25 vol.-% Li_2S after only three cycles. For the cells used in this work, the amount deposited on the lithium surface is much smaller, as affirmed by SEM images and EDX spectra of electrodes examined after cycling, see Fig. 5.28. Small amounts of sulfur are not detected by EDX, especially at low exposures (as indicated by the total number of counts in Fig. 5.28). Still, to keep the sulfur content in the negative electrode below the EDX detection limit of $\sim 2\%$ even after 200 cycles, no more than one ppm of Li_2S may be deposited during each cycle.

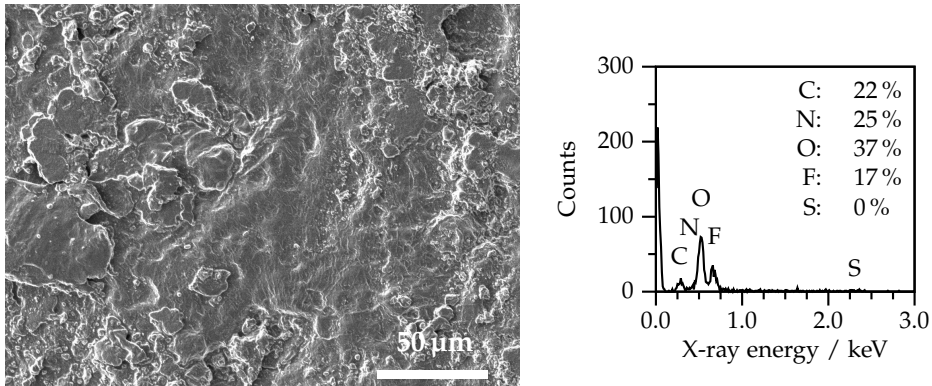


Figure 5.28: Left: SEM micrograph of a lithium electrode removed from a Li/S cell after 200 cycles. Magnification: 500 \times . The electrode's surface is more rough than the pristine Li foil, but no large depositions or even dendrites are present. Right: EDX spectrum of the same area, indicating considerable amounts of electrolyte decomposition products, but no signs of sulfur or Li_2S . Note that Li does not show up in the EDX spectra, cf. section 2.4.1.

Therefore, the additional parameters needed for the shuttle and degradation mechanism are not identical to Ref. [P3]. Neither are they calibrated, but simply assumed so that they result in a clearly visible effect, while not contradicting experimental findings. To achieve this, the precipitation rate is chosen identical to the positive electrode. This rate is rather fast, so that virtually all S^{2-} formed in the negative electrode is

precipitated in place. The CTR rate was lowered subsequently until the rate of Li₂S formation was slow enough, so that the above-mentioned one ppm per cycle is not exceeded. The values of the additional parameters are listed in Tab. 5.3.

Table 5.3: Additional parameters for the polysulfide shuttle model.

Reaction rate scaling factors ξ_q	
ξ_{CTR}	$2.5 \cdot 10^{-22}$
ξ_{precip}	1.0
Initial anode volume fractions ε_n	
Lithium	0.37
Li ₂ S	0.00
Electrolyte	0.63

With this parametrization, the effect on discharge and charge profiles is presented in Fig. 5.29. The overall shape of the profiles is not strongly affected, except for the position of the end of charge: The steep voltage rise that usually triggers the end of charge is shifted to the left on the capacity axis, way into the negative range: More charge is transferred into the cell than extracted in either the previous or the following discharge half-cycle. This is possible because the shuttle mechanism allows the cell to accept charge without changing the SoC.

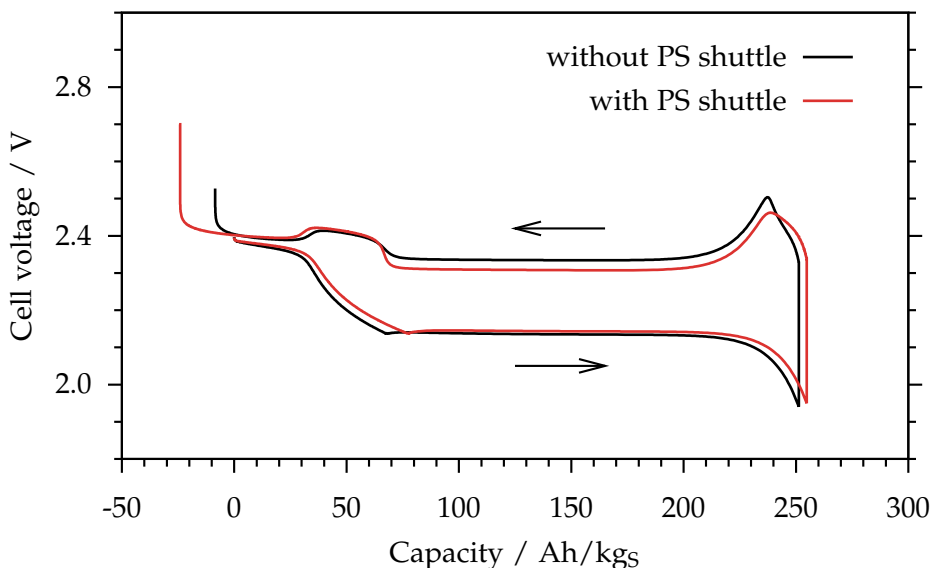


Figure 5.29: Effect of the polysulfide shuttle on discharge/charge profiles. Note that the capacity axis extends below zero, since more charge is transferred into the cell than extracted in the previous discharge.

The loss in Coulombic efficiency may be tolerable for some applications, but there is also a loss of active material. Unlike the reversible capacity decay discussed in section 5.1, this effect cannot be easily recovered by reasonably slow refresh cycles or CCCV charging (data not shown). Instead, the deposition of Li_2S on the negative electrode is practically irreversible. While technically, the reaction is implemented reversibly, the backward reaction does not proceed at a significant rate because it would require the oxidation of S_x^{2-} directly above the highly reducing lithium surface. Fig. 5.30 presents the simulated evolution of Li_2S during the first ten cycles. The amount of Li_2S formed is influenced by the relative rates in Tab. 5.3 (data not shown), but the formation of Li_2S per se is inevitable. For the cell simulated here, it takes several cycles to accumulate a few ppm of Li_2S . While this does not sound like a large amount, it causes the SoH to decrease at a slow, but steady rate. Additionally, the formation of a passivating layer of Li_2S on the lithium surface may affect the cell performance long before a significant fraction of the total sulfur is lost. Lacking fundamental information about other degradation modes in the cell, it could not be determined whether or not this effect contributes significantly to the capacity fade, neither could the ultimate cause for the experimentally observed degradation be identified.

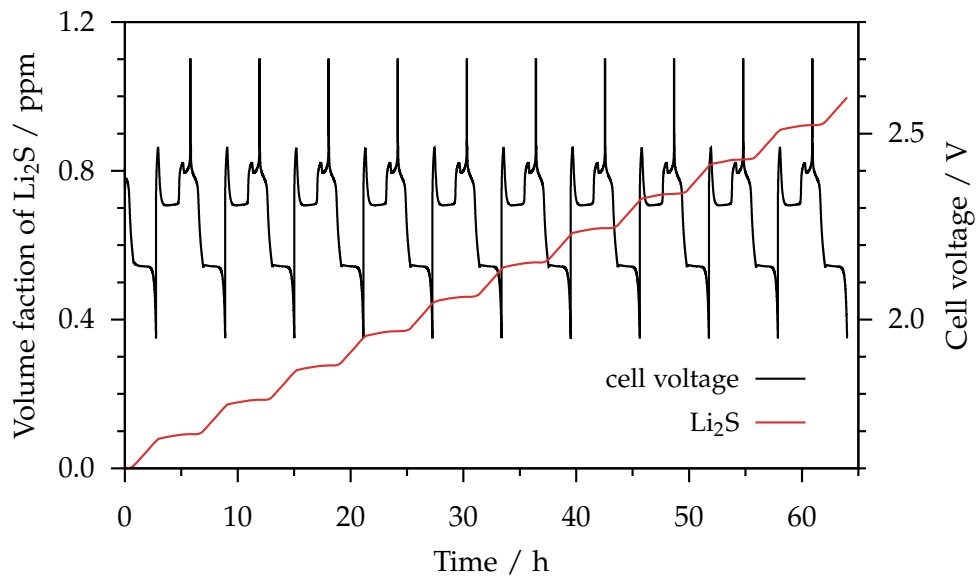


Figure 5.30: Evolution of the amount of Li_2S deposited at the negative electrode.

Besides analyzing one possible mode of degradation of the Li/S battery, the above section also illustrated that additional effects can be implemented easily in the existing modeling framework, potentially enabling the study of many interesting electrochemical effects in the Li/S cell.

5.7 Conclusions

5.7.1 Achievements

First of all, it is a major methodological achievement of this work to enable simulations of all relevant electrochemical techniques with just one consistent set of physically-based governing equations and one authoritative set of parameters. This is an accomplishment completely novel to the domain of Li/S batteries; even many established chemistries lack such a capable model.

Regarding the simulations, transport phenomena and charging modes of the cell were studied in section 5.1, on the basis of charge/discharge profiles and cycling plots obtained from the simplified global two-step model. Results of the more detailed multi-step model were introduced in section 5.2, with a parameter set obtained primarily from Ref. [196], and other pre-existing literature. The results include charge/discharge plots, also at different rates, as well as concentration profiles of lithium ions and polysulfide species during cycling. In addition, impedance spectra of the cell at various SoC were presented. Based on the evolution of solids in the positive electrode, the two voltage plateaus during discharge could be explained conclusively. In section 5.3, we could show that a rigorous calibration of the model in its present form is possible and meaningful, using data available from literature as well as data recorded experimentally. A highly selective determination of individual parameters could be achieved, since various key features of the charge/discharge profiles and impedance spectra are very sensitive to certain physical parameters of the model, e.g. the hysteresis of the plateau voltages, the onset and slope of the transition region between the voltage plateaus, or the high-frequency intercept of the impedance spectra, among others. The simulation results obtained from the calibrated multi-step model are considered plausible and could be partly validated in section 5.4. Even though discrepancies remain (see below), the model enables a thorough discussion of the charge and discharge behavior, cyclic voltammetry profiles, and electrochemical impedance spectra at different stages during the discharge. We could show what the performance would look like for different formation efficiencies, i.e. different fractions of activated Li_2S . In addition to reproducing experiments, many properties of the battery can be studied, which are not easily accessible to the experiment: for example, the volume changes in the positive electrode were analyzed and put in relation to the concentrations of dissolved polysulfides in section 5.5. The concentration of Li^+ across the cell was studied at different SoC. Finally, the model can assist with the interpretation of reversible and irreversible cell degradation. New reactions or effects can be accommodated easily in order to quickly study phenomena like the polysulfide shuttle or various degradation modes. Even though the accuracy of such studies cannot be ex-

pected to be very good without extensive validation, the model can promptly indicate trends and major effects.

5.7.2 Shortcomings

As discussed above, the model does not match the experimental results perfectly. Actually, it does not match nearly as well as a typical fitted equivalent circuit, cf. for example Refs. [182, 262, 263]. Also, as discussed in section 5.4, it falls short of explaining certain phenomena even qualitatively:

- The end of charge looks very different from experimental results for typical experiments, see e.g. Fig. 5.18. It also looks different from the simulations presented in section 5.2, compare e.g. Figs. 5.7a and 5.20. Since the voltage rise at the end of charge is of purely kinetic origin, an explanation might be that there are different reaction mechanisms in place for charge and discharge, which are not considered separately in the model.
- The end of discharge does not depend on the discharge rate as much as it should, see Fig. 5.18. This is a strong indication that there are actually more effects triggering the end of discharge than accounted for in the model.
- The voltage overshoot at the beginning of the charging half-cycle is considerably larger for the simulation than for the experimental reference data, see e.g. Fig. 5.13. This is a strong indication that the precipitation and dissolution of Li₂S, which is the root cause of the high overpotential, is not represented well by the single, symmetrical, non-electrochemical reaction in the multi-step model.
- Probably the most severe limitation of the model is that the reaction mechanism itself is not truly validated. Quite the contrary, it is known to be incomplete and some studies suggest that at least parts of the mechanism are implausible [44, 142, 264]. While different reaction mechanisms could be implemented in the model easily, these findings do question the value of the current calibration based on the multi-step mechanism.

Despite these limitations, the model is already very useful and versatile in its present state. Further improvements are suggested and discussed below:

5.7.3 Possible improvements and outlook

Improved parametrization. Of course, the values of all model parameters can be improved by fitting more precise and more reproducible data – or even simply fitting more data. Considering the large parameter space, though, the insight that can be gained by mere statistical improvements of the data base is limited at best, cf. section 4.3.3. A more promising approach is to determine more parameters *a priori* by explicit measurements. The values of all non-fitted parameters have been researched thoroughly, see section 5.3. However, there are many more parameters which could have been determined by external sources, if suitable data were available. Measuring such data would allow to reduce the number of fitted parameters and abolish the need to calibrate groups of parameters together. Some notable examples are listed below:

- The charge transfer processes can be studied by rotating disc electrode measurements [44], helping to verify or improve the reaction mechanism.
- X-ray absorption near edge structure (XANES) studies can provide a better understanding of the chemical composition of the electrodes before and after cycling [148, 264, 265], especially in conjunction with X-ray photoelectron spectroscopy (XPS) [265].
- In situ X-ray diffraction (XRD) can be used to analyze the composition of solids in the electrodes [155, 156].
- NMR experiments can provide diffusion coefficients of all dissolved species, see e.g. [266].
- UV–Vis spectroscopy can be used to analyze the composition polysulfide solutions semi-quantitatively [141, 142], or even to measure the speed of disproportionation reactions as well as diffusion constants [267].
- DFT calculations taking into account the effect of the electrolyte can provide more accurate thermodynamic data of the dissolved intermediates.
- HPLC with electrolytes extracted in operando can possibly tell polysulfides apart [268, 269].
- In operando imaging of single particles could improve the representation of the evolution of active surface areas in the model.

More important than this input to the model, however, is the improvement of the model itself, described in the following paragraphs:

Improved reaction mechanism. Even the more detailed multi-step reaction mechanism does not include all possible reactions in the Li/S cell. In fact, the inclusion of every possible effect is not an end in itself – approximations, simplifications, and exclusions are an essential part of every decent model. However, at least the addition of disproportionation reactions as well as a more detailed description of precipitation and dissolution are considered critical tasks. As discussed above, Refs. [44, 142, 264] provide a good starting point for formulating a revised reaction mechanism, fully supported by experiments.

Microstructure. While a full 3D model is beyond the scope and besides the purpose of our modeling activities, the parametrization could be improved by simulating representative elements of an electrode in full 3D or by analyzing the structure in other ways in order to obtain more accurate effective parameters. An approach similar to Refs. [270, 271] could be followed, using SEM, FIB-SEM, or TEM images to establish a realistic microstructure layout as a base for the computation of effective transport parameters and active surface areas as outlined in Ref. [272].

Degradation. Many more chemical degradation mechanisms may be added to the model in a straightforward fashion, ranging from simple parasitic reactions like solvent oxidation to a full SEI model in the style of Refs. [273–275]. Additionally, one can think of non-chemical degradation mechanisms such as mechanical deformation [276], cracking [218], agglomeration, or the build-up of insulating layers [277]. All of these directly affect the transport in the cell, but can also result in loss of electric contact in parts of the porous cathode [278]. However, lacking systematical studies on the degradation effects, it would be difficult to determine the right reaction mechanism(s) and parameters for even more side reactions. On the other hand, a first systematical and methodologically sound experimental analysis of the polysulfide shuttle has been published recently by Janek et al. [279], which might enable a better parametrization and hence more realistic simulation of this particular parasitic reaction in the future.

Transport in the liquid electrolyte. First of all, a more detailed description of the ionic liquid is required in order to improve the modeling of transport in the liquid electrolyte. Another interesting improvement would be the description of locally non-neutral concentrated electrolytes [207], potentially built on top of a thermodynamically consistent description of the ionic transport in liquid electrolytes [203]. The latter would also pave the way for a theoretically sound temperature-dependent model of the Li/S battery, outlined next.

Non-isothermal model. Adding a description of heat sources and transport to the model is straightforward from a theoretical point of view [280]. However, since almost all effects in the cell depend on the temperature one way or the other, this measure would effectively double the number of parameters required. Depending on the phenomenon, entropies, activation energies, temperature coefficients, and so on would need to be determined in addition to the present parameters. That issue put aside, this extension is desirable, because it would enable the use of this model as a back-end for higher level, system-scale simulations, which rely on a correct energy balance.

A full implementation of heat generation and transfer is available within the modeling framework DENIS, see e.g. Ref. [281]. The approach taken is to include an additional conservation equation for energy in addition to the conservation of mass and charge:

$$\frac{d}{dt} (w_{\text{el}} + w_{\text{chem}} + w_{\text{heat}}) = \text{div} (\vec{w}_{\text{heat}}) . \quad (5.1)$$

Here w_{el} is the electrical, w_{chem} the chemically stored energy density, and \vec{w}_{heat} , the heat flux. The total heat Q_{tot} equals w_{heat} times the volume of the CV; it is composed of several contributions including, among others, heat from exothermic reactions Q_{elchem} , polarization heating Q_{pol} , and resistive heating Q_{res} :

$$Q_{\text{tot}} = Q_{\text{elchem}} + Q_{\text{pol}} + Q_{\text{res}} + \dots . \quad (5.2)$$

These sources need to be implemented one by one. In addition, one more equation is needed, describing the transport of heat.

$$\varrho c_p \cdot \frac{\partial T}{\partial t} = -\text{div} (\vec{w}_{\text{heat}}) + \sum_j Q_j , \quad (5.3)$$

where Q_j are the heat sources as defined above, ϱ is the density, and c_p the effective heat capacity at constant pressure. Finally, boundary conditions are needed, describing the flux in and out of the computational domain. A detailed description of the theory and implementation can be found in Ref. [282, chap. 3.4].

To conclude, there are many possible extensions to the model; some exist only as concepts, some ready to use. The only limitation is the number of parameters that can be determined faithfully and reliably.

6 Conclusions and outlook

6.1 Summary of achievements

This work contributes to the field of Li/S battery research in two respects: First, the understanding of the electrochemistry of Li/S cells was improved by analyzing the system with the assistance of a physically-based electrochemical model. Second, a novel cathode material, carbon-coated Li_2S , has been demonstrated to work well in Li/S batteries. In the following, the achievements and major results of this work are summarized chapter by chapter.

In the introduction, the recent history of electrochemical energy storage was laid out, culminating in the ultimate motivation for this study – the need for better batteries. Furthermore, general features of the Li/S battery were presented and remaining challenges, which still prevent the widespread use of this promising electrochemical system were addressed. Chapter 1 closed with an overview of this work, defining the scope and goals for both the experimental and theoretical parts.

Materials and methods of the experimental work were described in chapter 2. Following an overview of the literature on Li_2S based electrodes, the material and electrode design was presented together with a detailed discussion of the goals and a summary of the processing steps. A special emphasis was on the preparation and analysis of the active material, carbon-coated Li_2S particles. The active material was prepared by ball-milling Li_2S powder and applying a carbon coating by CVD in a custom-designed tube furnace. Since Li_2S is very reactive with trace water as well as oxygen, a protective atmosphere was required during the entire preparation. Next, the other components of the cell were described, including the lithium counter electrode, the polypropylene separator, the ionic liquid based electrolyte with additives as well as the additional components of the positive electrode. The latter include the binder SBR and various forms of carbon, enhancing the specific surface area and conductivity. Also, the preparation of porous electrodes and the assembly of coin cells were illustrated.

The second part of chapter 2 elaborated on the characterization of the materials, electrodes, and cells. A sound characterization could only be achieved combining different techniques such as electron microscopy (SEM and TEM), spectroscopy (EDX,

Raman), chemical tests, and the entire spectrum of electrochemical tests, including galvanostatic and potentiostatic cycling, cyclic voltammetry, impedance spectroscopy, and combinations thereof. Finally, other methods or materials that did not work well were briefly discussed in section 2.5.

The experimental results were presented in chapter 3, which roughly followed the chronology of this work: First, the characterization of the active material and electrodes made thereof was presented in section 3.1. The effectivity of different coating protocols was evaluated by SEM imaging and EDX spectroscopy. The best results were obtained using acetylene as carbon precursor, deposited at 400–450 °C. Both Raman spectra and TEM images confirm that a regular, uniform carbon coating was applied to the particles. Next, SEM images and EDX spectra of several different electrodes were compared to optimize composition, fabrication, and handling.

Despite numerous tweaks and improvements to the active material, the electrolyte, and the electrode preparation, Li₂S was not contained in the electrode as intended. This could be shown by a chemical test as well as a run in a transparent beaker cell, where the leakage of polysulfides into the electrolyte was evident.

Nevertheless, cells prepared from the novel material exhibit a promising behavior as analyzed in section 3.2. To exploit their full potential, the activation (a.k.a. formation) needed to be adjusted, as discussed in section 3.2.3. We could show that almost all the capacity can be activated at voltages as low as 3.4 V. While an estimation of SoC and SoH based on impedance spectra was intended, the reproducibility of the results did not allow for an authoritative analysis. Next, the shape of the charge/discharge profiles was analyzed and found to be generally very similar to that of “regular” Li/S cells with sulfur/carbon electrodes, as analyzed in section 3.2.5. Finally, cycling results were presented for various cells and conditions, demonstrating a slow, but steady capacity decay. While the rate of decay, as well as the initial discharge capacity of slightly above $1000 \text{ Ah} \cdot \text{kg}_{\text{sulfur}}^{-1}$, leave room for improvement, the remaining capacity of almost $500 \text{ Ah} \cdot \text{kg}_{\text{sulfur}}^{-1}$ after 200 cycles was higher than any value published for Li₂S based electrodes at that time.

The modeling part started with a general recapitulation of the means and purpose of modeling in chapter 4, before the methodology of our physically-based continuum model was presented. The phenomena described by the model and underlying assumptions were discussed along with the equations used in the model. These include the transport in the liquid electrolyte, the electrochemical and electrical description of the cell as well as the representation of different phases and their microstructures in the one-dimensional model. Next, two different reaction mechanisms were introduced: the simple two-step global model and the more detailed multi-step model. Both comprise a set of electrochemical reactions and corresponding expressions for

the evolution of the phases' active surface areas. Finally, a possible mode of degradation – the formation of Li₂S at the negative electrode – was integrated into the model. The chapter continued with remarks on the steps taken to successfully implement the model as an extension to the existing modeling framework DENIS. Finally, the strategy for model calibration and a consideration of the relevant errors were presented.

The presentation of the simulation results in chapter 5 started off with the results of the global model in section 5.1. Here, transport in the liquid electrolyte and cycling protocols were studied, illustrating the advantages of suppressing sulfur mobility in the electrolyte and CCCV charging to fully recover the capacity after discharging. Also the effect of a slow “refresh” cycle was illuminated. The more detailed multi-step model was first presented with literature parametrization in section 5.2. As shown by discharge profiles, impedance spectra, and the evolution of solid and dissolved species, this model generally produces plausible results, including the well-known two distinct voltage plateaus during discharge and the formation/dissolution of solid S₈ and Li₂S. The results confirm the findings previously published in Ref. [196]. Similar to that publication, however, the end of discharge could not be explained conclusively. Therefore, in a second step, all parameters in the multi-step model were rigorously calibrated to match the experimental data presented in chapter 3. The calibration as well as a partial validation were described in sections 5.3 and 5.4. A broad selection of data was considered for the calibration, ranging from literature values to the experimentally known composition of the cell, and its electrochemical performance in the form of discharge profiles and impedance spectra. Several important parameters were determined by fitting this data. For each fit, a parameter variation was presented, illustrating the effect of the parameter. After correct parametrization, simulation results reproduced experiments to a reasonably good degree and could be used to better understand and explain the empirical findings. More simulations were presented in section 5.5, including the evolution of the grand total and individual concentrations of dissolved species, as well as a study of the formation of a passivating Li₂S film on the electrochemically active carbon in the positive electrode. For the calibrated model, the resistance of this film actually triggers the end of discharge for a wide range of operating conditions. Finally, the effect of adding the polysulfide shuttle and the related deposition of Li₂S at the negative electrode to the model was studied in section 5.6. For the highly porous cell simulated, the slightly reduced Coulombic efficiency and the deposition of several ppm Li₂S at the lithium electrode caused only minor effects in terms of capacity and voltage profiles.

6.2 Limitations of this work and ideas for future research

The work presented here is certainly not immaculate and complete in every respect. Instead, there are several known limitations and more research is needed to address them.

Some immediate suggestions for experimentally improving the Li₂S-based electrodes have been expounded in section 3.3.2, including the preparation of smaller and more uniform particles, the application of a more uniform and complete coating as well as calendering electrodes. Still, it is anything but clear whether these measures can help to effectively confine polysulfides within the carbon shell [165]. Interestingly, recent research showed that well-designed cells can tolerate polysulfides dissolved in the liquid electrolyte for some 1500 full cycles, even with a lithium metal counter electrode [76]. If confinement was no longer intended, the thickness of the coating and the carbon content could be further reduced, yielding electrodes with extremely high sulfur content, while maintaining large internal surfaces and good conductivity at the same time.

Regarding the model, several suggestions were made in section 5.7.3 to further improve the parametrization. More importantly, however, the reaction mechanisms implemented so far are known to be incomplete. Especially the precipitation and dissolution of Li₂S (and potentially other species) needs to be represented in more detail, e.g. by introducing asymmetric reaction pathways. Also, it was discovered that the disproportionation reactions among the dissolved polysulfides play a vital role for the electrochemistry of the cell [44, 142, 283]. They need to be added and calibrated in a future version of the multi-step reaction mechanism. While the set of electrochemical reactions in the Li/S cell is still not known in its entirety, the references cited above provide a good starting point for formulating a revised reaction mechanism. Also, more simulations can be run, exploiting the existing capabilities of the model, e.g. galvanostatic intermittent titration (GITT), or scans of the overpotential, i.e. fast-sweep cyclic voltammetry. On the other hand, the same simulations can be run with different cathode and electrolyte compositions. Finally, more side reactions can be added easily to study additional effects, e.g. thermal decomposition, self discharge, and further degradation modes. All in all, the model provides a flexible tool for further studies of Li/S batteries.

6.3 Outlook beyond academia

While Li/S batteries are not quite ready for the mass market yet, there is steady and inevitable progress that will virtually force this technology into the production lines eventually – even if only for certain applications. Cardinal remaining challenges for Li/S batteries, as often listed in review articles [37, 62, 284, 285], are the still incomplete understanding of the complex electrochemistry, the limited cycle life, the insufficient power density for cells with realistically high loadings, the failure to suppress side reactions including the polysulfide shuttle, and finally the not yet mature development of large scale, low-cost fabrication strategies. Despite a recent breakthrough [57], arguably the negative electrode is another issue [286, 287]. An increasing number of scientists and engineers is working on all aspects of the battery to overcome those remaining limitations; taking into account what could be achieved both in terms of technological advancement and gain of knowledge during just the last four years, prospects are good. It seems more than likely that the goals set by the German Bundesentwicklungsplan Elektromobilität [19], the U.S. DRIVE consortium [288], and other strategic key players are not only within reach, but will be met by advanced Li/S batteries sooner rather than later.

Unfortunately, the remarkable progress at the material or electrode level does not translate into an equally large gain at the system or application level. A realistic estimate of the impact of Li/S cells on the battery system performance in the context of electromobility can be found in Refs. [53, 289]. Because of various system necessities and restraints, the effective gain in specific energy would probably not exceed a factor of three compared to Li-ion batteries available in 2012 and a factor of approximately one compared to next-generation lithium intercalation materials. Figures for volumetric energy density look even worse. While this analysis might look discouraging at first glance, reaching the goals mentioned in the above publications would still be a big success. Even if there is little or no benefit in terms of energy density compared to future high-voltage Li-ion batteries, there are still the advantages in terms of cost, availability, safety, and environmental sustainability. On the contrary, one might even want to trade off some of the capacity in order to further simplify the battery: A lithium/polysulfide battery with a liquid positive electrode was recently proposed independently by two research groups [145, 157]. Skipping the last reduction steps (to avoid the formation of solid Li_2S) makes the battery more robust, reliable and affordable at the expense of only a fraction of the capacity. Also, some of the battery components are known to be available from renewable sources [290], improving long-term material availability and reducing environmental impact. Finally, there is the possibility to use the battery in a hybrid system together with another secondary battery, fuel cell, or supercapacitor, which completely changes the use profile [291–293]

and might alleviate some of the issues still associated with deep-cycling Li/S cells.

As prices go down – and potentially, the price of Li/S batteries could be very low [32, 33] – this technology also becomes more attractive for large-scale grid storage applications [9]. Already today, the electrochemical storage and controlled use of wind and solar energy is more cost-effective than immediately feeding all power into the electricity grid as it becomes available [294, 295]. Still, the segment of grid storage is dominated by pumped hydro-power. Other technologies such as high-temperature Na/S batteries or flywheels are used for special purposes only, e.g. short term high-power supply [9]. The further advancement of Li/S batteries, but also other technologies, e.g. novel flow batteries [296, 297], or improved fuel cells and electrolyzers [298–300], might fundamentally change the game.

To conclude, more research is needed in order to advance the understanding, optimization, and application of batteries in general and Li/S technology in particular. In this regard, it is a good sign that policy makers seem to realize that the development of next-generation systems for electrical energy storage is one of the high importance, high impact research topics of the next decade(s). Consequently, there is an increasing number of publicly and privately funded efforts worldwide [54]. These include the activities of the Helmholtz Society, the German Aerospace Center, and the Helmholtz Institute Ulm, promoting this dissertation.

A Appendix

A.1 List of symbols

Table A.1: List of symbols. Except for the indices, nomenclature follows Ref. [59].

symbol	unit	description
a_n	–	activity of dissolved species n
A_m^V	$\text{m}^2 \cdot \text{m}^{-3}$	volume-specific surface area of interface m
$c_n, c_{n,\text{ref}}$	$\text{mol} \cdot \text{m}^{-3}$	(reference) concentration of dissolved species n
$C_{\text{dl},m}$	$\text{F} \cdot \text{m}^{-2}$	area-specific double-layer capacity of interface m
(ds)	–	label for dissolved species
$D_n, D_{n,\text{eff}}$	$\text{m}^2 \cdot \text{s}^{-1}$	(effective) transport coefficient of species n
E	V	cell voltage
E_0	V	open-circuit voltage
$E_{\text{act},q}$	$\text{J} \cdot \text{mol}^{-1}$	activation energy of reaction q , set to $0 \text{ J} \cdot \text{mol}^{-1}$ for all reactions
F	$\text{As} \cdot \text{mol}^{-1}$	Faraday's constant, $9.6485 \cdot 10^4 \text{ As} \cdot \text{mol}^{-1}$
g_n	$\text{J} \cdot \text{mol}^{-1}$	molar Gibbs free energy of species n
ΔG_q	$\text{J} \cdot \text{mol}^{-1}$	Gibbs free energy of reaction q
i_{dl}^V	$\text{A} \cdot \text{m}^{-3}$	double-layer current source term
i_F^V	$\text{A} \cdot \text{m}^{-3}$	Faradaic current source term
i_{tot}	$\text{A} \cdot \text{m}^{-2}$	current density
i, j	–	general purpose indices
J_n	$\text{mol} \cdot \text{m}^{-2} \cdot \text{s}^{-1}$	flux of species n

symbol	unit	description
$k_{q,\text{fwd}}, k_{q,\text{rev}}$	$\text{mol} \cdot \text{m}^{-2} \cdot \text{s}^{-1}$	forward and reverse rate of reaction q
$k_{0,q,\text{fwd}}, k_{0,q,\text{rev}}$	$\text{mol} \cdot \text{m}^{-2} \cdot \text{s}^{-1}$	forward and reverse rate constants (pre-exponential factors) of reaction q
$L_{\text{CA}}, L_{\text{AN}}$	m	thickness of cathode and anode, respectively
l	m	thickness of a film or coating
m	—	index of interfaces
m	kg	mass
M	$\text{kg} \cdot \text{mol}^{-1}$	molar mass (for phases, M denotes the average molar mass)
\vec{n}_{CV}	—	normal vector of the CV surface
n	—	index of species
p_0	Pa	atmospheric pressure, $1.0133 \cdot 10^5$ Pa
p	—	index of phases
q	—	index of chemical reactions
q_{max}	$\text{Ah} \cdot \text{kg}^{-1}$	specific charge
Q	J	heat
r	m	particle radius
R	$\text{J} \cdot \text{mol}^{-1} \cdot \text{K}^{-1}$	universal gas constant, $8.3145 \text{ J} \cdot \text{mol}^{-1} \cdot \text{K}^{-1}$
R_p	$\text{mol} \cdot \text{m}^{-3}$	net production rate of phase p
(s)	-	label for solid species
$\dot{\mathbf{s}}_n, \dot{s}_n$	$\text{mol} \cdot \text{m}^{-3} \cdot \text{s}^{-1}, \text{mol} \cdot \text{m}^{-2} \cdot \text{s}^{-1}$	volume and area specific net rate of production of species n , respectively
t	s	time
T	K	temperature
$V_{\text{CV}}, \partial V_{\text{CV}}$	m^3, m^2	volume and surface of a CV, respectively
w	$\text{J} \cdot \text{m}^{-3}$	specific energy or specific heat

symbol	unit	description
W	J	work or energy
y	m	spatial position across the MEA (i.e. from cathode to anode)
\mathbf{y}	–	solution vector of the DAE system
z	–	number of electrons in a charge-transfer step
Z	$\Omega \cdot m^2$	complex impedance
α_q	–	symmetry factor of charge transfer reaction q , set to 0.5 for all reactions
β	–	temperature exponent in Arrhenius rate equation, set to 0 for all reactions
γ_n	–	activity coefficient of species n
ε_p	–	volume fraction of phase p
ϵ_r	–	dielectric constant (relative permittivity)
η	V	overpotential
μ_n	$J \cdot mol^{-1}$	chemical potential of species n
$\nu_{n,q}$	–	stoichiometric coefficient of species n in reaction q
ξ	variable	phenomenologically motivated fit parameter
ϱ	$kg \cdot m^{-3}$	density
ρ	$\Omega \cdot m$	resistivity
σ, σ^2	variable	uncertainty and variance of a statistical quantity
τ_p	–	tortuosity of phase p
$\phi_{CA, elde}, \phi_{AN, elde}$	V	potential of the cathode and anode, respectively
$\Delta\phi$	V	potential difference
χ^2	–	goodness-of-fit parameter

A.2 Calculation of specific capacities, energy densities and state of charge

One can find many slightly different values for the theoretical volumetric and gravimetric capacities of various cathode materials in the literature. However, since the specific charge is a fundamental material property, there is only one correct value for each material, which can be derived as follows

$$q_{\max} = z \cdot F \cdot M^{-1}, \quad (\text{A.1})$$

where z is the change in oxidation state, equal to the number of electrons transferred, M is the molar mass of the species, and F is Faraday's constant. Values of q_{\max} are reported in Tab. A.2 for several systems. The specific capacity q_{\max} can be calculated for either the charged or discharged state; for a fair comparison of different materials the heavier state should be used, as is reported in Tab. A.2. Contrary to this postulation, the specific capacity is often reported as Ah/kg_{sulfur}, not Ah/kg_{Li₂S}, in this work. This is a minor compromise to improve comparability with other works; the factor for conversion of Ah/kg_{sulfur} to Ah/kg_{Li₂S} is 0.698.

The specific charge contained in a battery electrode \tilde{q}_{\max} equals

$$\tilde{q}_{\max} = q_{\max} \cdot m_{\text{active material}} \cdot m_{\text{electrode}}^{-1}, \quad (\text{A.2})$$

where $m_{\text{active material}}$ and $m_{\text{electrode}}$ are the total mass of the active material and the entire electrode, respectively. Because q_{\max} is a fundamental property of each material, it is useful to compare different materials, especially from a theoretical point of view. On the other hand, \tilde{q}_{\max} takes the composition of the electrode into account and is therefore more popular among experimentalists, because of its technological relevance. Finally, there is $\tilde{\tilde{q}}_{\max}$, which is based on the system's weight – a figure popular among engineers. Of course, $\tilde{q}_{\max} < \tilde{\tilde{q}}_{\max} \leq q_{\max}$ always holds.

While the capacity of a cell depends on the oxidation state of the active material, the specific energy depends on the standard Gibbs free energy of reaction ΔG :

$$w_{\max} = \Delta G \cdot M^{-1}. \quad (\text{A.3})$$

Again, the value may also be expressed in units of electrode weight \tilde{w}_{\max} or system weight $\tilde{\tilde{w}}_{\max}$. In contrast, the specific energy is determined experimentally by integrating the charge density times the voltage at which it is extracted:

$$w_{\exp} = \int_{q=q_{\max}}^{q=0} E(q) dq. \quad (\text{A.4})$$

However, the cell voltage $E(q)$ and even the open-circuit voltage $E_0(q)$ are not intrinsic functions of the cathode active material. Instead, they depend on the electrode's microstructure as well as the electrolyte and counter electrode used. Therefore, it is reasonable for different authors to report significantly different (practical) energy densities $w_{\text{exp}} < w_{\text{max}}$.

That leaves two options for the definition of the SoC of a battery. According to the experimental definition, 100 % corresponds to the state at the end of charge and 0 % to the end of discharge. According to the theoretical definition, 100 % corresponds to the situation where all accessible sulfur in the cell is present in the form of S_8 , whereas 0 % corresponds to the situation where all accessible sulfur is present as Li_2S . Here, accessible means that the sulfur is present in a form which can be transformed into S_8 by means of (electro-)chemical reactions in the cell. While the latter is a more fundamental definition, it implies that the SoC will never be exactly 100 % or 0 %, since, for example, some sulfur will always be dissolved in the electrolyte. To avoid confusion, the latter definition is chosen in this work throughout.

Finally, the cell's SoH is unanimously defined as the fraction of the initial capacity that is still available at a given time.

Table A.2: Maximum theoretical specific capacity and specific energy of various materials. See also Ref. [1], Tab. V. Annotations: ^aestimate, actual ΔG varies with SoC, see Ref. [301]; ^bexcl. product water.

chemistry	M $\text{g} \cdot \text{mol}^{-1}$	z	ΔG $\text{MJ} \cdot \text{mol}^{-1}$	q_{max} $\text{Ah} \cdot \text{kg}^{-1}$	w_{max} $\text{kWh} \cdot \text{kg}^{-1}$
$\text{Be} + \frac{1}{2} \text{O}_2 \rightleftharpoons \text{BeO}$	25.01	2	0.609	2143	6.76
$2 \text{Li} + \text{O}_2 \rightleftharpoons \text{Li}_2\text{O}_2$	45.88	2	0.644	1168	3.9
$2 \text{Li} + \frac{1}{8} \text{S}_8 \rightleftharpoons \text{Li}_2\text{S}$	45.95	2	0.441	1166	2.67
$\text{Al} + \frac{3}{4} \text{O}_2 + \frac{3}{2} \text{H}_2\text{O} + \rightleftharpoons \text{Al}(\text{OH})_3$	78.00	3	1.272	1030	4.5
$\text{Li} + \text{CoO}_2 \rightleftharpoons \text{LiCoO}_2$	97.87	1	0.201 ^a	273	0.57 ^a
$\text{Li} + \text{LiFePO}_4 \rightleftharpoons \text{LiFePO}_4$	157.76	1	0.352 ^a	170	0.62 ^a
$\frac{1}{2} \text{Pb} + \frac{1}{2} \text{PbO}_2 + \text{H}_2\text{SO}_4 \rightleftharpoons \text{PbSO}_4 + \text{H}_2\text{O}$	303.26 ^b	2	0.088	177	0.08

A.3 List of chemicals

Table A.3: List of chemicals used.

chemical name	short name	mol. weight / g/mol	density / kg/m ³	state	purity	CAS number	source
Lithium (metal foil)	Li	6.94	535	s	≥ 99.9%	7439-93-2	FMC
Lithium sulfide	Li ₂ S	45.95	1640	s	99.98%	12136-58-2	Sigma Aldrich
1-Butyl-1-methylpyrrolidinium bis(trifluoromethanesulfonyl)imide	Pyr ₁₄ TFSI	422.41	1425	l	99%	223437-11-4	io-li-tec
Lithium bis(trifluoromethanesulfonyl)imide	LiTFSI	287.09	1330	s	99.95%	90076-65-6	Sigma Aldrich
Lithium nitrate	LiNO ₃	68.946	2380	s	99.99%	7790-69-4	Sigma Aldrich
Toluene	Toluene	92.138	867	l	HPLC grade	108-88-3	Sigma Aldrich
Poly(styrene-co-butadiene) rubber	SBR	~100 000	965	s	?	9003-55-8	Sigma Aldrich
Tetraethylene glycol dimethyl ether	TEGDM	222.28	1001	l	≥ 99%	143-24-8	Sigma Aldrich
Polyethylene glycol dimethyl ether	PEGDM	~240	~1080	l	?	24991-55-7	Sigma Aldrich
Carbon black	Super C65	—	1900	s	≥ 99.8%	1333-86-4	Timcal
1,3-Dioxolane	DOL	74.08	1060	l	99.8%	646-06-0	Sigma Aldrich
1,2-Dimethoxyethane (Dimethylglycol)	DME	90.12	867	l	99.5%	110-71-4	Sigma Aldrich
N-Methyl-2-pyrrolidone	NMP	99.13	1028	l	anhydrous, 99.5%	872-50-4	Sigma Aldrich
Multi-walled carbon nanotubes	MWCNT	—	—	s	> 95%	308068-56-6	Cheap Tubes
Argon	Ar	39.95	—	g	99.999%	7440-37-1	Praxair
Acetylene	C ₂ H ₂	26.04	—	g	?	74-86-2	Praxair
Ethylene	C ₂ H ₄	28.05	—	g	?	74-85-1	Praxair

A.4 List of equipment

Table A.4: List of equipment

device	name/model	manufacturer
high energy ball mill	8000M Mixer/Mill	Thomas Scientific, Swedesboro, NJ, USA
YSZ grinding balls	4039GM, diameter = 10, 5, and 3 mm	Inframet Advanced Materials, Manchester, CT, USA
CVD furnace	Lindberg Blue M Mini-Mite	Thermo Fisher Scientific, Waltham, MA, USA
glove box 1	UNILab	MBraun, Garching, Germany
glove box 2	LAB master 130	MBraun, Garching, Germany
TEM	F20 UT Tecnai	FEI, Hillsboro, OR, USA
Raman	LabRAM (confocal)	Horiba Jobin Yvon, Edison, NJ, USA
Karl Fischer titrator	DL39 Coulometer	Mettler Toledo, Greifensee, Switzerland
Ultrasonic tip	Digital Sonifier 450	Branson Ultrasonics Corporation, Danbury, CT, USA
Ultrasonic bath	2510 Ultrasonic Bath	Branson Ultrasonics Corporation, Danbury, CT, USA
Molecular sieves	Zeolite type 4Å	TRICAT, Hunt Valley, MD, USA
Arbin cycler	MSTAT	Arbin Instruments, College Station, TX, USA
BioLogic cycler (EIS)	VSP	BioLogic, Claix, France
BioLogic cycler (CVs)	VMP3	BioLogic, Claix, France
temperature chamber	Model TEC1	TestEquity LLC, Moorpark, CA, USA
SEM microscope	JSM-7000F	JEOL, Akishima, Tokyo, Japan
coin cell parts	Belleville Stack	National Research Council Canada, Montreal, QC, Canada
hot plate/magnetic stirrer	120V Stirrer/hot plate	Corning Inc., Corning, NY, USA

A.5 Parameter sets for the models

Table A.5: Parameters used for the global model. Values are given for $T = 303.15\text{ K}$ and $p = 101325\text{ Pa}$.

Thickness: 40 μm		Control volumes: 8		Species		Density / Initial concentration	Diffusion coefficient / $\text{m}^2 \cdot \text{s}^{-1}$
Bulk phases	Volume fraction ε_0	Tortuosity τ_0		$\text{S}_{8(\text{s})}$		$2.07 \cdot 10^3 \text{ kg} \cdot \text{m}^{-3}$	-
Sulfur	0.5	1.0		C		$2.26 \cdot 10^3 \text{ kg} \cdot \text{m}^{-3}$	-
Carbon	0.2	1.0		$\text{C}_4\text{H}_6\text{O}_3$		$1.20 \cdot 10^3 \text{ kg} \cdot \text{m}^{-3} / 1.18 \cdot 10^4 \text{ mol} \cdot \text{m}^{-3}$	-
Electrolyte	0.3	1.2		Li^+		$1.00 \cdot 10^3 \text{ mol} \cdot \text{m}^{-3}$	$1 \cdot 10^{-10}$
cathode				TFSI^-		$7.67 \cdot 10^2 \text{ mol} \cdot \text{m}^{-3}$	$1 \cdot 10^{-10}$
Lithium sulfide (Li_2S)				S_2^-		$2.36 \cdot 10^1 \text{ mol} \cdot \text{m}^{-3}$	$1 \cdot 10^{-10}$
Interfaces sulfur surface				S_2^-		$2.36 \cdot 10^1 \text{ mol} \cdot \text{m}^{-3}$	$1 \cdot 10^{-10}$
separatator				S_4^{2-}		$2.36 \cdot 10^1 \text{ mol} \cdot \text{m}^{-3}$	$1 \cdot 10^{-10}$
anode surface				S_6^{2-}		$2.36 \cdot 10^1 \text{ mol} \cdot \text{m}^{-3}$	$1 \cdot 10^{-10}$
Thickness: 100 μm				S_8^{2-}		$2.36 \cdot 10^1 \text{ mol} \cdot \text{m}^{-3}$	$1 \cdot 10^{-10}$
Thickness: 200 μm				$\text{S}_{8(\text{ds})}$		$3.54 \cdot 10^1 \text{ mol} \cdot \text{m}^{-3}$	$1 \cdot 10^{-10}$
Thickness: 400 μm				$\text{Li}_2\text{S}_{(\text{s})}$		$1.64 \cdot 10^3 \text{ kg} \cdot \text{m}^{-3}$	-
Thickness: 800 μm							Molar Gibbs free energy
Thickness: 1600 μm							$-441.4 \text{ kJ} \cdot \text{mol}^{-1}$
Thickness: 3200 μm							$15.0 \text{ kJ} \cdot \text{mol}^{-1}$
Thickness: 6400 μm							
Thickness: 12800 μm							
Thickness: 25600 μm							
Thickness: 51200 μm							
Thickness: 102400 μm							
Thickness: 204800 μm							
Thickness: 409600 μm							
Thickness: 819200 μm							
Thickness: 1638400 μm							
Thickness: 3276800 μm							
Thickness: 6553600 μm							
Thickness: 13107200 μm							
Thickness: 26214400 μm							
Thickness: 52428800 μm							
Thickness: 104857600 μm							
Thickness: 209715200 μm							
Thickness: 419430400 μm							
Thickness: 838860800 μm							
Thickness: 1677721600 μm							
Thickness: 3355443200 μm							
Thickness: 6710886400 μm							
Thickness: 13421772800 μm							
Thickness: 26843545600 μm							
Thickness: 53687091200 μm							
Thickness: 107374182400 μm							
Thickness: 214748364800 μm							
Thickness: 429496729600 μm							
Thickness: 858993459200 μm							
Thickness: 1717986918400 μm							
Thickness: 3435973836800 μm							
Thickness: 6871947673600 μm							
Thickness: 13743895347200 μm							
Thickness: 27487790694400 μm							
Thickness: 54975581388800 μm							
Thickness: 109951162777600 μm							
Thickness: 219902325555200 μm							
Thickness: 439804651110400 μm							
Thickness: 879609302220800 μm							
Thickness: 1759218604441600 μm							
Thickness: 3518437208883200 μm							
Thickness: 7036874417766400 μm							
Thickness: 14073748835532800 μm							
Thickness: 28147497671065600 μm							
Thickness: 56294995342131200 μm							
Thickness: 11258999068426400 μm							
Thickness: 22517998136852800 μm							
Thickness: 45035996273705600 μm							
Thickness: 90071992547411200 μm							
Thickness: 180143985094822400 μm							
Thickness: 360287970189644800 μm							
Thickness: 720575940379289600 μm							
Thickness: 1441151880758579200 μm							
Thickness: 2882303761517158400 μm							
Thickness: 5764607523034316800 μm							
Thickness: 1152921504606863200 μm							
Thickness: 2305843009213726400 μm							
Thickness: 4611686018427452800 μm							
Thickness: 9223372036854905600 μm							
Thickness: 18446744073709811200 μm							
Thickness: 36893488147419622400 μm							
Thickness: 73786976294839244800 μm							
Thickness: 147573952589678489600 μm							
Thickness: 295147905179356979200 μm							
Thickness: 590295810358713958400 μm							
Thickness: 1180591620717427916800 μm							
Thickness: 2361183241434855833600 μm							
Thickness: 4722366482869711667200 μm							
Thickness: 9444732965739423334400 μm							
Thickness: 18889465931478846668800 μm							
Thickness: 37778931862957693337600 μm							
Thickness: 75557863725915386675200 μm							
Thickness: 151115727451830773400000 μm							
Thickness: 302231454903661546800000 μm							
Thickness: 604462909807323093600000 μm							
Thickness: 1208925819614646187200000 μm							
Thickness: 2417851639229292374400000 μm							
Thickness: 4835703278458584748800000 μm							
Thickness: 9671406556917169497600000 μm							
Thickness: 19342813113834338995200000 μm							
Thickness: 38685626227668677990400000 μm							
Thickness: 77371252455337355980800000 μm							
Thickness: 154742504910674711961600000 μm							
Thickness: 309485009821349423923200000 μm							
Thickness: 618970019642698847846400000 μm							
Thickness: 1237940039285397695692800000 μm							
Thickness: 2475880078570795391385600000 μm							
Thickness: 4951760157141590782771200000 μm							
Thickness: 9903520314283181565542400000 μm							
Thickness: 19807040628566363131084800000 μm							
Thickness: 39614081257132726262169600000 μm							
Thickness: 79228162514265452524339200000 μm							
Thickness: 158456325228530905048678400000 μm							
Thickness: 316912650457061810097356800000 μm							
Thickness: 633825300914123620194713600000 μm							
Thickness: 1267650601828247240389427200000 μm							
Thickness: 2535301203656494480778854400000 μm							
Thickness: 5070602407312988961557708800000 μm							
Thickness: 1014120481462597792311417600000 μm							
Thickness: 2028240962925195584622835200000 μm							
Thickness: 4056481925850391169245670400000 μm							

Table A.6: Initial set of parameters for the multi-step model (for $T = 298\text{ K}$ and $p = 101325\text{ Pa}$).

Thickness: 41 μm					
Control volumes: 5					
Bulk phases	Volume fraction ε_0	Tortuosity τ_0	Species	Density / Initial concentration	Diffusion coefficient / $\text{m}^2 \cdot \text{s}^{-1}$
cathode	Sulfur	0.16	1.0	$\text{S}_{8(\text{s})}$	$2.07 \cdot 10^3 \text{ kg} \cdot \text{m}^{-3}$
	Carbon	0.0619	1.0	C	$2.26 \cdot 10^3 \text{ kg} \cdot \text{m}^{-3}$
	Electrolyte	0.778	1.0	$\text{C}_4\text{H}_6\text{O}_3$	$1.20 \cdot 10^3 \text{ kg} \cdot \text{m}^{-3}$
			Li^+	$1.024 \cdot 10^3 \text{ mol} \cdot \text{m}^{-3}$	$1 \cdot 10^{-10}$
			PF_6^-	$1.023 \cdot 10^3 \text{ mol} \cdot \text{m}^{-3}$	$4 \cdot 10^{-10}$
			S_2^-	$8.46 \cdot 10^{-10} \text{ mol} \cdot \text{m}^{-3}$	$4 \cdot 10^{-10}$
			S_4^-	$5.35 \cdot 10^{-7} \text{ mol} \cdot \text{m}^{-3}$	$1 \cdot 10^{-10}$
			S_4^-	$2.05 \cdot 10^{-2} \text{ mol} \cdot \text{m}^{-3}$	$1 \cdot 10^{-10}$
			S_6^-	$3.31 \cdot 10^{-1} \text{ mol} \cdot \text{m}^{-3}$	$6 \cdot 10^{-10}$
			S_8^-	$1.82 \cdot 10^{-1} \text{ mol} \cdot \text{m}^{-3}$	$6 \cdot 10^{-10}$
Lithium sulfide (Li_2S)			$\text{S}_{8(\text{ds})}$	$1.94 \text{ mol} \cdot \text{m}^{-3}$	$1 \cdot 10^{-9}$
	Interfaces	$1 \cdot 10^{-4}$	1.0	$\text{Li}_2\text{S}_{(\text{s})}$	$1.64 \cdot 10^3 \text{ kg} \cdot \text{m}^{-3}$
	Sulfur Electrolyte	$1 \cdot 10^5 \text{ m}^2 \cdot \text{m}^{-3}$	0 F $\cdot \text{m}^{-2}$	Area-specific capacity C_{dl}	Forward rate constant
	Carbon Electrolyte	$1 \cdot 10^5 \text{ m}^2 \cdot \text{m}^{-3}$	1.36 F $\cdot \text{m}^{-2}$	$\text{S}_{8(\text{s})} \rightleftharpoons \text{S}_{8(\text{ds})}$	Reverse rate constant
				$\text{S}_{8(\text{s})} + \text{e}^- \rightleftharpoons 1/2 \text{S}_8^{2-}$	$1.000 \cdot 10^3 \text{ mol} \cdot \text{m}^{-2} \cdot \text{s}^{-1}$
				$1/2 \text{S}_8^{2-} + \text{e}^- \rightleftharpoons 1/2 \text{S}_8^{2-}$	$2.940 \cdot 10^{-24} \text{ mol} \cdot \text{m}^{-2} \cdot \text{s}^{-1}$
				$3/2 \text{S}_8^{2-} + \text{e}^- \rightleftharpoons 2 \text{S}_6^{2-}$	$1.190 \cdot 10^{-20} \text{ mol} \cdot \text{m}^{-2} \cdot \text{s}^{-1}$
				$\text{S}_6^{2-} + \text{e}^- \rightleftharpoons 3/2 \text{S}_4^{2-}$	$4.191 \cdot 10^{-17} \text{ mol} \cdot \text{m}^{-2} \cdot \text{s}^{-1}$
				$1/2 \text{S}_4^{2-} + \text{e}^- \rightleftharpoons \text{S}_2^-$	$2.375 \cdot 10^{14} \text{ mol} \cdot \text{m}^{-2} \cdot \text{s}^{-1}$
				$1/2 \text{S}_2^{2-} + \text{e}^- \rightleftharpoons \text{S}_2^-$	$4.655 \cdot 10^{15} \text{ mol} \cdot \text{m}^{-2} \cdot \text{s}^{-1}$
Li ₂ S Electrolyte		$1 \cdot 10^5 \text{ m}^2 \cdot \text{m}^{-3}$	0 F $\cdot \text{m}^{-2}$	$2 \text{Li}^+ + \text{S}_2^- \rightleftharpoons \text{Li}_2\text{S}_{(\text{s})}$	$4.738 \cdot 10^{-19} \text{ mol} \cdot \text{m}^{-2} \cdot \text{s}^{-1}$
	Thickness: 9 μm			Control volumes: 5	$5.000 \cdot 10^{-11} \text{ mol} \cdot \text{m}^{-2} \cdot \text{s}^{-1}$
	Bulk phases	Volume fraction ε_0	Tortuosity τ_0	Species	Density
	Separator	0.37	1.0	none	
	Electrolyte	0.63	1.0	see cathode	$1.20 \cdot 10^3 \text{ kg} \cdot \text{m}^{-3}$
anode	Interfaces: none				
	Thickness: 100 μm			Control volumes: 5	
	Bulk phases	Volume fraction ε_0	Tortuosity τ_0	Species	Density
	Lithium	0.37	1.0	$\text{Li}_{(\text{s})}$	$5.34 \cdot 10^2 \text{ kg} \cdot \text{m}^{-3}$
	Electrolyte	0.63	1.0	see cathode	$1.20 \cdot 10^3 \text{ kg} \cdot \text{m}^{-3}$
Interface	Specific area A_0^V	Area-specific capacity C_{dl}	Reaction	Forward rate constant	Molar Gibbs free energy
	Lithium Electrolyte	$1 \cdot 10^6 \text{ m}^2 \cdot \text{m}^{-3}$	$1.80 \text{ F} \cdot \text{m}^{-2}$	$\text{Li}_{(\text{s})} \rightleftharpoons \text{Li}^+ + \text{e}^-$	$0.01 \cdot \text{mol}^{-1}$
				$4.09 \cdot 10^{-9}$	

Table A.7: Calibrated set of parameters for the multi-step model (for $T = 298$ K and $p = 101325$ Pa). Notes: * (elyte) is a placeholder species, representing the liquid electrolyte. Its density is chosen to match the composition of electrolyte #5 in Tab. 2.2 on page 25.

Thickness: 25 μm		Control volumes: 5			
Bulk phases	Volume fraction ε_0	Tortuosity τ_0	Species	Density / Initial concentration	Diffusion coefficient / $m^2 \cdot s^{-1}$
Sulfur	0.04140	1.00	$S_8(s)$	$2.07 \cdot 10^3 \text{ kg} \cdot m^{-3}$	-
Carbon	0.03248	1.00	C	$2.26 \cdot 10^3 \text{ kg} \cdot m^{-3}$	-
Styrene-butadiene rubber	0.02800	1.00	$[C_{58}H_{69}]_n$	$9.65 \cdot 10^2 \text{ kg} \cdot m^{-3}$	-
Electrolyte	0.69143	1.12	(elyte)*	$1.29 \cdot 10^3 \text{ kg} \cdot m^{-3}$	-
			Li^{+}	$1.51 \cdot 10^3 \text{ mol} \cdot m^{-3}$	$1 \cdot 10^{-11}$
			$TFSI^{-}$	$1.00 \cdot 10^3 \text{ mol} \cdot m^{-3}$	$1 \cdot 10^{-11}$
			NO_3^{-}	$5.00 \cdot 10^2 \text{ mol} \cdot m^{-3}$	$1 \cdot 10^{-11}$
			S^{2-}	$6.19 \cdot 10^{-25} \text{ mol} \cdot l^{-1}$	$1 \cdot 10^{-11}$
			S_2^{2-}	$3.65 \cdot 10^{-19} \text{ mol} \cdot l^{-1}$	$1 \cdot 10^{-11}$
			S_4^{2-}	$2.12 \cdot 10^{-7} \text{ mol} \cdot l^{-1}$	$1 \cdot 10^{-11}$
			S_6^{2-}	$7.16 \cdot 10^{-4} \text{ mol} \cdot l^{-1}$	$1 \cdot 10^{-11}$
			S_8^{2-}	$2.92 \cdot 10^{-1} \text{ mol} \cdot l^{-1}$	$1 \cdot 10^{-11}$
			$S_8^{(ds)}$	$9.38 \text{ mol} \cdot l^{-1}$	$1 \cdot 10^{-11}$
Lithium sulfide (Li_2S)	0.00120	1.00	$Li_2S(s)$	$1.64 \cdot 10^3 \text{ kg} \cdot m^{-3}$	-
Passive lithium sulfide (p- Li_2S)	0.10549	1.00	$Li_2S(s)$	$1.64 \cdot 10^3 \text{ kg} \cdot m^{-3}$	-
Argon	0.10000	1.00	Ar	$1.78 \text{ kg} \cdot m^{-3}$	-
Interfaces	Specific area A_0^V	Area specific capacity C_{dl}	Reactions	Forward rate constant	Molar Gibbs free energy
Sulfur Electrolyte	$1.4 \cdot 10^6 \text{ m}^2 \cdot m^{-3}$	$0.0 F \cdot m^{-2}$	$S_8(s) \rightleftharpoons S_8(ds)$	$3.0 \cdot 10^{-4} \text{ mol} \cdot m^{-2} \cdot s^{-1}$	$19.01 \cdot \text{mol}^{-1}$
Li_2S Electrolyte	$1.2 \cdot 10^6 \text{ m}^2 \cdot m^{-3}$	$0.0 F \cdot m^{-2}$	$2 Li^{+} + S_2^{2-} \rightleftharpoons Li_2S(s)$	$3.2 \cdot 10^{12} \text{ mol} \cdot m^{-2} \cdot s^{-1}$	$-120.0 \text{ kJ} \cdot \text{mol}^{-1}$
Carbon Electrolyte	$1.1 \cdot 10^7 \text{ m}^2 \cdot m^{-3}$	$0.2 F \cdot m^{-2}$	$1/2 S_8(ds) + e^{-} \rightleftharpoons 1/2 S_8^{2-}$	$4.0 \cdot 10^{14} \text{ mol} \cdot m^{-2} \cdot s^{-1}$	$-240.0 \text{ kJ} \cdot \text{mol}^{-1}$
			$3/2 S_8^{2-} + e^{-} \rightleftharpoons 2 S_6^{2-}$	$4.0 \cdot 10^{14} \text{ mol} \cdot m^{-2} \cdot s^{-1}$	$-201.6 \text{ kJ} \cdot \text{mol}^{-1}$
			$S_6^{2-} + e^{-} \rightleftharpoons 3/2 S_4^{2-}$	$4.0 \cdot 10^{14} \text{ mol} \cdot m^{-2} \cdot s^{-1}$	$-193.0 \text{ kJ} \cdot \text{mol}^{-1}$
			$1/2 S_4^{2-} + e^{-} \rightleftharpoons S_2^{2-}$	$4.0 \cdot 10^{11} \text{ mol} \cdot m^{-2} \cdot s^{-1}$	$-145.7 \text{ kJ} \cdot \text{mol}^{-1}$
			$1/2 S_2^{2-} + e^{-} \rightleftharpoons S_2^{2-}$	$4.0 \cdot 10^{14} \text{ mol} \cdot m^{-2} \cdot s^{-1}$	$-132.7 \text{ kJ} \cdot \text{mol}^{-1}$
Carbon Electrolyte interface passivation:	$r_{carbon} = 40 \text{ nm}$		$\xi_1 = 1.9 \cdot 10^9$	$\xi_2 = 50 \text{ nm}$	
Thickness: 25 μm		Control volumes: 5			
Bulk phases	Volume fraction ε_0	Tortuosity τ_0	Species	Density	
Separator	0.59	1.00	$[C_3H_6]_n$	$9.00 \cdot 10^2 \text{ kg} \cdot m^{-3}$	-
Electrolyte	0.41	1.77	see cathode	$1.29 \cdot 10^3 \text{ kg} \cdot m^{-3}$	
Interfaces: none					
Thickness (active top layer): 1 μm		Control volumes: 3			
Bulk phases	Volume fraction ε_0	Tortuosity τ_0	Species	Density	
anode	0.37	1.00	$Li(s)$	$5.34 \cdot 10^2 \text{ kg} \cdot m^{-3}$	
Lithium	0.38	1.05	see cathode	$1.29 \cdot 10^3 \text{ kg} \cdot m^{-3}$	
Electrolyte	0.63	1.77			
Interface	Specific area A_0^V	Area-specific capacity C_{dl}	Reaction	Forward rate constant	Molar Gibbs free energy
Lithium Electrolyte	$3.58 \cdot 10^6 \text{ m}^2 \cdot m^{-3}$	$0.2 F \cdot m^{-2}$	$Li(s) \rightleftharpoons Li^{+} + e^{-}$	$4.09 \cdot 10^{-5}$	$0.01 \cdot \text{mol}^{-1}$

Bibliography

Cited publications

- [1] E. J. Cairns. *Encyclopedia of Energy*, chapter Batteries, Overview, pp. 117–126. First edition. Elsevier Science (April 2004).
- [2] B. Scrosati, K. M. Abraham, W. A. van Schalkwijk, and J. Hassoun (Eds.). *Lithium Batteries: Advanced Technologies and Applications*. First edition. Wiley (2013).
- [3] K. Mizushima, P. C. Jones, P. J. Wiseman, and J. B. Goodenough. Li_xCoO_2 ($0 < x \leq 1$): A new cathode material for batteries of high energy density. *Materials Research Bulletin* **15**, 783–789 (1980).
- [4] R. Yazami and P. Touzain. A reversible graphite-lithium negative electrode for electrochemical generators. *Journal of Power Sources* **9**, 365–371 (1983).
- [5] *Global Lithium Ion Battery Market (Cathode, Anode, and Electrolytic solution) — Industry Analysis, Size, Share, Growth, Trends, and Forecast, 2013–2019*. published online (November 2013). <http://www.transparencymarketresearch.com/lithium-ion-battery-market.html>. Retrieved 5/5/2014.
- [6] Y. Gogotsi and P. Simon. True Performance Metrics in Electrochemical Energy Storage. *Science* **334**, 917–918 (2011).
- [7] M. L. Kyle, H. Shimotake, R. K. Steunenberg, M. F. J., R. R., and E. J. Cairns. *Lithium/sulfur batteries for electric vehicle propulsion*. Technical report, Argonne National Laboratory (1971).
- [8] B. G. Pollet, I. Staffell, and J. L. Shang. Current status of hybrid, battery and fuel cell electric vehicles: From electrochemistry to market prospects. *Electrochimica Acta* **84**, 235–249 (2012).
- [9] B. Dunn, H. Kamath, and J.-M. Tarascon. Electrical Energy Storage for the Grid: A Battery of Choices. *Science* **334**, 928–935 (2011).
- [10] C. Wadia, P. Albertus, and V. Srinivasan. Resource constraints on the battery energy storage potential for grid and transportation applications. *Journal of Power Sources* **196**, 1593–1598 (2011).

- [11] B. Simon and M. Weil. *Analysis of materials and energy flows of different lithium ion traction batteries*. Revue de Métallurgie **110**, 65–76 (2013).
- [12] A. Balducci, S. S. Jeong, G. T. Kim, S. Passerini, M. Winter, M. Schmuck, G. B. Appetecchi, R. Marcilla, D. Mecerreyes, V. Barsukov, V. Khomenko, I. Cantero, I. De Meatza, M. Holzapfel, and N. Tran. *Development of safe, green and high performance ionic liquids-based batteries (ILLIBATT project)*. Journal of Power Sources **196**, 9719–9730 (2011).
- [13] P. Albertus, C. Wadia, and V. Srinivasan. *Availability of the elements for scaling up batteries for grid and vehicle energy storage*. In *Beyond Lithium Ion IV conference proceedings* (2011). <http://bestar.lbl.gov/bli5/presentations/>. Retrieved 7/20/2014.
- [14] P. G. Bruce, S. A. Freunberger, L. J. Hardwick, and J.-M. Tarascon. *Li-O₂ and Li-S batteries with high energy storage*. Nature Materials **11**, 19–29 (2012).
- [15] J.-M. Tarascon and M. Armand. *Issues and challenges facing rechargeable lithium batteries*. Nature **414**, 359–367 (2001).
- [16] J. B. Goodenough and Y. Kim. *Challenges for rechargeable batteries*. Journal of Power Sources **196**, 6688–6694 (2011).
- [17] Bundesregierung Deutschland. *Energiekonzept für eine umweltschonende, zuverlässige und bezahlbare Energieversorgung*. published online (September 2010). <http://www.bundesregierung.de/Content/DE/StatischeSeiten/Breg/Energiekonzept/dokumente.html>. Retrieved 5/5/2014.
- [18] Bundesregierung Deutschland. *Regierungsprogramm Elektromobilität*. published online (May 2011). http://www.bmbf.de/pubRD/programm_elektromobilitaet.pdf. Retrieved 1/23/2014.
- [19] BMBF. *Nationaler Entwicklungsplan Elektromobilität*. published online (August 2009). http://www.bmbf.de/pubRD/nationaler_entwicklungsplan_elektromobilitaet.pdf. Retrieved 1/23/2014.
- [20] BMWi. *Forschung für eine umweltschonende, zuverlässige und bezahlbare Energieversorgung*. published online (July 2011). <http://www.bmwi.de/DE/Themen/Energie/Energieforschung-und-Innovationen/6-energieforschungsprogramm.html>. Das 6. Energieforschungsprogramm der Bundesregierung. Retrieved 1/23/2014.

- [21] BMWi. *Die Energiewende in Deutschland*. published online (September 2012). <http://www.bmwi.de/Dateien/BMWi/PDF/energiewende-in-deutschland>. Retrieved 1/23/2014.
- [22] BMBF. *Energieforschung*. published online (March 2013). <http://www.bmbf.de/pub/energieforschung.pdf>. Retrieved 1/23/2014.
- [23] BMWi. *Bundesbericht Energieforschung 2013*. published online (August 2013). <http://www.bmwi.de/BMWi/Redaktion/PDF/Publikationen/bundesbericht-energieforschung-2013>. Retrieved 1/23/2014.
- [24] Nationale Plattform Elektromobilität. *Fortschrittsbericht der Nationalen Plattform Elektromobilität*. published online (May 2012). http://www.bmbf.de/pubRD/NPE_Fortschrittsbericht_2012_VorlageBarrierefreiheit_n_DNK84g.pdf. Retrieved 1/23/2014.
- [25] U.S. Department of Energy. *National Action Plan for Energy Efficiency*. published online (November 2008). <http://www.epa.gov/cleanenergy/documents/suca/vision.pdf>. Retrieved 12/30/2014.
- [26] JCESR. *Joint Center for Energy Storage Research*. consortium website. <http://www.jcesr.org/>. Retrieved 6/5/2014.
- [27] USABC. *U.S. Advanced Battery Consortium*. consortium website. <http://www.uscar.org/guest/teams/12/U-S-Advanced-Battery-Consortium>. Retrieved 5/5/2014.
- [28] KLIB. *Kompetenznetzwerk Lithium Ionen Batterien*. consortium website. <http://www.klib-org.de/>. Retrieved 5/5/2014.
- [29] B. Scrosati and J. Garche. *Lithium batteries: Status, prospects and future*. Journal of Power Sources **195**, 2419–2430 (2010).
- [30] B. Scrosati, J. Hassoun, and Y.-K. Sun. *Lithium-ion batteries. A look into the future*. Energy & Environmental Science **4**, 3287–3295 (2011).
- [31] E. J. Cairns and P. Albertus. *Batteries for Electric and Hybrid-Electric Vehicles*. Annual Review of Chemical and Biomolecular Engineering **1**, 299–320 (2010).
- [32] M. Hagen, S. Dörfler, P. Fanz, T. Berger, R. Speck, J. Tübke, H. Althues, M. J. Hoffmann, C. Scherr, and S. Kaskel. *Development and costs calculation of lithium-sulfur cells with high sulfur load and binder free electrodes*. Journal of Power Sources **224**, 260–268 (2013).

- [33] B. Briddell, N. Bronstein, H. Drews, N. Young, and C. Zach. *High-Energy, Low-Weight Lithium Sulfur Batteries*. Technical report, Haas School of Business, University of California Berkeley (December 2012). Cleantech to Market.
- [34] J. Friedman-Rudovsky. *Dreams of a Lithium Empire*. Science **334**, 897–898 (November 2011).
- [35] Electrochemical Energy Storage Team. *Technology Development Roadmap*. published online (July 2006). https://www1.eere.energy.gov/vehiclesandfuels/pdfs/program/electrochemical_energy_storage_roadmap.pdf. Retrieved 5/5/2014.
- [36] H.-J. Ahn, K.-W. Kim, A. Jou-Hyeon, and G. Cheruvally. *Lithium-Sulfur*. In J. Garche (Ed.), *Encyclopedia of Electrochemical Power Sources*, pp. 155–161. Elsevier, Amsterdam (2009). Secondary Batteries – Lithium Rechargeable Systems.
- [37] D. Bresser, S. Passerini, and B. Scrosati. *Recent progress and remaining challenges in sulfur-based lithium secondary batteries - a review*. Chemical Communications **49**, 10545–10562 (2013).
- [38] D. Herbert and J. Ulam. *Electric Dry Cells and Storage Batteries*. U.S. Patent 3043896. Issued June 10, 1962.
- [39] E. J. Cairns and H. Shimotake. *High-Temperature Batteries*. Science **164**, 1347–1355 (1969).
- [40] J. C. Dobson, F. R. McLarnon, and E. J. Cairns. *Voltammetry of Lithium Polysulfides at Metal Electrodes*. Journal of The Electrochemical Society **133**, 1549–1554 (1986).
- [41] R. J. Bones, D. S. Demott, J. H. Duncan, R. S. Grodon, G. R. Miller, P. T. Moseley, R. W. Powers, and F. M. Stackpool. *The Sodium Sulfur Battery*. Chapman and Hall (1985).
- [42] R. D. Rauh, K. M. Abraham, G. F. Pearson, J. K. Surprenant, and S. B. Brummer. *A Lithium/Dissolved Sulfur Battery with an Organic Electrolyte*. Journal of The Electrochemical Society **126**, 523–527 (1979).
- [43] H. Yamin and E. Peled. *Electrochemistry of a nonaqueous lithium/sulfur cell*. Journal of Power Sources **9**, 281–287 (1983).
- [44] Y.-C. Lu, Q. He, and H. A. Gasteiger. *Probing the Lithium-Sulfur Redox Reactions: A Rotating-Ring Disk Electrode Study*. The Journal of Physical Chemistry C **118**, 5733–5741 (2014).

- [45] Sion Power Corporation. *The Rechargeable Battery Company*. company website. <http://www.sionpower.com/>. Retrieved 2/19/2011.
- [46] Oxis Energy. *Next Generation Battery Technology*. company website. <http://www.oxisenergy.com/>. Retrieved 5/5/2014.
- [47] PolyPlus. *Advanced lithium battery technology*. company website. <http://www.polyplus.com/>. Retrieved 5/5/2014.
- [48] J.-i. Yamaki, S.-i. Tobishima, K. Hayashi, K. Saito, Y. Nemoto, and M. Arakawa. *A consideration of the morphology of electrochemically deposited lithium in an organic electrolyte*. Journal of Power Sources **74**, 219–227 (1998).
- [49] K. Zaghib. *Lithium Metal Anode: Challenges and Opportunities*. In *17th International Meeting on Lithium Batteries*. Hydroquebec, Canada (June 2014).
- [50] X. He, J. Ren, L. Wang, W. Pu, C. Jiang, and C. Wan. *Expansion and shrinkage of the sulfur composite electrode in rechargeable lithium batteries*. Journal of Power Sources **190**, 154–156 (2009).
- [51] Y. V. Mikhaylik and J. R. Akridge. *Polysulfide Shuttle Study in the Li/S Battery System*. Journal of The Electrochemical Society **151**, A1969–A1976 (2004).
- [52] L. M. Moshurchak, C. Buhrmester, and J. R. Dahn. *Triphenylamines as a Class of Redox Shuttle Molecules for the Overcharge Protection of Lithium-Ion Cells*. Journal of The Electrochemical Society **155**, A129–A131 (2008).
- [53] F. T. Wagner, B. Lakshmanan, W. Gu, T. Greszler, and M. F. Mathias. *Electrons to Go: Electrochemistry and the Future of the Automobile*. ECS Transactions **41**, 13–26 (2011).
- [54] R. Van Noorden. *Sulphur back in vogue for batteries*. Nature **498**, 416–417 (2013).
- [55] J. Hassoun, M. Agostini, A. Latini, S. Panero, Y.-K. Sun, and B. Scrosati. *Nickel-Layer Protected, Carbon-Coated Sulfur Electrode for Lithium Battery*. Journal of The Electrochemical Society **159**, A390–A395 (2012).
- [56] G. Zheng, Q. Zhang, J. J. Cha, Y. Yang, W. Li, Z. W. Seh, and Y. Cui. *Amphiphilic Surface Modification of Hollow Carbon Nanofibers for Improved Cycle Life of Lithium Sulfur Batteries*. Nano Letters **13**, 1265–1270 (2013).
- [57] G. Zheng, S. W. Lee, Z. Liang, H.-W. Lee, K. Yan, H. Yao, H. Wang, W. Li, S. Chu, and Y. Cui. *Interconnected hollow carbon nanospheres for stable lithium metal anodes*. Nature Nanotechnology **9**, 618–623 (2014).

- [58] W. G. Bessler, S. Gewies, and M. Vogler. *A new framework for physically based modeling of solid oxide fuel cells*. *Electrochimica Acta* **53**, 1782–1800 (2007).
- [59] J. P. Neidhardt, D. N. Fronczek, T. Jahnke, T. Danner, B. Horstmann, and W. G. Bessler. *A flexible framework for modeling multiple solid, liquid and gaseous phases in batteries and fuel cells*. *Journal of The Electrochemical Society* **159**, A1528–A1542 (2012).
- [60] U.S. Department of Energy. *The Batteries for Advanced Transportation Technologies (BATT) Program*. consortium website. <https://batt.lbl.gov/>. Retrieved 4/23/2014.
- [61] H. Tao, Z. Feng, H. Liu, X. Kan, and P. Chen. *Reality and future of rechargeable lithium batteries*. *The Open Materials Science Journal* **5**, 204–214 (2011).
- [62] M.-K. Song, E. J. Cairns, and Y. Zhang. *Lithium/sulfur batteries with high specific energy: old challenges and new opportunities*. *Nanoscale* **5**, 2186–2204 (2013).
- [63] D. Marmorstein. *Solid State Lithium/Sulfur Batteries for Electric Vehicles: Electrochemical and Spectroelectrochemical Investigations*. Ph.D. thesis, University of California, Berkeley (2002). Supervisor: E. J. Cairns.
- [64] J. Hassoun and B. Scrosati. *Moving to a Solid-State Configuration: A Valid Approach to Making Lithium-Sulfur Batteries Viable for Practical Applications*. *Advanced Materials* **22**, 5198–5201 (2010).
- [65] Z. Lin, Z. Liu, W. Fu, N. J. Dudney, and C. Liang. *Lithium Polysulfidophosphates: A Family of Lithium-Conducting Sulfur-Rich Compounds for Lithium-Sulfur Batteries*. *Angewandte Chemie International Edition* **52**, 7460–7463 (2013).
- [66] M. Agostini, Y. Aihara, T. Yamada, B. Scrosati, and J. Hassoun. *A lithium-sulfur battery using a solid, glass-type $P_2S_5-Li_2S$ electrolyte*. *Solid State Ionics* **244**, 48–51 (2013).
- [67] L. Ji, M. Rao, H. Zheng, L. Zhang, Y. Li, W. Duan, J. Guo, E. J. Cairns, and Y. Zhang. *Graphene Oxide as a Sulfur Immobilizer in High Performance Lithium/Sulfur Cells*. *Journal of the American Chemical Society* **133**, 18522–18525 (2011).
- [68] Y. Cao, X. Li, I. A. Aksay, J. Lemmon, Z. Nie, Z. Yang, and J. Liu. *Sandwich-type functionalized graphene sheet-sulfur nanocomposite for rechargeable lithium batteries*. *Physical Chemistry Chemical Physics* **13**, 7660–7665 (2011).

- [69] X. Zhou, J. Xie, J. Yang, Y. Zou, J. Tang, S. Wang, L. Ma, and Q. Liao. *Improving the performance of lithium-sulfur batteries by graphene coating*. *Journal of Power Sources* **243**, 993–1000 (2013).
- [70] Y.-J. Choi, Y.-D. Chung, C.-Y. Baek, K.-W. Kim, H.-J. Ahn, and J.-H. Ahn. *Effects of carbon coating on the electrochemical properties of sulfur cathode for lithium/sulfur cell*. *Journal of Power Sources* **184**, 548–552 (2008).
- [71] S. Jeong, D. Bresser, D. Buchholz, M. Winter, and S. Passerini. *Carbon coated lithium sulfide particles for lithium battery cathodes*. *Journal of Power Sources* **235**, 220–225 (2013).
- [72] L. Duan, J. Lu, W. Liu, P. Huang, W. Wang, and Z. Liu. *Fabrication of conductive polymer-coated sulfur composite cathode materials based on layer-by-layer assembly for rechargeable lithium-sulfur batteries*. *Colloids and Surfaces A: Physicochemical and Engineering Aspects* **414**, 98–103 (2012).
- [73] N. Jayaprakash, J. Shen, S. S. Moganty, A. Corona, and L. A. Archer. *Porous Hollow Carbon@Sulfur Composites for High-Power Lithium-Sulfur Batteries*. *Angewandte Chemie* **123**, 6026–6030 (2011).
- [74] W. Zhou, X. Xiao, M. Cai, and L. Yang. *Polydopamine-Coated, Nitrogen-Doped, Hollow Carbon-Sulfur Double-Layered Core-Shell Structure for Improving Lithium-Sulfur Batteries*. *Nano Letters* **14**, 5250–5256 (2014).
- [75] Z. W. Seh, Q. Zhang, W. Li, G. Zheng, H. Yao, and Y. Cui. *Stable cycling of lithium sulfide cathodes through strong affinity with a bifunctional binder*. *Chemical Science* **4**, 3673–3677 (2013).
- [76] M.-K. Song, Y. Zhang, and E. J. Cairns. *A Long-Life, High-Rate Lithium/Sulfur Cell: A Multifaceted Approach to Enhancing Cell Performance*. *Nano Letters* **13**, 5891–5899 (2013).
- [77] K. Cai, M.-K. Song, E. J. Cairns, and Y. Zhang. *Nanostructured Li_2S -C Composites as Cathode Material for High-Energy Lithium/Sulfur Batteries*. *Nano Letters* **12**, 6474–6479 (2012).
- [78] Y. Yang, G. Zheng, S. Misra, J. Nelson, M. F. Toney, and Y. Cui. *High-Capacity Micrometer-Sized Li_2S Particles as Cathode Materials for Advanced Rechargeable Lithium-Ion Batteries*. *Journal of the American Chemical Society* **134**, 15387–15394 (2012).

- [79] G. Zheng, Y. Yang, J. J. Cha, S. S. Hong, and Y. Cui. *Hollow Carbon Nanofiber-Encapsulated Sulfur Cathodes for High Specific Capacity Rechargeable Lithium Batteries*. Nano Letters **11**, 4462–4467 (2011).
- [80] X. Ji, K. T. Lee, and L. F. Nazar. *A highly ordered nanostructured carbon-sulphur cathode for lithium-sulphur batteries*. Nature Materials **8**, 500–506 (2009).
- [81] X. Liang, Z. Wen, Y. Liu, M. Wu, J. Jin, H. Zhang, and X. Wu. *Improved cycling performances of lithium sulfur batteries with LiNO₃-modified electrolyte*. Journal of Power Sources **196**, 9839–9843 (2011).
- [82] S. Xiong, X. Kai, X. Hong, and Y. Diao. *Effect of LiBOB as additive on electrochemical properties of lithium-sulfur batteries*. Ionics **18**, 249–254 (2012).
- [83] R. Petibon, N. N. Sinha, J. C. Burns, C. P. Aiken, H. Ye, C. M. VanElzen, G. Jain, S. Trussler, and J. R. Dahn. *Comparative study of electrolyte additives using electrochemical impedance spectroscopy on symmetric cells*. Journal of Power Sources **251**, 187–194 (2014).
- [84] T. A. Skotheim, C. J. Sheehan, and Y. V. Mikhaylik. *Lithium Anodes for Electrochemical Cells*. U.S. patent 6733924. Issued May 11, 2004.
- [85] M.-S. Zheng, J.-J. Chen, and Q.-F. Dong. *The Enhanced Electrochemical Performance of Lithium/Sulfur Battery with Protected Lithium Anode*. Advanced Materials Research **476–478**, 676–680 (2012).
- [86] P. C. Howlett, D. R. MacFarlane, and A. F. Hollenkamp. *High Lithium Metal Cycling Efficiency in a Room-Temperature Ionic Liquid*. Electrochemical and Solid-State Letters **7**, A97–A101 (2004).
- [87] N. Schweikert, A. Hofmann, M. Schulz, M. Scheuermann, S. T. Boles, T. Haneemann, H. Hahn, and S. Indris. *Suppressed lithium dendrite growth in lithium batteries using ionic liquid electrolytes: Investigation by electrochemical impedance spectroscopy, scanning electron microscopy, and in situ ⁷Li nuclear magnetic resonance spectroscopy*. Journal of Power Sources **228**, 237–243 (2013).
- [88] S. S. Zhang. *Effect of Discharge Cutoff Voltage on Reversibility of Lithium/Sulfur Batteries with LiNO₃-Contained Electrolyte*. Journal of The Electrochemical Society **159**, A920–A923 (2012).
- [89] S. S. Zhang. *Role of LiNO₃ in rechargeable lithium/sulfur battery*. Electrochimica Acta **70**, 344–348 (2012).

- [90] P. Arora and Z. J. Zhang. *Battery Separators*. Chemical Reviews **104**, 4419–4462 (2004).
- [91] X. Huang. *Separator technologies for lithium-ion batteries*. Journal of Solid State Electrochemistry **15**, 649–662 (2011).
- [92] B. G. Morin and J. L. Schaeffer. *Single-layer lithium ion battery separator* (2012). U.S. patent app. 13/112,809.
- [93] M. Rao, X. Song, and E. J. Cairns. *Nano-carbon/sulfur composite cathode materials with carbon nanofiber as electrical conductor for advanced secondary lithium/sulfur cells*. Journal of Power Sources **205**, 474–478 (2012).
- [94] M. Rao, W. Li, and E. J. Cairns. *Porous carbon-sulfur composite cathode for lithium/sulfur cells*. Electrochemistry Communications **17**, 1–5 (2012).
- [95] J. Cannarella and C. B. Arnold. *Ion transport restriction in mechanically strained separator membranes*. Journal of Power Sources **226**, 149–155 (2013).
- [96] H. Zhao, S.-J. Park, F. Shi, Y. Fu, V. Battaglia, P. N. Ross, and G. Liu. *Propylene Carbonate (PC)-Based Electrolytes with High Coulombic Efficiency for Lithium-Ion Batteries*. Journal of The Electrochemical Society **161**, A194–A200 (2014).
- [97] J. T. Dudley, D. P. Wilkinson, G. Thomas, R. LeVae, S. Woo, H. Blom, C. Horvath, M. W. Juzkow, B. Denis, P. Juric, P. Aghakian, and J. R. Dahn. *Conductivity of electrolytes for rechargeable lithium batteries*. Journal of Power Sources **35**, 59–82 (1991).
- [98] T. Yim, M.-S. Park, J.-S. Yu, K. J. Kim, K. Y. Im, J.-H. Kim, G. Jeong, Y. N. Jo, S.-G. Woo, K. S. Kang, I. Lee, and Y.-J. Kim. *Effect of chemical reactivity of polysulfide toward carbonate-based electrolyte on the electrochemical performance of Li-S batteries*. Electrochimica Acta **107**, 454–460 (2013).
- [99] E. Peled, Y. Sternberg, A. Gorenstein, and Y. Lavi. *Lithium-Sulfur Battery: Evaluation of Dioxolane-Based Electrolytes*. Journal of The Electrochemical Society **136**, 1621–1625 (1989).
- [100] D.-R. Chang, S.-H. Lee, S.-W. Kim, and H.-T. Kim. *Binary electrolyte based on tetra(ethylene glycol) dimethyl ether and 1,3-dioxolane for lithium-sulfur battery*. Journal of Power Sources **112**, 452–460 (2002).
- [101] J.-W. Choi, J.-K. Kim, G. Cheruvally, J.-H. Ahn, H.-J. Ahn, and K.-W. Kim. *Rechargeable lithium/sulfur battery with suitable mixed liquid electrolytes*. Electrochimica Acta **52**, 2075–2082 (2007).

- [102] C. Barchasz, J.-C. Leprêtre, S. Patoux, and F. Alloin. *Electrochemical properties of ether-based electrolytes for lithium/sulfur rechargeable batteries*. *Electrochimica Acta* **89**, 737–743 (2013).
- [103] J. Scheers, S. Fantini, and P. Johansson. *A review of electrolytes for lithium-sulphur batteries*. *Journal of Power Sources* **255**, 204–218 (2014).
- [104] L. Suo, Y.-S. Hu, H. Li, M. Armand, and L. Chen. *A new class of Solvent-in-Salt electrolyte for high-energy rechargeable metallic lithium batteries*. *Nature Communications* **4:1481** (2013).
- [105] N. S. A. Manan, L. Aldous, Y. Alias, P. Murray, L. J. Yellowlees, M. C. Lagunas, and C. Hardacre. *Electrochemistry of Sulfur and Polysulfides in Ionic Liquids*. *The Journal of Physical Chemistry B* **115**, 13873–13879 (2011).
- [106] J.-W. Park, K. Ueno, N. Tachikawa, K. Dokko, and M. Watanabe. *Ionic Liquid Electrolytes for Lithium-Sulfur Batteries*. *The Journal of Physical Chemistry C* **117**, 20531–20541 (2013).
- [107] S. Xiong, K. Xie, E. Blomberg, P. Jacobsson, and A. Matic. *Analysis of the solid electrolyte interphase formed with an ionic liquid electrolyte for lithium-sulfur batteries*. *Journal of Power Sources* **252**, 150–155 (2014).
- [108] A. Matic and B. Scrosati. *Ionic liquids for energy applications*. *MRS Bulletin* **38**, 533–537 (2013).
- [109] J. H. Shin and E. J. Cairns. *N-Methyl-(n-butyl)pyrrolidinium bis(trifluoromethanesulfonyl)imide-LiTFSI-poly(ethylene glycol) dimethyl ether mixture as a Li/S cell electrolyte*. *Journal of Power Sources* **177**, 537–545 (2008).
- [110] J. Pitawala, M. A. Navarra, B. Scrosati, P. Jacobsson, and A. Matic. *Structure and properties of Li-ion conducting polymer gel electrolytes based on ionic liquids of the pyrrolidinium cation and the bis(trifluoromethanesulfonyl)imide anion*. *Journal of Power Sources* **245**, 830–835 (2014).
- [111] W. Zheng, Y. W. Liu, X. G. Hu, and C. F. Zhang. *Novel nanosized adsorbing sulfur composite cathode materials for the advanced secondary lithium batteries*. *Electrochimica Acta* **51**, 1330–1335 (2006).
- [112] L. Yuan, H. Yuan, X. Qiu, L. Chen, and W. Zhu. *Improvement of cycle property of sulfur-coated multi-walled carbon nanotubes composite cathode for lithium/sulfur batteries*. *Journal of Power Sources* **189**, 1141–1146 (2009).

- [113] J. Shim, K. A. Striebel, and E. J. Cairns. *The Lithium/Sulfur Rechargeable Cell: Effects of Electrode Composition and Solvent on Cell Performance*. Journal of The Electrochemical Society **149**, A1321–A1325 (2002).
- [114] Y. M. Lee, N.-S. Choi, J. H. Park, and J.-K. Park. *Electrochemical performance of lithium/sulfur batteries with protected Li anodes*. Journal of Power Sources **119–121**, 964–972 (2003).
- [115] Y. V. Mikhaylik and J. R. Akridge. *Low Temperature Performance of Li/S Batteries*. Journal of The Electrochemical Society **150**, A306–A311 (2003).
- [116] S.-C. Han, M.-S. Song, H. Lee, H.-S. Kim, H.-J. Ahn, and J.-Y. Lee. *Effect of Multi-walled Carbon Nanotubes on Electrochemical Properties of Lithium/Sulfur Rechargeable Batteries*. Journal of The Electrochemical Society **150**, A889–A893 (2003).
- [117] S. S. Zhang. *Liquid electrolyte lithium/sulfur battery: Fundamental chemistry, problems, and solutions*. Journal of Power Sources **231**, 153–162 (2013).
- [118] I. Kovalenko, B. Zdyrko, A. Magasinski, B. Hertzberg, Z. Milicev, R. Burtovyy, I. Luzinov, and G. Yushin. *A Major Constituent of Brown Algae for Use in High-Capacity Li-Ion Batteries*. Science **334**, 75–79 (2011).
- [119] Y. Wang, Y. Huang, W. Wang, C. Huang, Z. Yu, H. Zhang, J. Sun, A. Wang, and K. Yuan. *Structural change of the porous sulfur cathode using gelatin as a binder during discharge and charge*. Electrochimica Acta **54**, 4062–4066 (2009).
- [120] U. S. Vogl, P. K. Das, A. Z. Weber, M. Winter, R. Kostecki, and S. F. Lux. *Mechanism of Interactions between CMC Binder and Si Single Crystal Facets*. Langmuir **30**, 10299–10307 (2014).
- [121] S. F. Lux, F. Schappacher, A. Balducci, S. Passerini, and M. Winter. *Low Cost, Environmentally Benign Binders for Lithium-Ion Batteries*. Journal of The Electrochemical Society **157**, A320–A325 (2010).
- [122] M. He, L.-X. Yuan, W.-X. Zhang, X.-L. Hu, and Y.-H. Huang. *Enhanced Cyclability for Sulfur Cathode Achieved by a Water-Soluble Binder*. The Journal of Physical Chemistry C **115**, 15703–15709 (2011).
- [123] M. Rao, X. Song, H. Liao, and E. J. Cairns. *Carbon nanofiber-sulfur composite cathode materials with different binders for secondary Li/S cells*. Electrochimica Acta **65**, 228–233 (2012).
- [124] M. Wu, K. Eberman, and G. Liu. *The Effects of the Slurry Mixing Procedure on Silicon Based Composite Electrodes for Li-Ion Batteries*. In *PRiME 2012*, volume

MA2012-02, p. 982 (2012). <http://ma.ecsdl.org/content/MA2012-02/10/982.abstract>.

- [125] J.-W. Choi, G. Cheruvally, D.-S. Kim, J.-H. Ahn, K.-W. Kim, and H.-J. Ahn. *Rechargeable lithium/sulfur battery with liquid electrolytes containing toluene as additive*. Journal of Power Sources **183**, 441–445 (2008).
- [126] J. Brückner, S. Thieme, H. T. Grossmann, S. Dörfler, H. Althues, and S. Kaskel. *Lithium-sulfur batteries: Influence of C-rate, amount of electrolyte and sulfur loading on cycle performance*. Journal of Power Sources **268**, 82–87 (2014).
- [127] M. Hagen, P. Fanz, and J. Tübke. *Cell energy density and electrolyte/sulfur ratio in Li-S cells*. Journal of Power Sources **264**, 30–34 (2014).
- [128] J. A. Bearden. *X-Ray Wavelengths*. Reviews of Modern Physics **39**, 78–124 (Jan 1967).
- [129] J. I. Goldstein, D. E. Newbury, D. C. Joy, C. E. Lyman, P. Echlin, E. Lifshin, L. Sawyer, and J. R. Michael. *Scanning Electron Microscopy and X-ray Microanalysis*. Third edition. Springer (2003).
- [130] Y. Li, H. Zhan, S. Liu, K. Huang, and Y. Zhou. *Electrochemical properties of the soluble reduction products in rechargeable Li/S battery*. Journal of Power Sources **195**, 2945–2949 (2010).
- [131] E. Barsoukov and J. R. Macdonald (Eds.). *Impedance Spectroscopy: Theory, Experiment, and Applications*. Second edition. Wiley-Interscience (2005).
- [132] M. E. Orazem and B. Tribollet. *Electrochemical Impedance Spectroscopy*. The Electrochemical Society Series, first edition. Wiley (2008).
- [133] C. Nan, Z. Lin, H. Liao, M.-K. Song, Y. Li, and E. J. Cairns. *Durable Carbon-Coated Li₂S Core-Shell Spheres for High Performance Lithium/Sulfur Cells*. Journal of the American Chemical Society **136**, 4659–4663 (2014).
- [134] S.-E. Cheon, S.-S. Choi, J.-S. Han, Y.-S. Choi, B.-H. Jung, and H. S. Lim. *Capacity Fading Mechanisms on Cycling a High-Capacity Secondary Sulfur Cathode*. Journal of The Electrochemical Society **151**, A2067–A2073 (2004).
- [135] L. Yuan, X. Qiu, L. Chen, and W. Zhu. *New insight into the discharge process of sulfur cathode by electrochemical impedance spectroscopy*. Journal of Power Sources **189**, 127–132 (2009).

- [136] N. Everall, J. Lapham, F. Adar, A. Whitley, E. Lee, and S. Mamedov. *Optimizing Depth Resolution in Confocal Raman Microscopy: A Comparison of Metallurgical, Dry Corrected, and Oil Immersion Objectives*. Applied Spectroscopy **61**, 251–259 (March 2007).
- [137] F. Adar. *Depth Resolution of the Raman Microscope: Optical Limitations and Sample Characteristics*. Spectroscopy (May 2010).
- [138] L. Wang, T. Zhang, S. Yang, F. Cheng, J. Liang, and J. Chen. *A quantum-chemical study on the discharge reaction mechanism of lithium-sulfur batteries*. Journal of Energy Chemistry **22**, 72–77 (2013).
- [139] A. Matic. *Ionic liquid based electrolytes for Li-Sulfur batteries*. In *17th International Meeting on Lithium Batteries*. Como, Italy (June 2014).
- [140] R.-S. Kühnel, N. Böckenfeld, S. Passerini, M. Winter, and A. Balducci. *Mixtures of ionic liquid and organic carbonate as electrolyte with improved safety and performance for rechargeable lithium batteries*. Electrochimica Acta **56**, 4092–4099 (2011).
- [141] N. A. Cañas, D. N. Fronczek, N. Wagner, A. Latz, and K. A. Friedrich. *Experimental and Theoretical Analysis of Products and Reaction Intermediates of Lithium-Sulfur Batteries*. The Journal of Physical Chemistry C **118**, 12106–12114 (2014).
- [142] C. Barchasz, F. Molton, C. Duboc, J.-C. Leprêtre, S. Patoux, and F. Alloin. *Lithium/Sulfur Cell Discharge Mechanism: An Original Approach for Intermediate Species Identification*. Analytical Chemistry **84**, 3973–3980 (2012).
- [143] A. V. B. Cruz and T. Jacob. *Theoretical Investigation on Lithium-Sulfur Batteries*. In *HIU biannual meeting*. Helmholtz Institute Ulm (2012).
- [144] J. S. Newman and K. E. Thomas-Alyea. *Electrochemical Systems*. Electrochemical Society series, third edition. John Wiley & Sons (2004).
- [145] Y. Yang, G. Zheng, and Y. Cui. *A membrane-free lithium/polysulfide semi-liquid battery for large-scale energy storage*. Energy & Environmental Science **6**, 1552–1558 (2013).
- [146] J. Zheng, M. Gu, C. Wang, P. Zuo, P. K. Koech, J.-G. Zhang, J. Liu, and J. Xiao. *Controlled Nucleation and Growth Process of Li₂S₂/Li₂S in Lithium-Sulfur Batteries*. Journal of The Electrochemical Society **160**, A1992–A1996 (2013).
- [147] H. S. Ryu, Z. Guo, H. J. Ahn, G. B. Cho, and H. Liu. *Investigation of discharge reaction mechanism of lithium|liquid electrolyte|sulfur battery*. Journal of Power Sources **189**, 1179–1183 (2009).

- [148] M. Cuisinier, P.-E. Cabelguen, S. Evers, G. He, M. Kolbeck, A. Garsuch, T. Bolin, M. Balasubramanian, and L. F. Nazar. *Sulfur Speciation in Li-S Batteries Determined by Operando X-ray Absorption Spectroscopy*. *The Journal of Physical Chemistry Letters* **4**, 3227–3232 (2013).
- [149] M. U. M. Patel, R. Demir-Cakan, M. Morcrette, J.-M. Tarascon, M. Gaberscek, and R. Dominko. *Li-S Battery Analyzed by UV/Vis in Operando Mode*. *ChemSusChem* **6**, 1177–1181 (2013).
- [150] J. Gao, M. A. Lowe, Y. Kiya, and H. D. Abruña. *Effects of Liquid Electrolytes on the Charge-Discharge Performance of Rechargeable Lithium/Sulfur Batteries: Electrochemical and in-Situ X-ray Absorption Spectroscopic Studies*. *The Journal of Physical Chemistry C* **115**, 25132–25137 (2011).
- [151] C. Barchasz, J.-C. Leprêtre, F. Alloin, and S. Patoux. *New insights into the limiting parameters of the Li/S rechargeable cell*. *Journal of Power Sources* **199**, 322–330 (2012).
- [152] S.-E. Cheon, K.-S. Ko, J.-H. Cho, S.-W. Kim, E.-Y. Chin, and H.-T. Kim. *Rechargeable Lithium Sulfur Battery I. Structural Change of Sulfur Cathode During Discharge and Charge*. *Journal of The Electrochemical Society* **150**, A796–A799 (2003).
- [153] A. Manthiram, Y. Fu, and Y.-S. Su. *Challenges and Prospects of Lithium-Sulfur Batteries*. *Accounts of Chemical Research* **46**, 1125–1134 (2013).
- [154] S. Yang and H. Knickle. *Design and analysis of aluminum/air battery system for electric vehicles*. *Journal of Power Sources* **112**, 162–173 (2002).
- [155] N. A. Cañas, S. Wolf, N. Wagner, and K. A. Friedrich. *In-situ X-ray diffraction studies of lithium-sulfur batteries*. *Journal of Power Sources* **226**, 313–319 (2013).
- [156] J. Nelson, S. Misra, Y. Yang, A. Jackson, Y. Liu, H. Wang, H. Dai, J. C. Andrews, Y. Cui, and M. F. Toney. *In Operando X-ray Diffraction and Transmission X-ray Microscopy of Lithium Sulfur Batteries*. *Journal of the American Chemical Society* **134**, 6337–6343 (2012).
- [157] R. Demir-Cakan, M. Morcrette, Gangulibabu, A. Gueguen, R. Dedryvere, and J.-M. Tarascon. *Li-S batteries: simple approaches for superior performance*. *Energy & Environmental Science* **6**, 176–182 (2013).
- [158] T. Reddy. *Linden's Handbook of Batteries*. Fourth edition. McGraw-Hill (2010).
- [159] P. H. L. Notten, J. H. G. Op het Veld, and J. R. G. van Beek. *Boostcharging Li-ion batteries: A challenging new charging concept*. *Journal of Power Sources* **145**, 89–94 (2005).

- [160] C. Barchasz, J.-C. Leprêtre, S. Patoux, and F. Alloin. *Revisiting TEGDME/DIOX Binary Electrolytes for Lithium/Sulfur Batteries: Importance of Solvation Ability and Additives*. Journal of The Electrochemical Society **160**, A430–A436 (2013).
- [161] Z. Lin, D. N. Fronczek, C. Nan, S. E. Choi, Y. Zhang, E. J. Cairns, and M.-K. Song. *Improved Sulfur/Lithium Sulfide Nano-composite Electrodes for Next-Generation Lithium Cells*. In *CalCharge Kickoff Event*. Berkeley, CA, USA (May 2013). <http://elib.dlr.de/88983/>. Retrieved 4/8/2014.
- [162] Z. Guo, X. Qiu, G. Hou, B. Y. Liaw, and C. Zhang. *State of health estimation for lithium ion batteries based on charging curves*. Journal of Power Sources **249**, 457–462 (2014).
- [163] A. J. Smith, J. C. Burns, D. Xiong, and J. R. Dahn. *Interpreting High Precision Coulometry Results on Li-ion Cells*. Journal of The Electrochemical Society **158**, A1136–A1142 (2011).
- [164] T. M. Bond, J. C. Burns, D. A. Stevens, H. M. Dahn, and J. R. Dahn. *Improving Precision and Accuracy in Coulombic Efficiency Measurements of Li-Ion Batteries*. Journal of The Electrochemical Society **160**, A521–A527 (2013).
- [165] Z. Lin, C. Nan, Y. Ye, J. Guo, J. Zhu, and E. J. Cairns. *High-performance lithium/sulfur cells with a bi-functionally immobilized sulfur cathode*. Nano Energy **9**, 408–416 (2014).
- [166] N. A. Cañas. *Fabrication and characterization of lithium-sulfur batteries*. Ph.D. thesis, Universität Stuttgart (September 2015). <http://elib.uni-stuttgart.de/opus/volltexte/2015/10207/>. Supervisor: K. A. Friedrich.
- [167] B. Pascucci. *Zyklensstabilität von Lithium-Schwefel-Hochenergie-Batterien für die Elektromobilität*. Master's thesis, Hochschule Esslingen (April 2012). Supervisor: G. Meichsner.
- [168] J. Ott, B. Völker, Y. Gan, R. M. McMeeking, and M. Kamlah. *A micromechanical model for effective conductivity in granular electrode structures*. Acta Mechanica Sinica **29**, 682–698 (2013).
- [169] X. Zhang, G. Rumierz, K. Humiston, C. Haire, T. Fields, M. Braswell, and R. Proctor. *Biaxially oriented porous membranes, composites, and methods of manufacture and use* (2011). WO patent app. PCT/US2011/028,019.
- [170] C. Peters, T. Mohr, D. Busch, and B. Schmitz. *Membrane file for batteries, having a shut-off function* (2011). U.S. patent app. 12/990,228.

- [171] J. Jung and T. Gottfreund. *Biaxially Oriented polyolefin Film Having Improved Surface Properties*. U.S. patent 7824600. Issued November 2, 2010.
- [172] I. Bauer, S. Thieme, J. Brückner, H. Althues, and S. Kaskel. *Reduced polysulfide shuttle in lithium-sulfur batteries using Nafion-based separators*. Journal of Power Sources **251**, 417–422 (2014).
- [173] M. Kunze, S. Jeong, G. B. Appetecchi, M. Schönhoff, M. Winter, and S. Passerini. *Mixtures of ionic liquids for low temperature electrolytes*. Electrochimica Acta **82**, 69–74 (2012).
- [174] J. Reiter, E. Paillard, L. Grande, M. Winter, and S. Passerini. *Physicochemical properties of N-methoxyethyl-N-methylpyrrolidinium ionic liquids with perfluorinated anions*. Electrochimica Acta **91**, 101–107 (2013).
- [175] F. Castiglione, A. Famulari, G. Raos, S. V. Meille, A. Mele, G. B. Appetecchi, and S. Passerini. *Pyrrolidinium-Based Ionic Liquids Doped with Lithium Salts: How Does Li⁺ Coordination Affect Its Diffusivity?* The Journal of Physical Chemistry B **118**, 13679–13688 (2014).
- [176] J. C. Burns, A. Kassam, N. N. Sinha, L. E. Downie, L. Solnickova, B. M. Way, and J. R. Dahn. *Predicting and Extending the Lifetime of Li-Ion Batteries*. Journal of The Electrochemical Society **160**, A1451–A1456 (2013).
- [177] S. Passerini et al. *Ionic Liquid-based Electrolytes for Next Generation Batteries*. In *Beyond Lithium Ion V conference proceedings*. Berkeley, CA, USA (2012). <http://bestar.lbl.gov/bli5/presentations/>. Retrieved 7/20/2014.
- [178] V. R. Subramanian and R. D. Braatz. *Current Needs in Electrochemical Engineering Education*. Interface **19**, 37–38 (2010).
- [179] E. A. Carter. *Challenges in Modeling Materials Properties Without Experimental Input*. Science **321**, 800–803 (2008).
- [180] Y. S. Meng and M. E. Arroyo-de Dompablo. *First principles computational materials design for energy storage materials in lithium ion batteries*. Energy & Environmental Science **2**, 589–609 (2009).
- [181] F. Calle-Vallejo and M. T. M. Koper. *First-principles computational electrochemistry: Achievements and challenges*. Electrochimica Acta **84**, 3–11 (2012).
- [182] G. K. Prasad and C. D. Rahn. *Model based identification of aging parameters in lithium ion batteries*. Journal of Power Sources **232**, 79–85 (2013).

- [183] X. Hu, S. Li, H. Peng, and F. Sun. *Robustness analysis of State-of-Charge estimation methods for two types of Li-ion batteries*. Journal of Power Sources **217**, 209–219 (2012).
- [184] G. Pilatowicz, H. Budde-Meiwes, D. Schulte, J. Kowal, Y. Zhang, X. Du, M. Salman, D. Gonzales, J. Alden, and D. U. Sauer. *Simulation of SLI Lead-Acid Batteries for SoC, Aging and Cranking Capability Prediction in Automotive Applications*. Journal of The Electrochemical Society **159**, A1410–A1419 (2012).
- [185] H. J. Bergveld, W. S. Kruijt, and P. H. L. Notten. *Battery Management Systems: Design by Modelling*. Number 1 in Philips Research Book Series. Springer (2005).
- [186] C. Fleischer, W. Waag, H.-M. Heyn, and D. U. Sauer. *On-line adaptive battery impedance parameter and state estimation considering physical principles in reduced order equivalent circuit battery models: Part 1. Requirements, critical review of methods and modeling*. Journal of Power Sources **260**, 276–291 (2014).
- [187] C. Fleischer, W. Waag, H.-M. Heyn, and D. U. Sauer. *On-line adaptive battery impedance parameter and state estimation considering physical principles in reduced order equivalent circuit battery models: Part 2. Parameter and state estimation*. Journal of Power Sources **262**, 457–482 (2014).
- [188] A. Seaman, T.-S. Dao, and J. McPhee. *A survey of mathematics-based equivalent-circuit and electrochemical battery models for hybrid and electric vehicle simulation*. Journal of Power Sources **256**, 410–423 (2014).
- [189] W. G. Bessler. *Electrochemistry and Transport in Solid Oxide Fuel Cells*. Habilitation, Ruprecht-Karls-Universität Heidelberg (2008).
- [190] A. Wiebelt, T. Isermeyer, T. Siebrecht, and T. Heckenberger. *Thermomanagement von Lithium-Ionen-Batterien*. Automobiltechnische Zeitschrift **111**, 500–504 (2009).
- [191] D. N. Fronczek and W. G. Bessler. *Insight into lithium-sulfur batteries: Elementary kinetic modeling and impedance simulation*. Journal of Power Sources **244**, 183–188 (2013).
- [192] A. F. Hofmann, D. N. Fronczek, and W. G. Bessler. *Mechanistic modeling of polysulfide shuttle and capacity loss in lithium-sulfur batteries*. Journal of Power Sources **259**, 300–310 (2014).
- [193] T. R. Ferguson and M. Z. Bazant. *Nonequilibrium Thermodynamics of Porous Electrodes*. Journal of The Electrochemical Society **159**, A1967–A1985 (2012).

- [194] C. A. Hellwig. *Modeling, simulation and experimental investigation of the thermal and electrochemical behavior of a LiFePO₄-based lithium-ion battery*. Ph.D. thesis, Universität Stuttgart (November 2013). <http://elib.uni-stuttgart.de/opus/volltexte/2013/8685/>. Supervisor: W. G. Bessler.
- [195] K. Kumaresan. *Theoretical Analysis of the Discharge Performance of Lithium Ion and Lithium Sulfur Cells*. Ph.D. thesis, College of Engineering and Mining, University of South Carolina (2008). <http://search.proquest.com/docview/304459386>. Supervisor: R. E. White.
- [196] K. Kumaresan, Y. V. Mikhaylik, and R. E. White. *A mathematical model for a lithium-sulfur cell*. Journal of The Electrochemical Society **155**, A576–A582 (2008).
- [197] Y. V. Mikhaylik, I. Kovalev, R. Schock, K. Kumaresan, J. Xu, and J. Affinito. *High Energy Rechargeable Li-S Cells for EV Application: Status, Remaining Problems and Solutions*. In Z. Ogumi, N. Dudney, and S. Narayanan (Eds.), *216th ECS Meeting*, volume 25 (2009). <http://link.aip.org/link/ECSTF8/v25/i35/p23/s1>.
- [198] M. Ghaznavi and P. Chen. *Sensitivity analysis of a mathematical model of lithium-sulfur cells: Part I: Applied discharge current and cathode conductivity*. Journal of Power Sources **257**, 394–401 (2014).
- [199] M. Ghaznavi and P. Chen. *Sensitivity analysis of a mathematical model of lithium-sulfur cells: Part II: Precipitation reaction kinetics and sulfur content*. Journal of Power Sources **257**, 402–411 (2014).
- [200] S. Erhard, C. Gass, and A. Jossen. *Discharge Behavior of a Lithium-Sulfur Cell including Disproportionation and Precipitation*. In *14th Ulm ElectroChemical Talks* (2014).
- [201] J. Newman and W. Tiedemann. *Porous-electrode theory with battery applications*. AIChE Journal **21**, 25–41 (1975).
- [202] M. Landstorfer and T. Jacob. *Mathematical modeling of intercalation batteries at the cell level and beyond*. Chemical Society Reviews **42**, 3234–3252 (2013).
- [203] A. Latz and J. Zausch. *Thermodynamic consistent transport theory of Li-ion batteries*. Journal of Power Sources **196**, 3296–3302 (2011).
- [204] D. Danilov and P. H. L. Notten. *Mathematical modelling of ionic transport in the electrolyte of Li-ion batteries*. Electrochimica Acta **53**, 5569–5578 (2008).
- [205] A. Nyman, M. Behm, and G. Lindbergh. *Electrochemical characterisation and modelling of the mass transport phenomena in LiPF₆–EC–EMC electrolyte*. Electrochimica Acta **53**, 6356–6365 (2008).

- [206] V. Z. Zadin, D. Brandell, H. Kasemägi, A. Aabloo, and J. O. Thomas. *Finite element modelling of ion transport in the electrolyte of a 3D-microbattery*. Solid State Ionics **192**, 279–283 (2011).
- [207] C. W. Monroe and C. Delacourt. *Continuum transport laws for locally non-neutral concentrated electrolytes*. Electrochimica Acta **114**, 649–657 (2013).
- [208] J. Liu and C. W. Monroe. *Solute-volume effects in electrolyte transport*. Electrochimica Acta **135**, 447–460 (2014).
- [209] C. Delacourt. *Modeling Li-Ion Batteries with Electrolyte Additives or Contaminants*. Journal of The Electrochemical Society **160**, A1997–A2004 (2013).
- [210] L. Shen and Z. Chen. *Critical review of the impact of tortuosity on diffusion*. Chemical Engineering Science **62**, 3748–3755 (2007).
- [211] R. J. Kee, M. E. Coltrin, and P. Glarborg. *Chemically Reacting Flow*. First edition. John Wiley & Sons (2003).
- [212] A. Latz and J. Zausch. *Thermodynamic derivation of a Butler-Volmer model for intercalation in Li-ion batteries*. Electrochimica Acta **110**, 358–362 (2013).
- [213] S. Srinivasan. *Fuel Cells*, chapter 2.1 Double layer at electrode/electrolyte interfaces. First edition. Springer (2006).
- [214] W. Nernst. *Die elektromotorische Wirksamkeit der Ionen*. Zeitschrift für Physikalische Chemie **4**, 129–181 (1889).
- [215] J. P. Neidhardt. *Nickel oxidation in Solid Oxide Cells*. Ph.D. thesis, Universität Stuttgart (January 2013). <http://elib.uni-stuttgart.de/opus/volltexte/2014/8844/>. Supervisor: W. G. Bessler.
- [216] R. Kelling, J. Bickel, U. Nieken, and P. A. Zegeling. *An adaptive moving grid method for solving convection dominated transport equations in chemical engineering*. Computers & Chemical Engineering **71**, 467–477 (2014).
- [217] E. Bohn, T. Eckl, M. Kamlah, and R. McMeeking. *A Model for Lithium Diffusion and Stress Generation in an Intercalation Storage Particle with Phase Change*. Journal of The Electrochemical Society **160**, A1638–A1652 (2013).
- [218] E. V. Shilko, S. G. Psakhie, S. Schmauder, V. L. Popov, S. V. Astafurov, and A. Y. Smolin. *Overcoming the limitations of distinct element method for multiscale modeling of materials with multimodal internal structure*. Computational Materials Science **102**, 267 – 285 (2015).

- [219] R. R. Balokhonov, V. A. Romanova, S. Schmauder, and E. Schwab. *Mesoscale analysis of deformation and fracture in coated materials*. Computational Materials Science **64**, 306–311 (2012).
- [220] H.-S. Ryu, H.-J. Ahn, K.-W. Kim, J.-H. Ahn, and J.-Y. Lee. *Discharge process of Li/PVdF/S cells at room temperature*. Journal of Power Sources **153**, 360–364 (2006).
- [221] Y. Diao, K. Xie, S. Xiong, and X. Hong. *Shuttle phenomenon – The irreversible oxidation mechanism of sulfur active material in Li-S battery*. Journal of Power Sources **235**, 181–186 (2013).
- [222] M. Huber, W. Säckel, M. Hirschler, S. M. Hassanzadeh, and U. Nieken. *Modeling the Dynamics of Partial Wetting*. In M. Bischoff, E. Ramm, E. Oñate, R. Owen, and P. Wriggers (Eds.), *Particle-based Methods III: Fundamentals and Applications*, pp. 470–481 (2013). <http://dspace.library.uu.nl/handle/1874/309683>.
- [223] P. Albertus, G. Girishkumar, B. McCloskey, R. S. Sánchez-Carrera, B. Kozinsky, J. Christensen, and A. C. Luntz. *Identifying Capacity Limitations in the Li/Oxygen Battery Using Experiments and Modeling*. Journal of The Electrochemical Society **158**, A343–A351 (2011).
- [224] P. Arora, R. E. White, and M. Doyle. *Capacity Fade Mechanisms and Side Reactions in Lithium-Ion Batteries*. Journal of The Electrochemical Society **145**, 3647–3667 (1998).
- [225] M. Wohlfahrt-Mehrens, C. Vogler, and J. Garche. *Aging mechanisms of lithium cathode materials*. Journal of Power Sources **127**, 58–64 (2004).
- [226] R. Deshpande, M. Verbrugge, Y.-T. Cheng, J. Wang, and P. Liu. *Battery Cycle Life Prediction with Coupled Chemical Degradation and Fatigue Mechanics*. Journal of The Electrochemical Society **159**, A1730–A1738 (2012).
- [227] M. Dubarry, C. Truchot, and B. Y. Liaw. *Synthesize battery degradation modes via a diagnostic and prognostic model*. Journal of Power Sources **219**, 204–216 (2012).
- [228] P. Arora, M. Doyle, and R. E. White. *Mathematical Modeling of the Lithium Deposition Overcharge Reaction in Lithium-Ion Batteries Using Carbon-Based Negative Electrodes*. Journal of The Electrochemical Society **146**, 3543–3553 (1999).
- [229] Z. Li, L. Lu, M. Ouyang, and Y. Xiao. *Modeling the capacity degradation of LiFePO₄/graphite batteries based on stress coupling analysis*. Journal of Power Sources **196**, 9757–9766 (2011).

- [230] A. P. Schmidt, M. Bitzer, A. W. Imre, and L. Guzzella. *Model-based distinction and quantification of capacity loss and rate capability fade in Li-ion batteries*. Journal of Power Sources **195**, 7634–7638 (2010).
- [231] S. Renganathan, G. Sikha, S. Santhanagopalan, and R. E. White. *Theoretical Analysis of Stresses in a Lithium Ion Cell*. Journal of The Electrochemical Society **157**, A155–A163 (2010).
- [232] D. G. Goodwin, H. K. Moffat, R. L. Speth, et al. *Cantera: An object-oriented software toolkit for chemical kinetics, thermodynamics, and transport processes*. Available at <http://www.cantera.org> (2013). Version 2.0.2.
- [233] I. Berg et al. *muparser - fast math parser library*. Available at <http://muparser.beltoforion.de/> (2013). Version 2.2.2.
- [234] Konrad-Zuse-Zentrum für Informationstechnik Berlin. *Limex*. Available at <http://www.zib.de/de/numerik/software/codelib/ivpode.html> (2004). Version 4.3A.
- [235] P. Deuflhard, E. Hairer, and J. Zugck. *One-step and extrapolation methods for differential-algebraic systems*. Numerische Mathematik **51**, 501–516 (1987).
- [236] J. H. Ferziger and M. Perić. *Computational methods for fluid dynamics*. Third edition. Springer (2002).
- [237] W. G. Bessler. *Rapid Impedance Modeling via Potential Step and Current Relaxation Simulations*. Journal of The Electrochemical Society **154**, B1186–B1191 (2007).
- [238] W. M. Haynes and D. R. Lide (Eds.). *CRC Handbook of Chemistry and Physics*. 92nd edition. CRC Press (2012).
- [239] G. B. Less, J. H. Seo, S. Han, A. M. Sastry, J. Zausch, A. Latz, S. Schmidt, C. Wieser, D. Kehrwald, and S. Fell. *Micro-Scale Modeling of Li-Ion Batteries: Parameterization and Validation*. Journal of The Electrochemical Society **159**, A697–A704 (2012).
- [240] P. R. Bevington and D. K. Robinson. *Data Reduction and Error Analysis for the Physical Sciences*. Third edition. McGraw-Hill (2002).
- [241] E. Jones, T. Oliphant, P. Peterson, et al. *SciPy: Open source scientific tools for Python*. Available at <http://www.scipy.org/> (2001–2014). Version 0.13.
- [242] A. J. Durán, M. Pérez, and J. L. Varona. *The Misfortunes of a Trio of Mathematicians Using Computer Algebra Systems. Can We Trust in Them?* Notices of the AMS **61**, 1249–1252 (2014).

- [243] J. N. Reimers. *Algorithmic Improvements and PDE Decoupling, for the Simulation of Porous Electrode Cells*. Journal of The Electrochemical Society **160**, A811–A818 (2013).
- [244] S. S. Jeong, Y. T. Lim, Y. J. Choi, G. B. Cho, K. W. Kim, H. J. Ahn, and K. K. Cho. *Electrochemical properties of lithium sulfur cells using PEO polymer electrolytes prepared under three different mixing conditions*. Journal of Power Sources **174**, 745–750 (2007).
- [245] M. E. Wieser and T. B. Coplen. *Atomic weights of the elements*. Pure and Applied Chemistry **83**, 359–396 (2009). IUPAC Technical Report.
- [246] Wikipedia contributors. *Polypropylene – Wikipedia, The Free Encyclopedia*. published online (2014). <http://en.wikipedia.org/w/index.php?title=Polypropylene&oldid=631394105>. Retrieved 10/29/2014.
- [247] K. C. Mills (Ed.). *Thermodynamic data for inorganic sulphides, selenides and tellurides*, chapter Lithium–sulphur, pp. 413–414. First edition. Butterworths, London (1974).
- [248] S. Hunsicker, R. O. Jones, and G. Ganteför. *Rings and chains in sulfur cluster anions S^- to S_9^- : Theory (simulated annealing) and experiment (photoelectron detachment)*. The Journal of Chemical Physics **102**, 5917–5936 (1995).
- [249] S. L. Candelaria, Y. Shao, W. Zhou, X. Li, J. Xiao, J.-G. Zhang, Y. Wang, J. Liu, J. Li, and G. Cao. *Nanostructured carbon for energy storage and conversion*. Nano Energy **1**, 195–220 (2012).
- [250] J. Gamby, P. L. Taberna, P. Simon, J. F. Fauvarque, and M. Chesneau. *Studies and characterisations of various activated carbons used for carbon/carbon supercapacitors*. Journal of Power Sources **101**, 109–116 (2001).
- [251] A. G. Pandolfo and A. F. Hollenkamp. *Carbon properties and their role in supercapacitors*. Journal of Power Sources **157**, 11–27 (2006).
- [252] E. Frackowiak and F. Béguin. *Carbon materials for the electrochemical storage of energy in capacitors*. Carbon **39**, 937–950 (2001).
- [253] I. J. Ong and J. Newman. *Double-Layer Capacitance in a Dual Lithium Ion Insertion Cell*. Journal of The Electrochemical Society **146**, 4360–4365 (1999).
- [254] K. Kinoshita. *Carbon: Electrochemical and Physicochemical Properties*. First edition. Wiley-Interscience (1988).

- [255] M. Doyle, J. Newman, A. S. Gozdz, C. N. Schmutz, and J.-M. Tarascon. *Comparison of Modeling Predictions with Experimental Data from Plastic Lithium Ion Cells*. Journal of The Electrochemical Society **143**, 1890–1903 (1996).
- [256] Celgard, LLC, Charlotte, NC, USA. *Product data sheet*. published online (November 2009). http://www.celgard.com/pdf/library/Celgard_Product_Comparison_10002.pdf. Retrieved 10/20/2014.
- [257] I. V. Thorat, D. E. Stephenson, N. A. Zacharias, K. Zaghib, J. N. Harb, and D. R. Wheeler. *Quantifying tortuosity in porous Li-ion battery materials*. Journal of Power Sources **188**, 592–600 (2009).
- [258] FMC Lithium, Charlotte, NC, USA. *Product data sheet*. published online. <http://www.fmclithium.com/Portals/FMCLithium/content/docs/DataSheet/QS-PDS-2000%20r0.pdf>. Retrieved 10/20/2014.
- [259] S. Xiong, K. Xie, Y. Diao, and X. Hong. *Properties of surface film on lithium anode with LiNO₃ as lithium salt in electrolyte solution for lithium-sulfur batteries*. Electrochimica Acta **83**, 78–86 (2012).
- [260] K. Saito, M. Arakawa, S. Tobishima, and J. Yamaki. *Specific surface-area measurement of lithium anode in rechargeable lithium cells*. Journal of Power Sources **72**, 111–117 (1998).
- [261] V. Lesch, S. Jeremias, A. Moretti, S. Passerini, A. Heuer, and O. Borodin. *A Combined Theoretical and Experimental Study of the Influence of Different Anion Ratios on Lithium Ion Dynamics in Ionic Liquids*. The Journal of Physical Chemistry B **118**, 7367–7375 (2014).
- [262] N. A. Cañas, K. Hirose, B. Pascucci, N. Wagner, K. A. Friedrich, and R. Hiesgen. *Investigations of lithium-sulfur batteries using electrochemical impedance spectroscopy*. Electrochimica Acta **97**, 42–51 (2013).
- [263] J. Illig, M. Ender, T. Chrobak, J. P. Schmidt, D. Klotz, and E. Ivers-Tiffée. *Separation of Charge Transfer and Contact Resistance in LiFePO₄-Cathodes by Impedance Modeling*. Journal of The Electrochemical Society **159**, A952–A960 (2012).
- [264] M. A. Lowe, J. Gao, and H. D. Abruna. *Mechanistic insights into operational lithium-sulfur batteries by in situ X-ray diffraction and absorption spectroscopy*. RSC Advances **4**, 18347–18353 (2014).
- [265] X. Feng, M.-K. Song, W. C. Stolte, D. Gardenghi, D. Zhang, X. Sun, J. Zhu, E. J. Cairns, and J. Guo. *Understanding the degradation mechanism of rechargeable*

lithium/sulfur cells: a comprehensive study of the sulfur-graphene oxide cathode after discharge-charge cycling. Physical Chemistry Chemical Physics **16**, 16931–16940 (2014).

- [266] A. Noda, K. Hayamizu, and M. Watanabe. *Pulsed-Gradient Spin-Echo 1H and ^{19}F NMR Ionic Diffusion Coefficient, Viscosity, and Ionic Conductivity of Non-Chloroaluminate Room-Temperature Ionic Liquids.* The Journal of Physical Chemistry B **105**, 4603–4610 (2001).
- [267] S. G. Stewart and J. Newman. *The Use of UV/vis Absorption to Measure Diffusion Coefficients in LiPF₆ Electrolytic Solutions.* Journal of The Electrochemical Society **155**, F13–F16 (2008).
- [268] L. Terborg, S. Weber, S. Passerini, M. Winter, U. Karst, and S. Nowak. *Development of gas chromatographic methods for the analyses of organic carbonate-based electrolytes.* Journal of Power Sources **245**, 836–840 (2014).
- [269] L. Terborg, S. Nowak, S. Passerini, M. Winter, U. Karst, P. R. Haddad, and P. N. Nesterenko. *Ion chromatographic determination of hydrolysis products of hexafluorophosphate salts in aqueous solution.* Analytica Chimica Acta **714**, 121–126 (2012).
- [270] T. Danner. *Modeling and experimental investigation of transport processes in the porous cathode of aqueous Li-air batteries.* Ph.D. thesis, Universität Stuttgart (September 2014). <http://elib.uni-stuttgart.de/opus/volltexte/2015/10071/>. Supervisor: W. G. Bessler.
- [271] N. S. K. Gunda, H.-W. Choi, A. Berson, B. Kenney, K. Karan, and S. K. Pharoah, Jon G. and Mitra. *Focused ion beam-scanning electron microscopy on solid-oxide fuel-cell electrode: Image analysis and computing effective transport properties.* Journal of Power Sources **196**, 3592–3603 (2011).
- [272] G. M. Goldin, A. M. Colclasure, A. H. Wiedemann, and R. J. Kee. *Three-dimensional particle-resolved models of Li-ion batteries to assist the evaluation of empirical parameters in one-dimensional models.* Electrochimica Acta **64**, 118–129 (2012).
- [273] J. Deng, G. J. Wagner, and R. P. Muller. *Phase Field Modeling of Solid Electrolyte Interface Formation in Lithium Ion Batteries.* Journal of The Electrochemical Society **160**, A487–A496 (2013).
- [274] K. Leung. *Electronic Structure Modeling of Electrochemical Reactions at Electrode/Electrolyte Interfaces in Lithium Ion Batteries.* The Journal of Physical Chemistry C **117**, 1539–1547 (2013).

- [275] M. B. Pinson and M. Z. Bazant. *Theory of SEI Formation in Rechargeable Batteries: Capacity Fade, Accelerated Aging and Lifetime Prediction*. Journal of The Electrochemical Society **160**, A243–A250 (2013).
- [276] S. Schmauder. *Computational Mechanics*. Annual Review of Materials Research **32**, 437–465 (2002).
- [277] H. Yamin, A. Gorenstein, J. Penciner, Y. Sternberg, and E. Peled. *Lithium Sulfur Battery – Oxidation/reduction mechanisms of polysulfides in THF solutions*. Journal of The Electrochemical Society **135**, 1045–1048 (1988).
- [278] R. Elazari, G. Salitra, Y. Talyosef, J. Grinblat, C. Scordilis-Kelley, A. Xiao, J. Affinito, and D. Aurbach. *Morphological and Structural Studies of Composite Sulfur Electrodes upon Cycling by HRTEM, AFM and Raman Spectroscopy*. Journal of The Electrochemical Society **157**, A1131–A1138 (2010).
- [279] M. R. Busche, P. Adelhelm, H. Sommer, H. Schneider, K. Leitner, and J. Janek. *Systematical electrochemical study on the parasitic shuttle-effect in lithium-sulfur-cells at different temperatures and different rates*. Journal of Power Sources **259**, 289–299 (2014).
- [280] C. Forgez, D. V. Do, G. Friedrich, M. Morcrette, and C. Delacourt. *Thermal modeling of a cylindrical LiFePO₄/graphite lithium-ion battery*. Journal of Power Sources **195**, 2961–2968 (2010).
- [281] N. Tanaka and W. G. Bessler. *Numerical investigation of kinetic mechanism for runaway thermo-electrochemistry in lithium-ion cells*. Solid State Ionics **262**, 70–73 (2014).
- [282] N. Tanaka. *Modeling and Simulation of Thermo-Electrochemistry of Thermal Runaway in Lithium-Ion Batteries*. Ph.D. thesis, Universität Stuttgart (August 2014). <http://elib.uni-stuttgart.de/opus/volltexte/2015/10112/>. Supervisor: W. G. Bessler.
- [283] H.-L. Wu, L. A. Huff, and A. A. Gewirth. *In Situ Raman Spectroscopy of Sulfur Speciation in Lithium-Sulfur Batteries*. ACS Applied Materials & Interfaces **7**, 1709–1719 (2015).
- [284] M. Barghamadi, A. Kapoor, and C. Wen. *A Review on Li-S Batteries as a High Efficiency Rechargeable Lithium Battery*. Journal of The Electrochemical Society **160**, A1256–A1263 (2013).
- [285] L. F. Nazar, M. Cuisinier, and Q. Pang. *Lithium-sulfur batteries*. MRS Bulletin **39**, 436–442 (5 2014).

- [286] A. Ferrese and J. Newman. *Modeling Lithium Movement over Multiple Cycles in a Lithium-Metal Battery*. Journal of The Electrochemical Society **161**, A948–A954 (2014).
- [287] H. Sano, H. Sakaebe, H. Senoh, and H. Matsumoto. *Effect of Current Density on Morphology of Lithium Electrodeposited in Ionic Liquid-Based Electrolytes*. Journal of The Electrochemical Society **161**, A1236–A1240 (2014).
- [288] The Electrochemical Energy Storage Technical Team. *Electrochemical Energy Storage Technical Team Roadmap*. Technical report, U.S. DRIVE (June 2013). <http://www.uscar.org/guest/partnership/1/us-drive>. Retrieved 7/16/2014.
- [289] T. Greszler. *Li-Air and Li-Sulfur in an Automotive System Context*. In *Beyond Lithium Ion V* (2012). <http://bestar.lbl.gov/bli5/presentations/>. Retrieved 7/20/2014.
- [290] L. Zhang, Z. Liu, G. Cui, and L. Chen. *Biomass-derived materials for electrochemical energy storages*. Progress in Polymer Science pp. – (2014).
- [291] M. Abu Mallouh, E. Abdelhafez, M. Salah, M. Hamdan, B. Surgenor, and M. Youssef. *Model development and analysis of a mid-sized hybrid fuel cell/battery vehicle with a representative driving cycle*. Journal of Power Sources **260**, 62–71 (2014).
- [292] D. Cericola and R. Kötz. *Hybridization of rechargeable batteries and electrochemical capacitors: Principles and limits*. Electrochimica Acta **72**, 1–17 (2012).
- [293] H. S. Choi and C. R. Park. *Theoretical guidelines to designing high performance energy storage device based on hybridization of lithium-ion battery and supercapacitor*. Journal of Power Sources **259**, 1–14 (2014).
- [294] J. Li and M. A. Danzer. *Optimal charge control strategies for stationary photovoltaic battery systems*. Journal of Power Sources **258**, 365–373 (2014).
- [295] Energie-Forschungszentrum Niedersachsen. *Eignung von Speichertechnologien zum Erhalt der Systemsicherheit*. published online (March 2013). [https://www.efzn.de/index.php?id=238&tx_wiwiprojekte_pi4\[showUid\]=205&no_cache=1](https://www.efzn.de/index.php?id=238&tx_wiwiprojekte_pi4[showUid]=205&no_cache=1). Retrieved 4/30/2014.
- [296] B. Huskinson, M. P. Marshak, C. Suh, S. Er, M. R. Gerhardt, C. J. Galvin, X. Chen, A. Aspuru-Guzik, R. G. Gordon, and M. J. Aziz. *A metal-free organic-inorganic aqueous flow battery*. Nature **505**, 195–198 (2014).

- [297] EnerVault. *Safe, Reliable, Cost-Effective Energy Storage*. company website. <http://www.enervault.com/>. Retrieved 7/22/2014.
- [298] E. D. Wachsman and K. T. Lee. *Lowering the Temperature of Solid Oxide Fuel Cells*. Science **334**, 935–939 (2011).
- [299] M. A. Laguna-Bercero. *Recent advances in high temperature electrolysis using solid oxide fuel cells: A review*. Journal of Power Sources **203**, 4–16 (2012).
- [300] Y. Zhao, C. Xia, L. Jia, Z. Wang, H. Li, J. Yu, and Y. Li. *Recent progress on solid oxide fuel cell: Lowering temperature and utilizing non-hydrogen fuels*. International Journal of Hydrogen Energy **38**, 16498–16517 (2013).
- [301] D. K. Karthikeyan, G. Sikha, and R. E. White. *Thermodynamic model development for lithium intercalation electrodes*. Journal of Power Sources **185**, 1398–1407 (2008).
- [302] P. K. Janert. *Gnuplot in Action – Understanding Data with Graphs*. Manning Publications (2009).

Own publications

Peer-reviewed publications

- [P1] J. P. Neidhardt, D. N. Fronczek, T. Jahnke, T. Danner, B. Horstmann, and W. G. Bessler. *A flexible framework for modeling multiple solid, liquid and gaseous phases in batteries and fuel cells.* Journal of The Electrochemical Society **159**, A1528–A1542 (2012).
- [P2] D. N. Fronczek and W. G. Bessler. *Insight into lithium-sulfur batteries: Elementary kinetic modeling and impedance simulation.* Journal of Power Sources **244**, 183–188 (2013). 16th International Meeting on Lithium Batteries.
- [P3] A. F. Hofmann, D. N. Fronczek, and W. G. Bessler. *Mechanistic modeling of polysulfide shuttle and capacity loss in lithium-sulfur batteries.* Journal of Power Sources **259**, 300–310 (2014).
- [P4] N. A. Cañas, D. N. Fronczek, N. Wagner, A. Latz, and K. A. Friedrich. *Experimental and Theoretical Analysis of Products and Reaction Intermediates of Lithium-Sulfur Batteries.* The Journal of Physical Chemistry C **118**, 12106–12114 (2014).

An updated list of my publications can
be found on my ORCID profile page:
<http://orcid.org/0000-0003-4924-5415>



Presentations

- [C1] C. Hellwig, D. N. Fronczek, S. Sörgel, and W.G. Bessler. *Physically based modeling and simulation of a LiFePO₄-based lithium-ion battery* (poster). 8th Symposium on Fuel Cell and Battery Modeling and Experimental Validation. March 8–9, 2011, Jülich, Germany.
- [C2] D.N. Fronczek. *Modeling of electrochemistry and transport in the lithium-sulfur battery* (oral presentation). HIU meeting series. September 7, 2011. Stuttgart/Ulm/Karlsruhe, Germany.
- [C3] D.N. Fronczek and W.G. Bessler. *Lithium/sulfur batteries: global and elementary modeling approaches* (oral presentation). 9th Symposium on Fuel Cell and Battery Modeling and Experimental Validation. April 2–4, 2012, Sursee, Switzerland.
- [C4] D.N. Fronczek and W.G. Bessler. *Insight Into Li/S Batteries: Elementary Kinetic Modeling and Impedance Simulation* (poster). 16th International Meeting on Lithium Batteries. June 17–22, 2012, Jeju, South Korea.
- [C5] D.N. Fronczek and W.G. Bessler. *A virtual Li/S battery: Modeling, simulation and computer-aided development* (oral presentation). Next Generation Batteries 2012. July 18–20, 2012, Boston, MA, USA.
- [C6] D.N. Fronczek. *Electrochemical energy storage – an overview* (lecture). Diablo Valley College. December 15, 2012, Concord, CA, USA.
- [C7] D.N. Fronczek, S. E. Choi, A. Latz, W.G. Bessler, and E.J. Cairns. *Next Generation Battery Electrochemistry Analyzed: Towards a Validated Computational Model of the Lithium/Sulfur Cell* (oral presentation). 224th Meeting of the Electrochemical Society. October 28–November 2, 2013, San Francisco, CA, USA.
- [C8] D.N. Fronczek, A. Latz, E.J. Cairns, and W.G. Bessler. *Design and Validation of a Computational Model of the Lithium/Sulfur Cell* (poster). 17th International Meeting on Lithium Batteries. June 10–14, 2014, Como, Italy.

Contributions to miscellaneous works

- [X1] D. N. Fronczek, T. Danner et al. *Batterien im Einsatz*. tecTV (Verein Deutscher Ingenieure e. V.), March 7, 2012. <http://www.youtube.com/watch?v=WtJafStGkas>.
- [X2] D. N. Fronczek, T. Danner, B. Horstmann, and W. G. Bessler. *Modeling the next battery generation: Lithium-sulfur and lithium-air cells*. Kraftwerk Batterie. March 6–7, 2012, Münster, Germany.
- [X3] J. P. Neidhardt, T. Jahnke, D. N. Fronczek, T. Danner, B. Horstmann, and W. G. Bessler. *A flexible framework for modeling multiple solid, liquid and gaseous phases in batteries and fuel cells*. 9th Symposium on Fuel Cell and Battery Modeling and Experimental Validation (ModVal 9). April 2–4, 2012, Sursee, Switzerland.
- [X4] E. J. Cairns et al. *Beyond Lithium Ion: The Lithium/Sulfur Cell*. Beyond Lithium Ion V. June 5–7, 2012, Berkeley, CA, USA.
- [X5] J. P. Neidhardt, D. N. Fronczek, T. Jahnke, T. Danner, B. Horstmann, and W. G. Bessler. *A flexible modeling framework for multi-phase management in SOFCs and other electrochemical cells*. 10th European SOFC Forum 2012. June 26–29, 2012, Luzern, Switzerland.
- [X6] A. F. Hofmann, D. N. Fronczek, A. Latz, and W. G. Bessler. *Simulating the polysulfide shuttle effect: a thermodynamically consistent, fully reversible, numerical Li/S-battery model*. 10th Symposium for Fuel Cell and Battery Modeling and Experimental Validation (ModVal 10). March 18–20, 2013, Münster, Germany.
- [X7] Z. Lin, D. N. Fronczek, C. Nan, S. E. Choi, Y. Zhang, E. J. Cairns, and M.-K. Song. *Improved Sulfur/Lithium Sulfide Nano-composite Electrodes for Next-Generation Lithium Cells*. CalCharge Kickoff Event. May 3, 2013, Berkeley, CA, USA.
- [X8] A. F. Hofmann, A. Latz, D. N. Fronczek, and W. G. Bessler. *Simulating the polysulfide shuttle effect: a thermodynamically consistent, fully reversible, numerical Li/S-battery model*. 2nd International Conference on Materials for Energy (EnMat II). May 12–16, 2013, Karlsruhe, Germany.
- [X9] N. A. Cañas, B. Pascucci, N. Wagner, and K. A. Friedrich. *On the understanding and improvement of high capacity lithium/sulfur (Li/S) batteries*. 14th Ulm Electro-Chemical Talks (UECT2014). June 23–26, 2012, Ulm, Germany.

Events and workshops without original contribution

- [E1] *Next-generation battery activities at DLR.* Hannover Messe. April 4–6, 2011, Hannover, Germany.
- [E2] HE-Lion Battery school. July 20–21, 2011, Rauschholzhausen, Germany.
- [E3] First convention of the Helmholtz Institute Ulm for Electrochemical Energy Storage. October 20–22, 2011, Ulm, Germany.
- [E4] X-Raptor business game: Setup and commissioning of an intelligent factory. February 16–17, 2012, Düsseldorf, Germany.
- [E5] Beyond Lithium Ion V conference. June 5–7, 2012, Berkeley, CA, USA.
- [E6] MIC/ZAE Workshop: *Charakterisierung poröser Materialien.* April 8–9, 2014, Würzburg, Germany.
- [E7] 14th Ulm ElectroChemical Talks (UECT2014). June 23–26, 2014, Ulm, Germany.

Academic résumé

of Dipl.-Phys. David Norman Fronczek
born on November 23rd, 1983
in Würzburg, Germany



Education and research

01/2011–12/2014	Graduate student at the University of Stuttgart, supervisor: Prof. Dr. Wolfgang G. Bessler
01/2011–12/2014	Researcher at the German Aerospace Center (DLR), Institute of Engineering Thermodynamics, Stuttgart, Germany
04/2012–05/2013	Visiting research scholar at Lawrence Berkeley National Laboratory (LBNL), Berkeley, CA, USA
06/2013–12/2014	Associated researcher at the Helmholtz Institute Ulm for Electro- chemical Energy Storage (HIU), Ulm, Germany

10/2003–10/2010	Undergraduate student at the University of Würzburg, degrees earned: Physik-Diplom, 1. Staatsexamen Biologie/Physik
11/2008–10/2009	Diplom student at the Rudolf-Virchow-Center for Experimental Biomedicine (RVZ), Würzburg, Germany, supervisors: Dr. Ingrid Teßmer & Prof. Dr. Bert Hecht
11/2007–07/2008	Intern student at ZAE Bayern, Würzburg, Germany

09/1994–07/2003	Franz-Miltenberger-Gymnasium Bad Brückenau
-----------------	--

Honors and awards

- Graduate fellow of the Foundation of the German Industry (sdw)
- Awardee of grants by the German Academic Exchange Service (DAAD) and the Italian Elettrochimica ed Energia (e&e)

Trivia

- You are reading the 154th revision of this document.
- total number of DENIS simulation runs: 3494
- total number of successful DENIS runs: 1824
- data recorded and generated: 61.7 GB
- coin cells assembled: 237
- coin cells tested: 178
- parts, chemicals, and services ordered: 76
- number of e-mails sent (received): 2690 (9976)
- lines of code written or modified by the author: 14 628
(approx. 23 % of the simulation framework in 2014)
- number of commits to the code and model repository: 209
- total distance traveled for this thesis: 87 934 km
(not including the daily commute)
- different domiciles 2011–2014: 6
- LinkedIn contacts collected: 137
- cups of coffee consumed at work: 1022
- Scientific wordles (like the one on page) prepared and designed: 12
- This document was produced using free software: LyX/LaTeX for typesetting and gnuplot, Inkscape, chemfig, and the GIMP for illustrations.

Acknowledgments

First and foremost I would like to thank my supervisor Wolfgang Bessler. Already in 2011 you gave me a great start into this project. You did so not only by choosing a great topic to work on and teaching me what I needed to know, but also by trusting and believing in me right from the start. During the entire past four years you have been both demanding and promoting, determined yet open-minded, and always, always very cordial and encouraging.

Next, I would like to thank Elton Cairns, not only for hosting me at LBNL, but also for letting me tap from his enormous well of experience and expertise in long discussions, e-mails, and phone calls. You taught me to always keep the next goal in mind, but also look at the big picture, making me a better scientist.

Also, I would like to thank Arnulf Latz and Andreas Friedrich for hosting and funding me during my entire time at DLR and HIU, but particularly for your continued support and advice.

Finally, many thanks go to Stefano Passerini for joining the board of examiners.

Of course many more people contributed to the success of this work. In my group at DLR I am most thankful to (in no particular order) Timo Danner, Jonathan Neidhardt, Birger Horstmann, Christian Hellwig, Andreas Hofmann, and Klaus Göckelmann, who all directly supported my modeling work one way or the other. In my group at LBNL, I am most indebted to Chris Choi who has been working for me for nine months and made valuable contributions to almost all aspects of the experimental part of this work, to Kunpeng Cai who voluntarily and most comradely helped me to get started in the U.S. in general and at LBNL in particular, and to Min-Kyu Song from whom I could learn so much, but also to Caiyun Nan, Wujun Fu, and Zhan Lin who all have been working closely with me.

For many a good discussion, great ideas, and contributions I would like to thank Natalia Cañas, Vitaliy Yurkiv, Moritz Henke, Nico Hörmann, Valene Cruz, Bruno Scrosati, Ulrich Sauter, Jake Christensen, Michel Fouré, Burçak Ebin, Anthony Ferrese, John Newman, Venkat Srinivasan, Peter Therkelsen, Rutooj Desphande, Zhihui Wang, Charles Delacourt, Ulrike Vogl, and Simon Lux, the latter also for providing Raman spectroscopy data, and Xiangyun Song for the TEM images.

Also, I would like to thank all the people in the research groups of Arnulf Latz, Andreas Friedrich and Norbert Wagner in Stuttgart; the groups of Vince Battaglia, Gao Liu, Venkat Srinivasan, Jeff Urban, and John Kerr in Berkeley and the groups of Arnulf Latz, Max Fichtner, and Stefano Passerini in Ulm. Without the support and companionship of all of you, my time as a Ph.D. student would have been considerably less productive and most certainly less fun.

Thankfully, equipment and materials required for my experimental activities were provided by UC Berkeley and Lawrence Berkeley National Laboratory. In addition, I would like to acknowledge the funding I received during the past years by the German Academic Exchange Service (DAAD), the Elettrochimica ed Energia (e&e), and especially the Foundation of the German Industry (sdw). I am most thankful for the support of the sdw without which this work might still have been possible – but spending a year in the U.S. and raising two children at the same time would not.

In the end, I owe it all to my family – and especially my wife Stefanie – that I could do what I did and learn what I have learned to become who I am today. My appreciation is beyond words.

